Sede Amministrativa: Università degli Studi di Padova

Dipartimento di Scienze Chimiche

CORSO DI DOTTORATO DI RICERCA IN SCIENZE MOLECOLARI
CURRICOLO: SCIENZE CHIMICHE
CICLO XXIX

COMPUCHEM APPLIED TO THE STUDY OF SEMICONDUCTIVE TRANSITION METAL COMPLEXES ARCHITECTURES.

Coordinatore: Prof. Antonino Polimeno

Supervisore: Prof. Maurizio Casarin

Dottoranda: Giulia Mangione

Table of Contents

Estratto

Il presente lavoro di tesi comprende lo studio sperimentale e teorico della struttura elettronica occupata e virtuale di due macrocicli organici π-coniugati [5,10,15,20-tetrafenilporfirina (H_2TPP) e 5,10,15,20-tetrakis(pentafluorofenil)porfirina (H_2TPP(F))] e dei corrispondenti complessi di Cu(II) (CuTPP e CuTPP(F)) in forma di film sottili depositati su superfici metalliche. L'interesse per questa famiglia di composti è determinato dalla relativa facilità con cui, agendo sulla struttura molecolare, è possibile modificarne proprietà ottiche ed elettroniche, favorendone l'applicazione in ambiti tecnologici che spaziano dalla terapia fotodinamica, alla sensoristica ed al fotovoltaico. Dal punto di vista sperimentale, per ciascuno dei quattro composti, tutte le shell elettroniche rilevanti (dai livelli di core degli atomi di C, N, F e Cu agli orbitali molecolari di frontiera occupati e virtuali) sono state studiate in modo consistente e con un grado di dettaglio che non trova precedenti in letteratura. Contestualmente, gli stati elettronici fondamentali ed eccitati di H_2TPP/CuTPP e H_2TPP(F)/CuTPP(F) sono stati studiati da un punto di vista computazionale utilizzando metodologie di calcolo formulate nell'ambito del DFT. I risultati degli esperimenti numerici hanno guidato l'assegnazione degli spettri di fotoemissione e di assorbimento di raggi X permettendo, al contempo, di ottenere una dettagliata descrizione delle interazioni metallo-legante, nonché delle perturbazioni indotte nella struttura elettronica di H_2TPP/CuTPP dalla decorazione dei gruppi fenilici periferici con atomi di fluoro. Sottoprodotto del presente lavoro di tesi è la validazione dell'approccio *two-component relativistic* ZORA nell'ambito dell'approssimazione di Tamm-Dancoff per la simulazione degli spettri di assorbimento di raggi X alle soglie L_2 e L_3 del rame.

Abstract

Metalloporphyrins, although trackable in abiotic systems, play a central role in fundamental biological processes, such as oxygen transport and storage, photosynthesis and electron transport during cellular respiration and photosynthesis. The relevance of this class of molecules is not limited to the biological environment, but it extends to important technological fields such as electronics, solar cells and sensors. Thus, it explains the continuously growing interdisciplinary interest for them and the push to develop novel porphyrin-like molecules, whose electronic and optical properties may be tuned through molecular engineering. In this thesis it is presented an experimental and theoretical study of the occupied/unoccupied electronic structure of two π-conjugated organic macrocycles [5,10,15,20-tetraphenylporphyrin (H_2TPP) and 5,10,15,20-tetrakis(pentafluorophenyl) porphyrin (H_2TPP(F))] and their Cu(II) complexes (CuTPP e CuTPP(F)) deposited as films on metallic surfaces. Several papers have been published in the past on this issue; on the other hand, I believe that my study represents a significant advance because, for the first time, all the relevant electronic shells (from the core levels of C, N, F and Cu to the occupied and unoccupied molecular orbitals) are consistently investigated with unprecedented detail. The agreement between experiments and theory is noticeable, allowing the assignment of the main features of the valence and core level spectra, as well as to correlate these features with the different atomic contributions. Moreover, new insights into the empty states of the investigated molecules and the metal-ligand bonding scheme have been gained by combining XAS data at the C, N, F K-edge and Cu $L_{2,3}$-edges with open-shell relativistic ZORA TD-DFT calculations. The excellent agreement between experimental evidence and theoretical results encourages us to apply the open-shell TD-DFT approach to different ligands and corresponding Cu complexes.

List of acronyms

ALDA adiabatic local density approximation

AO atomic orbital

DFT density functional theory

EPR electron paramagnetic resonance

ESC elimination of small components

EXAFS extended X-ray absorption fine structure

GGA generalized gradient approximation

HK Hohenberg and Kohn

$\mathcal{L}$ Ligand

KS Kohn and Sham

LDA local density approximation

M Metal

MO molecular orbital

QM quantum mechanics

RHS right-hand side

SCF self-consistent field

SO spin-orbit

SOMO singly occupied molecular orbital

SR scalar relativistic

TD-DFT time-dependent density functional theory

TD-KS time-dependent Kohn-Sham

TF Thomas-Fermi

UPS ultraviolet photoelectron spectroscopy

UV ultraviolet

XANES X-ray absorption near-edge structure

XAS X-ray absorption spectroscopy

XC exchange-correlation

XPS X-ray photoelectron spectroscopy

ZORA zeroth order regular approximation

Introduction

Porphyrins and their related complexes play a crucial role for life and several are the examples of metalloporphyrins in biological processes. The chlorophyll molecules found in cyanobacteria and in the chloroplasts of plants and algae are the dominant green pigments on Earth. They have the double main function of visible light-harvesting complexes and of transferring energy to a couple of specific target chromophores in the reaction centres of the photosystems (the units of protein complexes in thylakoid membranes where the steps of photosythesis take place). Thus, these molecules are essential for both to the earlier step of photosynthesis, and for the charge separation and electron transfers essential for the whole photosynthetic process, respectively.[1] Even though a huge number of chlorophylls can be identified in Nature, all of them share the same magnesium chlorin core, a heterocyclic aromatic molecule with three pyrrole and one pyrroline rings bonded through four methine bridges (Figure 1a). The small chemical differences among them deeply influence their absorption spectra. Moreover, the heme group, an iron(II) porphyrin-based molecule (Figure 1b), constitutes the prosthetic group of the so-called hemoproteins, in particular hemoglobin, myoglobin, and cytochromes (a superfamily of proteins present in all the domains of life, involved in the electron transport during the cellular respiration and in the photosynthesis).[1] As far as the hemoglobin protein is concerned, it is responsible of the increase of the carrying capability of oxygen transport from the environment to the cells of tissues,[2] while the myoglobin has the main function

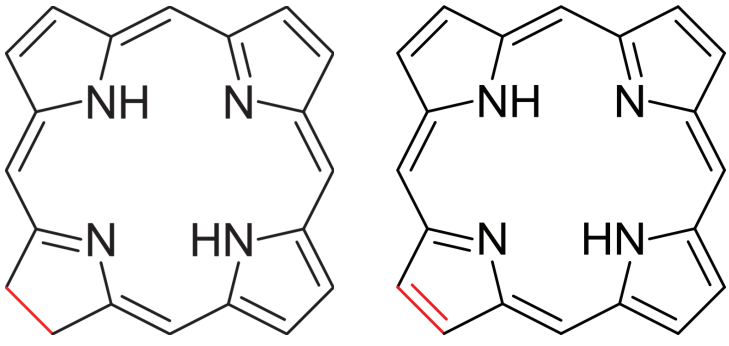

(a) Chlorin **(b)** Porphyrin

Figure 1: Structures of (a) chlorin and (b) porphyrin molecules, the fundamental cores of the chlorophyll and of the heme prosthetic group, respectively.

to facilitate the diffusion of oxygen in tissues.[1] Thus, looking at the complex and various chemistry performed in Nature by using these complexes, in the last decades great experimental and computation efforts have been invested to gain a deep understanding of the porphyrins' role in biological processes. The importance of this group of heterocyclic organic compounds is not limited to the biological environment but it spans over several important technological fields. Porphyrins are molecules that can be easily synthesized, and, acting on the three main components constituent the complexes (the central metal, the π-conjugated macrocycle and the peripheral substituent groups), the chemical properties of these systems can be finely tuned and enhanced. In particular, the macrocycle is the perfect platform on which act to achieve the desired chemical and physical properties. In fact, nowadays thanks to their versatile chemistry, both the free ligands and the metal complexes (particularly by acting as aggregates)[3] are widely used for several applications in electronics,[4] for solar photovoltaic cells[5] and for chemical sensing.[6,7] Therefore, it explains the increasing interdisciplinary interest for them and the push to develop novel porphyrin-like systems with the desired electronic and optical properties.[3,8] In particular, the possibility to employ porphyrins or related molecules (*e.g.*, phthalocyanines) with others (*e.g.*, quinones, fullerenes and carotenes)[9,10] to form dyades or triades to mimic the many constituent systems of the Photosystem II in the thylakoid membrane is very appealing.[1] The ultimate goal of such a mimicking approach is to obtain artificial devices with comparable capabilities of light-harvesting, energy and electron transfers of those taking part in natural photosynthesis for the development of a new generation of solar photovoltaic cells with comparable efficiencies to the

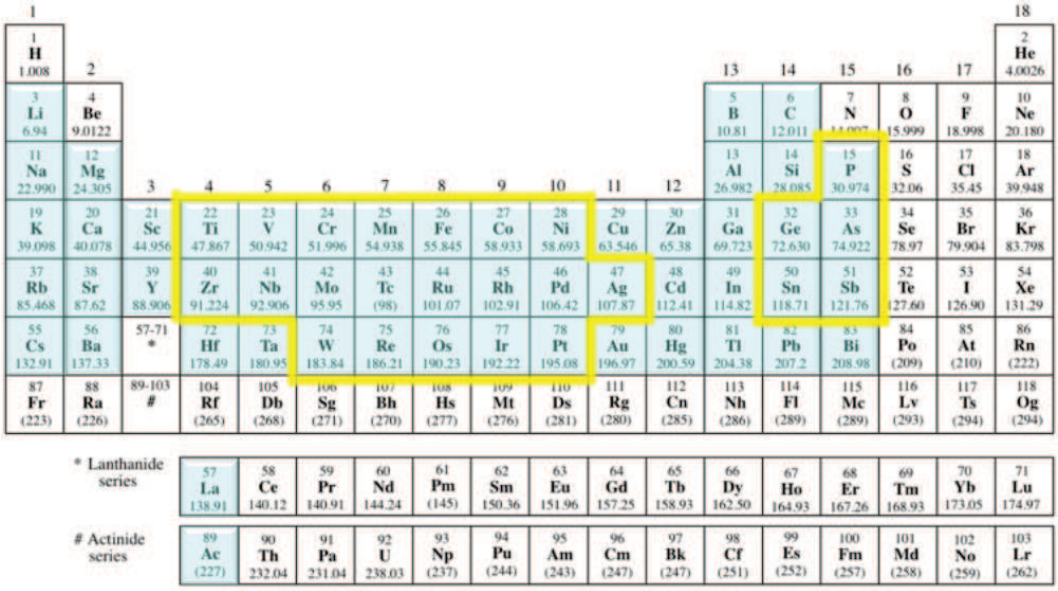

Figure 2: Periodic table showing the elements that are known to form complexes with porphyrin. Those in yellow boxes are known in more than one oxidation state within porphyrin complexes.

commonly used silicon-based solar cells.[11]

Beyond the several applications of porphyrins, it is well known that a large number of elements of the periodic table can be hosted in the coordinative pocket of these molecules (see Figure 2).[12] Due to the high versatility of these compounds, the knowledge as intimate as possible of their electronic structure is fundamental to develop the perfect architectures suitably designed for a particular application. For these reasons a deep understanding of the electronic properties of porphyrins is mandatory.

This Ph.D. thesis aims to study a specific family of compounds classified as "energy targeted materials" (corresponding to first-row transition metal complexes of π-conjugated macrocycles, such as porphyrins or their derivatives), and in particular their Cu(II) complexes. The ultimate goal of this study is to provide new insight into the electronic structure of these molecules and, in particular, into the the nature and the strength of the metal-ligand interactions by quantifying their degree of covalency.

Chapter 1

Theory of Quantum Mechanical Calculations

1.1 The Schrödinger equation

In quantum mechanics (QM) the physical state of a quantum system can be completely described, at a given moment, by a definite (in general complex) function Ψ, namely the *wave function*. Such a function is the solution of the time-dependent Schrödinger equation,[13–19] the fundamental equation of QM, describing the changes of a quantum state with time:

$$i\hbar\frac{\partial\Psi(t)}{\partial t} = \hat{H}\Psi(t) \tag{1.1.1}$$

where $\hat{H}$ is the Hamiltonian operator describing the total energy of the quantum system, and $\Psi(t)$ is the time-dependent wave function. When $\hat{H}$ does not depend explicitly by time, it coincides with the total energy operator and it corresponds to the sum of kinetic and potential energy operators. The form of the Hamiltonian operator defines the solution of the wave equation and so the wave function, as a solution of the following eigenvalue equation:

$$\hat{H}\Psi_i = \varepsilon_i\Psi_i \tag{1.1.2}$$

where the eigenvalue ε_i is the energy associated to the i-th eigenstate Ψ_i of the quantum system. Since the Hamiltonian is a Hermitian operator,* the eigenstates of $\hat{H}$ are orthogonal and form a complete basis set in the Hilbert space of the system.

The wave function itself has not a physical meaning, while its square modulus is

*An operator $\hat{A}$ is Hermitian or self-adjoint if $\hat{A}^\dagger = \hat{A}$. Eigenvalues of Hermitian operators are real and the corresponding eigenvectors are orthogonal.

associated to the probability of finding the particle described by the wave function at a given point and time. In particular, for an atomic or molecular system with N electrons, the electron density ρ is defined as the number of electrons per unit volume[20] and it is related to the square of the modulus of the wave function, $|\Psi|^2 = \Psi^*\Psi$. It is defined as:

$$\rho(\mathbf{r}) = N \int \mathrm{d}\mathbf{r}_2 \mathrm{d}\mathbf{r}_3 \ldots \mathrm{d}\mathbf{r}_N |\Psi(\mathbf{r}, \mathbf{r}_2, \mathbf{r}_3 \ldots, \mathbf{r}_N)|^2 \tag{1.1.3}$$

The equation (1.1.3) is valid if the wave function is normalized according to:

$$\langle \Psi_i \,|\, \Psi_j \rangle = \delta_{ij} \tag{1.1.4}$$

where δ_{ij} is the Kronecker delta. The integral of the electron density ρ then corresponds to the total number of electrons N:

$$\int \rho(\mathbf{r}) \mathrm{d}\mathbf{r} = N \tag{1.1.5}$$

In the non-relativistic framework, the Hamiltonian operator for a chemical system with N electrons $(i, j, \ldots)$ and M nuclei $(p, q, \ldots)$ with Z_p, Z_q, ... charges can be written as:[†]

$$\hat{H} = -\frac{1}{2m_p} \sum_{p=1}^{M} \hat{\nabla}_p^2 - \frac{1}{2} \sum_{i=1}^{N} \hat{\nabla}_i^2 - \sum_{p,i}^{M,N} \frac{Z_p}{r_{ip}} + \sum_{p<q}^{M,M} \frac{Z_p Z_q}{r_{pq}} + \sum_{i<j}^{N,N} \frac{1}{r_{ij}} \tag{1.1.6}$$

where the first and second terms refer to the kinetic energies of the nuclei and electrons, respectively, the third term accounts for the Coulomb electron-nucleus attractive interaction, while the fourth and the fifth ones are the Coulomb nucleus-nucleus and electron-electron repulsions, respectively. However, for most chemical applications, the electronic and nuclear motions can be decoupled as a consequence of the difference between the electron and the nucleus masses, and the Hamiltonian can be then written as a sum of nuclear and electronic contributions. This is known as the Born-Oppenheimer approximation,[21] and, within this approximation, the Hamiltonian of the quantum system can be rewritten as:

$$\hat{H}_\mathrm{e} = -\frac{1}{2} \sum_{i=1}^{N} \hat{\nabla}_i^2 - \sum_{p,i}^{M,N} \frac{Z_p}{r_{ip}} + \sum_{i<j}^{N,N} \frac{1}{r_{ij}} \tag{1.1.7}$$

where $\hat{H}_\mathrm{e}$ corresponds to the electronic Hamiltonian. The nuclear coordinates are treated as constants and the nuclear repulsion (the fourth term of the right-hand side (RHS) of equation (1.1.6)) is then a constant quantity for each

[†]Atomic units are used throughout the thesis.

nuclear configuration r_{pq}. The first term of $\hat{H}_{\mathrm{e}}$ corresponds to the kinetic energy operator for the N electrons ($\hat{T}$), the second one refers to the nucleus-electron Coulomb interaction ($\hat{V}_{\mathrm{ne}}$) and the third term is the electron-electron repulsion ($\hat{V}_{\mathrm{ee}}$). Interestingly, the equation (1.1.7) shows that the actual system of interest is involved in the Hamiltonian through the position and the charge of its nuclei and the total number of electrons N. If Ψ is given, the expectation value of any physical quantity can be defined as:[22]

$$\langle \hat{A} \rangle = \frac{\int \Psi^* \hat{A} \Psi \mathrm{d}x}{\int \Psi^* \Phi \mathrm{d}x} = \frac{\langle \Psi | \hat{A} | \Psi \rangle}{\langle \Psi | \Psi \rangle} \tag{1.1.8}$$

where $\hat{A}$ is the linear Hermitian operator associated to the physical quantity A.

In particular, if the wave function Ψ is normalized, the expectation values for the kinetic and the potential energies are

$$T[\Psi] = \langle \hat{T} \rangle = \int \Psi^* \hat{T} \Psi \mathrm{d}x \tag{1.1.9}$$

and

$$V[\Psi] = \langle \hat{V} \rangle = \int \Psi^* \hat{V} \Psi \mathrm{d}x \tag{1.1.10}$$

where the square brackets indicate that T and V are two distinct functionals of Ψ.[20,23]

1.2 Density Functional Theory

In the last few years the density functional theory (DFT) has not only influenced, but also revolutionized, the application of the QM principles to the study of complex systems, becoming one of the most active fields in physics during the last thirty years.[24] DFT is based on the Hohenberg and Kohn theorems,[25] the starting point for developing new computational methodologies whose ultimate goal is that of gaining a deep insight into the energetic, the structure and properties of atoms and molecules, with computational costs much lower than those associated to the use of traditional *ab-initio* methods.[26] In this section the fundamental aspects of the DFT will be shortly described, starting from the Thomas-Fermi model,[27–29] and arriving to the formulation provided by Kohn and Sham.[30]

1.2.1 The Thomas-Fermi model

The DFT stems from the Thomas-Fermi (TF) model,[27–29] according to which the quantum state of a uniform free electron gas in three dimensions can be described by its electronic density ρ_0 instead of the wave function. The electron

density can be expressed as function of the *Fermi momentum* p_f, which is defined for the highest energy one-electron occupied level as

$$p_f = \hbar k_f \tag{1.2.1}$$

$$k_f = (3\pi^2 N/V_f)^{\frac{1}{3}} \tag{1.2.2}$$

where k_f is the *Fermi wave vector*, N is the number of electrons and V_f is the spherical momentum space volume. The corresponding energy

$$\varepsilon_f = \hbar^2 k_f^2/2m \tag{1.2.3}$$

is the *Fermi energy.*[31] Thus, the electron density ρ_0 for a uniform electron gas is

$$\rho_0 = \frac{p_f^3}{3\pi^2\hbar^3} \tag{1.2.4}$$

This formulation is exact for the uniform electron gas. This has been then extended to inhomogeneous situations, such as atoms, molecules and solids in the presence of an external potential $\upsilon(\mathbf{r})$. If the inhomogeneous electron density at the point $\mathbf{r}$ is $\rho(\mathbf{r})$, when the equation defining ρ_0 is applied locally at $\mathbf{r}$, the expression for the total electronic energy is then:

$$E_{\mathrm{TF}}[\rho(\mathbf{r})] = C_{\mathrm{TF}} \int \rho^{\frac{5}{3}}(\mathbf{r})\mathrm{d}\mathbf{r} + \int \upsilon(\mathbf{r})\rho(\mathbf{r})\mathrm{d}\mathbf{r} + \frac{1}{2}\iint \frac{\rho(\mathbf{r}_1)\rho(\mathbf{r}_2)}{|\mathbf{r}_1 - \mathbf{r}_2|}\mathrm{d}\mathbf{r}_1\mathrm{d}\mathbf{r}_2 \tag{1.2.5}$$

where C_{TF} is a constant corresponding to

$$C_{\mathrm{TF}} = \frac{3}{10}(3\pi^2)^{2/3} \tag{1.2.6}$$

The first term of the RHS of the equation (1.2.5) is the kinetic energy of electrons, the second one accounts for the attraction between the electrons and the nuclei and the last term is the interelectronic repulsion. The important result they reached was that the total electronic energy for a system with N electrons, $E[\Psi]$, could be expressed as a functional, E_{TF}, of the charge density $\rho(\mathbf{r})$. The revolutionary aspect of this approach is that, for the first time, the ground state energy of a system is a functional of a physical observable like the electron density, and not a functional of the wave function, which does not correspond to a physical observable. Equation (1.2.5) is an approximate form of the rigorous expression for the electronic energy (*vide infra*), where only the stabilizing (nucleus-electron) and destabilizing (electron-electron) classical interactions are taken into account. The TF theory provides a reasonable description of the charge density for heavy atoms. In fact, it can be demonstrated that this theory is exact in the limit of

an atomic number $Z \to \infty$.[32] Nevertheless, it fails if it is applied to molecular systems, because it is unable to predict the existence of any chemical bonds: in the ambit of the TF theory, the minimum energy for an aggregate of atoms is always given by nuclei at infinite distance.[33]

1.2.2 The Hohenberg and Kohn theorems

Hohenberg and Kohn (HK)[25] revolutionized the world of theoretical chemistry demonstrating that the TF model had to be considered as an approximate form of an exact theory, now known as DFT. This is the consequence of the demonstration of the first and the second HK theorems. If we define an external potential $\upsilon(\mathbf{r}_i)$:

$$\upsilon(\mathbf{r}_i) = -\sum_p \frac{Z_p}{r_{ip}} \tag{1.2.7}$$

the first HK theorem justifies the use of $\rho(\mathbf{r})$ as basic variable. In fact, the first theorem establishes that *the external potential* $\upsilon(\mathbf{r})$ *is determined, apart from an additive constant, by the electron density* $\rho(\mathbf{r})$. Since the electron density integrates to the number of electrons N (see equation (1.1.5)), it follows that the ground state wave function and all the electronic properties of the chemical system are univocally determined by the electron density. The relation between $\rho(\mathbf{r})$ and $\upsilon(\mathbf{r})$, together with the normalization condition in (1.1.4), legitimates the use of ρ as basic variable, and allows to define the total energy in equation (1.2.5) as a functional of the electron density ρ:

$$E = E_\upsilon[\rho] = T[\rho] + V_{\mathrm{ee}}[\rho] + V_{\mathrm{ne}}[\rho] = F_{\mathrm{HK}}[\rho] + \int \rho(\mathbf{r})\upsilon(\mathbf{r})\mathrm{d}\mathbf{r} \tag{1.2.8}$$

with

$$V_{\mathrm{ne}}[\rho] = \int \rho(\mathbf{r})\upsilon(\mathbf{r})\mathrm{d}\mathbf{r} \tag{1.2.9}$$

$$F_{\mathrm{HK}}[\rho] = T[\rho] + V_{\mathrm{ee}}[\rho] \tag{1.2.10}$$

$$V_{\mathrm{ee}}[\rho] = J[\rho] + E_{\mathrm{xc}}[\rho] \tag{1.2.11}$$

where F_{HK} is the Hohenberg and Kohn functional, $J[\rho]$ represents the classic term of the Coulomb repulsion, while $E_{\mathrm{xc}}[\rho]$ corresponds to the non-classic exchange and correlation contributions to V_{ee}. It is noteworthy that $F_{\mathrm{HK}}[\rho]$ does not depend upon the external potential, resulting an universal functional of $\rho(\mathbf{r})$.

The second theorem provides the variational principle for the energy. It estab-

lishes that, *given a trial electron density* $\tilde{\rho}(\mathbf{r})$*, with* $\tilde{\rho}(\mathbf{r}) \geq 0$*, and* $\int \tilde{\rho}(\mathbf{r})\mathrm{d}\mathbf{r} = N$

$$E_0 \leq E_\upsilon[\tilde{\rho}] \tag{1.2.12}$$

where $E_\upsilon[\tilde{\rho}]$ is the energy functional obtained from equation (1.2.8) with $\rho = \tilde{\rho}(\mathbf{r})$ while E_0 is the exact ground state energy. The first HK theorem states that $\tilde{\rho}$ determines its own external potential $\upsilon(\mathbf{r})$ and its wave function $\tilde{\Psi}$, which can be used as a trial function for the minimization problem:

$$\langle\tilde{\Psi}|\hat{H}|\tilde{\Psi}\rangle = F_{\mathrm{HK}}[\tilde{\rho}] + \int \tilde{\rho}(\mathbf{r})\upsilon(\mathbf{r})\mathrm{d}\mathbf{r} = E(\tilde{\rho}) \geq E[\rho] = \langle\Psi|\hat{H}|\Psi\rangle \tag{1.2.13}$$

The validity of the HK theorems is limited by the fact that F_{HK} is defined only for those trial ρ that are *υ-representable*, where a υ-representable ρ is an electron density associated with an antisymmetric ground state wave function of an Hamiltonian having the form (1.1.7) for a local external potential $\upsilon(\mathbf{r})$. Actually, given a trial υ-representable ρ, $F_{\mathrm{HK}}[\rho]$ is a universal functional of ρ since the same value is obtained no matter what external potential is considered.[34] A limitation of $F_{\mathrm{HK}}[\rho]$ is that it is undefined for any ρ not υ-representable, and thus the theorems cannot be applied any longer. However, Hohenberg and Kohn pointed out that it has not been proved that an arbitrary density distribution containing an integral number of electrons can be realized by some external potential,[25,35] and thus $F_{\mathrm{HK}}[\rho]$ can be redefined for electrons densities ρ satisfying the weaker N-representability condition. A density is N-representable if it may be obtained from some antisymmetric wave function.[36] The conditions for an electron density ρ to satisfy the N-representability can be fulfilled by any reasonable density:[34,37]

$$\rho(\mathbf{r}) \geq 0, \qquad \int \rho(\mathbf{r})\mathrm{d}\mathbf{r} = N \qquad \text{and} \qquad \int |\nabla\rho(\mathbf{r})^{1/2}|^2 < \infty \tag{1.2.14}$$

Despite the great importance of the two HK theorems for DFT, they do not provide any operative strategy for any application. Particularly the second theorem is simply an existence theorem and does not provide any information about the construction of the ground state energy functional. In fact, the kinetic energy ($\hat{T}$) and the electron-electron interaction ($\hat{V_{\mathrm{ee}}}$) functionals in equation (1.2.8), *i.e.*, the universal functional F_{HK} in equation (1.2.10), are still unknown and the existence of an exact theory justifies the research of new functionals that, even though approximate, can be more and more accurate.

1.2.3 The Kohn-Sham equations

In 1965 Kohn and Sham (KS) proposed the most successful approach to treat indirectly the kinetic energy functional $\hat{T}[\rho]$, making DFT a powerful method for rigorous calculations.[30] Kohn and Sham proposed to introduce the orbitals into the problem in such a way that it could be possible to calculate the kinetic energy with a good approximation. The exact expression for the kinetic energy of the ground state can be expressed as:[20]

$$T[\rho] = -\frac{1}{2}\sum_{i=1}^{N} n_i \langle\psi_i|\nabla^2|\psi_i\rangle \tag{1.2.15}$$

where ψ_i are the spin orbitals and n_i are their occupation numbers. The Pauli exclusion principle[38] implies that $0 \leq n_i \leq 1$; furthermore, the first HK theorem ensures that the kinetic energy is a functional of the total charge density.[25] Any non-negative, continuous and normalized electron density ρ is N-representable and can be decomposed in:[37]

$$\rho(\mathbf{r}) = \sum_{i=1}^{N} n_i \sum_{s} |\psi_i(\mathbf{r}, s)|^2 \tag{1.2.16}$$

where $\psi_i(\mathbf{r}, s)$ represents a spin orbital with spatial coordinates $\mathbf{r}$ and spin coordinates s. Nevertheless, given an electron density, there is not an unique decomposition in terms of spin orbitals. Kohn and Sham started from considering the simplest expression for T and ρ:

$$T_{\mathrm{S}} = -\frac{1}{2}\sum_{i=1}^{N} \langle\psi_i|\nabla^2|\psi_i\rangle \tag{1.2.17}$$

and

$$\rho(\mathbf{r}) = \sum_{i=1}^{N} \sum_{s} |\psi_i(\mathbf{r}, s)|^2 \tag{1.2.18}$$

i.e., $n_i = 1$ for N spin orbitals, otherwise $n_i = 0$. The problem is to obtain an unique orbital decomposition providing one value of $T_{\mathrm{S}}[\rho]$. The simplified representation of the electron density and of the kinetic energy proposed by Kohn and Sham corresponds to a reference system of non-interacting electrons in the absence of any electron-electron repulsion, whose ground state electron density is exactly $\rho(\mathbf{r})$. In analogy with the definition of the universal functional $F_{\mathrm{HK}}[\rho]$, Kohn and Sham defined a fictitious system composed by non-interacting particles,

with ground state density $\rho(\mathbf{r})$ and Hamiltonian

$$\hat{H}_{\mathrm{S}} = -\frac{1}{2}\sum_{i=1}^{N}\nabla_i^2 + \sum_{i=1}^{N}\upsilon_{\mathrm{S}}(\mathbf{r}) \tag{1.2.19}$$

excluding any repulsive term. The ground state of such a system is exactly described by a single Slater determinant multi-electron wave function

$$\Psi_{\mathrm{S}} = \frac{1}{\sqrt{N!}}\det[\psi_1\psi_2\ldots\psi_N] \tag{1.2.20}$$

where ψ_i are the first N eigenvectors of the one-electron Hamiltonian

$$\hat{h}_{\mathrm{S}}\psi_i = \left[-\frac{1}{2}\nabla^2 + \upsilon_{\mathrm{S}}(\mathbf{r})\right]\psi_i = \varepsilon_i\psi_i \tag{1.2.21}$$

The kinetic energy of the reference system is simply $T_{\mathrm{S}}[\rho]$, given by the equation (1.2.17)

$$T_{\mathrm{S}}[\rho] = \left\langle \psi_{\mathrm{S}} \middle| -\frac{1}{2}\sum_{i=1}^{N}\nabla_i^2 \middle| \psi_{\mathrm{S}} \right\rangle = -\frac{1}{2}\sum_{i=1}^{N}\left\langle \psi_i \middle| \nabla^2 \middle| \psi_i \right\rangle \tag{1.2.22}$$

and the electron density is decomposed according to (1.2.18). Even though T_{S} can be defined univocally for any density, it is still not an exact kinetic energy functional, and the difference between the exact kinetic energy functional $T[\rho]$ and $T_{\mathrm{S}}[\rho]$ lies in its exchange-correlation part. The success of the KS method is related to the fact that $T_{\mathrm{S}}[\rho]$ is exactly the kinetic energy used to determine the ground state energy. This result can be obtained by writing

$$F[\rho] = T_{\mathrm{S}}[\rho] + J[\rho] + E_{\mathrm{xc}}[\rho] \tag{1.2.23}$$

$$J[\rho] = \frac{1}{2}\iint\frac{\rho(\mathbf{r})\rho(\mathbf{r}')}{|\mathbf{r}-\mathbf{r}'|}\mathrm{d}\mathbf{r}\mathrm{d}\mathbf{r}' \tag{1.2.24}$$

$$E_{\mathrm{xc}}[\rho] \equiv T[\rho] - T_{\mathrm{S}}[\rho] + V_{\mathrm{ee}}[\rho] - J[\rho] \tag{1.2.25}$$

where $E_{\mathrm{xc}}[\rho]$ is the exchange-correlation (XC) energy, and it includes the difference between $T[\rho]$ and $T_{\mathrm{s}}[\rho]$, usually a small quantity, and $V_{\mathrm{ee}}[\rho]$ non-classical contributions.

The Kohn and Sham iterative procedure operates as follows: defined an external potential $\upsilon(\mathbf{r})$, the orbitals are obtained by solving the N one-electron equations:

$$\left[-\frac{1}{2}\nabla^2 + \upsilon(\mathbf{r}) + \int\frac{\rho(\mathbf{r}')}{|\mathbf{r}-\mathbf{r}'|}\mathrm{d}\mathbf{r} + \upsilon_{\mathrm{xc}}(\mathbf{r})\right]\psi_i = \varepsilon_i\psi_i \tag{1.2.26}$$

where the XC potential $v_{xc}(\mathbf{r})$ is defined as the functional derivative of the XC energy $E_{xc}[\rho]$[20]

$$v_{xc}(\mathbf{r}) = \frac{\delta E_{xc}[\rho]}{\delta \rho(\mathbf{r})} \tag{1.2.27}$$

The electron density ρ is computed through the equation (1.2.18) and the new density ρ is substituted in the equation (1.2.26) where it is used to compute the new orbitals ψ_i. The iterative cycle is repeated until self-consistency is reached. The total energy for the system at each step is:

$$E = -\frac{1}{2}\sum_{i=1}^{N} \langle \psi | \nabla^2 | \psi_i \rangle + J[\rho] + E_{xc}[\rho] + \int v(\mathbf{r})\rho(\mathbf{r})\mathrm{d}\mathbf{r} \tag{1.2.28}$$

1.2.4 Electronic exchange and correlation

To evaluate the total energy of a chemical system (see equation (1.2.28)), thanks to Kohn and Sham a procedure to compute the kinetic energy has been developed. As far as the electron-electron repulsion V_{ee} is concerned, it has been already pointed out that it is the sum of two contributions, $J[\rho]$ and $E_{xc}[\rho]$ (see equation (1.2.11)). The exact form of the XC functional $E_{xc}[\rho]$ is still unknown, and thus several approximated forms have been so far proposed to gain fairly accurate results on different chemical systems. We can define the *exchange-correlation hole* as:

$$h_{xc}(\mathbf{r}_1, \mathbf{r}_2) = \frac{\rho_2(\mathbf{r}_1, \mathbf{r}_2)}{\rho(\mathbf{r}_1)} - \rho(\mathbf{r}_2) \tag{1.2.29}$$

where $\rho_2(\mathbf{r}_1, \mathbf{r}_2)$ is the pair density for a system with N electrons (*i.e.*, the probability of finding two electrons simultaneously within the volume elements $\mathrm{d}\mathbf{r}_1$ and $\mathrm{d}\mathbf{r}_2$), while the other $N-2$ electrons may be anywhere

$$\rho_2(\mathbf{r}_1, \mathbf{r}_2) = N(N-1)\int \mathrm{d}\mathbf{r}_3 \mathrm{d}\mathbf{r}_4 \ldots \mathrm{d}\mathbf{r}_N |\Psi(\mathbf{r}_1, \mathbf{r}_2, \ldots, \mathbf{r}_N)|^2 \tag{1.2.30}$$

Then the interelectronic repulsion V_{ee} can be rewritten:

$$\begin{aligned} V_{ee} &= \frac{1}{2}\iint \frac{1}{r_{12}}\rho(\mathbf{r}_1)\rho(\mathbf{r}_2)\mathrm{d}\mathbf{r}_1\mathrm{d}\mathbf{r}_2 + \frac{1}{2}\iint \frac{1}{r_{12}}\rho(\mathbf{r}_1)h_{xc}(\mathbf{r}_1, \mathbf{r}_2)\mathrm{d}\mathbf{r}_1\mathrm{d}\mathbf{r}_2 \\ &= J[\rho] + E_{xc} \end{aligned} \tag{1.2.31}$$

The exchange and the correlation maintain the electrons apart, so the exchange and the correlation contributions can be described in terms of a hole surrounding each electron and avoiding other electrons from approaching it. The better the h_{xc} is approximated, the better is the accuracy reached by the resulting functional $E_{xc}[\rho]$. The accuracy of DFT calculations strongly depends upon the quality of the approximations adopted for $v_{ex}(\mathbf{r})$ in equation (1.2.27), and for the corresponding

$E_{\mathrm{xc}}[\rho]$ in equation (1.2.11). It is noteworthy that the HK theorems are valid only with the exact XC functional, whereas they are not for the approximated forms. Thus, practical approaches to DFT are no longer variational.

Common approximated XC functionals can be divided in six main groups, each of them related to different levels of approximation. The simplest approximation is the local density approximation (LDA) and the XC functionals belonging to this groups depend only on the local value of the electron density $\rho(\mathbf{r})$:

$$E_{\mathrm{xc}}^{\mathrm{LDA}} = \int \rho(\mathbf{r})\varepsilon_{\mathrm{xc}}(\rho)\mathrm{d}\mathbf{r} \tag{1.2.32}$$

where $\varepsilon_{\mathrm{xc}}$ is the XC energy per electron and it is given by the uniform electron gas formula in the ambit of the TF theory. The XC energy can be split in two terms:

$$\varepsilon_{\mathrm{xc}} = \varepsilon_{\mathrm{x}} + \varepsilon_{\mathrm{c}} \tag{1.2.33}$$

where the exchange energy contribution ε_{x} is defined as:[39]

$$\varepsilon_{\mathrm{x}}^{\mathrm{LDA}}[\rho] = -\frac{3}{4}\left(\frac{3}{\pi}\right)^{1/3}\int \rho(\mathbf{r})^{4/3}\mathrm{d}\mathbf{r} \tag{1.2.34}$$

while the correlation term ε_{c} is obtained analytically by interpolating the quantum Monte Carlo results[40–43] or by adopting other approaches.[44–46] Despite the rather rough approximation, the LDA works surprisingly well for describing many real chemical systems. Later on, more complex schemes aimed to overcome the LDA limits have been proposed to reach a better accuracy of the method. In this regard, it is noteworthy that the main source of error in the LDA based $E_{\mathrm{xc}}[\rho]$ lies in the exchange component and many contributions have been then focused on the research of suitable corrections of ε_{x}. Thus, to go beyond LDA, the inhomogeneity of the electron density must be considered. The exchange energy is calculated by adding to the LDA based $E_{\mathrm{xc}}[\rho]$ the non-local correction term ($E_{\mathrm{x}}^{\mathrm{NL}}$), which depends upon the gradient of the electron density, in order to take somehow into account the non-uniformity of the density in a real system. This class of functionals are called *generalized gradient approximation* (GGA) functionals and the exchange functional has the following general form:

$$E_{\mathrm{x}}^{\mathrm{GGA}} = E_{\mathrm{x}}^{\mathrm{LDA}} - \int g(\chi)\rho^{4/3}(\mathbf{r})\mathrm{d}\mathbf{r} \tag{1.2.35}$$

where $g(\chi)$ is a function of the parameter χ

$$\chi = \frac{|\nabla\rho(\mathbf{r})|}{\left[\rho(\mathbf{r})\right]^{4/3}} \tag{1.2.36}$$

and the form of $g(\chi)$ depends on the particular GGA functional under consideration. Great attention has been devoted to find the gradient correction able to provide values of the exchange energy closer to the exact quantity, and in literature many non-local corrections are available.[47–54] A further family of XC functions is that of the so-called *meta-GGA* functionals, whose formula includes a contribution related to the positive kinetic energy density of the occupied KS orbitals.[55] Two other classes of XC functionals with approximations more complicated and more accurate can be considered: in the *hyper-GGA* functionals the exact exchange energy density is added,[56] while the *generalized random phase approximation* functionals consider the unoccupied orbitals.[57] It can be observed that increasing the approximations' complexity typically more accurate results can be achieved with computation costs increasing modestly from the LDA to the meta-GGA and much more steeply after that.[58] Finally, another important class of XC functionals uses the KS orbitals of the chemical system to compute the exchange through its exact formula from the Hartree-Fock theory, and for this reason these are called *hybrid* functionals.[59–61]

Chapter 2

Relativistic Effects in Quantum Mechanical Calculations

2.1 The effects of Relativity in Chemistry

One of the starting points of the special relativity[62,63] is that it is impossible to accelerate particles to speeds higher than the light speed c. This is caused by the mass increase:

$$m = \frac{m_0}{\sqrt{1 - \left(\frac{v}{c}\right)^2}} \tag{2.1.1}$$

where m_0 is the electron rest mass and v is its speed. In Chemistry, the relativity entails three main effects:[64,65]

1. the concomitant relativistic contraction and energetic stabilization of the s and p orbitals.
   The Bohr radius, a_0, contains the mass m in the denominator:

   $$a_0 = \frac{4\pi\varepsilon_0\hbar^2}{Zme^2} \tag{2.1.2}$$

   where Z is the atomic number and ε_0 is the vacuum dielectric constant. The contraction of the relativistic average radius is a consequence of the reduction of the Bohr radius for inner electrons, having higher speeds near the nucleus.

2. The spin-orbit (SO) splitting. In a relativistic approach neither ℓ, the quantum number related to the orbital angular momentum $\boldsymbol{\ell}$, nor s, the one associated to the spin angular momentum $\mathbf{s}$, are "good" quantum numbers. In fact, within the j-j scheme the "good" quantum numbers are j, related to the vector sum $\boldsymbol{\ell} + \mathbf{s} = \mathbf{j}$, and m_j, the quantum number associated to the projection of $\mathbf{j}$ along the z axis. Thus, for a p electron ($\ell = 1$) two values

of j (1/2, 3/2) are possible. Because the SO interaction increases when increasing Z, this effect becomes more and more important for heavy atoms.

3. the radial expansion and the energetic destabilization of d and f orbitals. The effective potential experienced by d and f electrons is weaker than that expected without considering the relativistic affects: the s and p atomic orbitals (AOs), more contracted, screen the nuclear attraction more efficiently. These effects justify the radial expansion of d and f AOs and their resultant energetic destabilization.

In the next sections, after introducing the Dirac equation (the starting point of the relativistic quantum mechanics), some information about the zeroth order regular approximation (ZORA), which includes the relativistic effects into the description of the electronic structure of complex systems, will be provided.

2.2 The Dirac equation

The time-dependent equation describing the motion of a free electron from a relativistic point of view has been developed by Dirac.[66,67] This equation is the relativistic analogous of the Schrödinger equation (1.1.1)

$$i\hbar\frac{\partial\Psi(\mathbf{r},t)}{\partial t} = \hat{H}_{\mathrm{D}}\Psi(\mathbf{r},t) \tag{2.2.1}$$

where $\hat{H}_{\mathrm{D}}$ is the four-component Dirac Hamiltonian

$$\hat{H}_{\mathrm{D}} = c\,\boldsymbol{\alpha}\cdot\mathbf{p} + m_0\,c^2\boldsymbol{\beta}. \tag{2.2.2}$$

The momentum operator is

$$\mathbf{p} = -i\hbar\nabla, \tag{2.2.3}$$

$\boldsymbol{\beta}$ is a traceless 4×4 diagonal matrix

$$\boldsymbol{\beta} = \begin{pmatrix} \mathbf{1}_2 & \mathbf{0} \\ \mathbf{0} & -\mathbf{1}_2 \end{pmatrix} \tag{2.2.4}$$

with

$$\mathbf{1}_2 = \begin{pmatrix} 1 & 0 \\ 0 & 1 \end{pmatrix}; \qquad \mathbf{0} = \begin{pmatrix} 0 & 0 \\ 0 & 0 \end{pmatrix}, \tag{2.2.5}$$

$\boldsymbol{\alpha}$ is a three-component vector $\boldsymbol{\alpha} = \big(\boldsymbol{\alpha}_x\, \boldsymbol{\alpha}_y\, \boldsymbol{\alpha}_z\big)$, where each component is a traceless 4×4 diagonal matrix

$$\boldsymbol{\alpha}_s = \begin{pmatrix} \mathbf{0} & \boldsymbol{\sigma}_s \\ \boldsymbol{\sigma}_s & \mathbf{0} \end{pmatrix} \quad \text{with } s = x, y, z \tag{2.2.6}$$

and $\boldsymbol{\sigma}_s$ are the Pauli spin matrices (a set of three complex, Hermitian and unitary matrices)

$$\boldsymbol{\sigma}_x = \begin{pmatrix} 0 & 1 \\ 1 & 0 \end{pmatrix};\ \boldsymbol{\sigma}_y = \begin{pmatrix} 0 & -i \\ i & 0 \end{pmatrix};\ \boldsymbol{\sigma}_z = \begin{pmatrix} 1 & 0 \\ 0 & -1 \end{pmatrix} \tag{2.2.7}$$

These matrices has been introduced by Pauli to describe the three components of the spin angular momentum.[68] As a whole, the Dirac equation consists of four differential equations, and the wave function $\Psi(\mathbf{r}, t)$ is a four-component vector called *spinor*. The four components of the spinor $\Psi(\mathbf{r}, t)$ represent two different two-component wave functions $\phi = (\phi_1, \phi_2)$ and $\chi = (\chi_1, \chi_2)$, known as *large* and *small* components, respectively:

$$\Psi(\mathbf{r}, t) = \begin{pmatrix} \phi_1(\mathbf{r}, t) \\ \phi_2(\mathbf{r}, t) \\ \chi_1(\mathbf{r}, t) \\ \chi_2(\mathbf{r}, t) \end{pmatrix} = \begin{pmatrix} \phi(\mathbf{r}, t) \\ \chi(\mathbf{r}, t) \end{pmatrix} \tag{2.2.8}$$

where ϕ_1, χ_1 and ϕ_2, χ_2 describe the spin up and the spin down of the free electron, respectively. Now, if a potential field V is considered, the Hamiltonian operator in the equation (2.2.1) becomes

$$\hat{H} = \hat{H}_{\mathrm{D}} + V = c\, \boldsymbol{\alpha} \cdot \mathbf{p} + m_0\, c^2 \boldsymbol{\beta} + V \tag{2.2.9}$$

Thus, the time-independent Dirac equation is

$$\big(E - V - m_0\, c^2 \boldsymbol{\beta} - c\, \boldsymbol{\alpha} \cdot \mathbf{p}\big)\Psi(\mathbf{r}, t) = 0 \tag{2.2.10}$$

The explicit solution of the Dirac equation can be obtained only for a hydrogen-like system.[69] To define the state of such a system four quantum numbers, which are not the ones derived by solving the Schrödinger equation, are needed. In addition to n and ℓ, the introduction of j and m_j is required. As already mentioned, the former is the total angular momentum quantum number, whose relationship with the total angular momentum $\mathbf{j}$ is:

$$|\mathbf{j}| = \sqrt{j(j+1)}\hbar \tag{2.2.11}$$

while the latter is associated to the $2j+1$ projections of $\mathbf{j}$ along the z axis:

$$j_z = m_j \hbar \tag{2.2.12}$$

2.3 The zeroth order regular approximation

Even though relativistic calculations are not much more complicated than the non-relativistic ones, they imply a relevant computational cost. In fact, the dimensions of the secular problem are very large due to the spinors' nature. Different basis sets for the small and large components of the Dirac spinors would be required, and this obviously would increase the basis set dimensions, implying significant computational costs and storage requirements. Thus, the study of complex systems with the inclusion of relativistic effects requires the use of approximate computational methods. The most frequent approach is that of transforming the four-component Dirac Hamiltonian in a two-component form. Several methods are available, and a standard approach to treat the problem is the elimination of small components (ESC).[70–72]

2.3.1 Regular expansion of the energy in relativistic quantum mechanics

Like other traditional approaches in relativistic QM for generating two-component Hamiltonians, the ESC is based on the expansion of the energy E of the chemical system in $(E-V)/2c^2$, an approach defective in the case of Coulomb-like potentials. For this reason, a "regular" expansion of the energy (the term has been coined by van Lenthe *et al.* in 1993[73] because of the expansion properties) in $E/(2c^2-V)$ has been introduced, which is valid for Coulomb-like potentials over all space.

In the relativistic quantum theory, the four-component Dirac equation (2.2.10) is the starting point. The Dirac Hamiltonian (2.2.9) works on a four-component wave function, defined in equation (2.2.8). The Dirac equation is:

$$V\phi + c\boldsymbol{\sigma}\cdot\mathbf{p}\chi = E\phi \tag{2.3.1}$$

$$c\boldsymbol{\sigma}\cdot\mathbf{p}\phi + \left(V - 2c^2\right)\chi = E\chi \tag{2.3.2}$$

To reduce the Hamiltonian to operate on a two-component wave function the small component is eliminated:[73]

$$\chi = \frac{1}{E+2c^2-V} c\,\boldsymbol{\sigma}\cdot\mathbf{p}\phi = \frac{1}{2c}\left(1+\frac{E-V}{2c^2}\right)^{-1}\boldsymbol{\sigma}\cdot\mathbf{p}\phi \equiv \bar{X}\phi \tag{2.3.3}$$

where $\bar{X}$ is the operator

$$\bar{X} = \frac{1}{2c}\left(1 + \frac{E-V}{2c^2}\right)^{-1} \boldsymbol{\sigma}\cdot\mathbf{p} \tag{2.3.4}$$

Thus,

$$\hat{H}^{\mathrm{ESC}}\phi = V\phi + c\,\boldsymbol{\sigma}\cdot\mathbf{p}\bar{X}\phi \equiv V\phi + \frac{1}{2}\boldsymbol{\sigma}\cdot\mathbf{p}\left(1 + \frac{E-V}{2c^2}\right)^{-1}\boldsymbol{\sigma}\cdot\mathbf{p}\phi \;= E\phi \tag{2.3.5}$$

where $\hat{H}^{\mathrm{ESC}}$ is energy dependent and it operates only on the large component ϕ, which, at variance with the four-component Ψ, is not normalized. For this reason, a normalization operator $\hat{O} = \sqrt{1 + \bar{X}^{\dagger}\bar{X}}$ is required to generate a normalized two-component wave function $\Phi = \hat{O}\phi$, and the corresponding Hamiltonian becomes

$$\hat{H} = \hat{O}\hat{H}^{\mathrm{ESC}}\hat{O}^{-1} = \sqrt{1 + \bar{X}^{\dagger}\bar{X}}\left(V + c\,\boldsymbol{\sigma}\cdot\mathbf{p}\bar{X}\right)\frac{1}{\sqrt{1 + \bar{X}^{\dagger}\bar{X}}} \tag{2.3.6}$$

Now, if the factor $\left[1 + (E-V)/\,2c^2\right]^{-1}$ in $\bar{X}$, for both $\hat{H}^{\mathrm{ESC}}$ and $\hat{O}$, is expanded in $(E-V)/2c^2$ and some manipulation is done, at the first order the Pauli Hamiltonian is obtained:

$$\hat{H}^{\mathrm{Pauli}} = V + \frac{p^2}{2} - \frac{p^4}{8c^2} + \frac{\Delta V}{8c^2} + \frac{1}{4c^2}\boldsymbol{\sigma}\cdot(\nabla V \times \mathbf{p}) \tag{2.3.7}$$

where the third term of the RHS $(-p^4/8c^2)$ is the mass–velocity term and it arises from the variation of the mass with the velocity; the fourth term $\left(\Delta V/8c^2\right)$ is the Darwin operator, and it has no classical analogue, and finally the last term includes the SO coupling. The solution of the eigenvalue equation $H^{\mathrm{Pauli}}\Phi = E\Phi$ presents many problems. To bypass them, its solution is possible by expanding the Hamiltonian $\hat{H}^{\mathrm{ESC}}$ in equation (2.3.5) in $1/\left(2c^2 - V\right)$ (or in $E/\left(2c^2 - V\right)$):

$$\hat{H}^{\mathrm{ESC}} \approx V + \boldsymbol{\sigma}\cdot\mathbf{p}\frac{c^2}{2c^2 - V}\boldsymbol{\sigma}\cdot\mathbf{p} - \boldsymbol{\sigma}\cdot\mathbf{p}\left(\frac{c^2}{2c^2 - V}\right)\frac{E}{2c^2 - V}\boldsymbol{\sigma}\cdot\mathbf{p} + \ldots \tag{2.3.8}$$

For a Coulomb-like potential, this expansion is justified even near the singularity of the potential at the nucleus. The zeroth order Hamiltonian within the zeroth order regular approximation can be now defined:

$$\hat{H}^{\mathrm{ZORA}} = V + \boldsymbol{\sigma}\cdot\mathbf{p}\frac{c^2}{2c^2 - V}\boldsymbol{\sigma}\cdot\mathbf{p} \tag{2.3.9}$$

The zeroth order Hamiltonian is expected to incorporate relativistic effects, which are traditionally included only at the Pauli Hamiltonian level.[73] As pointed out before, the ESC is just one of the available methods which can be used to derive the

zeroth order Hamiltonian. The Hamiltonian in equation (2.3.9) can be expanded as:

$$\hat{H}^{\mathrm{ZORA}} = V + \boldsymbol{\sigma}\cdot\mathbf{p}\frac{c^2}{2c^2-V}\boldsymbol{\sigma}\cdot\mathbf{p} = V + \mathbf{p}\frac{c^2}{2c^2-V}\mathbf{p} + \frac{c^2}{\left(2c^2-V\right)^2}\boldsymbol{\sigma}\cdot\left(\nabla V\times\mathbf{p}\right) \tag{2.3.10}$$

showing that the SO term, in the regularized form, is already present in this zeroth order Hamiltonian. The SO term is regular for the presence of the factor $(2c^2-V)^{-2}$, which does not generate any problem in variational calculations. The corresponding eigenvalue equation for fully relativistic calculations is then:

$$\begin{aligned}
\hat{H}^{\mathrm{ZORA}}\Phi^{\mathrm{ZORA}} &= \left(V + \boldsymbol{\sigma}\cdot\mathbf{p}\frac{c^2}{2c^2-V}\boldsymbol{\sigma}\cdot\mathbf{p}\right)\Phi^{\mathrm{ZORA}} \\
&= \left(V + \mathbf{p}\frac{c^2}{2c^2-V}\mathbf{p} + \frac{c^2}{\left(2c^2-V\right)^2}\boldsymbol{\sigma}\cdot\left(\nabla V\times\mathbf{p}\right)\right)\Phi^{\mathrm{ZORA}} \\
&= \left(H_{\mathrm{SR}}^{\mathrm{ZORA}} + H_{\mathrm{SO}}^{\mathrm{ZORA}}\right)\Phi^{\mathrm{ZORA}} \\
&= E^{\mathrm{ZORA}}\Phi^{\mathrm{ZORA}}
\end{aligned} \tag{2.3.11}$$

The Hamiltonian $\hat{H}^{\mathrm{ZORA}}$ in equation (2.3.11) is constituted by two terms $H_{\mathrm{SR}}^{\mathrm{ZORA}}$ and $H_{\mathrm{SO}}^{\mathrm{ZORA}}$ corresponding to the scalar relativistic (SR) and SO Hamiltonians, respectively. Therefore, the SR eigenvalue equation can be introduced:

$$\hat{H}_{\mathrm{SR}}^{\mathrm{ZORA}}\Phi_{\mathrm{SR}}^{\mathrm{ZORA}} = \left(V + \mathbf{p}\frac{c^2}{2c^2-V}\mathbf{p}\right)\Phi_{\mathrm{SR}}^{\mathrm{ZORA}} = E_{\mathrm{SR}}^{\mathrm{ZORA}}\Phi_{\mathrm{SR}}^{\mathrm{ZORA}} \tag{2.3.12}$$

Moreover, the one-electron energies can be further improved by defining the scaled ZORA energy for both fully relativistic calculations:[74]

$$E^{\mathrm{scaled}} = \frac{E^{\mathrm{ZORA}}}{1 + \langle\Phi^{\mathrm{ZORA}}|\boldsymbol{\sigma}\cdot\mathbf{p}\frac{c^2}{(2c^2-V)^2}\boldsymbol{\sigma}\cdot\mathbf{p}|\Phi^{\mathrm{ZORA}}\rangle} \tag{2.3.13}$$

and scalar relativistic calculations:

$$E_{\mathrm{SR}}^{\mathrm{scaled}} = \frac{E_{\mathrm{SR}}^{\mathrm{ZORA}}}{1 + \langle\Phi_{\mathrm{SR}}^{\mathrm{ZORA}}|\mathbf{p}\frac{c^2}{(2c^2-V)^2}\mathbf{p}|\Phi_{\mathrm{SR}}^{\mathrm{ZORA}}\rangle} \tag{2.3.14}$$

2.3.2 Relativistic Kohn-Sham equations

For practical applications, the one-electron wave functions expressed as Kohn-Sham orbitals are expanded in basis functions. Solving the SR-ZORA equations, the "kinetic energy" matrix elements between the basis functions ϕ_i and ϕ_j can be

obtained:

$$\langle \phi_i | T_{\mathrm{SR}}^{\mathrm{ZORA}} | \phi_j \rangle = \left\langle \phi_i \left| \mathbf{p} \frac{c^2}{2c^2 - V} \mathbf{p} \right| \phi_j \right\rangle \tag{2.3.15}$$

and usually the point group symmetry of the molecule is used to block-diagonalize the Hamiltonian matrix. When dealing with fully relativistic calculations (*i.e.*, the SO coupling is included in the ZORA Hamiltonian), in addition to the evaluation of the SR-ZORA "kinetic energy" in equation (2.3.15), the ZORA SO matrix elements are also needed:

$$\langle \phi_i^d | H_{\mathrm{SO}}^{\mathrm{ZORA}} | \phi_j^d \rangle = \left\langle \phi_i^d \left| \frac{c^2}{(2c^2 - V)^2} \boldsymbol{\sigma} \cdot (\nabla V \times \mathbf{p}) \right| \phi_j^d \right\rangle \tag{2.3.16}$$

where ϕ_i^d and ϕ_j^d are the double group symmetry adapted functions, $\phi_{i,j}(\mathbf{r}, s) = \phi_{i,j}^{\alpha}(\mathbf{r})\alpha + \phi_{i,j}^{\beta}(\mathbf{r})\beta$, where α and β are the spin up and spin down, respectively. Finally, the calculation of the fully relativistic scaled ZORA orbital energies in equation (2.3.13) requires the evaluation of the following matrix elements:

$$\begin{aligned} \left\langle \phi_i^d \left| \boldsymbol{\sigma} \cdot \mathbf{p} \frac{c^2}{(2c^2 - V)^2} \boldsymbol{\sigma} \cdot \mathbf{p} \right| \phi_j^d \right\rangle = \left\langle \phi_i^d \left| \mathbf{p} \frac{c^2}{(2c^2 - V)^2} \mathbf{p} \right| \phi_j^d \right\rangle + \\ + \left\langle \phi_i^d \left| \boldsymbol{\sigma} \cdot \nabla \left(\frac{c^2}{(2c^2 - V)^2} \right) \times \mathbf{p} \right| \phi_j^d \right\rangle \end{aligned} \tag{2.3.17}$$

where the first term is already present in the SR-ZORA case (see equation (2.3.14)). It is worth of note that these matrix elements must be computed only once since the scaled ZORA orbital energies are calculated only after self-consistency is reached.[74–78]

Chapter 3

Quantum Mechanical Calculations for Time-Dependent Systems

When a system in equilibrium conditions is subject to some external perturbation, *e.g.*, an electromagnetic field, the system responds to the perturbation, and if such a perturbation is weak enough, the response is linear with respect to it. For instance, in the UV-visible spectroscopy, most experiments involve the absorption of energy from a weak field. At variance to that, if the field is much stronger, non-linear optical effects take place. In the forthcoming discussion the latter effects will not be considered.

3.1 Time-Dependent Density Functional Theory

Time-dependent properties, *e.g.*, frequency-dependent polarizability and excitation energies, need a time-dependent theory to be applied. In 1984, Runge and Gross provided the theoretical basis of the time-dependent density functional theory (TD-DFT),[79] demonstrating the analogous of the HK theorems[25] for time-dependent systems. Density functional theory is based on the existence of an exact mapping between the electron density ρ and the external potential $v(\mathbf{r})$. In the ground state DFT the existence proof is based on the Rayleigh-Ritz minimum principle of energy, which cannot be extended in the time-dependent domain. For this reason, Runge and Gross started from the time-dependent Schrödinger equation:

$$i\frac{\partial}{\partial t}\Phi(t) = \hat{H}(t)\Phi(t), \qquad \Phi(t_0) = \Phi_0 \tag{3.1.1}$$

where the Hamiltonian consists of the kinetic energy of the electrons, a spin-independent electron-electron Coulomb repulsion term and a time-dependent, local, and spin independent single-particle potential; in addition to that, $\Phi(t_0)$ is the initial many-particle wave function.[79] By solving the equation (3.1.1) with

different potentials $v(\mathbf{r},t)$ and a fixed initial state Φ_0, a one-to-one mapping F between the time-dependent potential and the time-dependent state $v(\mathbf{r},t) \rightarrow \Phi(t)$ can be obtained. Later, they evaluated the densities for all the time-dependent wave functions resulting from F:

$$\rho(\mathbf{r},t) = \langle \Phi(t)|\hat{\rho}(\mathbf{r})|\Phi(t)\rangle \tag{3.1.2}$$

where $\hat{\rho}(\mathbf{r}) = \sum_s \hat{\psi}_s^\dagger(\mathbf{r})\hat{\psi}_s(\mathbf{r})$ is the density operator. This defines a new one-to-one mapping G between the time-dependent potential and the time-dependent densities: $v(\mathbf{r},t) \rightarrow \rho(\mathbf{r},t)$.[79] To demonstrate a time-dependent form of the HK theorems, it has to be shown that the map G is invertible, but a perfect one-to-one correspondence is not possible in a time-dependent case. In fact, for two potentials $V(t)$ and $\tilde{V}(t)$ differing by an additive time-dependent scalar function $c(t)$ ($\tilde{V}(\mathbf{r},t) = V(\mathbf{r},t) + c(t)$), the corresponding wave functions will differ by a time-dependent phase, $\tilde{\Phi}(t) = e^{-i\alpha(t)}\Phi(t)$, with $\dot{\alpha}(t) = c(t)$, so that the resulting electron densities will be identical, $\tilde{\rho}(\mathbf{r},t) = \rho(\mathbf{r},t)$. Nevertheless, if it is possible to demonstrate the invertibility of G up to the additive time-dependent function, then the wave function is fixed by the density up to the time-dependent phase: $\Phi(t) = FG^{-1}\rho(\mathbf{r},t)$ and any expectation value $\langle \Phi(t)|\hat{O}|\Phi(t)\rangle$ can be considered a functional of the density.[79] It has been already mentioned that the proof of the HK theorems, whose demonstration is not herein reported, is based on the Rayleigh-Ritz principle. As a consequence of the minimum principle unavailability in a time-dependent system, Runge and Gross proved the theorems only in two particular cases:

i. if the potential $v(\mathbf{r},t)$ is a function having a periodic dependence on time;

ii. if the potential consists of a static part and a small time-dependent perturbation ($v(\mathbf{r},t) = v_0(\mathbf{r}) + v_{\text{ext}}(\mathbf{r},t)$).

The latter case is the only one of interest in the forthcoming discussion.

3.2 Time-dependent Kohn-Sham equations

Analogously to the ground state DFT,[25,30] where the density of the system is provided by the Kohn-Sham equations, Runge and Gross started from non-interacting electrons moving in a local potential $v(\mathbf{r},t)$ to find the time-dependent density of the chemical system. A set of time-dependent KS (TD-KS) equations are introduced to define the density of a time-dependent system.[80] The density of

an interacting system is identical to:

$$\rho(\mathbf{r},t) = \sum_{i=1}^{\text{occ}} n_i |\phi_i(\mathbf{r},t)|^2 \tag{3.2.1}$$

which is the density of the non-interacting system moving in the local potential $v_{\text{S}}(\mathbf{r},t)$, described by the KS equation:

$$i\frac{\partial}{\partial t}\phi_i(\mathbf{r},t) = \left[-\frac{1}{2}\nabla^2 + v_{\text{S}}(\mathbf{r},t)\right]\phi_i(\mathbf{r},t) \tag{3.2.2}$$

Similarly to the static case, the time-dependent KS potential $v_{\text{S}}(\mathbf{r},t)$ in the equation (3.2.2) has the following definition:

$$v_{\text{S}}(\mathbf{r},t) = v_{\text{ext}}(\mathbf{r},t) + v_{\text{H}}(\mathbf{r},t) + v_{\text{xc}}(\mathbf{r},t) \tag{3.2.3}$$

where

$$v_{\text{H}}(\mathbf{r},t) = \int \mathrm{d}\mathbf{r}\,' \frac{\rho(\mathbf{r}\,',t)}{|\mathbf{r}-\mathbf{r}\,'|} \tag{3.2.4}$$

is the Hartree potential, which is trivially calculated from the density $\rho(\mathbf{r},t)$, $v_{\text{ext}}(\mathbf{r},t)$ is the external potential (corresponding to the Coulomb field generated by the nuclei $v_0(\mathbf{r})$ and, if present, the external fields), and $v_{\text{xc}}(\mathbf{r},t)$ is the time-dependent XC potential, an unknown functional of the time-dependent density.[81] By adopting the appropriate approximations for the time-dependent $v_{\text{xc}}(\mathbf{r},t)$, the TD-KS scheme consists of the iteratively solutions of equations (3.2.1) and (3.2.2) by employing the variational principle in a self-consistent field (SCF) scheme, to obtain the time-dependent density of the chemical system in the presence of a time-dependent external perturbation, *e.g.*, the electric field of an electromagnetic radiation.

3.3 Equations for the linear density response

If the perturbation is not intense, the problem can be discussed by using the time-dependent perturbation theory. Now, the response of the system is evaluated when the perturbation $v_1(\mathbf{r},t)$ is switched on adiabatically at time $t = t_0$. In fact, at $t < t_0$ the system is described by a time-independent density $\rho_0(\mathbf{r})$ resulting from the potential $v_0(\mathbf{r})$ solving the ground state KS equations.[30] If the external potential v_{ext} has the following structure:

$$v_{\text{ext}}(\mathbf{r},t) = \begin{cases} v_0(\mathbf{r}) & \text{if } t < t_0 \\ v_0(\mathbf{r}) + v_1(\mathbf{r},t) & \text{if } t \geq t_0 \end{cases} \tag{3.3.1}$$

the linear density response $\rho_1(\mathbf{r},t)$ can be evaluated in terms of the full response function $\chi(\mathbf{r},t;\mathbf{r}\,',t')$ of the interacting system:

$$\rho_1(\mathbf{r},t) = \int \mathrm{d}^3\mathbf{r}\,' \int_{t_0}^{\infty} \mathrm{d}t' \chi(\mathbf{r},t;\mathbf{r}\,',t') v_1(\mathbf{r}\,',t') \tag{3.3.2}$$

Alternatively, since the TD-KS equations (3.2.1) and (3.2.2) provide an exact way to compute the time-dependent electron density, the linear density response of the interacting system can be calculated as the density response of the non-interacting KS system, described by $\chi_{\mathrm{KS}}(\mathbf{r},t;\mathbf{r}\,',t')$:

$$\rho_1(\mathbf{r},t) = \int \mathrm{d}^3\mathbf{r}\,' \int_{t_0}^{\infty} \mathrm{d}t' \chi_{\mathrm{KS}}(\mathbf{r},t;\mathbf{r}\,',t') v_{\mathrm{S}}^{(1)}(\mathbf{r}\,',t') \tag{3.3.3}$$

where $v_{\mathrm{S}}^{(1)}$ is the KS potential calculated to the first-order of the perturbing potential v_1. The great advantage in the use of this procedure is that $\chi_{\mathrm{KS}}(\mathbf{r},t;\mathbf{r}\,',t')$ is easily computed. Then,

$$v_{\mathrm{S}}^{(1)}(\mathbf{r},t) = v_1(\mathbf{r},t) + \int \mathrm{d}^3\mathbf{r}\,' \frac{\rho_1(\mathbf{r},t)}{|\mathbf{r}-\mathbf{r}\,'|} + \int \mathrm{d}^3\mathbf{r}\,' \int \mathrm{d}t' f_{\mathrm{xc}}(\mathbf{r},t;\mathbf{r}\,',t') \rho_1(\mathbf{r}\,',t') \tag{3.3.4}$$

where f_{xc} is the XC response kernel, defined as the functional derivative of the time-dependent XC potential $v_{\mathrm{xc}}(\mathbf{r},t)$ in respect to the electron density $\rho(\mathbf{r}',t')$ evaluated at the initial ground state density $\rho_0(\mathbf{r})$:

$$f_{\mathrm{xc}}(\mathbf{r},t;\mathbf{r}\,',t') = \left. \frac{\delta v_{\mathrm{xc}}[\rho](\mathbf{r},t)}{\delta \rho(\mathbf{r}\,',t')} \right|_{\rho=\rho_0} \tag{3.3.5}$$

The f_{xc} kernel represents the change at the first-order of the time-dependent XC potential $v_{\mathrm{xc}}[\rho](\mathbf{r},t)$ due to the applied perturbation.[20] The equations (3.3.3) and (3.3.4) are the KS equations for the linear density response. By adopting some appropriate approximations for f_{xc}, the KS equations provide a self-consistent scheme to evaluate the linear density response $\rho_1(\mathbf{r},t)$ as a consequence of an external perturbation switching on. Moving from time to frequency (ω) domain, the KS response function can be obtained by calculating the Fourier transform of $\chi_{\mathrm{KS}}(\mathbf{r},t;\mathbf{r}\,',t')$ with respect to $(t-t')$

$$\chi_{\mathrm{KS}}(\mathbf{r},\mathbf{r}\,',\omega) = \sum_{j,k} (f_k - f_j) \frac{\phi_k^{(0)}(\mathbf{r})^* \phi_j^{(0)}(\mathbf{r}) \phi_j^{(0)}(\mathbf{r}\,')^* \phi_k^{(0)}(\mathbf{r}\,')}{\omega - (\varepsilon_j - \varepsilon_k) + i\delta} \tag{3.3.6}$$

with the sum running over all KS orbitals j,k (including the continuum states), f_k and f_j are the Fermi occupation factors, ε_k and ε_j are the Fermi energies, and δ is a positive, infinitesimal value.

3.4 Approximations for the exchange-correlation kernel

As far as the the XC kernel f_{xc} is concerned, some proper approximations are needed to define this quantity, due to the unknown nature of the XC potential. In particular, the so-called adiabatic local density approximation (ALDA)[82] is the simplest possible approximation in TD-DFT to treat the kernel f_{xc}. According to the adiabatic approximation, the complicated functional f_{xc} is reduced to a local in space, frequency-independent, and real function evaluated in correspondence of the local SCF electron density $\rho_0(\mathbf{r})$:

$$f_{\mathrm{xc}}^{\mathrm{ALDA}}(\mathbf{r}, \mathbf{r}\,', \omega) = \delta(\mathbf{r} - \mathbf{r}\,') \frac{\mathrm{d}\upsilon_{\mathrm{xc}}^{\mathrm{LDA}}}{\mathrm{d}\rho}\bigg|_{\rho=\rho_0(\mathbf{r})} \tag{3.4.1}$$

In the ALDA approximation it is assumed that the functional derivative in the equation (3.3.5) is nonzero iff $t = t'$, *i.e.*, this approximation is valid only for very slow time-dependent processes and if the system is initially in its ground state.

3.5 TD-DFT equations for excitation energies calculations

Within the TD-DFT framework, the excitation energies and oscillator strengths for the simulation of absorption spectroscopy experiments are obtained by the following eigenvalue equation:[83–85]

$$\Omega \mathbf{F}_I = \omega_I^2 \mathbf{F}_I \tag{3.5.1}$$

where the eigenvalues ω_I are the excitation energies and the eigenvectors $\mathbf{F}_I$ are the oscillator strengths. The direct solution of the previous eigenvalue equations for the excitation energies and the oscillator strengths is possible exclusively in principle, but it is infeasible for the computational and storage requirements. For this reason, for large molecules, it is preferable to solve the eigenvalue problem iteratively by employing the Davidson algorithm,[86] which requires low computational costs also for large matrices. In fact, this method makes restrictions to a few selected eigenvalues, generally the lowest excitation energies. For a generic system, the components of the four-index matrix Ω are:[87]

$$\Omega_{ia\sigma,jb\tau} = \delta_{\sigma\tau}\delta_{ij}\delta_{ab}(\varepsilon_{a\sigma} - \varepsilon_{i\sigma})^2 + 2\sqrt{\varepsilon_{a\sigma} - \varepsilon_{i\sigma}} K_{ia\sigma,jb\tau} \sqrt{\varepsilon_{b\tau} - \varepsilon_{j\tau}} \tag{3.5.2}$$

where a, b are the indices for virtual orbitals, i, j are those for occupied orbitals, σ and τ are indices for the spin and ε are the energies of the occupied and virtual KS orbitals. The coupling matrix K consists of a Coulomb part and an XC part:

$$K_{ai\sigma,bj\tau} = K^{\text{Coul}}_{ai\sigma,bj\tau} + K^{\text{xc}}_{ai\sigma,bj\tau} \tag{3.5.3}$$

$$K^{\text{Coul}}_{ai\sigma,bj\tau} = \int \mathrm{d}\mathbf{r} \int \mathrm{d}\mathbf{r}\,' \, \phi^*_{a\sigma}(\mathbf{r})\phi_{i\sigma}(\mathbf{r}) \frac{1}{|\mathbf{r} - \mathbf{r}\,'|} \phi^*_{b\tau}(\mathbf{r}\,')\phi_{j\tau}(\mathbf{r}\,') \tag{3.5.4}$$

$$K^{\text{xc}}_{ai\sigma,bj\tau} = \int \mathrm{d}\mathbf{r} \int \mathrm{d}\mathbf{r}\,' \, \phi^*_{a\sigma}(\mathbf{r})\phi_{i\sigma}(\mathbf{r}) f^{\sigma\tau}_{\text{xc}}(\mathbf{r}) \times \delta(\mathbf{r} - \mathbf{r}\,')\phi^*_{b\tau}(\mathbf{r}\,')\phi_{j\tau}(\mathbf{r}\,') \tag{3.5.5}$$

ϕ_i's correspond to the KS orbitals and $f^{\sigma\tau}_{\text{XC}}$ is the XC kernel, within the adiabatic approximation. In order to solve the eigenvalue equation (3.5.1), the correct approximations for $\mathbf{F}_I$ must be found. Two steps are involved in the TD-DFT procedure: the SCF step to generate the KS orbitals and orbital energies, and a post-SCF step to solve equation (3.5.1). In these two steps different approximate functionals may be used. However, the iterative solution of the eigenvalue equation (3.5.1) requires the formulation of an initial hypothesis about $\mathbf{F}_I$, and $K_{ai\sigma,bj\tau} = 0$ is usually a good starting point.[81] Thus, for the evaluation of the excitation energies, this implies that in the first cycle the excitation energies are considered to be equal to the difference between the eigenvalues of occupied and unoccupied KS orbitals.

TD-DFT has been widely used in theoretical calculations of excitation energies for both closed[85] and open shell systems.[87] Moreover, for systems containing heavy elements, relativistic effects (see chapter 2) must be considered to obtain reliable results. ZORA[73,75,78] can deal with the inclusion of the relativistic effect on the valence electrons with high accuracy. In most cases only the excitations of the valence electrons are considered, and the excitation energies based on the SR-ZORA TD-DFT method provide accurate results. In the framework of SR-ZORA TD-DFT, the excitation energies are calculated through a combined ZORA and TD-DFT approach, which implies that the one-electron energies and the KS orbitals that are used in the TD-DFT response equations are obtained by solving the one-electron SR-ZORA KS equations.[75,78] However, when dealing with deep core excitations, also SO coupling must be considered. Different formalisms have been designed to deal with SO coupling in relativistic TD-DFT calculations,[88–91] and the one proposed by Wang *et al.*,[90,91] which uses the two-component ZORA and the noncollinear XC potential, is consistent with the correct non-relativistic limit and the correct threefold degeneracy for the triplet excitations.

Chapter 4

Case studies

An effective approach to deal with the electronic structure of transition metal complexes cannot just imply the exploitation of a single spectroscopic tool. In fact, to provide as much information as possible, a multifaceted strategy is needed. In particular, by investigating the same systems with different techniques diverse information can be gained. During my Ph.D. thesis, I have carried out a combined experimental and computational study of the occupied and unoccupied electronic structure of tetraphenylporphyrins and their copper complexes to gain a deep understanding of the electronic properties making these compounds particularly important for the most varied technological applications. Due to the close relationship between electronic structure and electronic/optical properties of metalloporphyrins, the knowledge of their electronic structure is mandatory to develop architectures suitably designed for a specific application. In order to do so, two distinct spectroscopic studies have been carried out:

- the occupied electronic structure has been probed by means of photoemission spectroscopies: the core and valence levels have been investigated through X-ray photoelectron spectroscopy (XPS) and ultraviolet photoelectron spectroscopy (UPS), respectively;
- the unoccupied electronic structure, *i.e.* the low lying empty molecular orbitals (MOs), has been explored by using X-ray absorption spectroscopy (XAS).

The final aim of this study is not only to provide an interpretation of the experimental spectroscopic outcomes; rather, it is that of unraveling the electronic structure of these molecules by taking advantage of the experimental data. As such, I have predicted the spectroscopic properties of these molecules by starting from first principle calculations and by fully exploiting their symmetry properties. In the following sections a brief description of the spectroscopic tools used in this research and of the case studies will be provided.

4.1 Photoelectron spectroscopies

Among spectroscopic tools, the photoemission spectroscopy is very well suited to investigate the energetics of atoms, molecules or solids. It is based on the evidence that, when a chemical system is subject to a beam of photons with a certain energy, an induced emission of electrons with a well-defined energy spectrum (photoelectrons) is observed. This phenomenon was originally defined as "photoelectric effect", since a measurable electric current (photo-current) is generated, but nowadays it is called photoionization or photoemission. During the photoemission process the sample is irradiated with a monochromatic electromagnetic radiation having energy $h\nu$ and, if the photon energy is higher than the sample work function (*i.e.*, the minimum thermodynamic work required to extract an electron from the surface of a solid), the excited electron will experience a unbound state acquiring a certain kinetic energy, so that it will be ejected from the system.[31] Within the one-electron approximation, the energy balance is provided by the Einstein equation:[63]

$$h\nu = E_{\mathrm{b}} + E_K \tag{4.1.1}$$

where E_{b} and E_K are the ionization energy (or binding energy) and the kinetic energy of the K^{th} ejected electron, respectively. The photoionization process requires a threshold photon energy, which corresponds to the first ionization energy for gaseous samples and to the energy of the Fermi level (E_{F}) for solids. In the latter case, the Einstein equation for the energy balance must be corrected considering the work function of the solid ϕ_{s}:[92]

$$h\nu = E_{\mathrm{F}} + E_{\mathrm{K}} + \phi_{\mathrm{s}} \tag{4.1.2}$$

In principle, a beam of photons with sufficiently short wavelength can, in several photoionization processes, extract electrons from different atomic shells as well as from atoms of different species. All these electrons have different binding energies lower than $h\nu$. It should be clear that, even if the photoionization is a process induced by a monochromatic radiation, the overall phenomenon is polychromatic. In fact, the occupation of the energy levels is discrete and different levels have in general different energies. The determination of this distribution constitutes the photoelectron spectroscopy's focus. This technique has practical applications in many fields of science. In fact, the equation (4.1.2) establishes a relationship between the sample characteristics and the energy spectrum of the photoelectrons, suggesting the exploitation of the photoemission processes to develop a wide range of spectroscopic techniques aimed to investigate the electronic structure of matter in its various aggregation states. It is important to underline that the

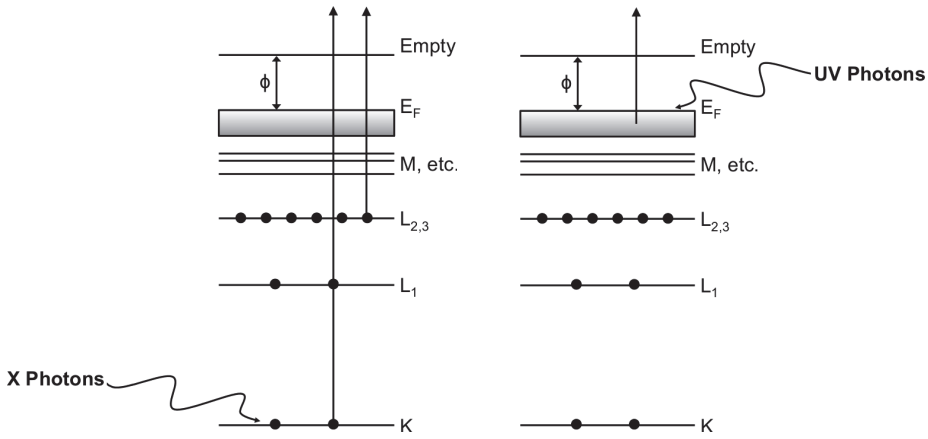

(a) XPS **(b)** UPS

Figure 4.1: Photoemission process for a solid sample at two different wavelengths: (a) X-rays and (b) UV.

outcome of the matter-radiation interaction varies with the wavelength of the radiation, and the information gained from the material under study will likewise vary. The XPS spectroscopy employs electromagnetic radiation with energies in the order of the keV (the X-rays energy range) for the investigation of occupied core energy levels (see Figure 4.1a). Core electrons have typical binding energies for each element depending on the energetics of the system; as such, XPS can be exploited for qualitative analysis, in addition to provide other physical and chemical information (*e.g.*, the oxidation state) of atomic species by referring to their core binding energies. As far as the ultraviolet radiation ($10 \div 100\,\text{eV}$) is concerned, it is employed to study occupied frontier energy levels, and the associated technique is called UPS (see Figure 4.1b).

The photoemission model is valid within the one-electron approximation, even though a more detailed description of the effects of the interaction of the ejected electron with the radiation should imply a much more complex model. To evaluate the photoemission effect, one has to measure the energy difference between the initial (characterized by N electrons) and final states (with $N-1$ electrons plus the photoelectron).[93] Thus, the photoionization process can be represented as:

$$\Psi^i_{\text{tot}}(N) \xrightarrow{h\nu} \Psi^f_{\text{tot}}(N, K) \tag{4.1.3}$$

where $\Psi^i_{\text{tot}}(N)$ and $\Psi^f_{\text{tot}}(N, K)$ are the wave functions of the N-electron initial state and of the K^{th} state, respectively. If it is assumed that the photoelectron is weakly coupled with the leaving ion, the final state is then described by the equation:

$$\Psi^f_{\text{tot}}(N, K) = \Psi^f_{\text{tot}}(N-1, K) + \phi^f(1)\chi^f(1) \tag{4.1.4}$$

where $\Psi^f_{\text{tot}}(N-1, K)$ is the wave function associated to the K^{th} final state with $N-1$ electrons, while $\phi^f(1)$ and $\chi^f(1)$ are the spatial and spin coordinates of the

photoelectron wave function, respectively. In order to interpret XPS spectra, the conservation of energy in equation (4.1.4) must be considered:

$$E^i_{\text{tot}} + h\nu = E^f_{\text{tot}}(N-1, K) + E_K \tag{4.1.5}$$

Thus,

$$E^f_{\text{tot}}(N-1, K) - E^i_{\text{tot}} = h\nu - E_K = E_{\text{b}} \tag{4.1.6}$$

where $E^f_{\text{tot}}(N-1, K)$ is the energy of the final state with $N-1$ electrons and E_K is the photoelectron kinetic energy. In order to formulate a complete model, the effects of correlation and relaxation, which are usually neglected in the one-electron approximation, must be included. The main drawback in the one-electron model when applied to XPS is its inability to include any interaction between the hole, created as a consequence of the photoemission process, and the electrons surrounding the hole. To a first approximation, the final state is considered to differ from the initial one exclusively by the presence of a hole in the K^{th} level. Thus, this situation corresponds to use the N one-electron wave functions solutions of the Schrödinger equation to generate the Slater determinants of both initial and final states (the former characterized by N, the latter by $N-1$ wave functions). The difference between the total energies associated to the two many-electrons wave functions is the binding energy of the electron in the K^{th} level. Within this approximation, the so-called Koopmans' theorem,[94] the binding energy of the K^{th}-electron is equal, in modulus, to the energy of the K^{th}-orbital. As a matter of fact, the presence of relaxation phenomena, induced by the presence of the hole in the K^{th}-orbital, reduces the energy of the final state, so that the effective photoelectron binding energy is different from that expected on the basis of the Koopmans' theorem.

4.2 X-ray Absorption Spectroscopy

Covalency for transition metal (M) complexes is defined as "the coefficients of the Ligand ($\mathcal{L}$) character in the valence metal d derived molecular orbitals".[95] There are several spectroscopic techniques that can be used to experimentally estimate the covalency, and Solomon has been the first that suggested the possible use of XAS as a direct experimental tool to estimate the covalency and the ligand field strength in transition metal complexes.[95,96] Traditional approaches to evaluate the M-$\mathcal{L}$ interaction covalency involve magnetic spectroscopies for the investigation of ground state properties. In electron paramagnetic resonance (EPR) spectroscopy, the most direct probe of the covalency is the ligand superhyperfine coupling, measured by double resonance or pulsed EPR methods.[97] The amplitude

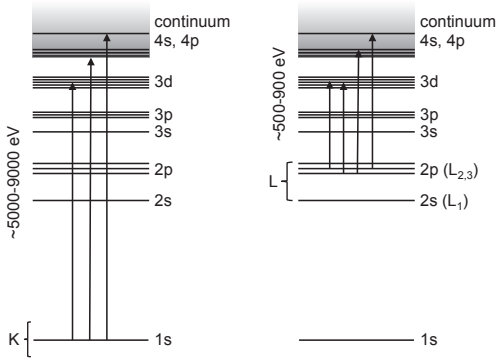

Figure 4.2: Energy level diagram comparing the K-edge and L-edge excitations for first-row transition metals.

and the anisotropy of the ligand superhyperfine coupling probe the delocalization of the electron spin density into the ligand's s and p orbitals and therefore the covalency. Obviously, this requires an EPR active site and molecular orbitals containing unpaired electrons.

Also photoemission spectroscopies can be used to quantify covalent mixing, by analysing the intensity dependence of the valence band peaks with the input photon energy and the intensity of shake up satellites in valence and core regions. However, the application of these tools is complicated by the large final states effects associated with the change in the interelectronic repulsion upon ionization. Much of these complications may be overcome through the employment of XAS spectroscopy. In a XAS experiment the wavelength of the incoming X-ray photon is tuned and the absorption is measured as a function of the photon energy. XAS of coordination compounds involving transition metal ions can provide information about:

i. the splitting of the valence d orbitals of the metal;

ii. the covalent mixing with the ligand environment.

XAS features are generated by localized excitations of core electrons to the unoccupied valence orbitals as well as to the continuum (see Figure 4.2), making this technique a chemically selective probe of the molecular unoccupied electronic structure. Both singly-occupied and unoccupied MOs of the metal complex can be investigated, and different edges for both the metal and the ligand may be used to investigate them. This technique can be exploited to look into the electronic properties of a coordination compound in a very diverse range of materials varying from solar cells to catalytic centres of metalloenzymes.[96] The XAS spectroscopies are classified on the basis of the shell from which the electron is excited (see Figure 4.2), the most common one being the 1s or K-shell.* For my purposes, two

*In a XAS experiment the absorption edge shows two significant structures both in the

edges, providing complementary information about the M-$\mathcal{L}$ covalency, have been considered: the XAS at the K-edge of the ligand's atoms directly bonded to the central metal and XAS at the metal $L_{2,3}$-edges.

4.2.1 Ligand K-edge XAS

Peculiar information on covalency can be gained through experiments at the ligand's donor atom K-edge (hereinafter, $\mathcal{L}$ K-edge). The $\mathcal{L}$ K-edge implies $1s^{\mathcal{L}} \rightarrow n\mathrm{p}^{\mathcal{L}}$ electric dipole allowed transitions, and every singly-occupied or unoccupied MO of the transition metal complex can be investigated, thus providing a direct probe of the M-$\mathcal{L}$ bond covalency. The lowest-lying transition (the so-called pre-edge feature) of the $\mathcal{L}$ K-edge accounts for the excitation of an electron from 1s orbital(s) (centred on the ligand's atom(s) directly bonded to M) to the singly occupied lowest-lying MO (SOMO), usually antibonding in nature with respect to the M-$\mathcal{L}$ interaction, *i.e.*, $1s^{\mathcal{L}} \rightarrow$ SOMO. Due to the localization of the 1s AO, the intensity of this transition may be used to quantify the np $\mathcal{L}$ character amount into the metal-based SOMO.[95] As a matter of fact, the SOMO is mainly localized on the central metal ion, and it accounts for the M-$\mathcal{L}$ antibonding interaction:

$$|\Psi^*\rangle = \sqrt{(1-\alpha^2)}\,|M\rangle - \alpha\,|\mathcal{L}\rangle \tag{4.2.1}$$

Therefore, the pre-edge provides an estimate of covalency, according to the following relation:[99,100]

$$I(1s \rightarrow \Psi^*) \propto \alpha^2 \tag{4.2.2}$$

where I is the intensity of the feature, Ψ^* indicates the SOMO and α^2 is the amount of the $\mathcal{L}$ character in the half-occupied metal-based MO; α is then a measure of the covalency. By looking at the relationship between the SOMO and the covalency in equation (4.2.1), it can be straightforwardly derived, up to other effects herein neglected, that the pre-edge transition intensity will increase as the ligand character in the SOMO increases.[99]

4.2.2 Metal L-edge XAS

Metal L-edge absorption features take into account transitions whose origin corresponds to the $2s^2\,2p^6$ shell (L-shell, Figure 4.2). The L_1 edge implies ex-

immediate vicinity of the edge jump and above the edge. The former is referred to as X-ray absorption near-edge structure (XANES), while the oscillations above the edge are related to the extended X-ray absorption fine structure (EXAFS). The XANES region is sensitive to oxidation state and geometry, whereas the EXAFS one accounts for the radial distribution of the electron density around the absorbing atom and it is used for the quantitative determination of bond lengths and coordination numbers.[98]

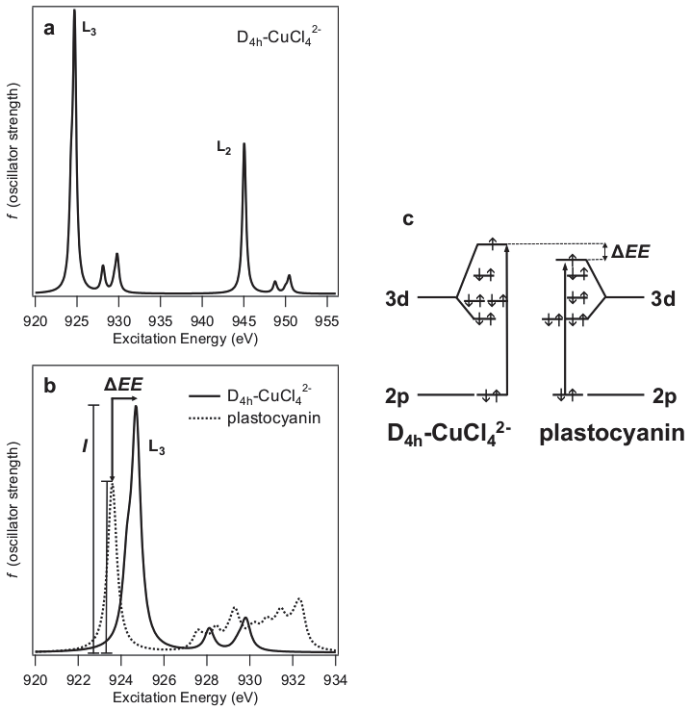

Figure 4.3: (a) Cu $L_{2,3}$-edges X-ray absorption spectrum of D_{4h}-$CuCl_4^{2-}$; (b) comparison between the L_3-edge of D_{4h}-$CuCl_4^{2-}$ and the blue copper site of plastocyanin. The intensity ($\boldsymbol{I}$) reflects the covalency, while the excitation energy shift ($\boldsymbol{\Delta EE}$) reflects the ligand field exerted on the Cu(II) centre; (c) the comparison between the ligand field splitting of D_{4h}-$CuCl_4^{2-}$ and plastocyanin indicates the origin of the excitation energy difference in the two Cu L_3-edge XAS spectra.[96]

citations of electrons from the 2s sub-shell, while both L_2 and L_3 edges arise from the SO splitting of the 2p sub-shell. Due to the nature of the L_1-edge XAS excitations, it offers little spectroscopic information; thus, when referring to the L-edge spectra of a first-row transition metal complex, this usually indicates the $L_{2,3}$ ones. The $L_{2,3}$-edges imply $2p \rightarrow n$d dipole-allowed transitions, which generate a $2p^5 n d^{n+1}$ final configuration. The orbital angular momentum ($\ell = 1$) of the $2p^5$ core configuration couples with the spin angular momentum ($s = \frac{1}{2}$) with the generation of the total angular momenta $j = \frac{3}{2}$ and $j = \frac{1}{2}$. In Cu(II) complexes, the $j = \frac{3}{2}$ state generates the L_3 feature, at ~ 930 eV, with an intensity approximately twice than the one having $j = \frac{1}{2}$ (the L_2 peak at ~ 950 eV, see Figure 4.3). Due to the localized nature of the $L_{2,3}$ excitations, the intensity of the $2p^{Cu} \rightarrow nd^{Cu}$ peaks reflects the amount of the Cu d character in the investigated unoccupied MO:

$$I(2p^{Cu} \rightarrow \Psi^*) = (1 - \alpha^2) I(2p^{Cu} \rightarrow 3d^{Cu}) \tag{4.2.3}$$

Intensities and relative positions of the Cu L_3 features, which are associated to $2p_{3/2} \rightarrow$ SOMO transitions, may be then employed as a gauge of the degree of Cu–$\mathcal{L}$ covalency and of the ligand field strength, respectively (see Figure 4.3).

4.3 Cu(II) complexes and case studies

In the simplest case of the d^9 Cu(II) ion, the $L_{2,3}$-edges involve the electric dipole allowed $2p^{Cu} \rightarrow 3d^{Cu}$ transitions with the generation of the $2p^5 3d^{10}$ final configuration (see section 4.2.2), which has only two term symbols; thus, the corresponding spectral splitting is dominated by the 2p SO coupling contribution and the overall energetics and intensities are strongly influenced by ligand field and covalency, respectively (see Figure 4.3).[96,101] In this Ph.D. thesis, I have focused my attention on the study of XAS at Cu(II) $L_{2,3}$-edges of several Cu(II) complexes with ligands exerting different ligand field strengths on the central ion: D_{4h}-$CuCl_4^{2-}$, the blue copper site of plastocyanin, copper phthalocyanine, copper acetylacetonate, CuTPP and CuTPP(F). With the D_{4h}-$CuCl_4^{2-}$ molecular ion as a reference, Solomon and co-workers[96,101] proposed the use of the normalized intensities and relative positions of the Cu $L_{2,3}$ features in different Cu(II) complexes as a gauge of the degree of Cu-$\mathcal{L}$ covalency and of the ligand field strength, respectively. In more detail, the larger the $L_{2,3}$ normalized intensity, the lower the Cu-$\mathcal{L}$ covalency; the higher the L_3 excitation energy, the stronger the ligand field exerted on the Cu centre (see Figure 4.3 and equation (4.2.3)). Thus, the final goal of this study has been that of testing the legitimacy of using the Cu(II) L_3-edge intensity and position to get information about the Cu-$\mathcal{L}$ covalency and ligand field strength generated by the different ligands, respectively.

Bibliography

[1] Voet, D.; Voet, J. G.; Pratt, C. W. *Fundamentals of Biochemistry: Life at the Molecular Level - Second Edition*; Wiley, 2006.

[2] Jensen, F. B.; Fago, A.; Weber, R. E. In *Fish Physiology*; Perry, S. F., Tufts, B. L., Eds.; Academic Press, San Diego, 1998; Vol. 17.

[3] Di Natale, C.; Monti, D.; Paolesse, R. *Mater. Today* **2010**, *13*, 46–52.

[4] Jurow, M.; Schuckman, A. E.; Batteas, J. D.; Drain, C. M. *Coord. Chem. Rev.* **2010**, *254*, 2297–2310.

[5] Yella, A.; Lee, H.-W.; Tsao, H. N.; Yi, C.; Chandiran, A. K.; Nazeeruddin, M.; Diau, E. W.-G.; Yeh, C.-Y.; Zakeeruddin, S. M.; Grätzel, M. *Science* **2011**, *334*, 629–634.

[6] Lvova, L.; Di Natale, C.; Paolesse, R. *Sensors and Actuators B* **2013**, *179*, 21–31.

[7] Ishihara, S.; Labuta, J.; Van Rossom, W.; Ishikawa, D.; Minami, K.; Hill, J. P.; Ariga, K. *Phys. Chem. Chem. Phys.* **2014**, *16*, 9713–9746.

[8] Gottfried, J. M. *Surf. Sci. Rep.* **2015**, *70*, 259–379.

[9] Garg, V.; Kodis, G.; Chachisvilis, M.; Hambourger, M.; Moore, A. L.; Moore, T. A.; Gust, D. *J. Am. Chem. Soc.* **2011**, *133*, 2944–2954.

[10] Megiatto, J. D. J.; Antoniuk-Pablant, A.; Sherman, B. D.; Kodis, G.; Gervaldo, M.; Moore, T. A.; Moore, A. L.; Gust, D. *Proc. Natl. Acad. Sci. USA* **2012**, *109*, 15578–15583.

[11] Saga, T. *NPG Asia Mater.* **2010**, *2*, 96–102.

[12] Sanders, J. K. M.; Bampos, N.; Clyde-Watson, Z.; Darling, S. A.; Hawley, J. C.; Kim, H.-J.; Mak, C. C.; Webb, S. J. In *The Porphyrin Handbook*; Kadish, K. M., Smith, K. M., Guilard, R., Eds.; Academic Press, San Diego, 2000; Vol. 3.

[13] Schrödinger, E. *Ann. Phys.* **1926**, *384*, 361–376.

[14] Schrödinger, E. *Ann. Phys.* **1926**, *384*, 489–527.

[15] Schrödinger, E. *Ann. Phys.* **1926**, *384*, 734–756.

[16] Schrödinger, E. *Ann. Phys.* **1926**, *385*, 437–490.

[17] Schrödinger, E. *Ann. Phys.* **1926**, *386*, 109–139.

[18] Schrödinger, E. *Naturwissenshaften* **1926**, *14*, 664–666.

[19] Schrödinger, E. *Phys. Rev.* **1926**, *28*, 1049–1070.

[20] Parr, R. G.; Yang, W. *Density Functional Theory of Atoms and Molecules*; Oxford University Press, New York, 1989.

[21] Born, M.; Oppenheimer, R. *Ann. Phys.* **1927**, *84*, 457–484.

[22] Landau, L. D.; Lifshitz, E. M. *Quantum Mechanics*; Pergamon Press, 1965.

[23] Volterra, V. *Theory of functionals*; Dover Publications, New York, 1959.

[24] Becke, A. D. *J. Chem. Phys.* **2014**, *140*, 18A301–18A318.

[25] Hohenberg, P.; Kohn, W. *Phys. Rev.* **1964**, *136*, B864–B871.

[26] Geerlings, P.; De Proft, F.; Langenaeker, W. *Chem. Rev.* **2003**, *103*, 1793–1874.

[27] Thomas, L. H. *Proc. Cambridge Phil. Soc.* **1927**, *23*, 542–548.

[28] Fermi, E. *Rend. Accad. Naz. Lincei* **1927**, *6*, 602–607.

[29] Fermi, E. *Z. Physik* **1928**, *48*, 73–79.

[30] Kohn, W.; Sham, L. J. *Phys. Rev.* **1965**, *140*, A1133–A1138.

[31] Kittel, C. *Introduction to Solid State Physics - Eighth Edition*; John Wiley & Sons, 2005.

[32] Lieb, E. H.; Simon, B. *Phys. Rev. Lett.* **1973**, *31*, 681–683.

[33] Teller, E. *Rev. Mod. Phys.* **1962**, *34*, 627–631.

[34] Levy, M. *Proc. Natl. Acad. Sci. USA* **1979**, *76*, 6062–6065.

[35] Gunnarsson, O.; Lundqvist, B. *Phys. Rev. B* **1976**, *13*, 4274–4298.

[36] Coleman, A. J. *Rev. Mod. Phys.* **1963**, *35*, 668–687.

[37] Gilbert, T. L. *Phys. Rev. B* **1975**, *12*, 2111–2120.

[38] Pauli, W. J. *Z. Physik* **1925**, *31*, 765–783.

[39] Dirac, P. A. M. *Math. Proc. Cambridge* **1930**, *26*, 376–385.

[40] Ceperley, D. M.; Alder, J. B. *Phys. Rev. Lett.* **1980**, *45*, 566–569.

[41] Vosko, S. H.; Wilk, L.; Nusair, N. *Can. J. Phys.* **1980**, *58*, 1200–1211.

[42] Perdew, J. P.; Zunger, A. *Phys. Rev. B: Condens. Matter* **1981**, *23*, 5048–5079.

[43] Perdew, J. P.; Wang, Y. *Phys. Rev. B: Condens. Matter* **1992**, *45*, 13244–13249.

[44] Wigner, E. *Phys. Rev.* **1934**, *46*, 1002–1011.

[45] Cole, L. A.; Perdew, J. P. *Phys. Rev. A* **1982**, *25*, 1265–1271.

[46] Lee, C.; Yang, W.; Parr, R. G. *Phys. Rev. B* **1988**, *37*, 785–789.

[47] Becke, A. D. *Int. J. Quantum Chem.* **1983**, *23*, 1915–1922.

[48] Perdew, J. P. *Phys. Rev. Lett.* **1985**, *55*, 1665–1668.

[49] Perdew, J. P. *Phys. Rev. B: Condens. Matter* **1986**, *33*, 8822–8824.

[50] Perdew, J. P.; Wang, Y. *Phys. Rev. B: Condens. Matter* **1986**, *33*, 8800–8802.

[51] Becke, A. D. *Phys. Rev. A* **1986**, *33*, 2786–2788.

[52] Becke, A. D. *J. Chem. Phys.* **1988**, *88*, 1053–1062.

[53] Becke, A. D. *J. Chem. Phys.* **1988**, *88*, 2547–2553.

[54] Becke, A. D. *Phys. Rev. A: At., Mol., Opt. Phys.* **1988**, *38*, 3098–3100.

[55] Tao, J.; Perdew, J. P.; Staroverov, V. N.; Scuseria, G. E. *Phys. Rev. Lett.* **2003**, *91*, 146401–146404.

[56] Perdew, J. P.; Staroverov, V. N.; Tao, J.; Scuseria, G. E. *Phys. Rev. A* **2008**, *78*, 052513–052525.

[57] Constantin, L. A.; Pitarke, J. M.; Dobson, J. F.; Garcia-Lekue, A.; Perdew, J. P. *Phys. Rev. Lett.* **2008**, *100*, 036401–036404.

[58] Perdew, J. P.; Ruzsinszky, A.; Constantin, L. A.; Sun, J.; Csonka, G. I. *J. Chem. Theory Comput.* **2009**, *5*, 902–908.

[59] Ernzerhof, M.; Scuseria, G. *J. Chem. Phys.* **1999**, *110*, 5029–5036.

[60] Adamo, C.; Barone, V. *J. Chem. Phys.* **1999**, *110*, 6158–6170.

[61] Stephens, P. J.; Devlin, F. J.; Chabalowski, C. F.; Frisch, M. *J. Phys. Chem.* **1994**, *98*, 11623–11627.

[62] Einstein, A. *Ann. Phys.* **1905**, *17*, 132–148.

[63] Einstein, A. *Ann. Phys.* **1905**, *17*, 891–921.

[64] Pyykkö, P.; Desclaux, J. P. *Acc. Chem. Res.* **1979**, *12*, 276–281.

[65] Pyykkö, P. *Chem. Rev.* **1988**, *88*, 563–594.

[66] Dirac, P. A. M. *Proc. R. Soc. Lond. A* **1928**, *117*, 610–624.

[67] Dirac, P. A. M. *Proc. R. Soc. Lond. A* **1928**, *118*, 351–361.

[68] Pauli, W. J. *Z. Physik* **1927**, *43*, 601–623.

[69] Darwin, C. G. *Proc. Roy. Soc. Lond. A* **1928**, *118*, 654–680.

[70] Dyall, K. G.; Grant, I. P.; Wilson, S. *J. Phys. B: At. Mol. Phys.* **1984**, *17*, L45–L50.

[71] Dyall, K. G.; Grant, I. P.; Wilson, S. *J. Phys. B: At. Mol. Phys.* **1984**, *17*, 1201–1209.

[72] Wood, J.; Grant, I. P.; Wilson, S. *J. Phys. B: At. Mol. Phys.* **1985**, *18*, 3027–3041.

[73] van Lenthe, E.; Baerends, E. J.; Snijders, J. G. *J. Chem. Phys.* **1993**, *99*, 4597–4610.

[74] van Lenthe, E.; Snijders, J. G.; Baerends, E. J. *J. Chem. Phys.* **1996**, *105*, 6505–6516.

[75] van Lenthe, E.; Baerends, E. J.; Snijders, J. G. *J. Chem. Phys.* **1994**, *101*, 9783–9792.

[76] van Leeuwen, R.; van Lenthe, E.; Baerends, E. J.; Snijders, J. G. *J. Chem. Phys.* **1994**, *101*, 1272–1281.

[77] Sadlej, A. J.; Snijders, J. G. *Chem. Phys. Lett.* **1994**, *229*, 435–438.

[78] van Lenthe, E.; Ehlers, A.; Baerends, E. J. *J. Chem. Phys.* **1999**, *110*, 8943–8953.

[79] Runge, E.; Gross, E. K. U. *Phys. Rev. Lett.* **1984**, *52*, 997–1000.

[80] Gross, E. K. U.; Kohn, W. *Adv. Quantum Chem.* **1990**, *21*, 255–291.

[81] van Gisbergen, S. J. A.; Snijders, J. G.; Baerends, E. J. *Comp. Phys. Commun.* **1999**, *118*, 119–138.

[82] Gross, E. K. U.; Kohn, W. *Phys. Rev. Lett.* **1985**, *55*, 2850–2852.

[83] Casida, M. In *Recent Advances in Density Functional Methods*; Chong, D. P., Ed.; World Scientific, Singapore, 1995; Vol. 1; p 155.

[84] Jamorski, C.; Casida, M. E.; Salahub, D. R. *J. Chem. Phys.* **1996**, *104*, 5134–5147.

[85] Bauernschmitt, R.; Ahlrichs, R. *Chem. Phys. Lett.* **1996**, *256*, 454–464.

[86] Davidson, E. R. *J. Comput. Phys.* **1975**, *17*, 87–94.

[87] Wang, F.; Ziegler, T. *Mol. Phys.* **2004**, *102*, 2585–2595.

[88] Toffoli, D.; Stener, M.; Decleva, P. *Phys. Rev. A* **2002**, *66*, 012501–012516.

[89] Gao, J.; Liu, W.; Song, B.; Liu, C. *J. Chem. Phys.* **2004**, *121*, 6658–6666.

[90] Wang, F.; Ziegler, T.; van Lenthe, E.; van Gisbergen, S.; Baerends, E. J. *J. Chem. Phys.* **2005**, *122*, 204103–204114.

[91] Wang, F.; Ziegler, T. *J. Chem. Phys.* **2005**, *123*, 154102–154114.

[92] Orchard, A. F. In *Handbook of X-ray and ultraviolet photoelectron spectroscopy*; Briggs, D., Ed.; Heyden, London, 1977.

[93] Ertl, G.; Küppers, J. *Low Energy Electrons and Surface Chemistry*; VCH, Weinheim, 1985.

[94] Koopmans, T. *Physica* **1934**, *1*, 104–113.

[95] Solomon, E. I.; Hedman, B.; Hodgson, K. O.; Dey, A.; Szilagyi, R. K. *Coord. Chem. Rev.* **2005**, *249*, 97–129.

[96] Hocking, R. K.; Solomon, E. I. *Struct. Bond.* **2012**, *142*, 155–184.

[97] Pirbrow, J. R. *Transition Ion Electron Paramagnetic Resonance*; Oxford University Press, London, 1990.

[98] De Groot, F.; Kotani, A. In *Core Level Spectroscopy of Solids*; Sarma, D. D., Kotliar, G., Tokura, Y., Eds.; CRC Press, 2008; Vol. 6.

[99] Neese, F.; Hedman, B.; Hodgson, K. O.; Solomon, E. I. *Inorg. Chem.* **1999**, 4854–4860.

[100] Shadle, S. E.; Hedman, B.; Hodgson, K. O.; Solomon, E. I. *Inorg. Chem.* **1994**, *33*, 4235–4244.

[101] George, S. J.; Lowery, M. D.; Solomon, E. I.; Cramer, S. P. *J. Am. Chem. Soc.* **1993**, *115*, 2968–2969.

List of publications

1) Mangione, G.; Sambi, M.; Nardi, M. V.; Casarin, M. A theoretical study of the L_3 pre-edge XAS in Cu(II) complexes. *Phys. Chem. Chem. Phys.* **2014**, *16*, 19852-19855;

2) Nardi, M. V.; Verucchi, R.; Pasquali, L.; Giglia, A.; Fronzoni, G.; Sambi, M.; Mangione, G.; Casarin, M. XAS of tetraphenyl- and tetrakis(pentafluorophenyl)- porphyrin: an experimental and theoretical study. *Phys. Chem. Chem. Phys.* **2015**, *17*, 2001-2011;

3) Mangione, G.; Pandolfo, L.; Sambi, M.; Ligorio, G.; Nardi, M. V.; Cossaro, A.; Floreano, L.; Casarin, M. Ligand-Field Strength and Symmetry-Restricted Covalency in Cu(II) Complexes- a Near-Edge X-ray Absorption Fine Structure Spectroscopy and Time-Dependent DFT Study. *Eur. J. Inorg. Chem.* **2015**, 2707-2713;

4) Mangione, G.; Carlotto, S.; Sambi, M.; Ligorio, G.; Timpel, M.; Vittadini, A.; Nardi, M. V.; Casarin, M. An experimental and theoretical study of the electronic structure of CuTPP and CuTPP(F) complexes I. *Phys. Chem. Chem. Phys.* **2016**, *18*, 18727-18738;

5) Mangione, G.; Sambi, M.; Carlotto, S.; Vittadini, A.; Ligorio, G.; Timpel, M.; Pasquali, L.; Giglia, A.; Nardi, M. V.; Casarin, M. Electronic structure of CuTPP and CuTPP(F) complexes. A combined experimental and theoretical study II. *Phys. Chem. Chem. Phys.* **2016**, *18*, 24890-24904.

PCCP

COMMUNICATION

View Article Online
View Journal | View Issue

Cite this: *Phys. Chem. Chem. Phys.*, 2014, **16**, 19852

Received 3rd June 2014,
Accepted 5th August 2014

DOI: 10.1039/c4cp02441a

www.rsc.org/pccp

A theoretical study of the L_3 pre-edge XAS in Cu(II) complexes†

G. Mangione,[a] M. Sambi,[a] M. V. Nardi[bc] and M. Casarin*[a]

$L_{2,3}$ spectra of Cu(II) complexes have been simulated by means of time dependent DFT. Besides the agreement between theory and experiment, the adopted approach provided further insights into the use of the Cu(II) L_3-edge intensity and position to investigate the Cu–ligand symmetry-restricted covalency and the ligand-field strength.

X-ray absorption spectroscopy (XAS) is unanimously recognized as a tool able to provide a site selective probe for the molecular unoccupied electronic structure.[1] XAS shows the excitation of core electrons to unoccupied valence orbitals as well as to the continuum, and its advantage is related to the localized character of core excitations, thus making K- and L-edge spectra sensitive to both the electronic structure and the local surroundings of the absorbing species. Cu(II) $L_{2,3}$ spectra are dominated by the electric dipole allowed 2p → 3d transitions, which provide information about the contribution of Cu 3d atomic orbitals (AOs) to the unoccupied molecular orbitals (MOs). In this regard, Solomon *et al.*[2] suggested the possible use of the intensity and position of the Cu(II) L_3 peak to get an experimental evaluation of the different degree of the Cu–ligands covalency as well as of the different ligand-field strengths, relative to some well-defined Cu(II) complexes. Specifically, they focused on the Cu $L_{2,3}$ spectra of D_{2d}-$Cs_2[CuCl_4]$, D_{4h}-$(N\text{-mph})_2[CuCl_4]$ (*N*-mph = *N*-methyl-*N*-phenethylammonium) and Cu(II) plastocyanin and, using D_{4h}-$[CuCl_4]^{2-}$ (**I**) as a reference, they assessed that the Cu–ligand interaction is more covalent in Cu(II) plastocyanin than in **I**. Since then, the simulation of $L_{2,3}$ spectra has represented a very dynamic line of work,[3–6] and the approach employed by Josefsson *et al.*,[4] which combines a high-level quantum chemical description of the chemical interactions and local atomic multiplet effects, is the actual state of art in this field.

As a part of a systematic investigation of the electronic properties of energy-targeted materials,[7] some of us have recently investigated the occupied and empty electronic structure of Cu(II) phthalocyanine (**II**, see Fig. 1) by exploiting photoelectron spectroscopies and XAS at the C and N K-edges as well as at the Cu $L_{2,3}$-edges.[7b] The assignment of experimental evidence, collected for thick films of randomly oriented molecules, was guided by the results of ADF (Amsterdam Density Functional) calculations[8] and, besides the very good agreement between experiment and theory, the comparison between homogeneous theoretical results pertaining to the ground states of **I** and **II** emphasized the more ionic nature of the Cu–N interaction compared to the Cu–Cl one.[7b]

In this communication, we have tested the capability of the time-dependent (TD) DFT[10] within the Tamm–Dancoff approximation (TDA)[11] coupled to the relativistic two-component zeroth-order regular approximation (ZORA)[12] including spin–orbit (SO) effects, as implemented in the latest version of ADF,[8] to simulate the Cu(II) $L_{2,3}$ spectra of **I**, **II** and of the blue copper active site in plastocyanin (**III**, see Fig. 1) in terms of their oscillator strength (f) distributions. A further aim of this study has been that of verifying the legitimacy of using the Cu(II) L_3-edge intensity and position to look into the Cu(II)–ligand symmetry-restricted covalency[13] and the ligand-field strength.

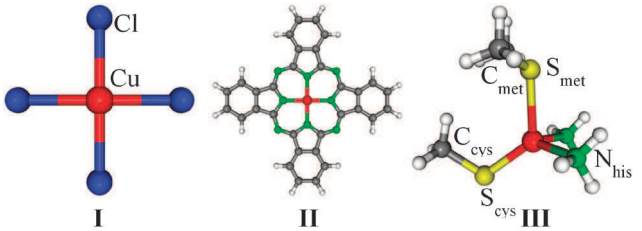

Fig. 1 Schematic representation of **I**, **II** and **III**. Each molecular species has a σ_h plane corresponding to the *xy* plane in the selected framework. The atom labelling of **III** is the same as that reported in ref. 9.

[a] *Department of Chemical Sciences and INSTM, via Marzolo 1, 35131 Padova, Italy. E-mail: maurizio.casarin@unipd.it*
[b] *Istituto dei Materiali per l'Elettronica ed il Magnetismo, Consiglio Nazionale delle Ricerche IMEM-CNR, Via alla Cascata 56/C – Povo, 38123 Trento, Italy*
[c] *Institut für Physik, Humboldt-Universität zu Berlin, Newtonstrasse 15, 12489 Berlin, Germany*

† Electronic supplementary information (ESI) available: Computational details. See DOI: 10.1039/c4cp02441a

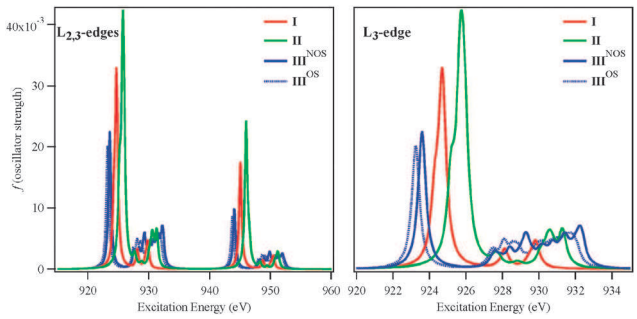

Fig. 2 SO-ZORA TDDFT-TDA Cu 2p excitation spectra of **I**, **II**, and **III**$^{NOS/OS}$. Convoluted profiles are obtained by a Lorentzian broadening of 0.25 eV.[6b]

Cu(II) electric dipole allowed 2p → 3d transitions generate two $2p^5 3d^{10}$ final states with different total angular momentum. The most relevant feature of the Cu(II) $L_{2,3}$ spectra is then the presence of the L_3 (at ~930 eV) and L_2 (at ~950 eV) features, the former having an intensity approximately twice that of the latter.[2,7b] The simulated *f* distributions of **I**, **II** and **III**$^{NOS/OS}$ (ref. 14) are displayed in Fig. 2; the left panel includes the *f* distributions in the 915–960 eV excitation energy (EE) range, while an expanded view of the 920–935 eV range is reported in the right panel.

Despite that the comparison between experiment[2,7b] and theory confirms the well-known EE underestimation (~7 eV, see Table 1), ultimately due to the XC potential deficiencies,[6] the SO-ZORA TDDFT-TDA *f* spectra correctly reproduce the L_3 and L_2 relative positions as well as the corresponding relative intensities in **I** and **III**.[2]

Nardi *et al.*[7b] ascribed the L_3 peak of **II** ($^{II}L_3$) to a single atom-like transition from the Cu $2p_{3/2}$ level to the $16b_{1g}$ spin-down (↓) lowest unoccupied MO (LUMO), significantly localized (52%) on the Cu-based $x^2 - y^2$ 3d AO. They also highlighted that the contribution of the same Cu-based AO to the $6b_{1g}$ LUMO(↓) of **I**, as obtained by homogeneous calculations, was significantly smaller (44%), thus indicating that the Cu–Cl interaction in **I** is more covalent than the Cu–N one in **II**. According to Solomon *et al.*,[2] this would imply, as actually found (see Fig. 2), that *f* values associated with transitions generating $^{II}L_3$ should be larger than those corresponding to transitions generating $^{I}L_3$. Besides this intensity difference, a blue (red) shift of the L_3/L_2 peaks, when moving from **I** to **II** (**III**), and the presence of a shoulder on the lower EE side of $^{I}L_3$ and $^{II}L_3$ are well evident in the right panel of Fig. 2. As far as the former point is concerned, Hocking and Solomon underlined that, in Cu(II) complexes, L_3-ΔEEs are mostly due to differences in the ligand-field strength, contemporarily emphasizing that the higher is the L_3-edge EE, the stronger is the ligand-field.[2b] Incidentally, neither the $^{III}L_3$ red shift[2] nor the $^{II}L_3$ blue shift[7b] relative to $^{I}L_3$ are unexpected. As a matter of fact, the weaker ligand field of **III** relative to **I** is related to the presence of only three (in **III**) rather than four (in **I**) equatorial ligands contributing to the destabilization of the Cu-based $x^2 - y^2$ 3d AO.[2b] Parallel arguments may be invoked to explain the $^{II}L_3$ blue shift, where both the different metal–ligand distances, shorter in **II** (1.968 Å) than in **I** (2.265 Å),[7b] and the ligand electronic properties (the presence of low lying empty π* MOs in the phthalocyanine ligand)[7b] concur to make the ligand-field in **II** stronger than in **I**.

Table 1 Experimental and theoretical excitation energies (eV) for the Cu 2p $L_{2,3}$ core excitation spectra of **I**, **II** and **III**$^{NOS/OS}$

	I	**II**	**III**^{NOS}	**III**^{OS}
$^{exp}L_3$	931.0[2]	931.4[7b]	930.7[2]	
$^{exp}L_2$	951.0[2]	951.4[7b]	[a]	
L_3	924.67	925.75	923.60	923.24
L_2	945.06	946.00	944.07	943.71

[a] The energy of the $^{III}L_2$-edge is not reported in ref. 2.

Before addressing the $^{I}L_3$ and $^{II}L_3$ asymmetric shape, it has to be pointed out that the **III**^{NOS} *f* distribution numerically reproduces the L_3 red shift (1.0 eV) relative to **I**,[2] while the negative ΔEE is overestimated (1.4 eV) in **III**^{OS}. Despite that such a result emphasizes the uselessness of a geometry optimization of **III** (see ESI†), the comparison of SO-ZORA TDDFT-TDA results pertaining to **III**^{NOS} and **III**^{OS} is a gauge of the sensitivity of the adopted theoretical approach to identify even minor ligand-field strength variations. A final remark concerns the overestimation of the theoretical L_3 blue shift of **II** relative to **I**, ~ twice the one experimentally determined, which can be tentatively associated with the different methods and uncertainties in the calibration of Cu(II) $L_{2,3}$ spectra.[15]

As already mentioned, the lower EE sides of $^{I}L_3$ and $^{II}L_3$ are characterized by the presence of a shoulder. SO-ZORA TDDFT-TDA outcomes pertaining to **I**, **II**, and **III** and having the $2p_{3/2}$-based levels as initial spinors (IS) reveal that more than one excitation contribute to $^{X}L_3$ (**X** = **I**, **II**, **III**). Compositions and *f* values of transitions generating $^{X}L_3$ are reported in Table 2.[16]

$^{III}L_3^1/^{III}L_3^2$ and, separately, $^{III}f_3^1/^{III}f_3^2$ values are very similar, thus explaining the absence of any shoulder in $^{III}L_3$. Moreover, all the transitions associated with $^{III}L_3$ have the same $108a_{1/2}$ final spinor (FS), strongly related (93%) to the scalar relativistic (SR) 18a″ LUMO, highly localized on the S_{cys} $3p_z$ (66%) and Cu $3d_{xz}$ (19%) AOs. Even though the 18a″ LUMO localization is quite different from that obtained by Penfield *et al.*[17] by means of spin-restricted self-consistent-field-Xα scattered-wave calculations (41 and 31% on S_{cys} 3p and Cu 3d AOs, respectively), results herein reported perfectly agree with those obtained by the Solomon group. As far as the ISs of transitions associated with $^{III}L_3$ are concerned, substantially all $2p_{3/2}$ Cu-based spinors participate in $^{III}L_3^1$ and $^{III}L_3^2$ (see Table 2). Differently from **III**, both $^{I}L_3^1$ and $^{I}L_3^2$ are generated by a single transition having the same $(100a_{1/2})$ FS, strongly related (96%) to the SR $6b_{1g}$ LUMO of **I** having a 44% localization on the $x^2 - y^2$ 3d AO. Interestingly, the $15a_{1/2} \rightarrow 100a_{1/2}$ transition, contrary to the $17a_{1/2} \rightarrow 100a_{1/2}$ one, involves spinors having a parentage with SR MOs completely localized in the molecular plane. In addition, the $^{I}L_3^2$ EE higher than the $^{I}L_3^1$ one by 0.42 eV explains the shoulder on the lower EE side of $^{I}L_3$.

Moving to the *f* distribution of **II**, SO-ZORA TDDFT-TDA results highlight the presence of three, rather than two, contributions to $^{II}L_3$. Moreover, the corresponding EE spread (0.72 eV)[18] is larger than in **I** (0.42 eV), thus providing a rationale for the more evident

Table 2 SO-ZORA TDDFT-TDA compositions[16] and $f \times 10^3$ values (in parentheses) of transitions generating $^{X}L_3^n$ excitations[a,b,c,d,e,f,g]

I	II	III^{NOS}
		$12a_{1/2} \rightarrow 108a_{1/2}^{(76)}$
L_3^1 $17a_{1/2} \rightarrow 100a_{1/2}^{(100)}$ (7.25)	$9a_{1/2} \rightarrow 294a_{1/2}^{(99)}$ (9.44)	$14a_{1/2} \rightarrow 108a_{1/2}^{(19)}$ (8.49)
		$13a_{1/2} \rightarrow 108a_{1/2}^{(4)}$
	$7a_{1/2} \rightarrow 294a_{1/2}^{(79)}$	$11a_{1/2} \rightarrow 108a_{1/2}^{(88)}$
L_3^2 $15a_{1/2} \rightarrow 100a_{1/2}^{(100)}$ (24.1)	$9a_{1/2} \rightarrow 295a_{1/2}^{(13)}$ (21.6)	$13a_{1/2} \rightarrow 108a_{1/2}^{(8)}$ (9.13)
	$10a_{1/2} \rightarrow 298a_{1/2}^{(8)}$	$14a_{1/2} \rightarrow 108a_{1/2}^{(3)}$
	$10a_{1/2} \rightarrow 298a_{1/2}^{(46)}$	
L_3^3	$9a_{1/2} \rightarrow 295a_{1/2}^{(33)}$ (12.1)	
	$7a_{1/2} \rightarrow 294a_{1/2}^{(20)}$	

[a] Contributions to IS → FS < 1% are not reported. [b] ($f \times 10^3$) values <5 are not reported. [c] $^{I}L_3^1$,$^{I}L_3^2$ EEs are 924.28 and 924.70 eV, respectively; $^{II}L_3^1$, $^{II}L_3^2$, $^{II}L_3^3$ EEs are 925.18, 925.69 and 925.90 eV, respectively; $^{III}L_3^1$, $^{III}L_3^2$ EEs are 923.57 and 923.60 eV, respectively. [d] Cu $2p_{3/2}$-based levels are: **I** ($15a_{1/2}$–$18a_{1/2}$, at 925.62, 925.57, 925.47, 925.46 eV), **II** ($7a_{1/2}$–$10a_{1/2}$, at 934.84, 934.76, 934.65, 934.65 eV), **III**^{NOS} ($11a_{1/2}$–$14a_{1/2}$, at 937.15, 937.14, 937.08, 937.08 eV).[16] [e] Parenthood of Cu $2p_{3/2}$-based levels with SR ZORA Cu 2p-based MOs is: **I** ($15a_{1/2} \rightarrow 2e_u^{(100)}$; $16a_{1/2} \rightarrow 2e_u^{(100)}$; $17a_{1/2} \rightarrow 1a_{2u}^{(67)} + 2e_u^{(33)}$; $18a_{1/2} \rightarrow 1a_{2u}^{(67)} + 2e_u^{(33)}$), **II** ($7a_{1/2} \rightarrow 1e_u^{(100)}$; $8a_{1/2} \rightarrow 1e_u^{(100)}$; $9a_{1/2} \rightarrow 1a_{2u}^{(67)} + 2e_u^{(33)}$; $10a_{1/2} \rightarrow 1a_{2u}^{(67)} + 2e_u^{(33)}$), **III** ($11a_{1/2} \rightarrow 5a'^{(60)} + 1a''^{(36)} + 6a'^{(4)}$; $12a_{1/2} \rightarrow 5a'^{(51)} + 1a''^{(49)}$; $13a_{1/2} \rightarrow 5a'^{(5)} + 1a''^{(32)} + 6a'^{(63)}$; $14a_{1/2} \rightarrow 5a'^{(17)} + 1a''^{(16)} + 6a'^{(67)}$). [f] Lowest unoccupied spinors of **I**, **II**, and **III** are the $100a_{1/2}$, $294a_{1/2}$, and $108a_{1/2}$ ones, respectively. [g] Parenthood of lowest unoccupied spinors of **I**, **II**, and **III** with SR ZORA LUMOs is: **I** ($100a_{1/2} \rightarrow 6b_{1g}^{(96)} + 5b_{1g}^{(3)}$), **II** ($294a_{1/2} \rightarrow 16b_{1g}^{(100)}$), **III** ($108a_{1/2} \rightarrow 18a''^{(93)} + 36a'^{(7)}$).

asymmetry of the $^{II}L_3$ feature. According to theoretical outcomes, $^{II}L_3^1$ is assigned to the single $9a_{1/2} \rightarrow 294a_{1/2}$ transition whose FS is highly reminiscent (99%) of the SR $16b_{1g}$ LUMO of **II**. At variance to that, three different transitions contribute to $^{II}L_3^2$; nevertheless, the main contribution (79%) comes from the $7a_{1/2} \rightarrow 294a_{1/2}$ one, which, similarly to **I**, involves spinors related with SR MOs completely localized in the molecular plane. Despite these similarities, $^{II}L_3^3$ strikingly distinguishes **II** from **I** and **III**. In fact, among the $^{II}L_3^3$ contributions, only the $7a_{1/2} \rightarrow 294a_{1/2}$ transition has a $2p_{3/2}$ AOs → $16b_{1g}$ LUMO character. In this regard, it is noteworthy that the four quasi degenerate $295a_{1/2}$–$298a_{1/2}$ spinors correspond to the SR ligand-based $7e_g$ MO, quite close in energy to the $16b_{1g}$ LUMO (see Fig. 7 of ref. 7*b*) and characterized by a very tiny participation of Cu 3d AOs.

Conclusions

Cu(II) $L_{2,3}$ spectra of **I**, **II** and **III** have been assigned by using the SO-ZORA TDDFT-TDA method implemented in the ADF package. Simulated *f* distributions along the investigated series properly reproduce relative intensities and positions. Moreover, the adopted approach confirms the legitimacy of using the Cu(II) L_3-edge position to get information about the ligand-field strength, contemporarily underlining the possibility of a Cu–ligand symmetry-restricted covalency underestimation when using the Cu(II) L_3-edge intensity as a gauge. Even though further validation is certainly needed, theoretical evidence herein reported indicates that the Cu(II) L_3-edge spectrum of **II** includes contributions that cannot be associated with Cu(II) $2p_{3/2} \rightarrow 3d$ transitions. This would then suggest the use of the Cu(II) L_3-edge intensity to get information about the Cu–ligand symmetry-restricted covalency with some caution because it might imply an underestimation (the higher the intensity, the lower the symmetry-restricted covalency) of such a contribution to the metal–ligand interaction. As far as the suitability of the SO-ZORA TDDFT-TDA method implemented in ADF to evaluate excitation energies for open-shell systems such as Cu(II) complexes in a spin-unrestricted TDDFT calculation including spin–orbit coupling is concerned, there is no doubt that further validations are needed; nevertheless, results herein reported are not only a successful application of the method to treat a particular chemical problem, but also a successful theory test for the SO-ZORA TDDFT-TDA.

Acknowledgements

This work was financially supported by the Italian Ministry of the University and Research (PRIN-2010BNZ3F2, project DESCARTES), and the University of Padova (CPDA134272/13, project S3MArTA). The Computational Chemistry Community of the University of Padova (C3P) at the Department of Chemical Sciences is also acknowledged for providing the computer facilities.

Notes and references

1 A. Bianconi, in *X-ray Absorption; Principles, Applications, Techniques of EXAFS, SEXAFS and XANES*, ed. D. C. Koningsberger and R. Prins, John Wiley & Sons, New York, 1988, pp. 573–662.
2 (*a*) S. J. George, M. D. Lowery, E. I. Solomon and S. P. Cramer, *J. Am. Chem. Soc.*, 1993, **115**, 2968; (*b*) R. K. Hocking and E. I. Solomon, *Struct. Bonding*, 2012, **142**, 155.
3 E. C. Wasinger, F. M. F. de Groot, B. Hedman, K. O. Hodgson and E. I. Solomon, *J. Am. Chem. Soc.*, 2003, **125**, 12894.
4 I. Josefsson, K. Kunnus, S. Schreck, A. Föhlisch, F. de Groot, P. Wernet and M. Odelius, *J. Phys. Chem. Lett.*, 2012, **3**, 3565, and references therein.
5 M. Roemelt, D. Maganas, S. DeBeer and F. Neese, *J. Chem. Phys.*, 2013, **138**, 204101.
6 (*a*) G. Fronzoni, M. Stener, P. Decleva, F. Wang, T. Ziegler, E. van Lenthe and E. J. Baerends, *Chem. Phys. Lett.*, 2005, **416**, 56; (*b*) M. Casarin, P. Finetti, A. Vittadini, F. Wang and T. Ziegler, *J. Phys. Chem. A*, 2007, **111**, 5270; (*c*) B. E. Van

Kuiken, M. Valiev, S. L. Daifuku, C. Bannan, M. L. Strader, H. N. Cho, N. Huse, R. W. Schoenlein, N. Govind and M. Khalil, *J. Phys. Chem. A*, 2013, **117**, 4444.

7 (*a*) F. Sedona, M. Di Marino, D. Forrer, A. Vittadini, M. Casarin, A. Cossaro, L. Floreano, A. Verdini and M. Sambi, *Nat. Mater.*, 2012, **11**, 970; (*b*) M. V. Nardi, F. Detto, L. Aversa, R. Verucchi, G. Salviati, S. Iannotta and M. Casarin, *Phys. Chem. Chem. Phys.*, 2013, **15**, 12864–12881; (*c*) M. V. Nardi, R. Verucchi, L. Aversa, M. Casarin, A. Vittadini, N. Mahne, A. Giglia, N. Nannarone and S. Iannotta, *New J. Chem.*, 2013, **37**, 1036; (*d*) M. V. Nardi, R. Verucchi, C. Corradi, M. Pola, M. Casarin, A. Vittadini and S. Iannotta, *Phys. Chem. Chem. Phys.*, 2010, **12**, 871.

8 Amsterdam Density Functional (ADF) version 2013.01. http://www.scm.com.

9 S. E. Shadle, J. E. Penner-Hahn, H. J. Schugar, B. Hedman, K. O. Hodgson and E. I. Solomon, *J. Am. Chem. Soc.*, 1993, **115**, 767.

10 F. Wang, T. Ziegler, E. van Lenthe, S. van Gisbergen and E. J. Baerends, *J. Chem. Phys.*, 2005, **122**, 204103.

11 S. Hirata and M. Head-Gordon, *Chem. Phys. Lett.*, 1999, **314**, 291.

12 (*a*) E. van Lenthe, E. J. Baerends and J. G. Snijders, *J. Chem. Phys.*, 1993, **99**, 4597; (*b*) E. van Lenthe, E. J. Baerends and J. G. Snijders, *J. Chem. Phys.*, 1994, **101**, 9783; (*c*) E. van Lenthe, A. Ehlers and E. J. Baerends, *J. Chem. Phys.*, 1999, **110**, 8943.

13 C. K. Jørgensen, *Absorption Spectra and Chemical Bonding in Complexes*, Pergamon Press, Oxford, 1962.

14 NOS and OS acronyms stand for Non-Optimized- and Optimized-Structure, respectively (see ESI†).

15 D_{4h}-(*N*-mph)$_2$[$CuCl_4$] and Cu(II) plastocyanin spectra were calibrated by taking as a reference the CuF_2 L_3 peak position (930.5 eV),[2a] while the $L_{2,3}$ CuPc spectrum was calibrated by referring to the $4f_{7/2}$ Au level (84.00 eV).[7b].

16 EE calculations have to be carried out with no symmetry. The spinor labelling is the one reported by P. W. M. Jacobs in *Group Theory With Applications in Chemical Physics*, Cambridge University Press, Cambridge, 2005, p. 450.

17 K. W. Penfield, A. A. Gewirth and E. I. Solomon, *J. Am. Chem. Soc.*, 1985, **107**, 4519.

18 The experimental $^{II}L_3$ full width at half maximum is 1.3 eV.[7b]

PCCP

PAPER

View Article Online
View Journal | View Issue

Cite this: *Phys. Chem. Chem. Phys.*, 2015, **17**, 2001

XAS of tetrakis(phenyl)- and tetrakis(pentafluorophenyl)-porphyrin: an experimental and theoretical study†

Marco Vittorio Nardi,*[ab] Roberto Verucchi,[b] Luca Pasquali,[c] Angelo Giglia,[d] Giovanna Fronzoni,[e] Mauro Sambi,[f] Giulia Mangione[f] and Maurizio Casarin*[fg]

Received 3rd September 2014,
Accepted 27th November 2014

DOI: 10.1039/c4cp03958k

www.rsc.org/pccp

The unoccupied electronic structure of tetrakis(phenyl)- and tetrakis(pentafluorophenyl)-porphyrin thick films deposited on SiO_2/Si(100) native oxide surfaces has been thoroughly studied by combining the outcomes of near-edge X-ray absorption fine structure spectroscopy at the C, N, and F K-edges with those of scalar relativistic zeroth order regular approximation time-dependent density functional theory calculations carried out on isolated molecules. Both experimental and theoretical results concur to stress the electronic inertness of pristine porphyrin macrocycle based $1s^C \rightarrow \pi^*$ and $1s^N \rightarrow \pi^*$ transitions whose excitation energies are substantially unaffected upon fluorination. The obtained results complement those published by the same group about the occupied states of both molecules, thus providing the missing tile to get a thorough description of the halide decoration effects on the electronic structure of the tetrakis(phenyl)-porphyrin.

1. Introduction

Semiconductive properties of π-conjugated organic molecules are well known and widely probed for thick film electronic and opto-electronic devices by exploiting their p-type carrier transport. Among these systems, great attention has been devoted to porphyrins and related derivatives as a consequence of their electronic and optical properties, which can be tuned and enhanced through molecular engineering.[1–3] In fact, the aromatic structure of these molecules makes them particularly appealing for use in electronics,[4] solar cells,[5] biological fields,[6] and sensing,[7] thus actually pushing towards the realization of a promising new generation of solid state devices. Moreover, the switch of electronic transport properties from p- to n-type through the substitution of hydrogen atoms on the outer molecular rim with halogen species such as fluorine is an intriguing opportunity, impelling research activity towards the study of organic systems having both electron acceptor and donor characteristics.[8] To this end, the investigation of the unoccupied electronic structure of tetrakis(phenyl)- and tetrakis(pentafluorophenyl)-porphyrin (hereafter, **I** and **II**, respectively) molecular films, complementing the one carried out by some of us on the occupied states of the same species, is reported herein.[8,9]

Thick films of **I** and **II** deposited on SiO_2/Si(100) native oxide surfaces by means of supersonic beams seeded using the organic precursor have been probed by using near-edge X-ray absorption fine structure (NEXAFS) spectroscopy to elucidate the nature, the localization and the relative energy positions of their low lying unoccupied molecular orbitals (MOs).[10] Actually, due to the highly localized character of core excitations, NEXAFS is solidly accepted as a site-sensitive probe of empty states. According to a well-established procedure,[8,9,11] NEXAFS spectra collected from thick films of both species have been rationalized with time-dependent density functional theory (TD-DFT)

[a] *Institute for Physics, Supramolecular Systems Division "SMS", Humboldt Universitat zu Berlin, Brook-Taylor-Straße 6, 12489 Berlin, Germany. E-mail: marco.nardi@physik.hu-berlin.de; Fax: +49 30 2093 7443; Tel: +49 30 2093 7716*

[b] *Istituto dei Materiali per l'Elettronica ed il Magnetismo, IMEM-CNR, Sezione di Trento, Via alla Cascata 56/C – Povo, 38100 Trento, Italy. E-mail: roberto.verucchi@cnr.it*

[c] *Dipartimento di Ingegneria "Enzo Ferrari", Università degli Studi di Modena e Reggio Emilia, Strada Vignolese 905, 41125 Modena, Italy. E-mail: luca.pasquali@unimore.it*

[d] *TASC-INFM, MM building in Area Science Park, s.s.14 km 163.5, 34012 Basovizza (Trieste), Italy. E-mail: angelo.giglia@ELETTRAdomain*

[e] *Dipartimento di Scienze Chimiche e Farmaceutiche, Università di Trieste, Via L. Giogieri 1, 34127 Trieste, Italy. E-mail: fronzoni@units.it*

[f] *Dipartimento di Scienze Chimiche, Università degli Studi di Padova, Via Marzolo 1, 35131 Padova, Italy. E-mail: maurizio.casarin@unipd.it; Fax: +39 049 8275161; Tel: +39 049 8275164*

[g] *Istituto per l'Energetica e le Interfasi, IENI-CNR, Via Marzolo 1, 35131 Padova, Italy*

† Electronic supplementary information (ESI) available: Energy-ordered linear combinations of heavy atom 1s AOs; Γ_{xs} representation products corresponding to electric dipole allowed transitions in D_{2h} symmetry; excitation energies and oscillator strengths *f* for the C and N (C, N and F) 1s excitation spectrum of **I** (**II**) from SR-ZORA TD-DFT calculations. See DOI: 10.1039/c4cp03958k

calculations[12–16] performed on isolated models. Although we are perfectly aware that the unoccupied electronic structure of **I** has been already studied both experimentally[17] and theoretically,[17b,18] we decided to revisit it to ensure that theoretical results pertaining to **I** and **II** are homogeneous between them.

2. Experimental and computational details

NEXAFS experiments have been carried out at the BEAR end station (BL8.1L), at the left exit of the 8.1 bending magnet of the ELETTRA synchrotron facility in Trieste (Italy).[19] NEXAFS spectra have been collected in total electron yield (TEY) mode (*i.e.*, drain current mode) at the C, N, and F K-edges, and normalized to the incident photon flux and to the clean substrate signal. Spectral energies have been calibrated by referring to the $4f_{7/2}^{Au}$ core level, which has been obtained from an Au(100) sputtered sample (*i.e.*, carbon free). The synchrotron beam was elliptically polarized with the dominating components lying in the horizontal (H) plane, and the corresponding ellipticity, defined as $\varepsilon = |\vec{E}_V|^2 \times |\vec{E}_H|^{-2}$, equal to 0.1 (V stands for the vertical plane and $\varepsilon = 1$ (0) for circularly (linearly) polarized light). Throughout the measurements, the incidence angle of the light with respect to the sample surface plane has been kept fixed at 10°. To correctly process the acquired data, each absorption spectrum has been first normalized to the drain current, which has been measured on an optical element (refocusing mirror) placed along the beam-line, and then normalized to the absorption spectrum attained under the same experimental conditions and energy range, on a Au(100) sputtered sample. The energy scale of each single spectrum has been re-calibrated taking into account the energy fluctuation of characteristic absorption features measured using the refocusing mirror.

Thick films of **I** and **II** (*i.e.*, 50 nm) have been grown in ultra high vacuum by supersonic molecular beam deposition in a preparation chamber (base pressure $< 5 \times 10^{-10}$ mbar) directly connected to the analysis chamber (base pressure $< 1 \times 10^{-10}$ mbar). The nominal film thickness (density, 2.2 g cm^{-3}) has been monitored by using a calibrated quartz crystal microbalance.

TD-DFT calculations have been carried out on **I** and **II** isolated species by using the Amsterdam Density Functional package.[12] The adopted geometrical parameters are those optimized in ref. 8 and 9 through the assumption of an idealized D_{2h} symmetry for both molecules. Ionization energies of N, C and F 1s-based MOs have been obtained by running scalar relativistic (SR) Zeroth Order Regular Approximation (ZORA) calculations,[20] and looking at the Kohn–Sham eigenvalues pertaining to the ground state (GS) electronic configuration. ZORA calculations have been run by adopting all-electron, triple-ζ with a polarization function, ZORA basis sets for all the atoms[21] and the LB94 approximate functional with the GS electronic configuration.[13,15] A further series of GS non-relativistic calculations have been run to get information about the lowest lying unoccupied frontier orbitals,[22] possible final MOs (fmos) of NEXAFS transitions. The outcomes of these numerical experiments have been graphically displayed as density of states (DOS). In fact, these plots, based on the Mulliken's prescription for partitioning the overlap density,[23] afford an easy inspection of the atomic composition of MOs over a broad energy range. Partial DOS (PDOS) and DOS have been computed by using eqn (1) and (2), respectively:[8,9,11]

$$\mathrm{PDOS}^{\nu}_{n\ell}(\varepsilon) = \sum_p \frac{\gamma}{\pi} \frac{f^{\nu}_{n\ell,p}}{\left(\varepsilon - \varepsilon_p\right)^2 + \gamma^2} \quad (1)$$

while

$$\mathrm{DOS}(\varepsilon) = \sum_{\nu,n,\ell} \mathrm{PDOS}^{\nu}_{n\ell}(\varepsilon) = \sum_p \frac{\gamma}{\pi} \frac{g_p}{\left(\varepsilon - \varepsilon_p\right)^2 + \gamma^2} \quad (2)$$

where $f^{\nu}_{n\ell,p}$ is Mulliken's population contribution from the atom ν and the state $n\ell$ to the pth MO of energy ε_p and degeneracy g_p. The Lorentzian broadening factor γ was fixed equal to 0.25 eV. The Mulliken's prescription,[23] even though uniquely defined, is rather arbitrary; nevertheless, it yields at least a qualitative idea of the electronic localization. Moreover, 3D contour plots have been also employed to assign the σ* or π* character of selected MOs.

K-edge NEXAFS spectra of **I** and **II** have been simulated by evaluating excitation energies and corresponding oscillator strengths (f) for transitions having the $1s^{C/N/F}$-based MOs as initial MOs (imos). To this end, SR-ZORA TD-DFT calculations[24] suitably tailored to treat core electron excitations have been run.[25] All electrons, quadruple-ζ with four sets of polarization functions, ZORA basis sets have been adopted for all the atoms;[21] moreover, two shells of diffuse functions, following the even tempered criterion, further augmented the basis sets of the F, N, and C atoms specifically involved in the excitations.[26] The adiabatic local density approximation[14] has been employed to approximate the XC kernel, while the LB94 approximate functional[15] with the GS electronic configuration has been adopted for the XC potential applied in the self consistent field calculations. Incidentally, Fronzoni *et al.*[13] have pointed out that, among approximate XC functionals having the correct asymptotic behaviour, a necessary condition for a proper description of high energy virtual orbitals and Rydberg states, the LB94 functional provides a satisfactory agreement between theory and experiment. Finally, scaled ZORA orbital energies[16] in the TD-DFT equations have been employed throughout to improve deep core excitation energies.

3. Results and discussion

I consists of the pristine porphyrin macrocycle (pmc) with four phenyl (Ph) rings bonded to the *meso* carbon atoms (C^5, C^{10}, C^{15}, and C^{20} in Fig. 1, where the recommended IUPAC 1–24 numbering system has been adopted) collectively tagged C^m.[27] Despite the bond delocalization (porphyrins are aromatic and they obey the Hückel's rule for aromaticity in that they possess $4n + 2$ delocalized π electrons),[28] different chemical species may be identified in the molecule: (i) the pyrrolic nitrogen atoms, N^{21} and N^{23} (N^{PyH}), (ii) the iminic nitrogen atoms, N^{22} and N^{24} (N^{Py}); (iii) the twenty-four phenyl carbon atoms (C^{Ph}, chemically very similar); (iv) the four C^m atoms.

Different species of carbons may also be recognized in the non equivalent pyrrole rings; *i.e.*, those occupying the so called

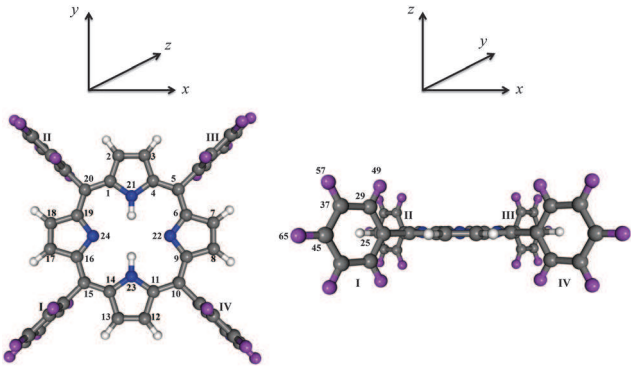

Fig. 1 Schematic representation (top and side view) of title molecules. Violet spheres correspond to H and F atoms in **H_2TPP** (**I**) and **H_2TPP(F)** (**II**), respectively. The atom numbering corresponds to the one recommended by IUPAC and adopted by Nardi *et al.* in ref. 8 and 9. In the selected framework, the pristine porphyrin macrocycle (pmc) lies in the *xy* plane and corresponds to the σ_h plane.

α (1, 4; 6, 9; 11, 14; 16, 19) and β (2, 3; 7, 8; 12, 13; 17, 18) positions, and, hereafter, collectively tagged C^{Py}. Besides those just mentioned, **II** includes a further atomic species (F) whose effects on the occupied electronic structure of **I** have been thoroughly discussed in ref. 8 (see PDOS and DOS reported in Fig. 2 and 3; in Fig. 2 the $1s^C$ core level spectra of **I** and **II** have been also included for comparison).

Among **I** and **II** heavy atoms (C, N and F), the pmc ones lie in the σ_h plane, while C^{Ph} and F species may be either parallel (||) or perpendicular ($\perp$) to it; C^{25}, C^{45}, F^{65} (C^{29}, C^{37}, F^{49}, F^{57}) and symmetry related atoms are then collectively tagged $C_{||}{}^{Ph}$ and $F_{||}$ ($C_{\perp}{}^{Ph}$ and $F_{\perp}$).

In the D_{2h} symmetry,[8,9] the linear combinations of 1s atomic orbitals (AOs) span the following irreducible representations (IRs): $a_g + b_{1g} + b_{2u} + b_{3u}$ (C^{Py}, C^m, $C_{||}{}^{Ph}$, $F_{||}$); $a_g + b_{1g} + b_{2g} + b_{3g} + a_u + b_{1u} + b_{2u} + b_{3u}$ ($C_{\perp}{}^{Ph}$ and $F_{\perp}$); $a_g + b_{2u}$ (N^{PyH}); $a_g + b_{3u}$ (N^{Py}).[29] Moreover, information about the localization of **I** and **II** unoccupied MOs, potential fmos in X-ray absorption processes, may be gained by referring to Fig. 3 where contributions from heavy atoms 2p AOs to the DOS of **I** and **II** are displayed (lowest lying peaks associated with the empty levels are alphabetically labelled).

The inspection of Fig. 3 clearly indicates that, both in **I** and **II**, the peak labelled as **L** is generated by 2p AOs of pmc atoms,[8,9] while major contributions to the higher lying features **M** and **N** come from C^{Ph} (**I**) and C^{Ph}/F (**II**) 2p AOs (**M**) and H 1s AOs (**N**). In more detail, two quasi degenerate $\pi_{\perp}$* MOs ($12b_{2g}/12b_{3g}$ in **I** and $21b_{2g}/21b_{3g}$ in **II**, see Fig. 4) contribute to **L**, while at least nine (thirteen) MOs participate in the generation of **M** in **I** (**II**).[30,32] Incidentally, among MOs generating **M**, only one $\pi_{\perp}$* orbital, namely the $11a_u$ MO in **I** (see Fig. 4) and the $20a_u$ MO in **II**, is present.

NEXAFS spectra

NEXAFS is unanimously recognized as an experimental tool able to provide a site-sensitive probe of the unoccupied electronic structure of molecules. Actually, since it implies the excitation of

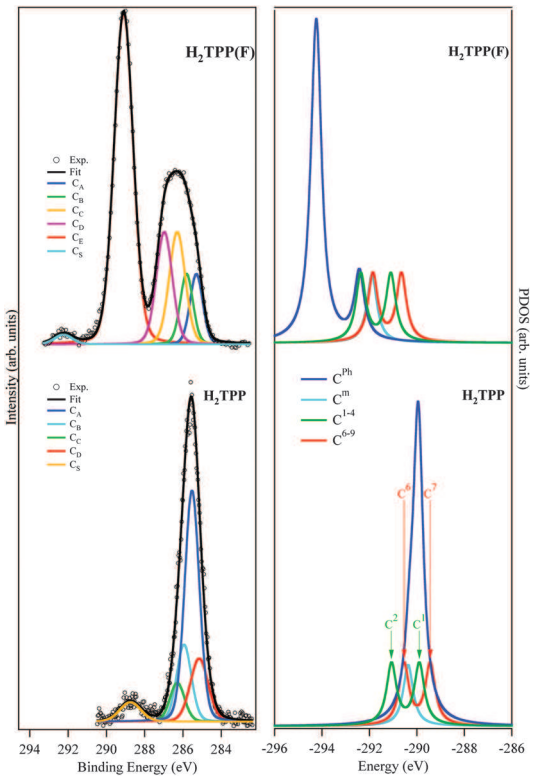

Fig. 2 (left panel) $1s^C$ core level spectra (background subtracted) from the **H_2TPP** (**I**) and **H_2TPP(F)** (**II**) films. The single components, shown in the legend, are related to the different carbon chemical species of the two molecules.[8,9] (right panel) SR-ZORA DFT **H_2TPP** (**I**) and **H_2TPP(F)** (**II**) $1s^C$ PDOS. Numerical labels adopted for both molecular species refer to the ones reported in Fig. 1.[8,9]

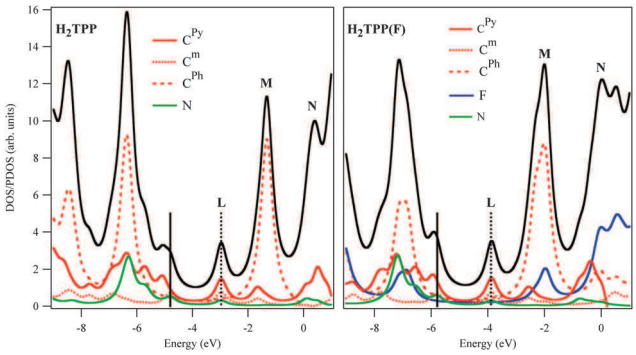

Fig. 3 **H_2TPP** (**I**) and **H_2TPP(F)** (**II**) DOS; contributions to the DOS coming from the heavy atoms 2p AOs are also included. Vertical bars represent the highest occupied MO (full line) and the lowest unoccupied MO (dotted line) energies.

core electrons to unoccupied albeit bound valence orbitals as well as to shallow states in the near continuum, the localized character of core excitations makes K-edge spectra very sensitive to both the electronic structure and the local surroundings of the absorbing atom.

Extended NEXAFS spectra at the C, N and F K-edges of **I** and **II** thick films are displayed in Fig. 5, where main features have been identified and labelled with capital letters.

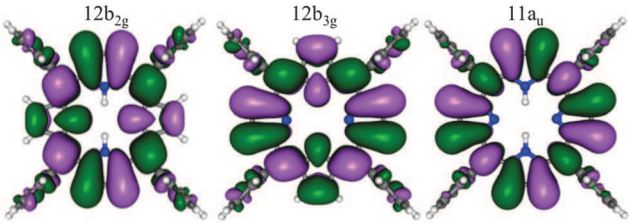

Fig. 4 3D plots of the **H_2TPP** (**I**) lowest lying unoccupied frontier orbitals. Displayed isosurfaces correspond to ± 0.02 $e^{1/2}$ $Å^{-3/2}$ values. Corresponding MOs in **H_2TPP(F)** (**II**) ($21b_{2g}$, $21b_{3g}$ and $20a_u$) are indistinguishable from those depicted in the figure.

Excitation energies taken into account range between 280 and 310 eV (C K-edge), 395 and 415 eV (N K-edge), 685 and 705 eV (F K-edge). According to the literature,[11a,33–35] the ranges we considered have been split into two regions ([i] and [ii] in Fig. 5); the former is usually associated with $1s^C/1s^N/1s^F \rightarrow \pi^*$ excitations, whereas the latter accounts for $1s^C/1s^N/1s^F \rightarrow \sigma^*$ valence transitions. The inspection of Fig. 5, in particular of the C K-edge spectra, testifies the massive perturbation undergone by the electronic structure of **I** upon Ph fluorination. Symmetry, orbitals and spectra[31] have been cooperatively used to rationalize the effects of such a decoration.

Now, before facing the assignment of NEXAFS spectra of **I** and **II**, it can be useful to spend a few words about title molecule spectroscopic differences foreseeable just on the basis of symmetry arguments. **I** and **II** electric dipole allowed transitions span the b_{1u}, b_{2u}, and b_{3u} IRs of the D_{2h} symmetry point group. In fact,

$$\Gamma_{GS} \otimes \Gamma_{\mu} \otimes \Gamma_{XS} \supset \Gamma_{a_g} \quad (3)$$

where Γ_{GS} is the electronic GS IR (a_g in the D_{2h} group), Γ_{μ} is the dipole moment operator IR (b_{1u}, b_{2u}, and b_{3u} in the D_{2h} group) and Γ_{XS} is the electronic excited state IR.[31] In the present case, electric dipole allowed transitions imply that

$$\Gamma_{\mu} = \Gamma_{XS} \quad (4)$$

with

$$\Gamma_{XS} = \Gamma_{imo} \otimes \Gamma_{fmo} \quad (5)$$

where, within the approximation, which reduces the complete one-electron excited configurations space (1h–1p space) to the subspace where only the core electrons are excited, Γ_{imo} and Γ_{fmo} are the IRs of the initial and final MOs, respectively.[36] As such, and before tackling experimental evidences, it can be useful to remind that, in the adopted geometry,[8,9] Ph rings are assumed to be perpendicular to σ_h (see Fig. 1); π^* orbitals are then $\perp$ ($\pi_\perp^*$) or || ($\pi_{||}^*$) to σ_h according to their localization: $\perp$ if localized on the pmc atoms, || if localized on the C^{Ph} or F ones. Dipole allowed $1s \rightarrow \pi_\perp^*$ ($1s \rightarrow \pi_{||}^*$) transitions will be therefore of b_{1u} (b_{2u} or b_{3u}) symmetry. Constraints for imos and fmos are summarized in Table S2 (ESI†).[31]

These considerations, simply based on symmetry arguments, point out that C-based $1s \rightarrow \pi^*$ excitations may be split into two sets, one including transitions of b_{1u} symmetry (hereafter, $\Pi_\perp$), the other including b_{2u} or b_{3u} transitions (hereafter, $\Pi_{||}$). Focusing our attention on the former set, this can be further split into two subsets, one including transitions from ^{pmc}C 1s-based imos (see Table S1, ESI;† hereafter, $^{pmc}\Pi_\perp$), the other encompassing transitions from C^{Ph} 1s-based imos (hereafter, $^{Ph}\Pi_\perp$). Since $^{pmc}\Pi_\perp$ transitions are completely localized on the pmc, they may be used as an internal gauge of the fluorination effects on the porphyrin electronic structure when moving from **I** to **II**.

C K-edge spectra

The [i] region of the C K-edge spectra of **I** and **II** is characterized by the presence of four main features, which cover an energy range of $\sim$5 eV (see the fitted spectrum in Fig. 6);[37] moreover, a shoulder **S**, more evident in **II** than in **I**, is present on the lower energy side of the **A** band. In both spectra, the [i] region needed seven components, whose positions are reported in Table 1, to be properly fitted.

Before entering into the detail of the assignment of the C K-edge spectral features of **I** and **II** (see Tables S3 and S4, ESI† and Fig. 7), it may be useful to remind that Nardi *et al.* succeeded in identifying all carbon chemical species contributing to the complex C 1s spectrum of **II**.[9] In particular, the combined use of X-ray photoelectron spectroscopy and SR-ZORA DFT calculations allowed some of us to state that the Ph ring fluorination results in a higher binding energy of the C^{Ph} 1s core levels, while the

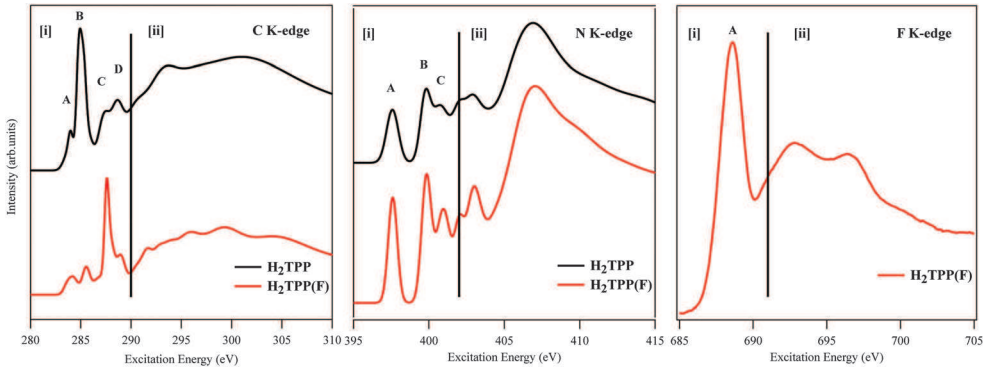

Fig. 5 Extended NEXAFS spectra of thick films of **H_2TPP** (**I**) (black line) and **H_2TPP(F)** (**II**) (red line) deposited on SiO_2/Si(100) native oxide surfaces. Vertical lines at 290 eV (left), 402 eV (middle) and 691 eV (right) separate [i] and [ii] regions (see text).

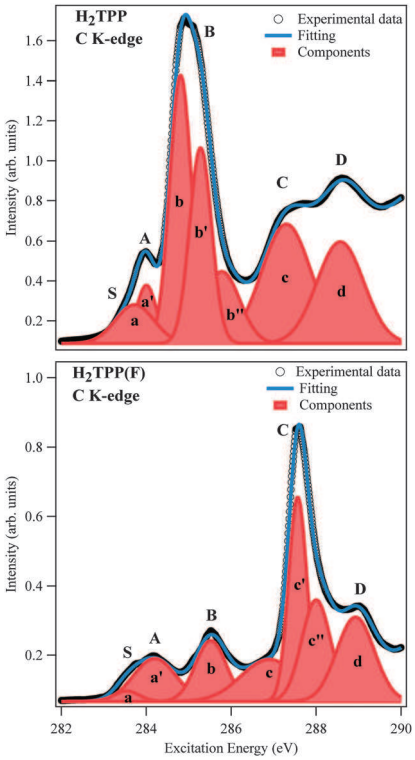

Fig. 6 Fitted [i] region of the C K-edge NEXAFS spectra of **H_2TPP** (**I**) (top) and **H_2TPP(F)** (**II**) (bottom).

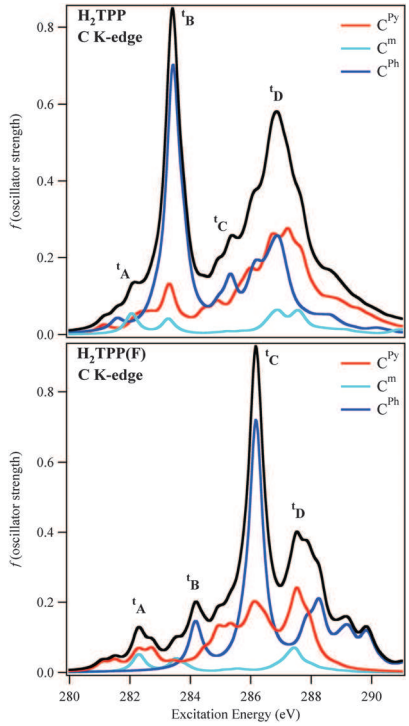

Fig. 7 SR-ZORA TD-DFT C 1s excitation spectra of **H_2TPP** (**I**) (top) and **H_2TPP(F)** (**II**) (bottom). Contributions from the different imols are also displayed. Convoluted profiles have been obtained by using a Lorentzian broadening of 0.25 eV. SR-ZORA ionization limits may be deduced from the right panels of Fig. 2.[8,9,39]

Table 1 Excitation energy position (eV) of C K-edge transitions (components **a–d**) for the fit of **H_2TPP** (**I**) and **H_2TPP(F)** (**II**) thick films spectra reported in Fig. 6. ΔE between similar features for **I** and **II** are also reported

Component	I	ΔE	II	ΔE
a	283.72	—	283.53	—
a′	284.00	0.28	284.19	0.66
b	284.81	1.09	285.53	2.00
b′	285.28	1.56	—	
b″	285.78	2.06	—	
c′	—		286.90	3.37
c	287.30	3.58	287.57	4.04
c″	—		288.00	4.47
d	288.57	4.85	288.93	5.40

pmc C chemical species show less relevant differences when moving from **I** to **II** (see Fig. 2).

A preliminary, sketchy assignment of the C K-edge spectra of **I** and **II** may be then attempted by exploiting the hypothesis that $^{pmc}\Pi_{\perp}$ transitions should have similar excitation energies in **I** and **II**, while the $\Pi_{||}$ and, to a minor extent, the $^{Ph}\Pi_{\perp}$ ones should be blue shifted on passing from **I** to **II**. Accordingly, major contributions to the lowest lying band envelope **S** + **A** of both NEXAFS spectra should come from excitations (see Table S1, ESI,† Fig. 2 and 3) associated with transitions from the b_{2u}/b_{3u} linear combinations of C^{m}-/C^{Py}-based 1s AOs to the lowest unoccupied MOs (LUMOs) of **I** ($12b_{2g}$ and $12b_{3g}$ MOs) and **II** ($21b_{2g}$ and $21b_{3g}$ MOs).

Relative intensity variations of bands **B** and **C** when moving from **I** to **II** ultimately state that the main contribution to the intensity of **B** in **I** and **C** in **II** has to be associated with $\Pi_{||}$ and $^{Ph}\Pi_{\perp}$. Moreover, as far as the leftover band **B** in **II** and at least one component of **B** in **I** are concerned, they could be tentatively ascribed to a single excitation event corresponding to a transition having a b_{1g} linear combination of C^{m}-/C^{Py}-based 1s AOs as imo, and the $11a_u$ ($20a_u$) MO as fmo in **I** (**II**) (see Table S2, ESI† and Fig. 4).[32] Besides these considerations, two further points need to be emphasized: (i) the number of $1s^{C}$-based possible imos is rather large and it corresponds to the number of C atoms present in the molecular skeleton (*i.e.*, 44, see Fig. 1 and Table S1, ESI†); (ii) the energy range covered by the 44 linear combinations of the $1s^{C}$-based possible imos is quite wide (1.6 and 3.6 eV in **I** and **II**, respectively, see Fig. 2). Highest lying NEXAFS features of the [i] region of both **I** and **II** might then include contributions not only from 1s → π* but also from 1s → σ* excitations, the former (latter) having the $1s^{C}$-based linear combinations with the highest (lowest) binding energies as imos.

Excitation energies and *f* values for the C 1s excitation spectrum of **I** and **II** as obtained from SR-ZORA TD-DFT[24] calculations are reported in Tables S3 and S4, ESI,† respectively, while the corresponding *f* distributions between 280 and 291 eV are displayed in Fig. 7.

The comparison between NEXAFS patterns and the $^{I}f^{C}/^{II}f^{C}$ distributions confirms the well-known excitation energy underestimation (in the present case ~2 eV), ultimately due to the XC potential deficiencies.[11,13b,25] Nevertheless, SR-ZORA TD-DFT

outcomes prove that, even though the reference to the carbon PDOS of **I** and **II** (see Fig. 2 and 3) allows us to forecast the major contributions to the NEXAFS features, theoretical results are unavoidable to look into their details.

Starting with calculated data regarding **I**, the inspection of Table S3, ESI† suggests that, according to our symmetry- and GS-based predictions (see Fig. 2 and 3), the **S** + **A** band envelope has to be associated with the seven lowest lying excitations, all of them corresponding to $\Pi_\perp$ transitions. More specifically, the $^{pmc}\Pi_\perp$ $10b_{2u}$ + $10b_{3u}$ → LUMOs[30] and the $^{Ph}\Pi_\perp$ $7b_{3u}$ → LUMO[30] transitions should contribute to **S**, while the remaining five excitations, all but one ($6b_{1g}$ → $11a_u$) corresponding to $^{pmc}\Pi_\perp$ transitions, should be hidden under the **A** feature of Fig. 6 (top). Such an assignment perfectly agrees with that proposed by Di Santo *et al.*[17a] on a purely experimental ground, it concurs with theoretical results reported by Diller *et al.*[17b] and it sheds new light on the angle-dependent linear dichroism characterizing the NEXAFS C K-edge spectrum of a multilayer of **I**.[40] Nevertheless, it has to be remarked that the numerical agreement obtained by Diller *et al.*[17b] between theory and experiment is better than that we herein reported.

Even applying a quite severe filtering to the excitation selection (only those with $^{I}f^{C} \geq 10 \times 10^{-3}$ have been included in Table S3, ESI†), the analysis of theoretical outcomes states that, as preliminary foreseen, a really large number of excitations contributes to **B**, **C** and **D**.

This means that any detailed assignment of these features would simply be a matter of taste. Nevertheless, useful information can be obtained by looking into SR-ZORA TD-DFT results (see Fig. 7). The first thing to be noted is that the excitation energy range covered by the **I** [i] region (~5 eV, see Fig. 6 (top) and Table 1) is well reproduced by the $^{I}f^{C}$ distribution reported in Fig. 7 (top). The same holds for the $\Delta E_{\mathbf{b}'-\mathbf{b}}$ (0.47 eV, see Table 1), which is quantitatively reproduced by the range (0.54 eV, see Table S3, ESI†) covered by the closely spaced excitations 8–19,[41] all but one ($3b_{1g}$ → $11a_u$) associated with 1s → $\pi_{||}$* transitions having the linear combinations of Ph-based e_{2u} π* MOs as fmos.[40,42] The agreement of such an assignment with NEXAFS data of Di Santo *et al.*[17a] is twice as important because both the use of the isolated molecule approach to simulate NEXAFS features of a multilayer of weakly interacting molecules[8,9,11] and the assumption of a D_{2h} symmetry for **I**[9] are further reinforced.

In addition to the above considerations, the proposed assignment implies that the **b**″ component of the NEXAFS spectrum of **I** has to be ascribed to a single excitation (the 20th in the Table S3, ESI†) associated with the C^7-based $10b_{2u}$ + $10b_{3u}$ → $14b_{3g}$ + $14b_{2g}$ transition. Incidentally, the energy difference (0.69 eV) between the 20th and the 19th excitation (see Table S1, ESI†) agrees pretty well with the $\Delta E_{\mathbf{b}''-\mathbf{b}'}$(0.5 eV, see Table 1).

Moving to the broad and ill resolved bands **C** and **D** in Fig. 6, the only things that can be mined by theoretical outcomes and deserve to be mentioned are: (i) C^m-based 1s AOs negligibly contribute to **C**; (ii) C^{Py}- and C^{Ph}-based 1s AOs comparably contribute to **D**; (iii) 1s → $\pi_{||}$* transitions associated with excitations hidden under **D** have the linear combinations of the Ph-based b_{2g} π* orbitals as fmos;[42] (iv) more than 50% of the excitations reported in Table S3, ESI† and associated with the feature **D** corresponds to 1s → σ* transitions. With specific reference to this last result, it has to be noted that, once again, it perfectly agrees with literature data.[17]

The striking differences characterizing the C K-edge NEXAFS spectra of **I** and **II** (see Fig. 6) have been already emphasized and, at a first look, they are quite well reproduced by the SR-ZORA TD-DFT $^{I}f^{C}$ and $^{II}f^{C}$ distributions. Moreover, the comparison of data reported in Table S3, ESI† with those of Table S4, ESI† indicates that $^{pmc}\Pi_\perp$ transitions, viable as an internal gauge, can be straightforwardly identified in **II**.[43] Besides the very large blue shift of the $\Pi_{||}$ set upon the Ph ring fluorination,[44] a careful inspection of theoretical outcomes, including those that for space saving reasons are not included in the ESI,† reveals that the lower excitation energy regions of **I** and **II** include the same number of transitions (seven) with $f \geq 10 \times 10^{-3}$. Nevertheless, their localization, intensities and composition are different. More specifically, the 2nd and 7th excitations of **I** (see Table S3, ESI†), corresponding to transitions having as imos the C^{29}-based 1s AOs, are strongly blue shifted upon the Ph ring fluorination[44] and substituted by the two C^2-based $12b_{3u}$ + $12b_{2u}$ → $21b_{2g}^{(70)}$ + $21b_{3g}^{(30)}$ and $11b_{1g}$ → $20a_u^{(99)}$ transitions, lying at 281.50 ($^{II}f^{C}$ = 18.646 × 10^{-3}) and 282.75 eV ($^{II}f^{C}$ = 18.838 × 10^{-3}) (see Table S4, ESI†). Transitions reminiscent in **I** of those just described in **II** correspond to the C^2-based $8b_{3u}$ → $12b_{2g}^{(100)}$ at 281.57 eV and $7b_{1g}$ → $11a_u^{(100)}$ at 282.81 eV, not included in Table S3, ESI† as a consequence of the adopted filtering (their $^{I}f^{C}$ values are 0.49948 × 10^{-3} and 0.38949 × 10^{-3}, respectively). Such a result provides first information, among many others (*vide infra*), about the effects induced by the F decoration of Ph rings on the pmc electronic properties: it may magnify the *f* values of excitations associated with specific transitions without significantly affecting their excitation energies.[45]

As far as the assignment of the NEXAFS features of **II** is concerned, SR-ZORA TD-DFT calculations induce us to assign all excitations hidden under the band envelope **S** + **A** and the lower excitation energy side of the leftover band **B** to transitions belonging to the $^{pmc}\Pi_\perp$ subset. In more detail, the shoulder **S** is ascribed to the lowest lying, C^7-based, $13b_{2u}$ → $21b_{3g}$ transition, while the whole **A** feature is associated with the excitations 2–7 and the lower excitation energy side of the leftover band **B** to the $^{pmc}\Pi_\perp$ $9b_{1g}$ → $20a_u$ transition. Interestingly, the whole band envelope **S** + **A** is substantially unaffected by the Ph ring fluorination. As a matter of fact, data reported in Table 1 indicate that, on passing from **I** to **II**, the **a**′ component is slightly blue shifted (0.19 eV), while the **a** one is even red-shifted by the same amount. Both evidences are perfectly reproduced by SR-ZORA TD-DFT calculations, which ultimately establish the unresponsiveness upon fluorination of the selected internal gauge (compare in Tables S3 and S4, ESI† the energies of the excitation selected as the internal gauge).[43] Other excitations reasonably hidden under **B** are those (see Table S4, ESI†) associated with 1s → $\pi_{||}$* transitions localized on non-fluorinated $C_{||}^{Ph}$.

A comparison between components of bands **B** and **C** in **I** and **II**, similar to that considered for the band envelope **S** + **A**, is prevented by the substantial perturbation undergone by **B** and **C** upon fluorination; nevertheless, it is noteworthy that the above mentioned unresponsiveness of the $^{pmc}\Pi_{\perp}$ subset is systematically confirmed by comparing correlated transitions in the two molecules. A further example is provided by the comparison between the C[7]-based $9b_{1g} \rightarrow 13a_u$ transition in **I** (excitation lying at 284.86 eV, see Table S3, ESI†) and the C[7]-based $12b_{1g} \rightarrow 23a_u$ transition in **II** (284.90 eV, see Table S4, ESI†), both associated with the lower energy side of **C** in the corresponding NEXAFS spectra.[46] Moreover, even though the excitations hidden under **C** with the highest *f* values correspond to $^{Ph}\Pi_{||}$ transitions localized on fluorinated C atoms and involving Ph-based $e_{2u}\ \pi_{||}^*$ orbitals, the contribution from excitations associated with $1s \rightarrow \pi_{\perp}^*$ and $1s \rightarrow \sigma^*$ transitions cannot be neglected (see Table S4, ESI†). Differently to **I**, SR-ZORA TD-DFT outcomes indicate that no $^{Ph}\Pi_{||}$ transition having a linear combination of the Ph-based $b_{2g}\ \pi_{||}^*$ orbitals as fmo is present in the selected range (see Table S4, ESI†).

As already mentioned, the inspection of Fig. 2 and 3 clearly shows that both core levels and the unoccupied electronic structure of **I** are considerably perturbed upon fluorination; nevertheless, the calculated blue shifts undergone by the core levels, in particular by the C^{Ph}-based 1s AOs, are significantly different with respect to the ones calculated for the unoccupied electronic structure.[47] Even though we are perfectly aware that different excitations imply different relaxation processes and that excitation energies cannot be directly compared with Kohn–Sham orbital energy differences, the similar blue shift undergone by $^{pmc}\pi_{\perp}^*$ and ^{pmc}C-based 1s AOs upon fluorination provides a rationale of the experimental unresponsiveness, theoretically confirmed, of the $^{pmc}\Pi_{\perp}$ subset.

N K-edge spectra

The [i] region of the N K-edge spectra of **I** and **II** is characterized by the presence of three main features, alphabetically labelled in Fig. 8, which cover an energy range of ~4 eV. These features have been fitted with three components whose excitation energy positions are reported in Table 2.

The low number of possible imos (four, see Table S1, ESI†), the severe symmetry constraints and the consequent inherent simplicity of the N K-edge spectra make their preliminary assignment straightforward.[30,32]

As a matter of fact, the information pertaining to the relative positions of the N core levels (see Fig. 9, where experimental and calculated $1s^N$ spectra are compared)[8,9,48] and the unoccupied electronic structure of **I** and **II** (see Fig. 3) allows us to confidently ascribe the lower excitation energy region of **I** and **II** to $1s \rightarrow {}^{pmc}\pi_{\perp}^*$ transitions.

In particular, the lowest lying feature **A** has to be associated, both in **I** and **II**, with a single excitation event corresponding to the $b_{1u}\ N^{Py}$-based $1b_{3u} \rightarrow 12b_{2g}$ transition in **I** and the $4b_{3u} \rightarrow 21b_{2g}$ one in **II**. Similarly, a single excitation associated with the $b_{1u}\ N^{PyH}$-based $1b_{3u} \rightarrow 12b_{2g}$ ($4b_{3u} \rightarrow 21b_{2g}$) transition in **I** (**II**) is hidden under **B**. Qualitatively, the assignment of the feature **C** should include excitations associated with transitions whose fmos lie necessarily beyond the feature **M** of Fig. 3.[30,32]

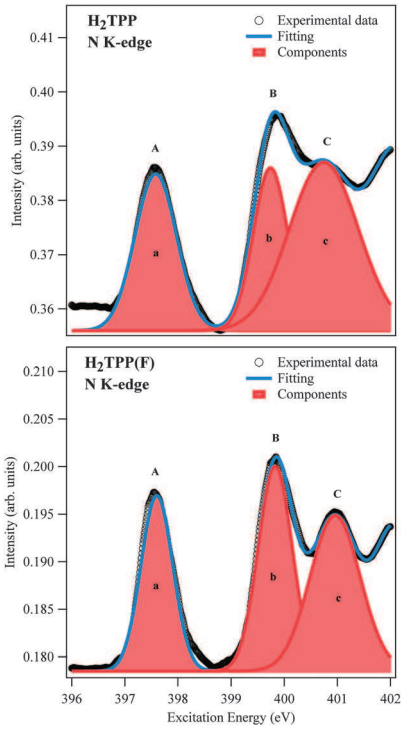

Fig. 8 Fitted [i] region of the N K-edge NEXAFS spectra of **H_2TPP** (**I**) (top) and **H_2TPP(F)** (**II**) (bottom).

Table 2 Excitation energy position (eV) of N K-edge transitions for **I** and **II** thick films. ΔE between similar features for **I** and **II** are also reported

Component	I	ΔE	II	ΔE
a	397.57	—	397.60	—
b	399.74	2.17	399.83	2.23
c	400.75	3.18	400.96	3.36

Before moving to the analysis of SR-ZORA TD-DFT results, both the unresponsiveness of the $^{pmc}\Pi_{\perp}$ subset (see Table 2) and the agreement of such an assignment with the angle-dependent linear dichroism characterizing the NEXAFS N K-edge spectrum of a multilayer of **I**[17a] and the DFT transition potential results of Diller *et al.*[17b] deserve to be highlighted.

Qualitative predictions of the number of components in the experimental spectra perfectly fit the SR-ZORA TD-DFT results (see Tables S5 and S6, ESI† and Fig. 10). Nevertheless, the comparison of the N K-edge NEXAFS spectra (Fig. 8) with the $^{I}f^{N}$ and $^{II}f^{N}$ distributions of Fig. 10 testifies a really poor quantitative agreement between experimental evidence and theoretical data.

In fact, besides the already revealed systematic excitation energy underestimation (in the present case ~2.5 eV),[13b,25] the relative position of the feature ^{t}**B** (see Fig. 10) poorly reproduces the experimental outcomes for both **I** and **II**. In more detail, ^{t}**A** and ^{t}**B** features of Fig. 10 top and bottom are both due to a single excitation associated with the above indicated transitions. As far as ^{t}**C** is concerned, its lower energy side is generated by one excitation associated with the $2a_g \rightarrow 15b_{1u}$ ($5a_g \rightarrow 24b_{1u}$) transition in **I** (**II**), while its higher EE side includes one (two)

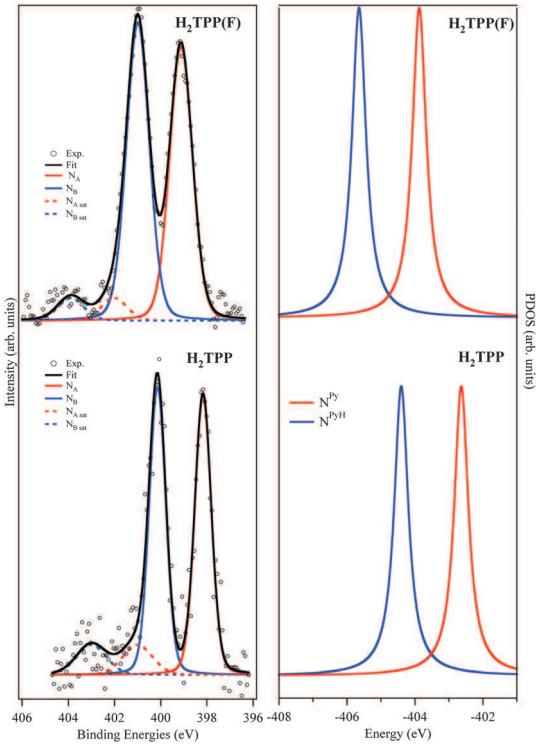

Fig. 9 (left panel) $1s^N$ core level spectra (background subtracted) from the **H_2TPP** (**I**) and **H_2TPP(F)** (**II**) films. The single components, shown in the legend, are related to the different nitrogen chemical species of the two molecules.[8,9] (right panel) SR-ZORA DFT **H_2TPP** (**I**) and **H_2TPP(F)** (**II**) $1s^N$ PDOS.[8,9]

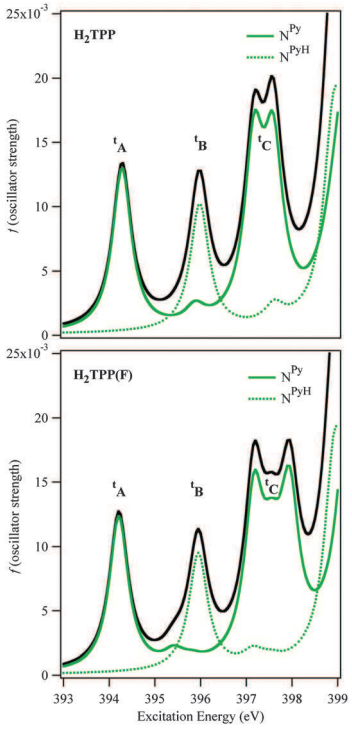

Fig. 10 SR-ZORA TD-DFT N 1s excitation spectra of **H_2TPP** (**I**) (top) and **H_2TPP(F)** (**II**) (bottom). Contributions from the different imols are also displayed. Convoluted profiles have been obtained by using a Lorentzian broadening of 0.25 eV. SR-ZORA ionization limits may be deduced from the right panels of Fig. 9.[8,9]

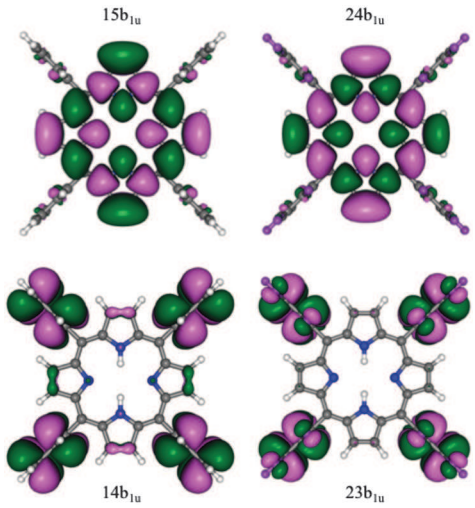

Fig. 11 3D plots of the $14b_{1u}$ and $15b_{1u}$ ($23b_{1u}$ and $24b_{1u}$) MOs of **H_2TPP** (**I**) **H_2TPP(F)** (**II**). Displayed isosurfaces correspond to ± 0.01 $e^{1/2}$ $Å^{3/2}$ values.

excitation(s) in **I** (**II**) (see Tables S5 and S6, ESI†). Incidentally, both the $15b_{1u}$ MO in **I** and the $24b_{1u}$ orbital in **II** correspond, as previously foreseen, to high lying $^{pmc}\pi_\perp{}^*$ levels with no nodes on N atoms (see 3D plots in Fig. 11), while lower lying $14b_{1u}$ and $23b_{1u}$ orbitals are e^1_{2u} Ph-based $\pi_{||}{}^*$ levels.[32]

Moving to the analysis of $^{\mathbf{I}}f^N$ and $^{\mathbf{II}}f^N$ features, the comparison of experimental/theoretical excitation energy relative positions $(\Delta E(\mathbf{b}–\mathbf{a})/\Delta E(^t\mathbf{B}–^t\mathbf{A}) = 2.17/1.70$ eV in **I** and 2.23/1.74 eV in **II**, $\Delta E(\mathbf{c}–\mathbf{a})/\Delta E(^t\mathbf{C}–^t\mathbf{A}) = 3.18/3.10$ eV in **I** and 3.36/3.15 eV in **II**, see Tables S5 and S6, ESI† and Table 2)[49] states that the energy of the component **b** is underestimated by $\sim$3.0 rather than $\sim$2.5 eV as those of components **a** and **c**.[50]

Such a failure of the adopted theoretical approach, even though herein particularly evident as a consequence of the very low number of expected and observed bands in the N K-edge spectra of **I** and **II**, is not particularly surprising. In fact, homogeneous theoretical results pertaining to the free phthalocyanine (H_2Pc)[11a,53] provided a ΔE between the lowest lying N^{Py}- and N^{PyH}-based 1s $\rightarrow$ $\pi_\perp{}^*$ transitions even smaller (1.55 eV) than the $\Delta EE(^t\mathbf{B}–^t\mathbf{A})$ herein reported. The effect on the H_2Pc f^N distribution was less evident than in **I** and **II** as a consequence of the presence of the four *meso* N atoms, which concurred to increase the complexity of the H_2Pc NEXAFS spectrum. Moreover, it can be useful to remind that H_2Pc excitations associated with N^m-based 1s $\rightarrow$ $\pi_\perp{}^*$ transitions abut against the N^{PyH}-based ones (Fig. 17 of ref. 11*a*).

As a final consideration, it is noteworthy that, despite the above mentioned failure, SR-ZORA TD-DFT results perfectly reproduce the experimental unresponsiveness of the $^{pmc}\Pi_\perp$ subset, thus stressing the negligible perturbation induced by the Ph F decoration in the excitation energies of 1s $\rightarrow$ $^{pmc}\pi_\perp{}^*$ independent of the imos localization.

F K-edge spectrum

The [i] region of the F K-edge NEXAFS spectrum (see Fig. 12) consists of a single intense band centred at 688.51 eV.

The experimental information is surely rather poor, nevertheless the combined use of symmetry, orbitals and spectra appears to be once again the Hobson's choice to get some information from experimental evidence.

As reported in Table S1, ESI,† the $F_{||}$-based linear combinations of 1s AOs correspond to the $1a_g + 1b_{1g} + 1b_{2u} + 1b_{3u}$ MOs, while those localized on $F_{\perp}$ span all the eight IRs of the D_{2h} point group. Although the number of F 1s-based MOs is quite large (20), they are closely spaced and the energy range they cover is quite narrow (see Fig. 13).[8]

Excitation energies and *f* values for the F 1s excitation spectrum as obtained from SR-ZORA TD-DFT[24] calculations are reported in Table S7, ESI,† while the corresponding f^F distribution in the range 680–683 eV is displayed in Fig. 14 with contributions of different symmetries rather than of different imols. The agreement between experiment and theory is satisfactory (the absolute excitation energies are underestimated by $\sim$7 eV).[13b,25]

Moreover, consistently with the inversed linear dichroism in F K-edge NEXAFS data recently published by de Oteyza *et al.* for fluorinated planar aromatic molecules,[54] SR-ZORA TD-DFT outcomes indicate that F-based b_{2u} and b_{3u} 1s $\rightarrow \pi_{||}^*$ and b_{1u} 1s $\rightarrow \sigma^*$ transitions share the same energy region (see Fig. 14). In more detail, the quite broad band reported in Fig. 12 includes excitations associated with transitions having the $\pi_{||}^*$ and σ^* orbitals contributing to the feature **M** of Fig. 3 as fmos.[32] Interestingly, no transition having linear combinations of the Ph-based $e_{2u}{}^2$ MOs as fmos and $f^F \geq 10 \times 10^{-3}$ is present in the energy range taken into account in Fig. 14.

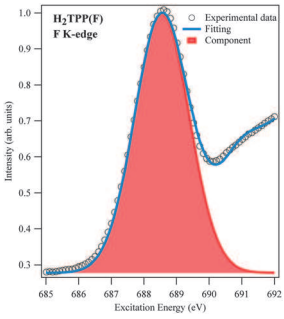

Fig. 12 Fitted [i] region of the fluorine K-edge NEXAFS spectra of **H_2TPP(F)** (**II**).

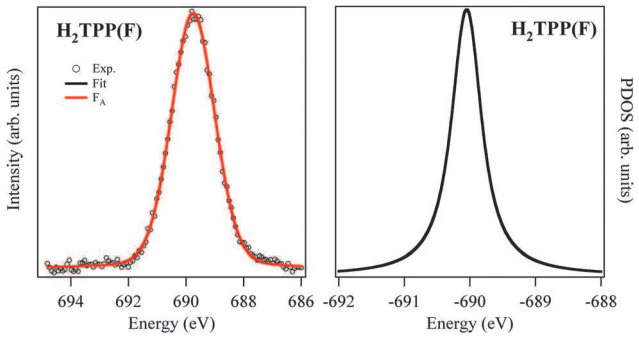

Fig. 13 (left panel) $1s^F$ core level spectra (background subtracted) of the **H_2TPP(F)** (**II**) film.[8] (right panel) SR-ZORA DFT **H_2TPP(F)** (**II**) $1s^F$ PDOS.

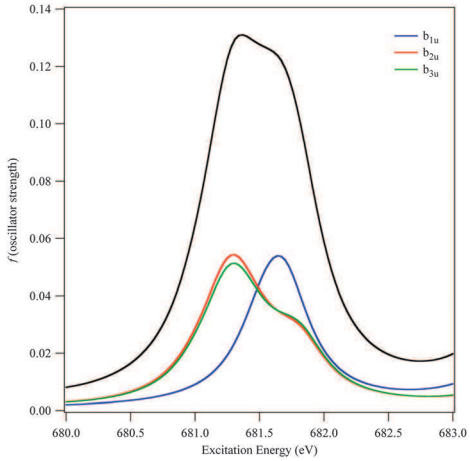

Fig. 14 SR-ZORA TD-DFT F 1s excitation spectrum **H_2TPP(F)** (**II**). Contributions from the different symmetry are also displayed. Convoluted profiles have been obtained by using a Lorentzian broadening of 0.25 eV. SR-ZORA ionization limits may be deduced from the right panel of Fig. 13.[8]

4. Conclusions

Unoccupied states of two π-conjugated molecules, the tetrakis-(phenyl)- and tetrakis(pentafluorophenyl)-porphyrin, have been thoroughly investigated by means of NEXAFS spectroscopy at the C, N and F K-edges. According to a well established procedure, the rationalization of experimental results collected from thin films of both molecules has been successfully guided by the outcomes of calculations carried out for isolated species in the framework of TD-DFT. Besides shedding new light on literature experimental results,[17a] theoretical outcomes herein reported provide valuable information about perturbations induced by the Ph fluorination on the unoccupied electronic structure of the pristine porphyrin macrocycle. The most evident, and rather unexpected, result is the electronic inertness of $^{pmc}\Pi_{\perp}$ transitions whose excitation energies, but not their *f* values, are substantially unaffected upon fluorination. Differently, $\Pi_{||}$ and, to a minor extent, $^{Ph}\Pi_{\perp}$ transitions undergo the expected blue shift when moving from **I** to **II**. Results herein reported complement those we published in the near past about the occupied electronic structure of **I** and **II**, thus providing the missing tile to get a thorough description of the halide decoration effects on the occupied and unoccupied electronic structure of title species, a necessary condition to address the electronic properties of their transition metal complexes.

The intrinsic simplicity of the N K-edge spectra of **I** and **II**, ultimately due to the presence of only two types of non-equivalent nitrogen atoms, revealed a sort of inappropriateness of the adopted theoretical method to quantitatively reproduce the energy difference between the lowest lying N-based 1s $\rightarrow \pi_{\perp}^*$ transitions. Further investigations are needed to clarify this point.

Acknowledgements

Italian Ministry of the University and Research (PRIN-2010BNZ3F2, project DESCARTES), University of Padova (CPDA134272/13,

project S_3MArTA), and Computational Chemistry Community (C_3P) of the University of Padova are kindly acknowledged.

Notes and references

1 *The Porphyrin Handbook*, ed. K. M. Kadish, K. M. Smith and R. Guilard, Academic Press, New York, 2000.
2 D. Dini and M. Hanack, *J. Porphyrins Phthalocyanines*, 2004, **8**, 915.
3 C. Di Natale, D. Monti and R. Paolesse, *Mater. Today*, 2010, **13**, 37.
4 A. Tsuda and A. Osuka, *Science*, 2001, **293**, 79.
5 M. Planells, A. Forneli, E. Martínez-Ferrero, A. Sánchez-Díaz, M. A. Sarmentero, P. Ballester, E. Palomares and B. C. O'Regan, *Appl. Phys. Lett.*, 2008, **92**, 153506.
6 A. P. Castano, P. Mroz and M. R. Hamblin, *Nat. Rev. Cancer*, 2006, **6**, 535.
7 N. A. Rakow and K. S. Suslick, *Nature*, 2000, **406**, 710.
8 M. Nardi, R. Verucchi, L. Aversa, M. Casarin, A. Vittadini, N. Mahne, A. Giglia, S. Nannarone and S. Iannotta, *New J. Chem.*, 2013, **37**, 1036.
9 M. Nardi, R. Verucchi, C. Corradi, M. Pola, M. Casarin, A. Vittadini and S. Iannotta, *Phys. Chem. Chem. Phys.*, 2010, **12**, 871.
10 A detailed description of the supersonic molecular beam deposition approach can be found in ref. 8 and 9.
11 (*a*) M. V. Nardi, F. Detto, L. Aversa, R. Verucchi, G. Salviati, S. Iannotta and M. Casarin, *Phys. Chem. Chem. Phys.*, 2013, **15**, 12864; (*b*) G. Mangione, M. Sambi, M. V. Nardi and M. Casarin, *Phys. Chem. Chem. Phys.*, 2014, **16**, 19852.
12 Amsterdam Density Functional version 2013.01. http://www.scm.com.
13 (*a*) M. Stener, G. Fronzoni and M. de Simone, *Chem. Phys. Lett.*, 2003, **373**, 115; (*b*) M. Casarin, P. Finetti, A. Vittadini, F. Wang and T. Ziegler, *J. Phys. Chem. A*, 2007, **111**, 5270.
14 E. K. U. Gross and W. Kohn, *Adv. Quantum Chem.*, 1990, **21**, 255.
15 R. van Leeuwen and E. J. Baerends, *Phys. Rev. A: At., Mol., Opt. Phys.*, 1994, **49**, 2421.
16 J. H. van Lenthe, S. Faas and J. G. Snijders, *Chem. Phys. Lett.*, 2000, **328**, 107.
17 (*a*) G. Di Santo, C. Castellarin-Cudia, M. Fanetti, B. Taleatu, P. Borghetti, L. Sangaletti, L. Floreano, E. Magnano, F. Bondino and A. Goldoni, *J. Phys. Chem. C*, 2011, **115**, 4155; (*b*) K. Diller, F. Klappenberger, M. Marschall, K. Hermann, A. Nefedov, C. Wöll and J. V. Barth, *J. Chem. Phys.*, 2012, **136**, 014705.
18 S. Narioka, H. Ishii, Y. Ouchi, T. Yokoyama, T. Ohta and K. Seki, *J. Phys. Chem.*, 1995, **99**, 1332.
19 (*a*) L. Pasquali, A. De Luisa and S. Nannarone, *AIP Conf. Proc.*, 2004, **705**, 1142; (*b*) S. Nannarone, F. Borgatti, A. De Luisa, B. P. Doyle, G. C. Gazzadi, A. Giglia, P. Finetti, N. Mahne, L. Pasquali, M. Pedio, G. Selvaggi, G. Naletto, M. G. Pelizzo and G. Tondello, *AIP Conf. Proc.*, 2004, **705**, 450; (*c*) S. Nannarone, A. Giglia, N. Mahne, A. De Luisa, B. Doyle, F. Borgatti, M. Pedio, L. Pasquali, G. Naletto, M. G. Pelizzo and G. Tondello, *Notiz. Neutr. Luce Sincr.*, 2007, **12**, 8.
20 (*a*) E. Van Lenthe, E. J. Baerends and J. G. Snijders, *J. Chem. Phys.*, 1993, **99**, 4597; (*b*) E. Van Lenthe, E. J. Baerends and J. G. Snijders, *J. Chem. Phys.*, 1994, **101**, 9783; (*c*) E. Van Lenthe, A. W. Ehlers, E. J. Baerends and J. G. Snijders, *J. Chem. Phys.*, 1999, **110**, 8543.
21 E. van Lenthe and E. J. Baerends, *J. Comput. Chem.*, 2003, **24**, 1142.
22 G. L. Miessler, P. J. Fischer and D. A. Tarr, *Inorg. Chem.*, Pearson, New York, 5th edn, 2013, p. 137.
23 R. S. Mulliken, *J. Chem. Phys.*, 1955, **23**, 1833.
24 F. Wang, T. Ziegler, E. van Lenthe, S. van Gisbergen and E. J. Baerends, *J. Chem. Phys.*, 2005, **122**, 204103 and references therein.
25 G. Fronzoni, M. Stener, P. Decleva, F. Wang, T. Ziegler, E. van Lenthe and E. J. Baerends, *Chem. Phys. Lett.*, 2005, **416**, 56.
26 It is well known[25] that this kind of function is needed to properly describe transitions toward Rydberg states.
27 G. P. Moss, *Pure Appl. Chem.*, 1987, **59**, 779.
28 (*a*) E. Hückel, *Z. Phys.*, 1931, **70**, 204; (*b*) E. Hückel, *Z. Phys.*, 1931, **72**, 310; (*c*) E. Hückel, *Z. Phys.*, 1932, **76**, 628.
29 The energy-ordered linear combinations of heavy atoms 1s AOs are collected in Table S1 of the ESI†.
30 pmc unoccupied π^* frontier orbitals[22] transform as b_{2g} + b_{3g} + a_u + b_{1u}. The low-lying $\pi_\perp{}^*$ MOs are: the $12b_{2g}$, $12b_{3g}$ and $11a_u$ MOs in **I** ($21b_{2g}$, $21b_{3g}$ and $20a_u$ MOs in **II**), all of them characterized by a quite homogeneous localization on pmc atoms (see Fig. 4). Besides the σ_h nodal plane, common to all of them, (i) b_{2g} orbitals are anti-symmetric with respect to the σ_{yz} symmetry plane; namely, they have a nodal plane $\perp$ to σ_h and passing through N^{PyH}; (ii) b_{3g} orbitals are anti-symmetric with respect to the σ_{xz} symmetry plane; namely, they have a nodal plane $\perp$ to σ_h and passing through N^{Py}; (iii) a_u orbitals are anti-symmetric with respect to both σ_{xz} and σ_{yz} symmetry planes; namely, they have two nodal planes $\perp$ to σ_h, the former passing through N^{Py}, the latter through N^{PyH}; (iv) b_{1u} orbitals are symmetric with respect to both σ_{xz} and σ_{yz} symmetry planes.[31] Nodal properties of π^* frontier orbitals have been here emphasized because they can be helpfully exploited to qualitatively foresee the localization of 1s $\rightarrow$ π^* electric dipole allowed transitions.
31 (*a*) M. Orchin and H. H. Jaffé, *Symmetry, Orbitals, and Spectra (S.O.S.)*, Wiley Interscience, New York, 1971; (*b*) B. E. Douglas and C. A. Hollingsworth, *Symmetry in Bonding and Spectra*, Academic Press, New York, 1985.
32 The MOs of **I** contributing to **M** in Fig. 3 are the $11a_u$ + $33a_g$ + $30b_{2u}$ + $30b_{3u}$ + $14b_{1u}$ + $27b_{1g}$ + $12a_u$ + $13b_{2g}$ + $13b_{3g}$ ones. With the exclusion of the $\pi_\perp{}^*$ $11a_u$ MO (see Fig. 4), the remaining eight orbitals correspond to the linear combinations of the Ph-based e_{2u} $\pi_{||}{}^*$ levels. Among them, the $12a_u$, $13b_{2g}$, $13b_{3g}$, and $14b_{1u}$ MOs are the e_{2u}-like $\pi_{||}{}^*$ partners with a node on the C^{25} and C^{45} atoms (hereafter, e^1_{2u}). The MOs of **II** contributing to **M** in Fig. 3 are the

$20a_u + 44a_g + 41b_{3u} + 41b_{2u} + 38b_{1g} + 23b_{1u} + 21a_u + 22b_{2g} + 22b_{3g} + 45a_g + 42b_{2u} + 42b_{3u} + 39b_{1g}$ ones. Similarly to **I**, the $\pi_\perp$* $20a_u$ MO is localized on the pmc atoms, while the following eight orbitals correspond to the linear combinations of the Ph-based e_{2u} $\pi_{||}$* levels, antibonding in nature with respect to the C–F π interaction. Moreover, the $21a_u + 22b_{2g} + 22b_{3g} + 23b_{1u}$ MOs are the e^1_{2u}-like $\pi_{||}$* partners with a node on the C^{25}, C^{45} and F^{65} atoms. As far as the last four orbitals ($45a_g + 42b_{2u} + 42b_{3u} + 39b_{1g}$ MOs) are concerned, they have a C–F σ* character. Both in **I** and **II**, a huge number of closely spaced π* and σ* MOs is present beyond **M**. Their detailed list is useless and is not reported herein due to space reasons.

33 R. De Francesco, M. Stener and G. Fronzoni, *J. Phys. Chem. A*, 2012, **116**, 2885.

34 M. Linares, S. Stafstrom and P. Norman, *J. Chem. Phys.*, 2009, **130**, 104305.

35 V. Yu. Aristov, O. V. Molodtsova, V. Maslyuk, D. V. Vyalikh, V. M. Zhilin, Yu. A. Ossipyan, T. Bredowe, I. Mertig and M. Knupfer, *Appl. Surf. Sci.*, 2007, **254**, 20.

36 Γ_{XS} representation products corresponding to the electric dipole allowed transitions in the D_{2h} symmetry are summarized in Table S2, ESI†.

37 The NEXAFS spectrum of **I** at the C K-edge perfectly matches the one recently published by some of us for *trans*-$TPP(NH_2)_2$.[38].

38 A. Basagni, L. Colazzo, F. Sedona, M. Di Marino, T. Carofiglio, E. Lubian, D. Forrer, A. Vittadini, M. Casarin, A. Verdini, A. Cossaro, L. Floreano and M. Sambi, *Chem. – Eur. J.*, 2014, **20**, 14296.

39 NEXAFS spectra reported in Fig. 6 extend for ∼5 eV (see also Table 1). The selected fmo number allowed us to cover an excitation energy range of ∼8 eV.

40 The angle-dependent linear dichroism in the NEXAFS C K-edge spectrum of a multilayer of **I** is characterized by the disappearance of the lowest lying **S** + **A** band envelope when switching from the light polarization ⊥ to pmc ($\theta = 90°$, *p*-polarization), to the light polarization || to pmc ($\theta = 0°$, *s*-polarization).[17] Accordingly, Di Santo *et al.*[17a] assigned the **S** + **A** band envelope to $\Pi_\perp$ transitions, without entering in more detail. Moreover, consistently with the *quasi* ⊥ orientation of Ph rings with respect to pmc in the isolated **I**, they found that the intense peak due to the Ph-based 1s → π* transitions in *p*-polarization still dominate the NEXAFS spectrum recorded in *s*-polarization.

41 Among the excitations 8–19, the 12–19 ones correspond to $\Pi_{||}$ transitions with the highest $^{\mathbf{I}}f^{C}$ values.

42 The six π orbitals of an isolated Ph ring transform, in the D_{6h} symmetry, as: $a_{2u} + e^1_{1g} + e^2_{1g} + e^1_{2u} + e^2_{2u} + b_{2g}$. The first (second) three are occupied (unoccupied).[31].

43 Excitations selected as internal gauge imply the following correlations: $1^{\mathbf{I}} \leftrightarrow 1^{\mathbf{II}}$, $3^{\mathbf{I}} \leftrightarrow 4^{\mathbf{II}}$, $4^{\mathbf{I}} \leftrightarrow 3^{\mathbf{II}}$, $5^{\mathbf{I}} \leftrightarrow 5^{\mathbf{II}}$, $6^{\mathbf{I}} \leftrightarrow 6^{\mathbf{II}}$, $9^{\mathbf{I}} \leftrightarrow 8^{\mathbf{II}}$.

44 The huge blue shift of the $\Pi_{||}$ set involves transitions localized on fluorinated C^{Ph} atoms. Excitation energies corresponding to transitions whose imos are C^{25}-based 1s AOs are scarcely affected.

45 The increase of *f* values upon fluorination is ultimately due to the rise of an order of magnitude of the corresponding *z* contributions to the transition dipole moments. Irrespective of their low *f* values, both C^2-based $8b_{3u} \rightarrow 12b_{2g}{}^{(100)}$ and $7b_{1g} \rightarrow 11a_u{}^{(100)}$ transitions belong to the $^{pmc}\Pi_\perp$ subset.

46 The $13a_u$ ($23a_u$) MO is the third (fourth) unoccupied level of a_u symmetry in **I** (**II**). The comparison between the 3D plots, not herein reported, of the $22a_u$ and $23a_u$ MOs of **II** revealed the σ* nature of the former and the $\pi_\perp$* character of the latter.

47 Upon fluorination, C^{Py}- and C^m-based 1s AOs are blue shifted by ∼1.25 eV and 1.60 eV, respectively. The shift toward higher binding energies is much more pronounced for C^{Ph}-based 1s AOs: 2.5 and 4.3 eV for non-fluorinated and fluorinated C atoms, respectively. Blue shifts of $^{pmc}\pi_\perp$* and $^{Ph}\pi_{||}$* levels are 0.9 and 0.7 eV, respectively.

48 The experimental (theoretical) ΔE between N^{Py} and N^{PyH} 1s-based levels is 1.90 (1.73) eV both in $\mathbf{I}^9$ and **II**.[8] Upon fluorination, N^{Py}- and N^{PyH}-based 1s AOs are both blue shifted by 0.80 eV,[8,9] while $^{pmc}\pi_\perp$* levels are downshifted by 0.9 eV.[47].

49 The **C** excitation energy has been estimated, for both **I** and **II**, as the mean energy values between the 3rd and 4th excitation energies (Tables S5 and S6, ESI†).

50 A further series of numerical experiments, carried out either by reducing the D_{2h} symmetry through the pmc tilting, or by using an exchange correlation potential (SAOP)[51] having the correct asymptotic behaviour but different from the LB94 functional did not improve the ^{t}**B** relative position.[52].

51 P. R. T. Schipper, O. V. Gritsenko, S. J. A. van Gisbergen and E. J. Baerends, *J. Chem. Phys.*, 2000, **112**, 1344.

52 Fronzoni *et al.* showed that both relative EEs and *f* are not very sensitive to the exchange correlation potential choice, provided the asymptotic behaviour is correct.[25].

53 The quasi degenerate H_2Pc $6b_{3g}$ and $6b_{2g}$ unoccupied frontier[22] orbitals have the same symmetry, localization and nodal properties[30] of the $12b_{3g}$ and $12b_{2g}$ ones in **I**.

54 D. G. de Oteyza, A. Sakko, A. El-Sayed, E. Goiri, L. Floreano, A. Cossaro, J. M. Garcia-Lastra, A. Rubio and J. E. Ortega, *Phys. Rev. B: Condens. Matter Mater. Phys.*, 2012, **86**, 075469.

EurJIC European Journal of Inorganic Chemistry

ChemPubSoc Europe

FULL PAPER

DOI:10.1002/ejic.201500222

Ligand-Field Strength and Symmetry-Restricted Covalency in Cu^{II} Complexes – a Near-Edge X-ray Absorption Fine Structure Spectroscopy and Time-Dependent DFT Study

Giulia Mangione,[a] Luciano Pandolfo,[a] Mauro Sambi,[a] Giovanni Ligorio,[b] Marco Vittorio Nardi,[b,c] Albano Cossaro,[d] Luca Floreano,[d] and Maurizio Casarin*[a,e]

Keywords: Density functional calculations / Ligand effects / NEXAFS spectroscopy / X-ray absorption spectroscopy / Copper

The low-lying empty orbitals of bis(acetylacetonato)copper have been probed by near-edge X-ray absorption fine structure (NEXAFS) spectroscopy at the Cu $L_{2,3}$ edges and time-dependent density functional theory (TDDFT) calculations within the Tamm–Dancoff approximation (TDA) coupled to the relativistic zeroth-order regular approximation including spin–orbit effects (SO-ZORA TDDFT-TDA). Both the relative positions of NEXAFS features and their linear dichroism are satisfactorily reproduced. Moreover, a comparison with literature data pertaining to two other square-planar Cu^{II} complexes ($[CuCl_4]^{2-}$ and copper phthalocyanine) provided information about how metal-to-ligand charge-transfer transitions associated with excitations from Cu^{II} 2p orbitals to low-lying, ligand-based π^* molecular orbitals in a simplified one-electron picture may contribute to the Cu^{II} $L_{2,3}$ edge intensity and, thus, weaken its believed relationship with the Cu^{II}–ligand symmetry-restricted covalency.

Introduction

Near-edge X-ray absorption fine structure (NEXAFS) spectroscopy is unanimously recognized as an experimental tool able to provide a chemically selective probe of molecular unoccupied electronic structures.[1,2] NEXAFS features are generated by the excitation of core electrons to the unoccupied valence orbitals as well as to the continuum; thus, *K*- and *L*-edge spectra are very sensitive to both the electronic structure and the local surroundings of the absorbing atom.[3] Metal (M) *K*-edge spectral features are determined by the electric-dipole-forbidden, but quadrupole-allowed,[4,5] $1s^M \rightarrow nd^M$ transitions, which may gain intensity in noncentrosymmetric complexes through the involvement of $(n + 1)p^M$ atomic orbitals (AOs) into frontier virtual molecular orbitals (MOs). In variance to that, the M $L_{2,3}$ structures are generated by the electric-dipole-allowed $2p^M \rightarrow nd^M$ transitions and, thus, provide information about the contribution of nd^M AOs to the low-lying unoccupied MOs.

In general, both the simulation and the analysis of the $L_{2,3}$ spectra of first-row transition metal complexes are challenging issues. In addition to ligand-field and covalency effects, the spin–orbit (SO) coupling between the possibly many final-state multiplets needs to be considered.[6,7] In this regard, Cu^{II} complexes represent the simplest possible case[6] because electric-dipole-allowed $2p^{Cu(II)} \rightarrow 3d^{Cu(II)}$ transitions generate a $2p^53d^{10}$ configuration, which has only two term symbols, and the corresponding "spectral splitting is dominated by the 2p SO coupling contribution and the overall energetics and intensities are strongly influenced by ligand field and covalency, respectively".[7e] As such, with the D_{4h} $[CuCl_4]^{2-}$ molecular ion (**I**, Figure 1) as a reference, Solomon and co-workers[8a,9] proposed the use of the normalized intensities and relative positions of the $^{Cu(II)}L_{2,3}$ features in different Cu^{II} complexes as a gauge of the degree of Cu^{II}–ligand covalency and of the ligand-field strength, respectively. In more detail, the larger the $L_{2,3}$ normalized intensity, the lower the metal–ligand symmetry-restricted covalency [the effect associated with the dilution, ruled by the complex symmetry, of d orbitals to make them become linear combinations of atomic orbitals (LCAO-MOs)];[10] the higher the L_3 excitation energy (EE), the stronger the ligand field exerted on the Cu^{II} centre.[8,9]

[a] Department of Chemical Sciences, Università di Padova, Via F. Marzolo 1, 35131 Padova, Italy
E-mail: maurizio.casarin@unipd.it
[b] Institute for Physics, Supramolecular Systems Division "SMS", Humboldt Universität zu Berlin, Brook-Taylor-Straße 6, 12489 Berlin, Germany
[c] Istituto dei Materiali per l'Elettronica ed il Magnetismo, IMEM-CNR, Sezione di Trento, Via alla Cascata 56/C – Povo, 38100 Trento, Italy
[d] CNR-IOM, Laboratorio TASC, Basovizza SS-14, Km 163.5, 34149 Trieste, Italy
[e] Istituto per l'Energetica e le Interfasi, IENI-CNR, Via Marzolo 1, 35131 Padova, Italy
http://www.chimica.unipd.it/maurizio.casarin/pubblica/casarin.htm

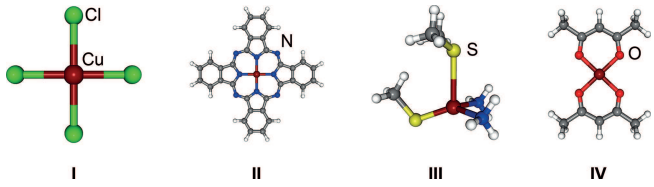

Figure 1. Schematic representation of **I**, **II**, **III** and **IV**. The σ_h plane along the whole series (the symmetry properties of **I**/**II**, **III** and **IV** are described by the D_{4h}, C_s and D_{2h} point groups, respectively) corresponds to the *xy* plane in the selected framework.

Recently,[11] some of us have successfully simulated the $L_{2,3}$ spectra of **I**,[8a] copper phthalocyanine (**II**, Figure 1)[12] and the so-called oxidized blue copper site in plastocyanin (**III**, Figure 1)[8a,13] through time-dependent density functional theory (TDDFT) calculations within the Tamm–Dancoff approximation (TDA) coupled to the relativistic zeroth-order regular approximation (ZORA) including SO effects. More specifically, the relative intensities and relative positions of the $^{X}L_{2,3}$ (X = **I**–**III**) features satisfactorily agreed with theoretical oscillator strength distributions (^{X}f). Such a result, combined with estimates of (1) a Cu–S interaction in **III** more covalent than the Cu–Cl one in **I**,[9,11] (2) a Cu–N interaction in **II** less covalent than the Cu–Cl one in **I**,[11,12] (3) a ligand field in **III** weaker than that in **I**[15] and (4) a ligand field in **II** stronger than that in **I**[15] represented a successful test of the SO-ZORA TDDFT-TDA method when applied to the modelling of $^{Cu II}L_{2,3}$ spectra. Interestingly, the composition analysis of the excitations associated with $^{II}L_3$ revealed that, in addition to $2p_{3/2} \rightarrow 3d$ transitions,[18] metal-to-ligand charge-transfer (MLCT) transitions involving low-lying ligand-based π* MOs contribute to the $^{II}L_3$ intensity and, thus, weaken its believed relationship with the M–L covalency. As such, bis(acetylacetonato)copper (**IV**) represents an ideal candidate to further test the legitimacy of the adopted theoretical approach to simulate the $L_{2,3}$-edge spectra of Cu^{II} complexes and the possible contribution of MLCT transitions to the L_3 intensity. The square-planar Cu^{II} coordination in **I**, **II** and **IV** is determined by four equivalent donor ions/atoms: chloride ions in **I**, iminic nitrogen atoms in **II** and ketonic oxygen atoms in **IV** (see Figure 1).

In this regard, it can be useful to remember that the ligand positions in the spectrochemical series[10,19] are determined largely by their donor atoms, which implies the following sequence: I < Br < Cl < S < F < O < N < C.[20] The oxygen position in this series, coupled with the presumed relationship between the relative positions of the Cu^{II} $L_{2,3}$ edges and the ligand-field strength, would induce us to foresee that the Cu^{II} $^{IV}L_{2,3}$-edges should lie between those of $^{I}L_{2,3}$ and $^{II}L_{2,3}$. However, this cannot be taken for granted because, for instance, the Cu^{II} $^{I}L_{2,3}$ edges lie at EEs higher than those corresponding to CuF_2 (951.0/931.0[8a] vs. 950.5/930.5 eV)[21,22] although the crystal field generated by F^- ions is notoriously stronger than that associated with the crystal field generated by Cl^- ions.[19,20,23] A reliable test of the legitimacy of the SO-ZORA TDDFT-TDA method to simulate the Cu^{II} $L_{2,3}$-spectra will then require a comparison of experimental and theoretical results pertaining to complexes with the same coordination geometry around the Cu^{II} ion. Finally, as far as the possible contribution of MLCT transitions to the L_3 intensity is concerned, it can be useful to remember that the lowest-lying unoccupied MOs of the acetylacetonate anion (labelled as π_4 and π_5 in ref.[25]) have a π* character. Both π_4 and π_5 are C–O antibonding; moreover, π_4 has a node on the methinic carbon atom [C(H)], and π_5 is also C–C(H) antibonding. In-phase (π_4^+/π_5^+) and out-of-phase (π_4^-/π_5^-) linear combinations of π_4 and π_5 will be present in **IV**. In D_{2h} symmetry, π_4^+ and π_5^+ (π_4^- and π_5^-) transform as b_{2g} and b_{1u} (a_u and b_{3g}) irreducible representations, respectively.

The NEXAFS spectra recorded at the Cu^{II} $L_{2,3}$ edges of **IV** deposited as a thin film on Au(100) are presented and discussed with reference to the results of SO-ZORA TDDFT-TDA calculations on the isolated molecule. The adopted computational setup[11,12,26] allowed a comparison with homogeneous literature data pertaining to both **I** and **II**. Moreover, insights into the Cu–X (X = Cl, N and O) symmetry-restricted covalency of the different CuX_4 square-planar chromophores have been gained by exploiting both experimentally and theoretically the dependence of NEXAFS spectra of **II** and **IV** deposited on Au(100) on the direction of the photon electric field.

Results and Discussion

Electric-dipole-allowed $2p^{Cu(II)} \rightarrow 3d^{Cu(II)}$ excitations generate two final states with different total angular momentum so that the most-relevant feature of the Cu^{II} 2p excitation spectra is the presence of the L_3 (ca. 930 eV) and L_2 (ca. 950 eV) components.[8,12,21] The NEXAFS spectra recorded at the Cu^{II} $L_{2,3}$ edges of highly oriented thin films of **II** and **IV** are displayed in Figure 2.

The left panel of Figure 2 includes spectra recorded in the EE region 927–960 eV, and an expanded view including the dependence of the spectra on the direction of the photon electric field is displayed in the right panel. The experimental (Exp) and theoretical (Theo) L_3 and L_2 EEs are collected in Table 1, and the $^{I}L_{2,3}$ EEs have been also included for comparison. The simulated ^{IV}f distribution is compared with those of **I**[12] and **II**[12] in Figure 3, in which the EE region reported in the upper panel extends from 921 to 954 eV, and an expanded view including the dependence of *f* on the light polarization orientation is reported in the lower panel.

The comparison of experimental and theoretical $^{X}L_{2,3}$ (X = **I**, **II** and **IV**) values confirms the well-known EE underestimation (ca. 6 eV, see Table 1), which is ultimately due to exchange-correlation (XC) potential deficiencies;[12,29] nonetheless, SO-ZORA TDDFT-TDA calculations successfully reproduce the position of the Cu^{II} $^{IV}L_{2,3}$ edge between $^{I}L_{2,3}$ and $^{II}L_{2,3}$, in accordance with the strength of the acetylacetonate ligand field midway between those of chlorido and porphyrinato ligands.[19,20]

The NEXAFS absolute intensities of **II** and **IV** in Figure 2 cannot be directly compared because of the different

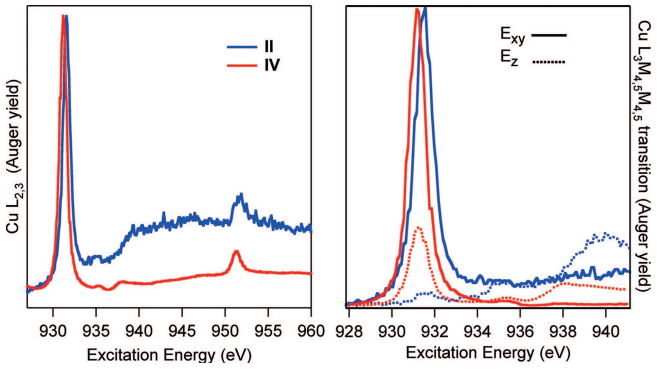

Figure 2. Cu $L_{2,3}$-edge spectra from thin films of **II** and **IV** on Au(100) as measured at the Cu $L_3M_{4,5}M_{4,5}$ Auger transition, which yields solely the Coster–Kronig contribution at the L_2 edge. The literature $L_{2,3}$-edge spectrum of **I**[8a] has not been included because it was calibrated differently[22] with respect to those of **II** and **IV**. Left panel: NEXAFS spectra at the Cu $L_{2,3}$ ionization threshold for the surface oriented at the magic angle (at which the transition dipole has no dependence on the orbital angular momentum); the spectra have been rescaled to the maximum intensity of the white line. Right panel: NEXAFS spectra for the surface oriented parallel (full lines) and nearly perpendicular (dotted lines) to the electric field; each set of spectra has been rescaled to the intensity of the white line for the surface parallel to the electric field.

Table 1. Experimental and theoretical EEs [eV] for the Cu 2p $L_{2,3}$ core excitation spectra of **I**, **II** and **IV**.

	I	II	IV
$^{Exp}L_3$	931.0[8a,8c]	931.6[a]	931.2
$^{Exp}L_2$	951.0[8a,8c]	951.6	951.2
$^{Theo}L_3$	924.67[11]	925.75[11]	925.03
$^{Theo}L_2$	945.06[11]	946.00[11]	945.28

[a] The $^{Exp}L_3$ value herein reported is slightly different from that of refs.[11,12] (931.4 eV) as a consequence of the EE absolute calibration (see Experimental Section).

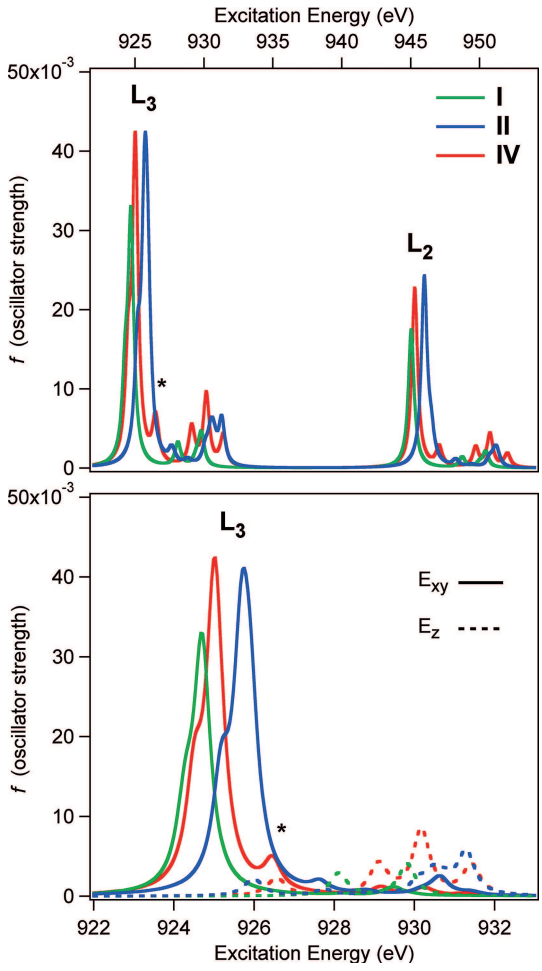

Figure 3. SO-ZORA TDDFT-TDA Cu 2p excitation spectra of **I**, **II** and **IV**. The convoluted profiles were obtained with a Lorentzian broadening of 0.25 eV.[11,29c]

film thicknesses and molecular tilts (see Experimental Section); nevertheless, the *f* values associated with the transitions that generate $^{II}L_3$ and $^{IV}L_3$ (see the upper panel of Figure 3) are consistent with a similar Cu–N and Cu–O symmetry-restricted covalency, in both cases lower than the Cu–Cl one. Now, before the experimental and theoretical data concerning the dependence of the L_3-edge spectra on the light polarization orientation are addressed (see the right panel of Figure 2 and the lower panel of Figure 3), two further points deserve to be emphasized: (1) $^{IV}L_3$ has an evident shoulder on its lower EE side, likewise **I** and **II**; (2) ^{IV}f is characterized by a weak but well evident feature at ca. 926.5 eV, marked by an asterisk in Figure 3. We remark that both features were not detected in the present measurements or in those previously reported for **II**.[12,30] This is likely due to the overall shortening of the lifetimes of the excited states in the condensed phase; the resulting broadening of the spectral lines is well beyond the experimental resolution, which is estimated to be ca. 0.5 eV in the present case.

The compositions, *f* values and EEs of the transitions associated with $^{IV}L_3$ are reported in Table 2 (the values for **I** and **II**[11] are also included for comparison).[31] Similarly to **I** and **II**, more than one excitation ($^{IV}L_3^1$ and $^{IV}L_3^2$) contribute to $^{IV}L_3$; furthermore, analogously to **I**, a single transition is associated with both of them: the $9a_{1/2} \rightarrow 136a_{1/2}$ for $^{IV}L_3^1$ and the $7a_{1/2} \rightarrow 136a_{1/2}$ for $^{IV}L_3^2$. Incidentally, the $7a_{1/2}$ and $9a_{1/2}$ initial spinors (IS) are related to the scalar relativistic (SR) $2p_{x,y}^{Cu(II)}$ and $2p_z^{Cu(II)}$ AOs, respectively, whereas the $136a_{1/2}$ final spinor (FS) is related to the SR $11b_{1g}$ singly occupied MO (SOMO), Cu–O σ antibonding (σ*), significantly localized (52%) on the $3d_{xy}^{Cu(II)}$ AO (see the corresponding 3D contour plot in Figure 4).

In addition to providing a rationale for the asymmetric shape of $^{IV}L_3$ [$\Delta EE(^{IV}L_3^2 - {}^{IV}L_3^1) = 0.49$ eV], the results of the SO-ZORA TDDFT-TDA calculations so far considered are perfectly consistent with the relationship between the Cu^{II} L_3-edge EE and the ligand-field strength exerted on the central M ion as well as between the Cu^{II} $L_{2,3}$-edge intensity and the Cu^{II}–ligand symmetry-restricted covalency. With specific reference to the latter point, it can be useful to consider the parentage of the $294a_{1/2}$ lowest unoccupied spinor of **II** [the FS of transitions associated with $^{II}L_3^1$ and $^{II}L_3^2$ (see Table 2)] with the SR $16b_{1g}$ SOMO

Table 2. SO-ZORA TDDFT-TDA compositions, $f \times 10^3$ and EEs values (in parentheses) of the transitions that generate $^{X}L_3^g$ excitations (X = **I**, **II** and **IV**).[a–g]

	I	**II**	**IV**
L_3^1	$17a_{1/2} \rightarrow 100a_{1/2}^{(100)}$ (7.25, 924.28 eV)	$9a_{1/2} \rightarrow 294a_{1/2}^{(99)}$ (9.44, 925.18 eV)	$9a_{1/2} \rightarrow 136a_{1/2}^{(100)}$ (9.43, 924.51 eV)
L_3^2	$15a_{1/2} \rightarrow 100a_{1/2}^{(100)}$ (24.1, 924.70 eV)	$7a_{1/2} \rightarrow 294a_{1/2}^{(79)}$	$7a_{1/2} \rightarrow 136a_{1/2}^{(99)}$ (31.5, 925.02 eV)
		$9a_{1/2} \rightarrow 295a_{1/2}^{(13)}$ (21.6, 925.69 eV)	
		$10a_{1/2} \rightarrow 298a_{1/2}^{(8)}$	
L_3^3		$10a_{1/2} \rightarrow 298a_{1/2}^{(46)}$	
		$9a_{1/2} \rightarrow 295a_{1/2}^{(33)}$ (12.1, 925.90 eV)	
		$7a_{1/2} \rightarrow 294a_{1/2}^{(20)}$	

[a] Contributions to initial spinor (IS)→final spinor (FS) of less than 1% are not reported. [b] ($f \times 10^3$) values of less than 5 are not reported. [c] The Cu $2p_{3/2}$-based levels are **I**: $15a_{1/2}$–$18a_{1/2}$ at 925.62, 925.57, 925.47, and 925.46 eV; **II**: $7a_{1/2}$–$10a_{1/2}$ at 934.84, 934.76, 934.65, and 934.65 eV; **IV**: $7a_{1/2}$–$10a_{1/2}$ at 934.01, 933.94, 933.85, and 933.84 eV. [d] The parenthood of the Cu $2p_{3/2}$-based levels with scalar relativistic (SR) ZORA Cu 2p-based MOs is **I**: $15a_{1/2} \rightarrow 2e_u^{(100)}$, $16a_{1/2} \rightarrow 2e_u^{(100)}$, $17a_{1/2} \rightarrow 1a_{2u}^{(67)} + 2e_u^{(33)}$, $18a_{1/2} \rightarrow 1a_{2u}^{(67)} + 2e_u^{(33)}$; **II**: $7a_{1/2} \rightarrow 1e_u^{(100)}$, $8a_{1/2} \rightarrow 1e_u^{(100)}$, $9a_{1/2} \rightarrow 1a_{2u}^{(67)} + 2e_u^{(33)}$, $10a_{1/2} \rightarrow 1a_{2u}^{(67)} + 2e_u^{(33)}$; **IV**: $7a_{1/2} \rightarrow 1b_{3u}^{(54)} + 1b_{2u}^{(46)}$, $8a_{1/2} \rightarrow 1b_{3u}^{(57)} + 1b_{2u}^{(42)} + 1b_{1u}^{(1)}$, $9a_{1/2} \rightarrow 1b_{1u}^{(67)} + 1b_{2u}^{(21)} + 1b_{3u}^{(12)}$, $10a_{1/2} \rightarrow 1b_{1u}^{(66)} + 1b_{2u}^{(24)} + 1b_{3u}^{(10)}$. [e] The lowest unoccupied spinors of **I**, **II** and **IV** are the $100a_{1/2}$, $294a_{1/2}$ and $136a_{1/2}$ ones, respectively. [f] The parenthood of the lowest unoccupied spinors of **I**, **II** and **IV** with SR ZORA SOMOs is **I**: $100a_{1/2} \rightarrow 6b_{1g}^{(96)} + 5b_{1g}^{(3)}$; **II**: $294a_{1/2} \rightarrow 16b_{1g}^{(100)}$; **IV**: $136a_{1/2} \rightarrow 11b_{1g}^{(100)}$.

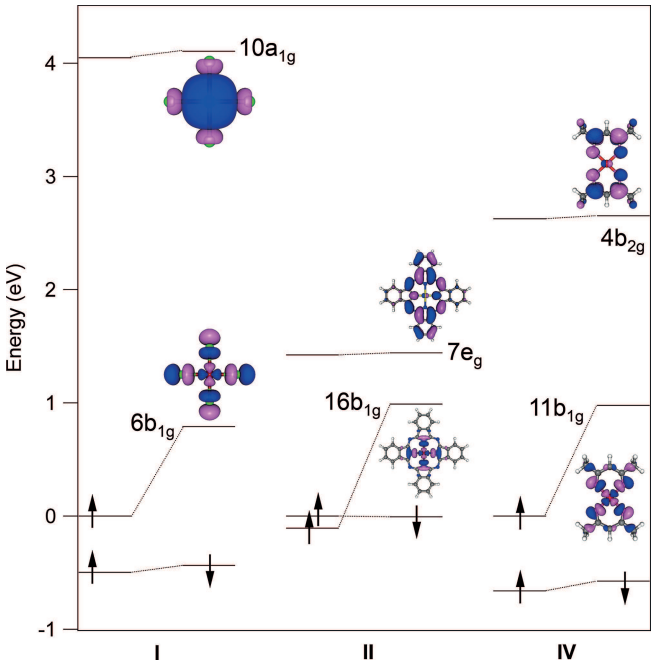

Figure 4. Relative energy positions (with respect to the HOMO energy) of the BP86-GS frontier MOs of **I**, **II** and **IV**. 3D plots of the SOMO and LUMO levels of **I**, **II** and **IV** are also displayed (isosurfaces correspond to ± 0.03 $e^{1/2}$ Å$^{-3/2}$ values).

of **II** (see Figure 4), the localization of which in the x^2–y^2 3d AO (52%) orbital and the Cu–N σ* character perfectly match those of the SR $11b_{1g}$ SOMO of **IV** (see Figure 4).[32]

The compositions and f values of the two transitions that trigger the weak, asterisked feature at ca. 926.5 eV in Figure 3 have not been included in Table 2 because the corresponding $^{IV}f \times 10^3$ value is less than 5 ($^{IV}f_1 = 2.625 \times 10^{-3}$, $EE_1 = 926.46$; $^{IV}f_2 = 1.058 \times 10^{-3}$, $EE_2 = 926.62$ eV). Nevertheless, it is noteworthy that the FSs of both transitions (the $137a_{1/2}$ and $138a_{1/2}$ spinors) are related to the SR $4b_{2g}$ lowest unoccupied MO (LUMO; see the corresponding 3D contour plot in Figure 4), a π* ligand-based orbital with a negligible localization in the Cu^{II} $3d_{xz}$ AO and reminiscent of the π_4^+ level. This indicates that (1) the asterisked feature in Figure 3 and $^{II}L_3^3$ (see Table 2),[33] hidden under the higher EE side of $^{II}L_3$, share the same origin, namely, 2p $^{Cu^{II}}_{3/2} \rightarrow \pi^*$ MLCT transitions, (2) the ΔEE between the asterisked feature and $^{IV}L_3^1$ (ca. 2 eV) is larger than that between $^{II}L_3^3$ and $^{II}L_3^1$ (0.72 eV) as the energy position of the $4b_{2g}$ LUMO in **IV** is higher than that of the $7e_g$ LUMOs in **II** (see Figure 4).

Even though there could be no doubt of the SOMO nature and localization along the investigated series, the polarization-dependent NEXAFS spectra (right panel of Figure 2) are perfectly consistent with SOMO σ* character both in **II** and **IV**. As such, the different degree of linear dichroism observed in **II** and **IV** is indicative of a larger tilt angle of the molecular plane of **IV** with respect to the substrate surface, possibly because of the larger film thickness. Furthermore, an inspection of the lower panel of Figure 3 clearly testifies that $^{IV}f_{xy} > {}^{II}f_{xy}$ as a consequence of the weak $^{II}L_3^3$ contribution (see above), which is ultimately due to MLCT $2p_{3/2}^{Cu(II)} \rightarrow \pi^*$ transitions. This is a rather crucial point because it emphasizes the usefulness of polarized NEXAFS experiments to eventually eliminate spurious contributions, which would result in estimations of symmetry-restricted covalency lower that the actual one.

We are aware that the quite poor resolution of the polarization-dependent NEXAFS spectra does not allow us to confirm the asymmetric shape of $^{X}L_3$ (X = **II** and **IV**) or the presence of the weak, asterisked feature on the higher EE side of $^{IV}L_3$. Nevertheless, the presence of spurious contributions hidden under $^{II}L_3$ ($^{II}L_3^3$) can be indirectly confirmed by referring to the low-lying EE region of the N *K*-edge NEXAFS spectra of the phthalocyanine free-base (H_2Pc) and its Cu^{II} complex (**II**).[12] The H_2Pc N *K*-edge NEXAFS profile is dominated by an intense and rather sharp peak fitted by Nardi et al. with a single component centred at 398.35 eV (see Figure 16 of ref.[12]). At variance with that, the corresponding main peak in the N *K*-edge NEXAFS spectrum of **II** has an asymmetric shape, which needed two components (*a* and *a'* in Figure 16 of ref.[12]) centred at 398.6 (*a*) and 399.35 eV (*a'*) to produce an adequate fit. SR ZORA TDDFT calculations pertaining to **II**

allowed all but one of the N *K*-edge low-lying excitations to be assigned to $1s^N \rightarrow \pi^*$ transitions of a_{2u} symmetry;[12] the exception is the $2e_u \rightarrow 16b_{1g}$ lowest-lying transition, which has $1s^N \rightarrow \sigma^*$ character.[34] Among the excitations of a_{2u} symmetry, the one that generates the component *a′* at 399.35 eV was associated with the $2e_u \rightarrow 7e_g$ transition,[33] the ΔEE value of which with the lowest-lying $2e_u \rightarrow 16b_{1g}$ transition amounts to 0.72 eV (see Table 5 of ref.[12]). Such a ΔEE value quantitatively reproduces the ΔEE value between the components *a′* and *a* (0.75 eV, see above) in the N *K*-edge NEXAFS spectrum of **II** and perfectly matches the ΔEE value between $^{II}L_3^3$ and $^{II}L_3^1$ (0.72 eV, see Table 2).

A further point of some relevance to be addressed concerns the linear dichroism of **II** and **IV** for the NEXAFS peaks at 5–9 eV from the white line (right panel of Figure 2). Again, the use of SO-ZORA TDDFT-TDA is decisive. An inspection of Figure 3 testifies to the presence of complex structures centred at ca. 5 eV from $^{II}L_3$ and $^{IV}L_3$, which are polarized along *z*, in agreement with the experimental results. In both cases, these structures imply excitations associated with transitions with ISs as the $9a_{1/2}$ and $10a_{1/2}$ spinors, both of which are mainly related to the SR $2p_z^{Cu(II)}$ AO (see footnote [d] of Table 2), and with FSs as the $144a_{1/2}$, $154a_{1/2}$ and $204a_{1/2}$ spinors for **IV** and the $320a_{1/2}$, $330a_{1/2}$ and $346a_{1/2}$ spinors for **II**, all of which are strongly related to the unoccupied SR $4s^{Cu(II)}$ AO.

Finally, the faint experimental feature, substantially insensitive to the photon electric field orientation (see the right panel of Figure 2), 3.6 (4.2) eV from $^{II}L_3$ ($^{IV}L_3$) is poorly reproduced by our SO-ZORA TDDFT-TDA calculations. A thorough inspection of the whole ^{II}f spectrum (330 excitations) revealed the presence of three excitations between 927.63 and 927.73 eV ($^{II}f_1 = 0.37514 \times 10^{-3}$; $^{II}f_2 = 0.53348 \times 10^{-3}$; $^{II}f_3 = 0.21967 \times 10^{-3}$), all of which are associated with $2p_{3/2}^{Cu(II)} \rightarrow \pi^*$ transitions.[35,36] For **IV**, no excitation with $f > 5 \times 10^{-5}$ is present between 926.62 and 929.05 eV in the whole ^{IV}f spectrum (282 excitations).

Conclusions

The Cu^{II} $L_{2,3}$ polarized spectra of **II** and **IV** have been assigned by using the SO-ZORA TDDFT-TDA method implemented in the Amsterdam Density Functional (ADF) package.[38] The simulated *f* distributions properly reproduce the relative positions and dependence of NEXAFS spectra on the direction of the photon electric field. The legitimacy of using the Cu^{II} L_3-edge position to get information about the ligand-field strength exerted on the Cu^{II} centre is confirmed. Moreover, the results herein reported further support the possibility of a Cu–ligand covalency underestimation if the Cu^{II} L_3-edge intensity of complexes with low-lying ligand-based π* orbitals is used as a gauge. Finally, the Cu–O symmetry-restricted covalency characterizing the square-planar CuO_4 chromophore is estimated to be slightly smaller than the Cu–N one that typifies the square-planar CuN_4 chromophore.

Experimental Section

General: The NEXAFS spectra of **II** and **IV** were measured at the ANCHOR endstation of the ALOISA branchline (Elettra Synchrotron), which provides a high photon throughput at the high photon energy of the Cu $L_{2,3}$ edges.[39] The photon energy resolution was set to 0.5 eV across the Cu $L_{2,3}$ ionization threshold. The absorption spectra have been collected in Auger yield by a PSP hemispherical analyzer (120 mm) equipped with a two-dimensional delay-line detector. The electron kinetic energy was set to the maximum of the $L_3M_{4,5}M_{4,5}$ Auger peak at 913 eV with an energy window of ca. 8 eV, which excludes the $L_2M_{4,5}M_{4,5}$ Auger peak at ca. 20 eV higher kinetic energy. As a consequence, the residual NEXAFS intensity detected at the L_2 edge only has contributions from its Coster–Kronig decay onto the L_3 subshell. We performed an absolute energy calibration of the NEXAFS spectra in two steps. First, the spectrometer work function was determined by collecting a series of photoemission spectra from the Au substrate across the N K edge with a gas-phase NEXAFS spectrum collected simultaneously from N_2 with the in-line windowless ionization chamber integrated into the Exit Slits of the ALOISA branchline. With reference to the Au $4f_{7/2}$ binding energy of 84.0 eV[40] and to the second vibrational state of the N $1s \rightarrow \pi^*$ transition at 401.10 eV,[39] we determined a work function value of 4.36 ± 0.02 eV. Then, we followed the same procedure of measuring the photoemission spectra from the molecular film across the so-called white line (vide infra) of the Cu L_3 edge to detect the Au 4f peak from the substrate in correspondence with the maximum of the white line of **II**. The overall indetermination of this absolute energy calibration was ca. ±50 meV. Finally, the orientation of the surface with respect to the linear polarization of the photon beam was changed from s to quasi-p by changing the incidence angle from normal to grazing. A powder specimen of **II** (from Sigma, sublimed grade) was evaporated from a boron nitride Knudsen cell on a Au(100) sample at room temperature. To obtain a film with a good planar orientation of the molecules, the thickness was limited to ca. two to three layers. At this thickness, the core level shifts of the molecular species owing to substrate screening effects were no longer detectable, but the Au 4f signal from the substrate was still intense enough for the energy calibration of NEXAFS spectra. The almost-perfect NEXAFS dichroism displayed by the white line indicates an excellent coplanar stacking of the **II** layers. A powder specimen of **IV** (from Sigma, purity 99.99%) was used to fill a differentially pumped Pyrex vial and evaporated by heating the vial at 340 K. We verified that the deposition of a sample at room temperature yields a single monolayer at saturation. Multilayer films were obtained by depositing **IV** on the sample kept at ca. 210 K. The X-ray photoelectron spectroscopy (XPS) and NEXAFS spectra were then recorded with the substrate held at low temperature to prevent the desorption of the multilayer. We did not observed any spectral changes owing to irradiation damage after the XPS or NEXAFS measurements. Owing to the low evaporation temperature of **IV**, it was not possible to achieve a good reproducibility of the evaporation rate, and the spectra shown correspond to a film thickness almost twice that of the films of **II**. Nonetheless, the polarization-dependent NEXAFS spectra display a strong dichroism (the residual intensity of the white line in p polarization is 25% of that measured in s polarization), which indicates that the molecular plane of **IV** is tilted by ca. 35° from the surface plane. The different film thickness together with the intrinsic surface sensitivity of the Auger yield detection technique produce a different background signal (intensity and slope), which prevented a direct comparison of the NEXAFS intensity between the two molecular systems.

Computational Details: Numerical experiments were run by employing the latest version of the Amsterdam Density Functional (ADF) package.[38] SO-ZORA TDDFT-TDA calculations were performed by using an all-electron QZ4P ZORA basis set for all atoms.[41] The adiabatic local density approximation was employed to approximate the XC kernel,[29,42] whereas the LB94 approximate functional with the ground-state electronic configuration was adopted for the XC potential applied in the self-consistent field calculations.[43] Scaled ZORA orbital energies[44] instead of the ZORA orbital energies in the TDDFT equations were employed to improve deep-core excitation energies. Although the energy difference between the Cu $2p_{3/2}$ and $2p_{1/2}$ spinors should be large enough (ca. 20 eV)[11] to avoid any coupling with each other in transitions starting from them, the whole Cu $2p_{3/2}/2p_{1/2}$ set was considered as the initial state. The SO-ZORA TDDFT-TDA calculations pertaining to **I** and **II** were run by assuming the geometrical parameters adopted by Gewirth et al.[17] and Nardi et al.,[12] respectively. For **IV**, the SO-ZORA TDDFT-TDA oscillator strength distribution was obtained for optimized coordinates evaluated by running nonrelativistic spin-unrestricted calculations with generalized gradient corrections self-consistently included through the Becke–Perdew formula (BP86)[45] by adopting a triple-ζ polarized (TZP) Slater-type basis set for all atoms and by keeping the $(1s–2p)^{Cu}$, $1s^{O}$ and $1s^{C}$ cores frozen throughout the calculations. The numerical experiments were run by assuming an idealized D_{2h} symmetry. Notably, the BP86 structural parameters (bond lengths and bond angles) are negligibly modified with respect to those evaluated by Rancan et al.[27] by using the hybrid B3LYP exchange-correlation functional, including dispersive contributions and by adopting a double-ζ polarized (DZP) all-electron basis set.

Acknowledgments

The Italian Ministry of the University and Research (MIUR) (PRIN-2010BNZ3F2, project DESCARTES), the University of Padova (CPDA134272/13, project S_3MArTA) and the Computational Chemistry Community (C_3P) of the University of Padova are kindly acknowledged.

[1] A. Bianconi, in: *X-ray Absorption: Principles, Applications, Techniques of EXAFS, SEXAFS and XANES* (Eds.: D. C. Koningsberger, R. Prins), John Wiley & Sons, New York, **1988**, p. 573–662.
[2] J. Stöhr, *NEXAFS Spectroscopy*, Springer, Berlin, **1992**.
[3] The absorption edges are labelled in the order of increasing energy, K, L_1, L_2, L_3, M_1, ..., corresponding to the excitation of an electron from the 1s ($S_{1/2}$), 2s ($S_{1/2}$), 2p ($P_{1/2}$), 2p ($P_{3/2}$), 3s ($S_{1/2}$), ... orbitals (states), respectively.
[4] B. E. Douglas, C. A. Hollingsworth, *Symmetry in Bonding and Spectra: An Introduction*, Academic Press, Orlando, **1985**, p. 256–257.
[5] Electric-quadrupole transitions involve states of the same parity and are approximately two orders of magnitude weaker than electric-dipole transitions.
[6] a) F. de Groot, *Coord. Chem. Rev.* **2005**, *249*, 31–63; b) F. de Groot, A. Kotani, *Core Level Spectroscopy of Solids*, CRC Press, Boca Raton, **2008**.
[7] a) P. S. Bagus, H. Freund, H. Kuhlenbeck, E. S. Ilton, *Chem. Phys. Lett.* **2008**, *455*, 331–334; b) H. Ikeno, T. Mizoguchi, I. Tanaka, *Phys. Rev. B* **2011**, *83*, 155107; c) I. Josefsson, K. Kunnus, S. Schreck, A. Föhlisch, F. de Groot, P. Wernet, M. Odelius, *J. Phys. Chem. Lett.* **2012**, *3*, 3565–3570; d) M. Roemelt, F. Neese, *J. Phys. Chem. A* **2013**, *117*, 3069–3083; e) M. Roemelt, D. Maganas, S. DeBeer, F. Neese, *J. Chem. Phys.* **2013**, *138*, 204101; f) D. Maganas, M. Roemelt, M. Hävecker, A. Trunschke, A. Knop-Gericke, R. Schlögl, F. Neese, *Phys. Chem. Chem. Phys.* **2013**, *15*, 7260–7276; g) D. Maganas, M. Roemelt, T. Weyhermüller, R. Blume, M. Hävecker, A. Knop-Gericke, S. DeBeer, R. Schlögl, F. Neese, *Phys. Chem. Chem. Phys.* **2014**, *16*, 264–276; h) D. Maganas, S. DeBeer, F. Neese, *Inorg. Chem.* **2014**, *53*, 6374–6385.
[8] a) S. J. George, M. D. Lowery, E. I. Solomon, S. P. Cramer, *J. Am. Chem. Soc.* **1993**, *115*, 2968–2969; b) S. DeBeer George, M. Metz, R. K. Szilagyi, H. Wang, S. P. Cramer, Y. Lu, W. B. Tolman, B. Hedman, K. O. Hodgson, E. I. Solomon, *J. Am. Chem. Soc.* **2001**, *123*, 5757–5767; c) R. Sarangi, N. Aboelella, K. Fujisawa, W. B. Tolman, B. Hedman, K. O. Hodgson, E. I. Solomon, *J. Am. Chem. Soc.* **2006**, *128*, 8286–8296.
[9] R. K. Hocking, E. I. Solomon, *Struct. Bonding (Berlin)* **2012**, *142*, 155–184.
[10] C. K. Jørgensen, *Absorption Spectra and Chemical Bonding in Complexes*, Pergamon Press, Oxford, UK, **1962**, p. 77.
[11] G. Mangione, M. Sambi, M. V. Nardi, M. Casarin, *Phys. Chem. Chem. Phys.* **2014**, *16*, 19852–19855.
[12] M. V. Nardi, F. Detto, L. Aversa, R. Verucchi, G. Salviati, S. Iannotta, M. Casarin, *Phys. Chem. Chem. Phys.* **2013**, *15*, 12864–12881.
[13] In ref.[11] the plastocyanin oxidized blue copper site has been modelled by adopting the same positively charged cluster proposed by Solomon et al.[14] {$[Cu\{S(CH_3)_2\}(SCH_3)(NH_3)_2]^+$; hereafter **III**}.
[14] K. W. Penfield, A. A. Gewirth, E. I. Solomon, *J. Am. Chem. Soc.* **1985**, *107*, 4519–4529.
[15] The weaker ligand field of **III** relative to that of **I** is due to the presence of only three (in **III**) rather than four (in **I**) equatorial ligands contributing to the destabilization of the Cu^{II}-based $x^2–y^2$ 3d AO.[9] The different Cu^{II}–(donor atom) distances, which are shorter in **II** [the optimized[12]/experimental[16] Cu–N bond lengths are 1.968/1.935(22) Å] than in **I** (2.265 Å),[17] and the ligand electronic properties (the presence of low-lying empty π* MOs in the phthalocyanine ligand)[12] make the ligand field in **II** stronger than that in **I**.
[16] V. Mastryukov, C.-y. Ruan, M. Fink, Z. Wang, R. Pachter, *J. Mol. Struct.* **2000**, *556*, 225–237.
[17] a) A. A. Gewirth, S. L. Cohen, H. J. Schugar, E. I. Solomon, *Inorg. Chem.* **1987**, *26*, 1133–1146; b) R. L. Harlow, W. J. Wells III, G. W. Watt, S. H. Simonsen, *Inorg. Chem.* **1974**, *13*, 2106–2111.
[18] The higher-energy side of $^{II}L_3$ includes a component ascribable to the $2p_{3/2} \rightarrow 7e_g$ transition. The ligand-based $7e_g$ orbitals correspond to the LUMOs; they have a π symmetry and are quite close in energy to the Cu^{II}-based $16b_{1g}$ SOMO; see figure 7 in ref.[12]
[19] a) J. S. Griffith, *The Theory of Transition Metal Ions*, Cambridge University Press, London, **1961**, p. 309; b) C. J. Ballhausen, *Introduction to Ligand Field Theory*, McGraw-Hill, New York, **1962**, p. 91; c) A. B. P. Lever, *Inorganic Electronic Spectroscopy*, 2nd ed., Elsevier, Amsterdam, **1984**; d) J. E. Huheey, E. A. Keiter, R. L. Keiter, *Inorganic Chemistry: Principles of Structure and Reactivity*, 4th ed., HarperCollins College Publisher, New York, **1993**, p. 405; e) B. N. Figgis, M. A. Hitchman, *Ligand Field Theory and Its Applications*, Wiley-VCH, New York, **2000**, p. 215.
[20] W. W. Porterfield, *Inorganic Chemistry: A Unified Approach*, 2nd ed., Academic Press, San Diego, **1993**, p. 574.
[21] a) A. S. Koster, *Mol. Phys.* **1973**, *26*, 625–632; b) P. Verma, R. C. Pratt, T. Storr, E. C. Wasinger, T. D. P. Stack, *Proc. Natl. Acad. Sci. USA* **2011**, *108*, 18600–18605.
[22] The Cu^{II} L_3 peak position of CuF_2 (930.5 eV with an uncertainty of 0.2 eV) was used by George et al.[8a] to calibrate the Cu^{II} $L_{2,3}$ spectra of **I**, D_{2d} $[CuCl_4]^{2–}$ and the blue copper site in plastocyanin.
[23] The CuF_2 crystal structure is a distorted variant of the rutile structure with a (4+2) coordination about the Cu^{II} centre. The $L_{2,3}$ EE order in **I** and CuF_2, opposite to that foreseeable by

referring to the I < Br < Cl < S < F < O < N < C series, is ultimately due to the different Cu^{II} coordination in **I** (square planar) and CuF_2 [pseudo-octahedral with four short (1.92 Å) and two long (2.32 Å) Cu–F bond lengths].[24]

[24] P. C. Burns, F. C. Hawthorne, *Powder Diffr.* **1991**, *6*, 156–158.

[25] F. D. Lewis, G. D. Salvi, D. R. Kanis, M. A. Ratner, *Inorg. Chem.* **1993**, *32*, 1251–1258.

[26] The electronic properties of the CuO_4 chromophore were recently investigated by Rancan et al. by combining UV/Vis spectroscopy measurements with DFT and TDDFT calculations.[27] Unfortunately, the DFT results therein reported and pertaining to the ground state (GS) of **IV** cannot be used to compare the Cu–O symmetry-restricted covalency with that estimated for Cu–Cl and Cu–N in the $CuCl_4$ and CuN_4 chromophores[11,12] as a consequence of the different exchange-correlation functional adopted in the two cases.[28]

[27] M. Rancan, J. Tessarolo, M. Casarin, P. L. Zanonato, S. Quici, L. Armelao, *Inorg. Chem.* **2014**, *53*, 7276–7287.

[28] The GSs of **IV** and a constitutional dynamic library of Cu^{II} metallo-supramolecular polygons, all of which are characterized by the presence of the CuO_4 chromophore, have been investigated by Rancan et al.[27] by using the hybrid B3LYP exchange-correlation functional including dispersive contributions and by adopting DZP all-electron basis sets. At variance with that, the GS of **I** and **II** has been investigated by employing the BP86 exchange-correlation functional and TZP basis sets (see the Experimental Section). Moreover, throughout the BP86-GS calculations, the $(1s–2p)^{Cu}$, $(1s–2p)^{Cl}$, $1s^{N}$ and $1s^{C}$ cores have been kept frozen.[12]

[29] a) G. Fronzoni, M. Stener, P. Decleva, F. Wang, T. Ziegler, E. van Lenthe, E. J. Baerends, *Chem. Phys. Lett.* **2005**, *416*, 56–63; b) G. Fronzoni, M. Stener, P. Decleva, M. De Simone, M. Coreno, P. Franceschi, C. Furlani, K. C. Prince, *J. Phys. Chem. A* **2009**, *113*, 2914–2925; c) M. Casarin, P. Finetti, A. Vittadini, F. Wang, T. Ziegler, *J. Phys. Chem. A* **2007**, *111*, 5270–5279.

[30] G. Dufour, C. Poncey, F. Rochet, H. Roulet, M. Sacchi, M. De Santis, M. De Crescenzi, *Surf. Sci.* **1994**, *319*, 251–266.

[31] The EE calculations were performed with no symmetry. The spinor labelling is the one reported in: P. W. M. Jacobs, *Group Theory With Applications in Chemical Physics*, Cambridge University Press, Cambridge, **2005**, p. 450.

[32] Although CuX_4 (X = Cl, N and O) chromophores share the same local coordination environment (square planar), the different symmetry properties of **I/II** and **IV** imply that the Cu^{II} 3d-based SOMO corresponds to the $x^2–y^2$ orbital in **I** and **II**, whereas it is the *xy* orbital in **IV**.

[33] Among the $^{II}L_3^3$ contributions, only the $7a_{1/2} \rightarrow 294a_{1/2}$ transition has a Cu^{II} $2p_{3/2} \rightarrow 16b_{1g}$ character (see Table 2). The four, closely spaced $295a_{1/2}$–$298a_{1/2}$ spinors correspond to the SR ligand-based $7e_g$ π* LUMOs (the 3D contour plot of one partner of the $7e_g$ MOs is displayed in Figure 4).

[34] In **II**, the linear combinations of pyrrolic nitrogen 1s-based AOs correspond to the $1b_{1g} + 3a_{1g} + 2e_u$ SR MOs.[12]

[35] The SR ligand-based π* MO related to the FSs of these transitions is systematically the $8e_g$ level; the first gerade virtual orbital lies above the $7e_g$ LUMO of **II**.

[36] The weak feature at 3.6 eV for $^{II}L_3$, labelled by Dufour et al.[30] as A1, was assigned by Carniato et al.[37] to the $2p_{3/2}^{Cu(II)} \rightarrow$ LUMO (in our notation) transition. In this regard, it is of some relevance to point out that Carniato et al. simulated the Cu^{II} L_3-edge NEXAFS spectrum of **II** by running their gradient-corrected DFT calculations on the model compound copper tetraazaporphyrin.

[37] S. Carniato, Y. Luo, H. Ågren, *Phys. Rev. B* **2001**, *63*, 085105.1–085105.6.

[38] *Amsterdam Density Functional (ADF)*, SCM, Theoretical Chemistry, Vrije Universiteit, Amsterdam; http://www.scm.com.

[39] L. Floreano, A. Cossaro, R. Gotter, A. Verdini, G. Bavdek, F. Evangelista, A. Ruocco, A. Morgante, D. Cvetko, *J. Phys. Chem. C* **2008**, *112*, 10794–10802.

[40] A. Cossaro, L. Floreano, A. Verdini, L. Casalis, A. Morgante, *Phys. Rev. Lett.* **2009**, *103*, 119601.1.

[41] E. van Lenthe, E. J. Baerends, *J. Comput. Chem.* **2003**, *24*, 1142–1156.

[42] E. K. U. Gross, W. Kohn, *Adv. Quantum Chem.* **1990**, *21*, 255–291.

[43] R. van Leeuwen, E. J. Baerends, *Phys. Rev. A* **1994**, *49*, 2421–2431.

[44] J. H. van Lenthe, S. Faas, J. G. Snijders, *Chem. Phys. Lett.* **2000**, *328*, 107–112.

[45] a) A. D. Becke, *Phys. Rev. A* **1988**, *38*, 3098–3100; b) J. P. Perdew, *Phys. Rev. B* **1986**, *33*, 8822–8824.

Received: March 1, 2015
Published Online: May 8, 2015

PCCP

PAPER

View Article Online
View Journal | View Issue

Cite this: *Phys. Chem. Chem. Phys.*, 2016, **18**, 18727

Electronic structures of CuTPP and CuTPP(F) complexes. A combined experimental and theoretical study I†

Giulia Mangione,[a] Silvia Carlotto,[a] Mauro Sambi,[a] Giovanni Ligorio,[b] Melanie Timpel,[bc] Andrea Vittadini,[d] Marco Vittorio Nardi[bc] and Maurizio Casarin*[ad]

Received 1st March 2016,
Accepted 26th April 2016

DOI: 10.1039/c6cp01423b

www.rsc.org/pccp

Copper complexes of tetraphenylporphyrin (H_2TPP) and tetrakis(pentafluorophenyl)porphyrin (H_2TPP(F)) deposited as thin films on Au(111) have been studied experimentally and theoretically. Core level emissions from C 1s, N 1s, F 1s and Cu 2p as well as valence states of CuTPP and CuTPP(F) have been investigated using surface photoelectron spectroscopy. The interpretation of experimental results has been guided by theoretical calculations carried out on isolated species in the habit of the density functional theory. Reference to experimental and theoretical outcomes pertaining to H_2TPP and H_2TPP(F) allowed a confident and detailed assignment of the title molecules' X-ray and ultraviolet photoemission data. With specific reference to the latter, similar to copper phthalocyanine (CuPc), whose coordinative pocket mirrors the CuTPP/CuTPP(F) ones, the lowest ionization energy of the title compounds implies electron ejection from a ring orbital rather than from the Cu 3d-based singly occupied molecular orbital. Moreover, analogous to CuPc, the ionic contribution appears to play an important role in the Cu–N bonding. Nevertheless, differences in the number, symmetry, nature and relative position of CuTPP/CuTPP(F) occupied frontier orbitals compared to CuPc may be stated only by considering in great detail the Cu-ligand covalent interactions.

1. Introduction

"Porphyrins are everywhere, as far as the living world is concerned"[1] and, although trackable in abiotic systems, the central role played by metalloporphyrins in fundamental biological processes, such as oxygen transport and storage (haemoglobin and myoglobin),[2] photosynthesis (chlorophyll)[4] and electron transport during cellular respiration and photosynthesis (cytochromes),[3] justifies the evocative classification "pigments of life".[5] In addition, it is noteworthy that photosensitizers employed in clinical trials and used in the treatment of cancer are mostly based on porphyrins and their derivatives.[6] The relevance of this class of molecules is not limited to the biological environment but it extends to important technological fields such as electronics,[7] solar cells[8] and sensors,[9] thus explaining the continuously growing interdisciplinary interest for them and the push to develop novel porphyrin-like molecules whose electronic and optical properties may be tuned through molecular engineering.[10–13]

As a part of a systematic investigation of the electronic properties of materials usually labelled as energy-targeted,[14] some of us have recently investigated the occupied[14a,b] and empty[14c] electronic structure of tetraphenyl and tetrakis(pentafluorophenyl)porphyrin (H_2TPP and H_2TPP(F), respectively) by exploiting ultraviolet and X-ray photoelectron spectroscopies (UPS and XPS, respectively) and X-ray absorption spectroscopy at the C, N and F K-edges. The ultimate goal of these investigations[14a–c] was obtaining a thorough understanding of the effects induced by the fluorine decoration of the peripheral phenyl (Ph) groups on the H_2TPP electronic structure. As such, it is noteworthy that the switch of electronic transport properties from the p- to n-type through the substitution of hydrogen peripheral atoms with halogen species such as fluorine is an intriguing opportunity, pushing the research activity towards the synthesis of organic systems having both electron acceptor and donor characteristics and smoothing the path for the creation of a p–n junction fully based on organic materials.

Among porphyrin transition metal complexes, a number of properties distinguish CuTPP from both the free ligand and complexes with other metals.[15,16] In this contribution, the bonding scheme of CuTPP and CuTPP(F) has been explored experimentally

[a] *Dipartimento di Scienze Chimiche, Università di Padova, Via F. Marzolo 1, 35131 Padova, Italy. E-mail: maurizio.casarin@unipd.it*
[b] *Department of Physics, Supramolecular Systems Division "SMS", Humboldt Universität zu Berlin, Brook-Taylor-Straße 6, 12489 Berlin, Germany*
[c] *Istituto dei Materiali per l'Elettronica ed il Magnetismo, IMEM-CNR, Sezione di Trento, Via alla Cascata 56/C - Povo, 38100 Trento, Italy*
[d] *Istituto di Chimica della Materia Condensata e di Tecnologie per l'Energia - ICMATE, via F. Marzolo 1, 35131 Padova, Italy*

† Electronic supplementary information (ESI) available: Optimized coordinates of CuTPP, CuTPP(F) and CuPc; 3D contour plots of (i) TPP^{2-} and Pc^{2-} frontier π/σ MOs; (ii) CuTPP and CuPc $2a_{1u}$ MO; (iii) CuPc $4a_{2u}$ MO. See DOI: 10.1039/c6cp01423b

and theoretically by combining the UPS and XPS results pertaining to CuTPP and CuTPP(F) thin films with relativistic density functional theory (DFT) calculations. More specifically, the valence band and the $1s^{C/N/F}$ and $2p^{Cu}$ core levels of the title molecules have been rationalized by referring to the outcomes of relativistic DFT numerical experiments[17] carried out on the isolated species. Incidentally, such an approach has been already successfully applied to investigate the occupied and empty electronic structures of H_2TPP and H_2TPP(F) thick films as well as layers of the free phthalocyanine (H_2Pc) and its copper complex (CuPc).[14] Even though the occupied electronic structure of CuTPP has been already investigated both experimentally and theoretically,[18–26] we decided to revisit it to ensure the comparison between homogeneous theoretical results.

2. Experimental and computational details

CuTPP(F) synthesis

H_2TPP(F) and $CuCl_2{\cdot}2H_2O$ were purchased from Aldrich and used as received. The synthesis of CuTPP(F) was achieved according to a procedure slightly modified with respect to the one reported in the literature.[27] H_2TPP(F) (1 g, 1.03 mmol) was dissolved in *ca.* 80 mL of refluxing dimethylformamide (DMF) under stirring. After 2 min 206 mg of $CuCl_2{\cdot}2H_2O$ (1.14 mmol) were added; heating and stirring were maintained and the reaction progress was spectroscopically (UV-Vis) monitored. After 30 min 72 mg of $CuCl_2{\cdot}2H_2O$ (0.42 mmol) were added and the solution was refluxed for further 4 h. The solution was then maintained at 140 °C for 3 h and then let to cool at room temperature overnight. The solution was treated with 100 mL of water in small portions (4–5 mL) under stirring, obtaining a very subtle microcrystalline red-brown solid which was filtered, washed with three portions of 150 mL of water and dried under vacuum. CuTPP(F): Yield 778 mg, 0.75 mmol, 73%. Elem. anal. calcd for $C_{44}H_8F_{20}N_4Cu$: C = 51.01; H = 0.78; N = 5.41. Elem. anal. calcd for $C_{44}H_8F_{20}N_4Cu$(DMF): C = 50.89; H = 1.36; N = 6.31. Found: C = 51.93; H = 1.71; N = 6.75. Both the elemental analysis data and the infrared spectrum of the CuTPP(F) sample are consistent with a DFM contamination (an evident signal is present at 1649 cm^{-1}); nevertheless, it is noteworthy that the intensity of this spurious signal decreased on prolonged drying under vacuum. The ultra high vacuum conditions associated with UPS and XPS measurements ensured the contaminant removal.

UPS and XPS measurements

Photoemission experiments have been performed using our laboratory facilities. The interconnected preparation (base pressure 1×10^{-8} mbar) and analysis (base pressure 1×10^{-9} mbar) chambers enabled sample preparation and transfer without breaking ultrahigh vacuum conditions. The substrate, an Au(111) single crystal, has been cleaned by repeated Ar^+ ion sputtering and annealing (up to 550 °C) cycles. The absence of surface contaminations (C, N, F, O, and Cu) has been checked by means of XPS. CuTPP (purchased from Sigma-Aldrich) and CuTPP(F) (synthetized and purified in our laboratory, *vide supra*) have been deposited in the preparation chamber (during evaporation, pressure $< 5 \times 10^{-8}$ mbar) *via* sublimation from a resistively heated pinhole source onto the Au(111) crystal surface. The molecular layer mass-thickness has been monitored using a quartz crystal microbalance. The evaporation rate for both CuTPP and CuTPP(F) was approximately 0.1 Å s^{-1} (bulk density assumed to be 1.6 g cm^{-3}). The final thickness for both molecular thin films on Au(111) has been estimated to be $\sim$5 nm. After the film depositions, the samples have been transferred into the analysis chamber for UPS and XPS analyses.

UPS and XPS spectra have been recorded with the He(I) resonance line (21.21 eV) and the non-monochromatized Al Kα radiation (1486.6 eV) as excitation sources. An Omicron EA125 hemispherical electron energy analyser has been used to collect the spectra (energy resolutions for UPS and XPS measurements, as determined from the Au Fermi edge and the Au $4f_{7/2}$ peak, were 120 meV and 150 meV, respectively).[28] Secondary electron cut-off spectra to determine the ionization energies (IEs) have been measured with a sample bias of −10 V to clear the analyser work function. All measurements have been performed at room temperature. The analysis of XPS spectra has been carried out by background subtraction of a Shirley function and Voigt lineshape deconvolution.[29] The typical precision for each component energy positioning is ±0.05 eV. The uncertainty for the full width at half maximum (FWHM) is less than ±5%, while it is about ±2.5% for the area evaluation. The absolute atomic contribution of each single chemical species can be evaluated to be ±1 atom.

Computational details

Multilayers of randomly oriented and weakly interacting CuTPP and CuTPP(F) molecules have been modelled by adopting the single molecule approach.[14] DFT calculations have been carried out by using the Amsterdam Density Functional (ADF) suite of programs (version 2014.01).[17] Numerical experiments have been run by assuming an idealized D_{4h} symmetry with phenyl groups perpendicular to the pristine porphyrin macrocycle (PMC). Non-relativistic spin-unrestricted calculations with generalized gradient corrections self-consistently included in the Becke–Perdew formula[30] have been used to optimize the CuTPP and CuTPP(F) molecular geometries (see Tables S1 and S2 of the ESI†). Triple-ζ with one polarization function (TZP) Slater-type orbitals have been adopted for all the atoms; moreover, the $(1s–2p)^{Cu}$, $1s^{F/N/C}$ cores have been kept frozen throughout the calculations. The IEs of occupied frontier[31] molecular orbitals (MOs) have been estimated by means of spin-unrestricted Slater Transition State (STS) calculations.[32] At variance with that, the IEs of $1s^{C/N/F}$-based MOs have been estimated by running all-electron spin-unrestricted scalar relativistic (SR) zeroth-order regular approximation (ZORA) calculations[33] on the non-relativistic optimized geometries, and looking at the Kohn–Sham eigenvalues pertaining to the ground state (GS) electron configuration (throughout this paper, the MO numbering will be the one corresponding to the all-electron calculations independent of the adoption of the frozen core approximation). As far as the Cu $2p_{1/2}/2p_{3/2}$ IEs are concerned, they have been evaluated by means of spin-unrestricted two-component relativistic ZORA calculations including the

treatment of spin–orbit effects. DFT-ZORA numerical experiments have been carried out by adopting an all-electron TZP ZORA basis set for all the atoms[34] and employing the LB94 approximate functional with the GS electronic configuration.[35,36] We are perfectly aware that this choice implies to neglect core hole relaxations; nevertheless, it is unavoidable if interested to compare herein reported theoretical data with those pertaining to H_2TPP, $H_2TPP(F)$ and CuPc.[14] Further insights into the bonding scheme of the title molecules have been gained by making an extensive use of the Extended TS (ETS) method[37] and by considering, as interacting fragments, the central Cu(II) ion and the TPP^{2-}/$TPP(F)^{2-}$ moieties. Additional information about the localization and the bonding/antibonding character of selected MOs over a broad range of energies has been obtained by referring to the partial density of states (PDOS), to the DOS and to the overlap population DOS (also known as crystal orbital overlap population – COOP).[38] Corresponding curves were computed by weighting one-electron energy levels by their basis orbital percentage and by applying a 0.25 eV Lorentzian broadening factor. These plots, based on Mulliken's prescription for partitioning the overlap density,[39] allow an easy inspection of the atomic composition of MOs over a broad range of energies. Finally, 3D contour plots have been obtained to further look into the localization and the bonding/antibonding character of selected MOs.

3. Results and discussion

Porphyrins are heterocyclic organic molecules constituted of four pyrrole subunits bonded through four methine bridges ($C^5/C^{10}/C^{15}/C^{20}$, collectively tagged as C^m in Fig. 1, where the recommended IUPAC numbering system has been adopted)[40] at their carbon atoms in α positions. Despite the fact that the symmetry assumed for CuTPP and CuTPP(F) complexes (D_{4h}) is higher than that adopted for H_2TPP and $H_2TPP(F)$ free ligands in ref. 14*a–c* (D_{2h}), many different chemical species are still present: besides the central Cu(II) ion, (i) four equivalent pyrrolic nitrogen atoms ($N^{21}/N^{22}/N^{23}/N^{24}$), (ii) two different sets of eight carbon atoms occupying the so-called α ($C^1/C^4/C^6/C^9/C^{11}/C^{14}/C^{16}/C^{19}$) and β ($C^2/C^3/C^7/C^8/C^{12}/C^{13}/C^{17}/C^{18}$) positions with respect to N and collectively tagged as C^{Py}; (iii) the already mentioned C^m carbon atoms; (iv) the twenty-four Ph carbon atoms (C^{Ph}). As far as CuTPP(F) is concerned, the fluorinated species includes twenty fluorine atoms bonded to as many C^{Ph}.

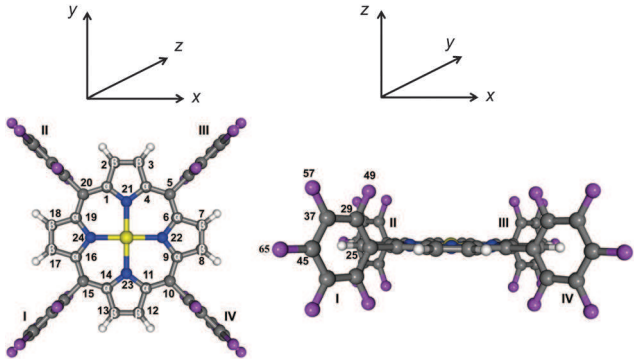

Fig. 1 Schematic plot of top (left) and side views (right) of CuTPP/CuTPP(F). The atom numbering corresponds to the one adopted by Nardi *et al.* in ref. 14*a–c*. The yellow sphere corresponds to the Cu(II) ion, while the purple ones represent the H and F atoms in CuTPP and CuTPP(F), respectively.

Valence band spectra

A better understanding of the forthcoming discussion concerning the CuTPP/CuTPP(F) bonding scheme and the assignment of its UPS spectra may take advantage of a preliminary qualitative description of the title molecules' frontier orbitals.[31] Such a description will be based on symmetry arguments, overlap considerations and the outcomes of recent studies concerning the electronic structure of the H_2TPP[14*a,c*] and $H_2TPP(F)$[14*b,c*] free ligands as well as of CuPc,[14*d*] whose coordinative pocket mirrors the CuTPP one.[41]

The square planar arrangement of the central Cu(II) ion both in CuTPP and CuTPP(F) lifts the five-fold degeneracy of the Cu 3d atomic orbitals (AOs) to generate four low-lying, completely occupied, MOs of symmetry a_{1g}, b_{2g}, and e_g as well as a singly occupied b_{1g} MO (SOMO). The Cu–N interactions involving the Cu 3d-based a_{1g} (z^2), b_{1g} ($x^2 - y^2$), and b_{2g} (xy) AOs have a σ character, while those implying the e_g (xz, yz) orbitals are π in nature. Besides the σ character and a high localization on the Cu(II) central ion, a Cu–N antibonding nature may be also foreseen for the b_{1g} SOMO.[14*d–f*,44] Such a qualitative picture perfectly matches ADF results as demonstrated by the inspection of Fig. 2 where spin up (↑) CuTPP PDOS and Cu–N COOPs are displayed.

Interestingly, at variance with CuPc,[14*d*] the CuTPP highest occupied MO (HOMO) corresponds to the Cu based SOMO and exactly the same thing holds for CuTPP(F). The rationalization of such an outcome is not straightforward because several effects could in principle affect the relative energy order of frontier MOs[31] when moving from CuPc to CuTPP; namely, the absence of condensed benzene rings in CuTPP, the presence of different atoms in the *meso* positions (N^m in CuPc and C^m in CuTPP), and the presence of Ph groups bonded to C^m in CuTPP. Moreover, neither the Cu–N bond distance (quite similar in CuTPP and CuPc)[41] nor a different Cu–N bond order[45] may be invoked.

Being strongly convinced that a thorough comprehension of the CuTPP/CuTPP(F) bonding scheme cannot escape the rationale of this finding, we firstly attempted to work out this matter by looking at the Pc^{2-} and TPP^{2-} electronic structure (see Fig. 3) but preliminary results seemed unable to shed light on it.

As such, the inspection of Fig. 3 clearly indicates that, upon the $Pc^{2-} \rightarrow TPP^{2-}$ switching, the N^{Py} based linear combinations of σ (a_{1g}, b_{1g}, and e_u in symmetry) and π (e_g, a_{2u}, and b_{2u} in symmetry) pairs behave differently.[48] More specifically, the N^{Py}-based σ Fragment MOs (the $17a_{1g}$, $28e_u$ and $15b_{1g}$ FMOs in Pc^{2-}; the $21a_{1g}$, $29e_u$ and $11b_{1g}$ FMOs in TPP^{2-}), corresponding to peaks a, b and c in Fig. 3, are rather uniformly upshifted by 0.7/0.8 eV when moving from Pc^{2-} to TPP^{2-}. At variance with that, the upward shift (1.4 eV) undergone by the N^{Py} based a_{2u} π orbital ($4a_{2u}$ and $10a_{2u}$ FMOs in Pc^{2-} and TPP^{2-}, respectively) is significantly larger than that ($\sim$1 eV) associated with the closely spaced

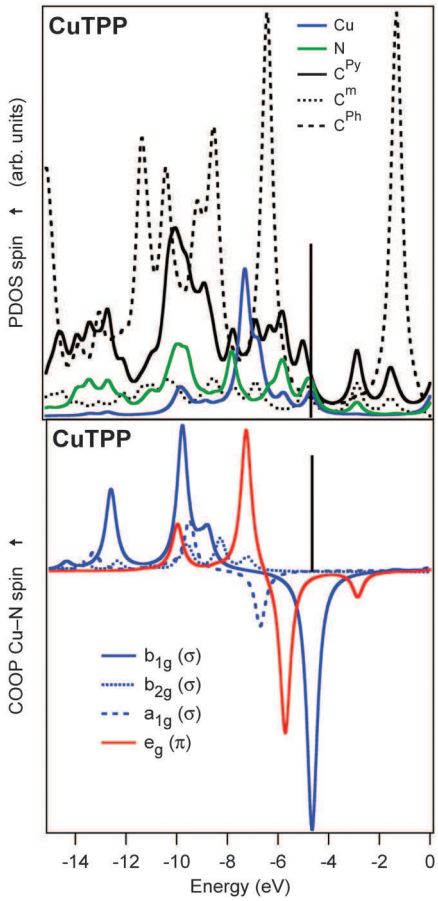

Fig. 2 C, N, and Cu PDOS of the valence states of CuTPP (upper panel). CuTPP COOP between Cu 3d AOs and σ/π N-based MOs (lower panel). Bonding (antibonding) states correspond to positive (negative) peaks in the COOP plot. Vertical bars correspond to the HOMO energy.

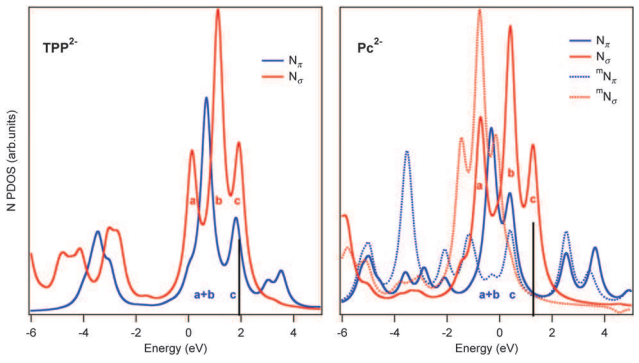

Fig. 3 TPP^{2-} (left panel) and Pc^{2-} (right panel) frontier N PDOS. Vertical bars represent the HOMO energies. Non-relativistic numerical experiments pertaining to TPP^{2-} and Pc^{2-} have been carried out by adopting the geometrical parameters optimized for CuTPP and CuPc, respectively (see Tables S1 and S3 of the ESI†).

N^{Py} based b_{2u} and e_g FMOs (the $5e_g$ and $3b_{2u}$ FMOs in Pc^{2-}; the $3b_{2u}$ and $11e_g$ FMOs in TPP^{2-}).[49]

The keystone to explain not only the different behaviour of the N^{Py} based σ/π pairs in TPP^{2-}/Pc^{2-} fragments but especially the different HOMO nature in CuTPP and CuPc has been

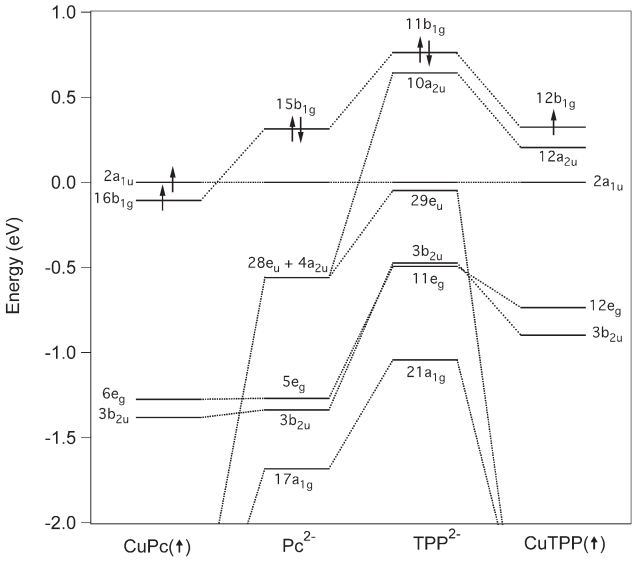

Fig. 4 Relative energy positions of N^{Py} based linear combinations of σ (a_{1g}, b_{1g}, and e_u) and π (e_g, a_{2u}, and b_{2u}) Pc^{2-} and TPP^{2-} frontier FMOs. Only MOs related to σ/π Pc^{2-} and TPP^{2-} frontier FMOs are reported for CuPc and CuTPP. The zero energy corresponds to the energy of the $2a_{1u}$ MO in each species. Non-relativistic numerical experiments pertaining to TPP^{2-} and Pc^{2-} have been carried out by adopting the geometrical parameters optimized for CuTPP and CuPc, respectively (see Tables S1 and S3 of the ESI†).

considering the relative position of frontier MOs/FMOs with respect to the $2a_{1u}$ MO (see Fig. 4).

As a matter of fact, both the localization and the nodal properties (see Fig. S2 of the ESI†)[50] of this $^{Py}\pi_3$-based level contribute to minimizing the effects of those factors influencing the relative energy order of CuPc and CuTPP frontier MOs.[52]

Now, the exploitation of the ETS method[37] combined with a thorough analysis of the Pc^{2-}/TPP^{2-} FMO composition and with the use of data reported in Fig. 3 and 4 points out that: (i) on passing from TPP^{2-} to Pc^{2-}, the presence of N^m atoms downward shifts all but one (the a_{2u} FMO) frontier FMOs by 0.7/1.0 eV (the contribution of N^m AOs to the $15b_{1g}$, $28e_u$, $4a_{2u}$, $5e_g$, $3b_{2u}$ and $17a_{1g}$ Pc^{2-} FMOs amounts to 0%, 4%, 40%, 4%, 0%, and 7%, respectively); (ii) the anomalous stabilization of the Pc^{2-} $4a_{2u}$ FMO (1.4 eV, see Fig. 4) has ultimately to be traced back to the massive participation of the N^m $2p_z$ AOs (40%) to this orbital; (iii) the stabilization energy between scaled b_{1g} MOs upon metalation is very similar: $(E(15b_{1g}) - E(16b_{1g}) = 0.42$ eV; $E(11b_{1g}) - E(12b_{1g}) = 0.44$ eV); (iv) the participation of the TPP^{2-} $10a_{2u}$ FMO to the CuTPP $12a_{2u}$ orbital (the highest occupied CuTPP a_{2u} MO) is huge (84%), while the contribution of the Pc^{2-} $4a_{2u}$ FMO to the CuPc $5a_{2u}$ orbital (the highest occupied CuPc a_{2u} MO) is much lower (11%). Conversely, the Pc^{2-} $4a_{2u}$ FMO greatly contributes (83%) to the CuPc $4a_{2u}$ MO (see Fig. S3 of the ESI†), a highly delocalized π orbital, Cu–N^{Py} bonding, involving the Cu $4p_z$ AO and the in-phase linear combination of N^{Py} $2p_z$ AOs.

A very similar stabilization energy undergone by Pc^{2-}/TPP^{2-} b_{1g} FMOs upon metalation, the stabilizing interaction between outermost a_{2u} FMOs and the Cu $4p_z$ AO (weaker in CuTPP than

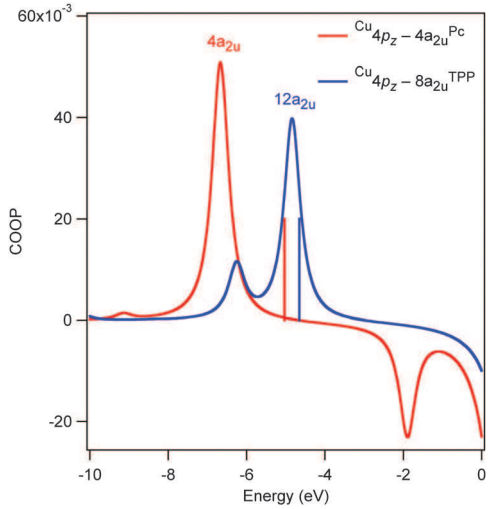

Fig. 5 COOP between the Cu $4p_z$ AO and the TPP^{2-} (Pc^{2-}) based $8a_{2u}$ ($4a_{2u}$) FMO. Bonding (antibonding) states correspond to positive (negative) peaks. Vertical bars correspond to the HOMO energies.

in CuPc, see Fig. 5) and the upward energy shift induced by the substitution of N^m with C^m upon the $Pc^{2-} \rightarrow TPP^{2-}$ switching concur to modify the number and the symmetry of the topmost lying occupied MOs when moving from CuPc to CuTPP (see Fig. 4).

As such, it can be of some relevance to mention that the relative energy order of the CuTPP topmost occupied MOs (see Fig. 4) is the same as that obtained by Ellis and Berkovitch-Yellin for the copper porphine by adopting the spin-polarized discrete-variational-method within the self-consistent-charge approximation and using iterated bases.[53]

Khandelwal and Roebber[23,24] in their paper devoted to the investigation of gas-phase UPS spectra of H_2TPP and some MTPP (M = Mg(II), Mn(II), Fe(II), Ni(II), Cu(II), and Zn(II)) proposed to assign the closely spaced first and second peak of the CuTPP He(I) spectrum to the ionization from an a_{2u} MO (6.49 eV) and an a_{1u} MO (6.66 eV), respectively, without commenting upon the assignment of the SOMO. The ADF GS results herein reported point out that the CuTPP $12b_{1g}$ SOMO, the $12a_{2u}$ and the $^{Py}\pi_3$-based $2a_{1u}$ ↑ orbitals are very close in energy (see the upper panel of Fig. 2 and 4);[54] nevertheless, similar to CuPc,[14d] the accounting of the electronic structure relaxation upon ionization through STS calculations[32] partially removed such a quasi-degeneracy. More specifically, theoretical IEs of the spin ↑ $12b_{1g}$, $12a_{2u}$ and $2a_{1u}$ MOs amount to 6.95, 6.58 and 6.71 eV, respectively. Before going on, it has to be emphasized that Ellis and Berkovitch-Yellin[53] carried out a series of STS calculations;[32] nevertheless, they did not mention any differential relaxation of the outermost $\ldots(a_{1u})^2(a_{2u})^2(b_{1g})^1$ MOs able to modify the GS energy order.

Besides the quantitative agreement with the Khandelwal and Roebber outcomes,[23] theoretical results so far considered provide information about: (i) the energy position of the CuTPP SOMO ionization, reasonably hidden under the higher energy side of the lowest lying feature A centred at 6.3 eV in the CuTPP valence band UPS spectrum (see Fig. 6, upper panel); (ii) the different

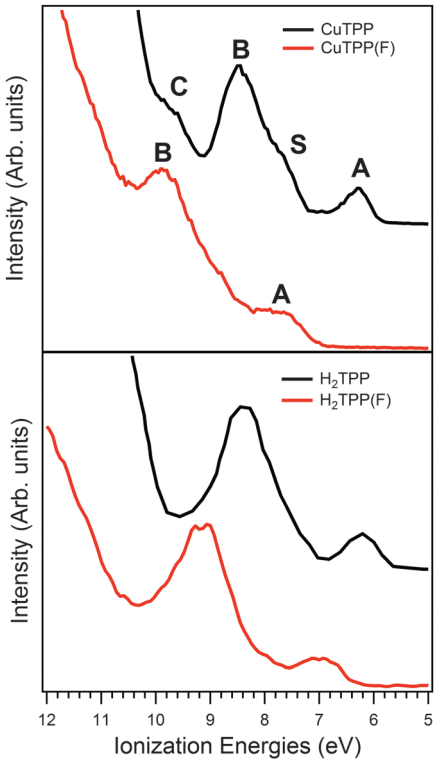

Fig. 6 UPS valence band spectra of CuTPP and CuTPP(F) (upper panel) thin films on Au(111) taken at an excitation photon energy of 21.2 eV. Valence band spectra of H_2TPP[14a] and $H_2TPP(F)$[14b] (lower panel) have been also reported for comparison. Neither the spectra of CuTPP/CuTPP(F) nor those of the free ligands are background subtracted.

number and symmetry of the topmost CuPc and CuTPP MOs;[14d,23,55] (iii) the close similarity between the H_2TPP and the CuTPP valence band UPS spectra (see Fig. 6).[56,57]

Besides the lowest lying feature at 6.3 eV, the IE region up to 9 eV of the CuTPP UPS spectrum includes a further rather intense band (B) centred at 8.5 eV with an evident shoulder S on its lower IE side (see Fig. 6, upper panel). The assumption that STS Hamiltonians for MOs with similar spatial character are comparable[58] induces us to propose the assignment of the shoulder S to the ionization from the $12e_g + 3b_{2u}$ $^{Py}\pi_2$ MOs.[48] Incidentally, the $12e_g$ MO corresponds to the antibonding partner of the Cu–N π interaction (see Fig. 2), while the bonding counterpart is accounted by the $9e_g$ level. As far as the B feature is concerned, besides the involvement of two $^{Py}\pi$ MOs (the fourth $^{Py}\pi_2$ $11a_{2u}$ and the $^{Py}\pi_3$ $10e_g$ orbitals),[59] ionizations from both $^{Ph}\pi_2$ ($8a_{2g} + 31e_u + 11b_{1g}$) and $^{Ph}\pi_3$ ($11e_g + 2b_{2u} + 1a_{1u}$) MOs contribute to its intensity. The last spectral feature of the CuTPP valence band UPS spectrum herein considered is the weak band C centred at ~9.6 eV. The comparison with experimental and theoretical data pertaining to CuPc,[14d] its relative position with respect to $^{Ph}\pi$ MOs (see Fig. 2) and the STS values evaluated for the $19b_{2g}$ (9.42 eV), $9e_g$ (9.67 eV) and $25a_{1g}$ (9.78 eV) MOs prompt us to tentatively assign the feature C to the ionization from the Cu 3d based MOs. The GS participation percentage of Cu based 3d AOs to the $19b_{2g}$, $9e_g$ and $25a_{1g}$ MOs amounts to 89, 82 and 87%, respectively.

It has been already mentioned that the CuTPP(F) UPS spectrum is compared in the upper panel of Fig. 6 with that of the CuTPP. The combined use of symmetry, orbitals and data pertaining to CuTPP and H_2TPP/H_2TPP(F) ligands[14a,b] appears to be the Hobson's choice to get some useful information from the experimental results. Two things deserve to be highlighted before anything else: (i) likewise H_2TPP and H_2TPP(F), the features A and B characterizing the CuTPP(F) UPS spectrum are uniformly blue-shifted by ~1.4 eV upon the CuTPP → CuTPP(F) functionalization (see Fig. 6, upper panel);[14a,b] (ii) the CuTPP(F) band B does not show any shoulder on its lower energy side. ADF outcomes nicely match the former experimental result and provide a rationale for the latter.

Similar to CuTPP, the CuTPP(F) topmost occupied frontier ↑ MOs are the closely spaced $15b_{1g}$, $4a_{1u}$ and $19a_{2u}$ levels lying at 5.59, 5.89 and 5.92 eV, respectively; moreover, STS calculations[32] carried out for each of them provide the following theoretical IEs: 7.79, 7.53 and 7.53 eV, respectively. The assignment of the CuTPP(F) band A is then the same suggested for the lowest lying feature of the CuTPP spectrum. More specifically, even though the GS SOMO and HOMO coincide both in CuTPP and CuTPP(F), the lowest lying IE involves, in both cases, a PMC-based π MO. As far as the absence of any shoulder on the lower energy side of the CuTPP(F) band B is concerned, a few words about perturbations induced by the Ph fluorine decoration on the CuTPP ^{Ph}π orbitals are preliminarily needed.

It is known that the blue-shift undergone by ^{Ph}π levels upon the H_2TPP → H_2TPP(F) functionalization is somehow counter-intuitive;[14a,b] *i.e.* smaller than that corresponding to ^{PMC}π MOs as a consequence of the interaction between ^{Ph}π MOs and F AOs of π symmetry.[60] Even though any detailed assignment of B would simply be a matter of taste, the ADF results suggest that the CuTPP(F) lower IE side of B should be still generated by the ionizations from the $^{Py}\pi_2$-based MOs ($21e_g$ + $5b_{2u}$); nevertheless, they do not generate anymore a detectable shoulder because they are very close in energy to the $20e_g$ orbital, the lowest lying $^{Ph}\pi_3$-based MO.

Core level spectra

The CuTPP and CuTPP(F) $1s^C$ core level spectra are displayed in the left panels of Fig. 7. The CuTPP $1s^C$ peak lineshape is very similar to the H_2TPP one[14a] and it appears to be dominated by a single structure centred at 284.6 eV (peak A in the left, upper panel of Fig. 7); *i.e.* red-shifted by 1 eV (see Table 1) with respect to the free ligand. Such an apparently unexpected red-shift[61] is not particularly surprising and it can be straightforwardly explained by considering that, in our previous studies,[14a,b] both H_2TPP and H_2TPP(F) have been deposited as thicker films (30[14a] and 40[14b] nm, respectively) on an insulating substrate (*i.e.* SiO_2/Si(100) native oxide),[14a,b] while CuTPP and CuTPP(F) thin films (~5 nm) have been grown on a conductive metallic substrate, namely Au(111). As a whole, thinner thicknesses and different substrate conductivities allow a better charge compensation during photoemission experiments and a more efficient substrate-induced screening effect, both of them concurring to determine lower $1s^C$ binding energies (BEs) in CuTPP and CuTPP(F).

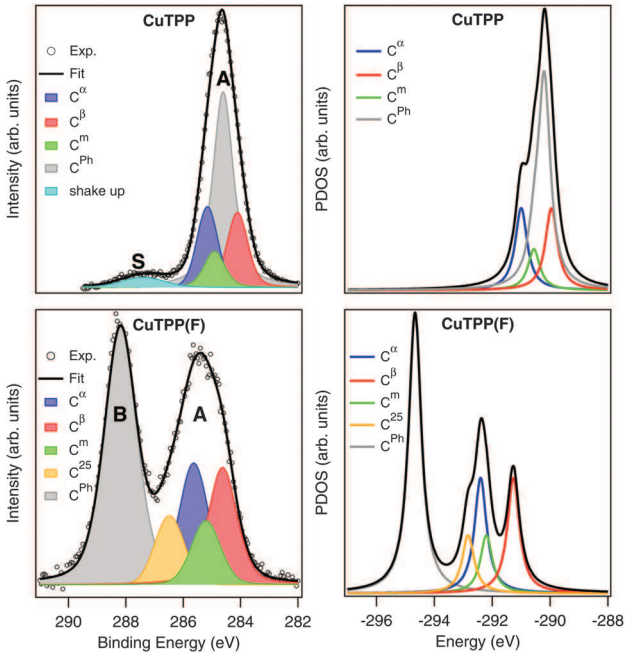

Fig. 7 Experimental $1s^C$ core level (background subtracted) as a function of binding energy of CuTPP (left, upper panel) and CuTPP(F) (left, lower panel) thin films deposited on Au(111). CuTPP (right, upper panel) and CuTPP(F) (right, lower panel) $1s^C$ SR DFT-ZORA PDOS. The colour code adopted to identify the different fitting components of the CuTPP(F) $1s^C$ core level spectrum is the same as that assumed for the CuTPP one.

In agreement with the results herein reported, the $1s^C$ BEs for MTPP (M = Co, Ni and Cu) films on gold are 284.6, 284.7 and 284.5 eV, respectively,[21] while the $1s^C$ BE for H_2TPP films on gold ranges between 284.0[19] and 285.0[62] eV. As a final consideration, similar to the $1s^C$ core level spectrum of H_2TPP, the asymmetric broadening at the base of the CuTPP peak A suggests the presence of more than one component, especially on the higher BE side.

The Voigt analysis of the CuTPP $1s^C$ core level spectrum leads to the introduction of four different fitting components (grey, red, green and blue in Fig. 7, left, upper panel) to properly fit the peak A. The full width at half maximum (FWHM), the absolute/relative energy position and the relative weight of each fitting component are reported in Table 1. Percentages of the total $1s^C$ area of C^{Ph}, C^{β}, C^{α} and C^{m} components[63] are 54.6%, 18.2%, 18.2% and 9.0%, respectively, corresponding to emission from about 24, 8, 8 and 4 carbon atoms, respectively. The C^{Ph} component (grey component) is by far the most intense of the four fitting functions and it can be ascribed with confidence to the emission from the 24 C^{Ph} 1s-based MOs. Taking advantage of H_2TPP literature data,[14a] as well as of the herein reported ZORA outcomes (see the right panels of Fig. 7 and Table 1), the assignment of the CuTPP C^{β}, C^{α} and C^{m} components to the emission from C^{β}, C^{α} and C^{m} 1s-based MOs is then straightforward. As such, it is noteworthy that the FWHM of the A feature (1.1 eV) is quantitatively reproduced by the ΔE (1.1 eV) between the lowest (C^{β}) and the highest (C^{α}) lying $1s^C$-based MOs. As far as the weak and broad feature S on the higher BE side of A is

Table 1 Experimental and theoretical $1s^C$, $1s^N$ and $2p^{Cu}$ core levels of CuTPP; H_2TPP $1s^C$ and $1s^N$ core levels[14a] have been also included (in parentheses) for comparison. The component name and the energy position are given in Fig. 7–10. The percentage corresponds to the fraction of the component area over the whole core level area. ΔE is the energy difference between a specific $1s^C$ component and the C^{Ph} one. The comparison between experimental and theoretical results has been favored by reporting, for the latter, the modulus |eV|

		Experimental analysis				Theoretical analysis		
Core level	Component		eV	FWHM	ΔE	%	Component	eV	ΔE
C 1s	A	C^{β}	284.1 (285.2)	0.8	−0.5 (−0.4)	18.2	C^{β}	290.0[a]	−0.2
		C^{Ph}	284.6 (285.6)	0.8	0.0 (0.0)	54.6	C^{Ph}	290.2 (289.9)	0.0
		C^{m}	285.0 (286.0)	0.9	0.4 (0.4)	9.0	C^{m}	290.6 (290.4)	0.4
		C^{α}	285.2 (286.3)	0.8	0.6 (0.7)	18.2	C^{α}	291.0[a]	1.0
	S		287.4 (288.8)	2.8 (3.2)					
N 1s	A		398.6 (398.2/400.1)					403.9 (402.6/404.4)	
Cu $2p_{3/2}$	A		935.2				934.18, 934.10, 933.98, 933.98		
	A'		942.1						
	A''		944.8						
Cu $2p_{1/2}$	B		955.2				954.66, 954.61		
	B'		962.4						
	B''		964.4						

[a] In H_2TPP there are two non-equivalent pyrrole rings according to the saturated (>NH)/unsaturated (>N) nature of N atoms. Theoretical BEs of C^{α}(>N) and C^{β}(>N) 1s core levels are 290.5 and 289.4 eV, respectively; those of C^{α}(>NH) and C^{β}(>NH) 1s core levels are 291.1 and 289.9 eV, respectively.

concerned, both its energy position (2.8 eV from the main C^{Ph} component, see Table 1) and its FWHM (significantly larger than that corresponding to C^{Ph}, C^{β}, C^{α} and C^{m} fitting functions, see Table 1) suggest, similar to H_2TPP,[14a] the association with a shakeup process of the photoelectrons originated from one (or more) carbon species,[64] whose identification is not forthright due to the presence of too many carbon chemical species. As a whole, CuTPP $1s^C$ core level spectra herein described are consistent with those reported by Reid *et al.* in ref. 22;[26] nevertheless, the Voigt analysis herein reported combined with spin-unrestricted SR DFT-ZORA calculations[33] allowed us to identify all carbon chemical species present in the molecule.[65]

Likewise for CuTPP/H_2TPP, the CuTPP(F) $1s^C$ core level spectrum is very similar to the H_2TPP(F) one[14b] and it consists of a complex lineshape characterized by the presence of two main peaks (A and B in the left, lower panel of Fig. 7) centred at 285.4 and 288.2 eV (see Table 2); *i.e.* once again red-shifted by ~1 eV with respect to the free ligand[61] as a consequence of the different experimental conditions mentioned above. At least four components (corresponding FWHM, absolute/relative energy positions and percentage areas are reported in Table 2) are needed to properly fit the asymmetric shape of the wider structure A, while the peak B has been aptly represented by the single C^{Ph} component. The C^{Ph} component at 288.2 eV represents the main peak with 45.4% of the total C 1s emission area. If we estimate the number of carbon units generating XPS peaks by analysing the corresponding percentage areas of the C 1s area (see Table 2), C^{α} and C^{β} components are equivalent to 8 atoms each, C^{m} and C^{25} to 4 atoms each and C^{Ph} to 20 atoms.

As expected, the comparison of CuTPP(F) $1s^C$ data with the CuTPP ones (see Fig. 7, Tables 1 and 2) allows us to appreciate the two most evident effects associated with the CuTPP Ph fluorine decoration: (i) a significant $1s^C$ BE blue-shift (see the grey component in the left, lower panel of Fig. 7); (ii) the splitting of the CuTPP A peak in the spectral features A and B. Moreover, the H_2TPP[14a] and H_2TPP(F)[14b] literature assignments of the $1s^C$ core level spectra combined with the herein reported SR DFT-ZORA calculations (see the right, lower panel of Fig. 7) make the rationalization of the whole CuTPP(F) $1s^C$ spectrum straightforward. As far as the highest lying C^{Ph} component at 288.2 eV is concerned, it can be assigned with confidence to the photoemission from fluorine saturated C^{Ph} 1s core levels.[64] Furthermore, the lower number of non-equivalent C atoms in the more symmetric CuTPP(F) species (compared to H_2TPP(F)) combined with SR DFT-ZORA outcomes makes the assignment of the broad peak A clear-cut. In detail, the higher (lower) BE side of A has to be associated with the photoemission processes involving the four (eight) C^{25} (C^{β}) 1s-based MOs, while the central part of the band is generated by the ionization from the eight (four) C^{α} (C^{m}) 1s-based MOs. As a whole, the relative position of different components contributing to the CuTPP(F) $1s^C$ spectrum is mainly determined by the distance from the fluorinated Ph groups; *i.e.* the longer the distance the lower the BE.

Before tackling the CuTPP/CuTPP(F) $1s^N$ core level spectra (see the left panels of Fig. 8), two further things need to be emphasized:

Table 2 Experimental and theoretical $1s^C$, $1s^N$, $1s^F$ and $2p^{Cu}$ core levels of CuTPP(F); H_2TPP(F) $1s^C$, $1s^N$ and $1s^F$ core levels[14b] have been also reported (in parentheses) for comparison. The component name and the energy position are given in Fig. 7–10. The percentage corresponds to the fraction of the component area over the whole core level area. ΔE is the energy difference between a specific $1s^C$ component and the C^{Ph} one. The comparison between experimental and theoretical results has been favored by reporting, for the latter, the modulus |eV|

			Experimental analysis				Theoretical analysis		
Core level		Component	eV	FWHM	ΔE	%	Component	|eV|	ΔE
C	1*s*	A	C^{β} 284.7 (285.8)	1.18	−3.5 (−3.8)	18.2	C^{β}	291.3[a]	−3.4
			C^{m} 285.2 (286.3)	1.18	−3.0 (−3.3)	9.1	C^{m}	292.2 (291.8)	−2.5
			C^{α} 285.7 (286.8)	1.18	−2.5 (−2.8)	18.2	C^{α}	292.4[a]	−2.3
			C^{25} 286.5 (287.5)	1.18	−1.7 (−2.1)	9.1	C^{25}	292.8 (292.3)	−3.4
		B	C^{Ph} 288.2 (289.6)	1.35	0.0 (0.0)	45.4	C^{Ph}	294.7 (294.1)	0.0
N	1*s*	A	399.2 (399.0/400.9)				405.2 (403.9/405.6)		
F	1*s*	A	688.5 (689.6)				690.6 (690.1)		
Cu	$2p_{3/2}$	A	935.7				935.35, 935.27, 935.15, 935.14		
		A'	942.1						
		A''	945.1						
	$2p_{1/2}$	B	955.8				955.82, 955.79		
		B'	962.6						
		B''	964.7						

[a] In H_2TPP(F) there are two non-equivalent pyrrole rings according to the saturated (>NH)/unsaturated (>N) nature of nitrogen atoms. Theoretical BEs of C^{α}(>N) and C^{β}(>N) 1s core levels are 291.8 and 290.7 eV, respectively; those of C^{α}(>NH) and C^{β}(>NH) 1s core levels are 292.3 and 291.1 eV, respectively.

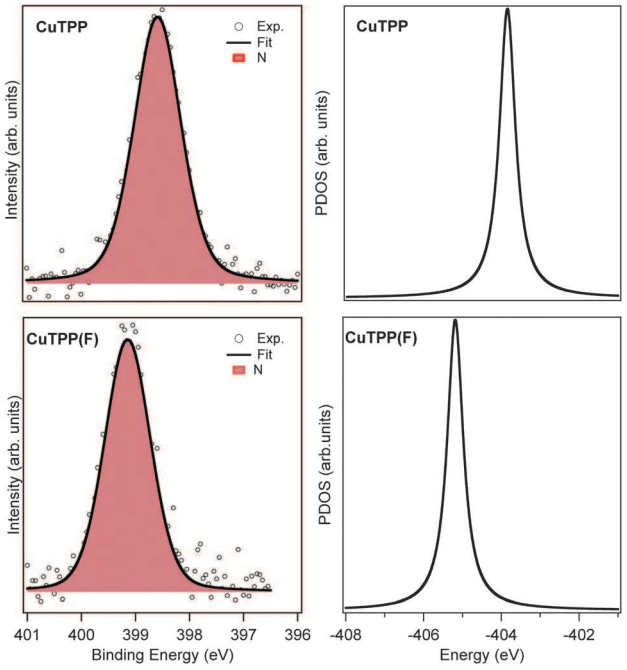

Fig. 8 Experimental $1s^N$ core level spectra (background subtracted) as a function of binding energy of CuTPP (left, upper panel) and CuTPP(F) (left, lower panel) thin films deposited on Au(111). CuTPP (right, upper panel) and CuTPP(F) (right, lower panel) $1s^N$ SR DFT-ZORA PDOS.

(i) even though ΔE values between different components contributing to the peak A of CuTPP(F) are appropriately reproduced by SR DFT-ZORA calculations, the absolute blue-shift associated with the fluorination of the CuTPP Ph rings is overestimated by ~1 eV (compare the theoretical energy position of the C^{Ph} component in Tables 1 and 2); (ii) the comparison between the $1s^C$ core level spectra of the free ligands and those of the corresponding Cu(II) complexes testifies the presence of a systematic red-shift of ~1 eV in the latter.

As a consequence of the CuTPP/CuTPP(F) symmetry, higher than that of H_2TPP/H_2TPP(F) ligands, the lineshapes of the $1s^N$ peak are very different in the complexes and in the free ligands: a single peak centred at 398.6[66] and 399.2 eV in CuTPP and CuTPP(F), respectively (see Fig. 8, Tables 1 and 2), and two well-resolved peaks at 398.2/400.1 and 399.0/400.9 eV in H_2TPP[14a] and H_2TPP(F),[14b] respectively (see Tables 1 and 2). BEs of $1s^N$-based MOs may be then either blue-shifted (H_2TPP → CuTPP: 0.4 eV; H_2TPP(F) → CuTPP(F): 0.2 eV) or red-shifted (H_2TPP → CuTPP: 1.5 eV; H_2TPP(F) → CuTPP(F): 1.7 eV) upon metalation according to the nature, iminic (>N) or pyrrolic (>NH), of the free ligand N atoms.[67] The SR DFT-ZORA results are consistent with a shift toward higher (lower) BEs of iminic (pyrrolic) $1s^N$-based MOs when moving from the free ligands to the copper complexes; nevertheless, it has to be remarked that theoretical ΔBEs poorly reproduce the experimental ones. More specifically,

blue-shifts amount to 1.3 eV both in $H_2TPP \rightarrow CuTPP$ and $H_2TPP(F) \rightarrow CuTPP(F)$; red-shifts amount to 0.5 and 0.4 eV in $H_2TPP \rightarrow CuTPP$ and $H_2TPP(F) \rightarrow CuTPP(F)$, respectively (see Tables 1 and 2). On the other hand, it would be unreasonable that the systematic red-shift of $\sim$1 eV revealed for $1s^C$ core level spectra (*vide supra*)[68] when moving from the free ligands to the corresponding copper complexes would not affect the $1s^N$ core level spectra too.

SR DFT-ZORA calculations are clearly unable to account for such a red-shift and this certainly favours the disagreement between theory and experiment; nevertheless, if the systematic red-shift of $\sim$1 eV would be neglected (pseudo CuTPP/CuTPP(F) $1s^N$ BEs would then lie at $\sim$399.6/$\sim$400.2 eV), blue-shifts (1.4/1.2 eV) and red-shifts (0.5/0.7 eV) with respect to the $H_2TPP/H_2TPP(F)$ $1s^{>N}$ and $1s^{>NH}$ BEs would be quantitatively reproduced by SR DFT-ZORA calculations.[65,69]

Before moving to the analysis of experimental and theoretical data pertaining to the lineshape of the $1s^F$ core level spectrum, it is of some relevance to mention that the overestimation of the effect of the Ph fluorine decoration on the $1s^N$ BE perfectly mirrors the one estimated when moving from H_2TPP to $H_2TPP(F)$.[14a,b,70]

The $1s^F$ core level spectrum of CuTPP(F) is displayed in the left panel of Fig. 9. It consists of a single peak located at 688.5 eV whose FWHM (1.6 eV) is larger than those of the $1s^{C/N}$ single components. A possible explanation of this broadening could be the slightly different chemical environment generated by the different spatial orientations of the molecules in the CuTPP(F) thin film as well as by the different directions of carbon–fluorine bonds associated with the Ph tilt with respect to the PMC plane in each CuTPP(F) molecule.

Similar to the experimental results previously described for CuTPP/CuTPP(F) $1s^C$ core level spectra, the BE of the single peak characterizing the CuTPP(F) $1s^F$ core level spectrum is affected by a systematic red-shift of $\sim$1 eV with respect to $H_2TPP(F)$. Despite the different positions of fluorine atoms on the phenyl rings (see Fig. 1 and 9, right panel), the occurrence of a single peak testifies the presence of a single chemical species. The agreement between experiment and SR DFT-ZORA calculations would be remarkable if the systematic red-shift would be neglected.

Spin orbit coupling splits the degenerate Cu 2p core levels into the doublet $2p_{1/2}$ (L_2-edge) and $2p_{3/2}$ (L_3-edge). Accordingly, the

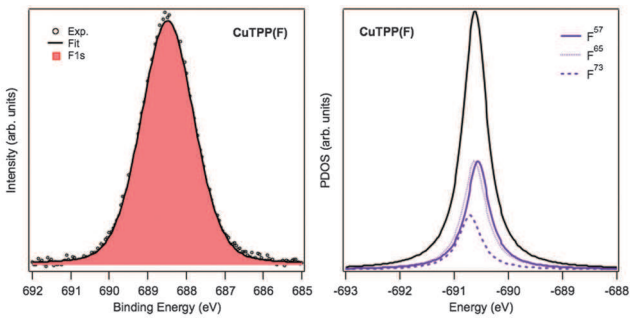

Fig. 9 Experimental $1s^F$ core level spectrum (background subtracted) of a thin film of CuTPP(F) deposited on Au(111) (left). CuTPP(F) (right) $1s^F$ SR DFT-ZORA PDOS.

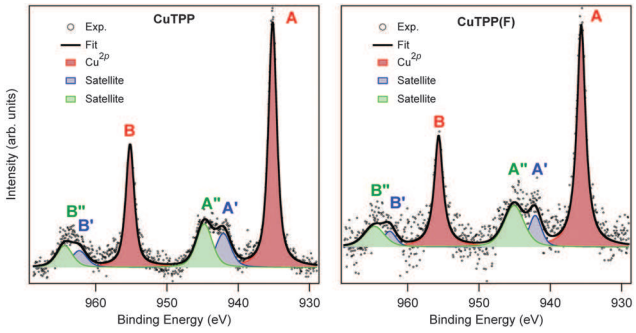

Fig. 10 Experimental $2p^{Cu}$ core level spectra (background subtracted) of thin films of CuTPP (left) and CuTPP(F) (right) deposited on Au(111).

CuTPP $2p^{Cu}$ core level spectrum includes two main peaks (A and B in Fig. 10) and other minor structures.[71]

In more detail, similar to CuPc,[14d] the $2p_{3/2}$ component can be divided into the well-screened peak A at 935.20 eV (Fig. 10, red component), corresponding to a $2p3d^{10}L$ final state (characterized by a 2p core hole and a hole in the ligand band), and two satellites at 942.1 and 944.8 eV (peaks A′ and A″ in Fig. 10), both related to a $2p3d^9$ final state.[72] As far as the $2p_{1/2}$ peak is concerned, the B feature lies at 955.2 eV (Fig. 10, red component), *i.e.* 20 eV from A as a consequence of the well-known Cu $2p_{3/2}/2p_{1/2}$ spin–orbit energy gap.[14d–f] Moreover, analogous to the $2p_{3/2}$ band envelope, two satellite features (B′ and B″ in Fig. 10) are present on the higher energy side of B. Incidentally, $\Delta E_{(B'-B)}$ and $\Delta E_{(B''-B)}$ are similar to $\Delta E_{(A'-A)}$ and $\Delta E_{(A''-A)}$ (see Table 1). The intensity ratio between the $2p_{3/2}$ and $2p_{1/2}$ components is 2.0, in agreement with the theoretical value of 2.0 determined from the multiplicity of the degenerate $2p_{1/2}$ to $2p_{3/2}$ electron configurations. In quantitative agreement with experimental findings, spinors related to the Cu $2p_{1/2}$ and $2p_{3/2}$ atom-like levels and evaluated by running two-component spin–orbit relativistic DFT-ZORA calculations lie at 954.66, 954.61, 934.18, 934.10, 933.98, and 933.98 eV.

In much the same way as CuTPP, the spin orbit coupling splits the degenerate Cu 2p core levels of CuTPP(F) into the doublet $2p_{1/2}$ and $2p_{3/2}$. The $2p^{Cu}$ core level spectrum of CuTPP(F) then includes two main peaks (A and B in Fig. 10) and other minor structures. In more detail, similar to CuTPP and CuPc,[14d] the $2p_{3/2}$ component can be divided into the well-screened peak A at 935.70 eV (Fig. 10, red component), blue-shifted by 0.5 eV with respect to the same peak in CuTPP, corresponding to a $2p3d^{10}L$ final state, and two satellites at 942.1 and 945.1 eV. As far as the $2p_{1/2}$ peak is concerned, B lies at 955.8 eV (Fig. 10, red component), *i.e.* 20.1 eV from A as a consequence of the well-known Cu $2p_{3/2}/2p_{1/2}$ spin–orbit energy gap.[14d–f] Moreover, analogous to the $2p_{3/2}$ band envelope, two satellite features (B′ and B″ in Fig. 10) are present on the higher energy side of B. The intensity ratio between the $2p_{3/2}$ and $2p_{1/2}$ components is 2.0, in agreement with the expected theoretical value. Once again in quantitative agreement with experimental findings, spinors related to the Cu $2p_{1/2}$ and $2p_{3/2}$ atom-like levels and evaluated by running two-component ZORA spin–orbit relativistic DFT calculations lie at 955.82, 955.79, 935.35, 935.27, 933.15, and 935.14 eV.

4. Conclusions

Occupied core and valence levels of two π-conjugated molecules, namely the copper complexes of tetraphenyl porphyrin and tetrakis(pentafluorophenyl)porphyrin, have been thoroughly investigated by combining UPS, XPS analysis and DFT-ZORA calculations. According to a well-established procedure, the experimental results collected from thin films of both molecules have been discussed and compared with the outcomes of numerical experiments carried out for the isolated species. Several papers have been devoted in the past to the investigation of the occupied electronic structure of CuTPP; nevertheless, none of them provided reliable information about the nature, the localization, the numbers and the IEs of occupied frontier orbitals. The combined use of the Slater TS approximation[32] and of the extended TS approach[37] allowed us to propose a detailed assignment of experimental data and to look into the perturbations induced into the CuTPP electronic structure by the fluorine decoration of Ph peripheral groups. Similar to CuPc, the combined use of photoemission spectroscopies and DFT-ZORA results ultimately testifies the relevant role played by the ionic contribution in the bonding between the Cu(II) and the nitrogen atoms of the PMC coordinative pocket. Nevertheless, the different number, symmetry, nature and relative position of occupied frontier orbitals upon the CuPc → CuTPP/CuTPP(F) switching can be rationalized only by considering in great detail the Cu-ligand covalent interactions. Similar to H_2TPP → H_2TPP(F), the blue-shift accompanying the outermost IEs upon CuTPP → CuTPP(F) swapping is not uniform. In particular, those apparently less affected are the $^{Ph}\pi$ MOs as a consequence of two opposite effects: (i) the electron withdrawing properties of fluorine and (ii) the extensive mixing between fluorine decorated ^{Ph}C(F) and F π orbitals.

Acknowledgements

Prof. Luciano Pandolfo is acknowledged for the synthesis of CuTPP(F). The Italian Ministry of the University and Research (PRIN-2010BNZ3F2, project DESCARTES), The University of Padova (CPDA134272/13, project S_3MArTA), and The Computational Chemistry Community (C_3P) of the University of Padova are kindly acknowledged. Dr Melanie Timpel gratefully acknowledges the support of a Feodor-Lynen-Fellowship of the Alexander v. Humboldt foundation, Bonn (Germany).

References

1 A. Ghosh, *Letters to a young chemist*, Wiley-Interscience, 2011, p. 34.
2 The heme group, a non-polypeptide prosthetic group consisting of the protoporphyrin IX and a central iron atom, is present in myoglobin, hemoglobin and many other proteins[3a] whose biological functions include the detection and transportation of diatomic gases, chemical catalysis and electron transfer.
3 (*a*) D. L. Nelson and M. M. Cox, *Lehninger Principles of Biochemistry*, W.H. Freeman, 6th edn, 2012; (*b*) J. M. Berg, J. L. Tymoczko and L. Stryer, *Biochemistry*, W.H. Freeman, 5th edn, 2002.
4 Chlorophyll is a chlorin pigment structurally similar to the protoporphyrin of haemoglobin whose coordinative pocket hosts a Mg^{2+} ion. Chlorophylls are the most important light-absorbing pigments in the thylakoid membranes.[3]
5 (*a*) A. R. Battersby, C. J. R. Fookes, G. W. J. Matcham and E. McDonald, *Nature*, 1980, **285**, 17; (*b*) A. R. Battersby, *Nat. Prod. Rep.*, 1987, **4**, 77.
6 (*a*) A. E. O'Connor, W. M. Gallagher and A. T. Byrne, *Photochem. Photobiol.*, 2009, **85**, 1053; (*b*) A. P. Castano, P. Mroz and M. R. Hamblin, *Nat. Rev. Cancer*, 2006, **6**, 535.
7 A. Tsuda and A. Osuka, *Science*, 2001, **293**, 79.
8 M. Planells, A. Forneli, E. Martínez-Ferrero, A. Sánchez-Díaz, M. A. Sarmentero, P. Ballester, E. Palomares and B. C. O'Regan, *Appl. Phys. Lett.*, 2008, **92**, 153506.
9 N. A. Rakow and K. S. Suslick, *Nature*, 2000, **406**, 710.
10 *The Porphyrin Handbook*, ed. K. M. Kadish, K. M. Smith and R. Guilard, Academic Press, New York, 2000.
11 D. Dini and M. Hanack, *J. Porphyrins Phthalocyanines*, 2004, **8**, 915.
12 C. Di Natale, D. Monti and R. Paolesse, *Mater. Today*, 2010, **13**, 46.
13 J. M. Gottfried, *Surf. Sci. Rep.*, 2015, **70**, 259.
14 (*a*) M. Nardi, R. Verucchi, C. Corradi, M. Pola, M. Casarin, A. Vittadini and S. Iannotta, *Phys. Chem. Chem. Phys.*, 2010, **12**, 871; (*b*) M. Nardi, R. Verucchi, L. Aversa, M. Casarin, A. Vittadini, N. Mahne, A. Giglia, S. Nannarone and S. Iannotta, *New J. Chem.*, 2013, **37**, 1036; (*c*) M. V. Nardi, R. Verucchi, L. Pasquali, A. Giglia, G. Fronzoni, M. Sambi, G. Mangione and M. Casarin, *Phys. Chem. Chem. Phys.*, 2015, **17**, 2001; (*d*) M. V. Nardi, F. Detto, L. Aversa, R. Verucchi, G. Salviati, S. Iannotta and M. Casarin, *Phys. Chem. Chem. Phys.*, 2013, **15**, 12864; (*e*) G. Mangione, M. Sambi, M. V. Nardi and M. Casarin, *Phys. Chem. Chem. Phys.*, 2014, **16**, 19852; (*f*) G. Mangione, L. Pandolfo, M. Sambi, G. Ligorio, M. V. Nardi, A. Cossaro, L. Floreano and M. Casarin, *Eur. J. Inorg. Chem.*, 2015, 2709.
15 V. A. Nefedov and A. M. Pavlov, *Russ. J. Org. Chem.*, 2009, **45**, 449.
16 H_2TPP and copper powder exposed to atmospheric oxygen allow the direct synthesis of CuTPP, while the same does not hold when H_2TPP and other metals, such as Zn, are considered. The CuTPP electronic spectrum includes just one absorption band centred at 540 nm, while both the free ligand and complexes with other metals include up to four absorption bands in the wavelength region extending from 500 to 650 nm.[15]
17 Amsterdam Density Functional (ADF) version 2014.01 http://www.scm.com.
18 Y. Niwa, H. Kobayashi and Y. Tsuchiya, *J. Chem. Phys.*, 1974, **60**, 799.
19 D. H. Karweik and N. Winograd, *Inorg. Chem.*, 1976, **15**, 2336.
20 D. A. Case and M. Karplus, *J. Am. Chem. Soc.*, 1977, **99**, 6182.
21 L. Scudiero, D. E. Barlow and K. W. Hipps, *J. Phys. Chem. B*, 2000, **104**, 11899.

22 I. Reid, Y. Zhang, A. Demasi, A. Blueser, L. Piper, J. E. Downes, A. Matsuura, G. Hughes and K. E. Smith, *Appl. Surf. Sci.*, 2009, **256**, 720.
23 S. C. Khandelwal and J. L. Roebber, *Chem. Phys. Lett.*, 1975, **34**, 355.
24 The CuTPP He(I) vapour-phase UPS spectrum is not displayed in ref. 23. Khandelwal and Roebber[23] limited themselves to report the position of the major bands in the UPS spectra of H_2TPP and MTPP (M = Mg(II), Mn(II), Fe(II), Ni(II), Cu(II), and Zn(II)) and to display the MgTPP and ZnTPP spectra underlying the fact that "free base H_2TPP and all the metallic derivatives which we have examined have surprisingly similar PE spectra".
25 K. Diller, F. Klappenberger, M. Marschall, K. Hermann, A. Nefedov, C. Wöll and J. V. Barth, *J. Chem. Phys.*, 2012, **136**, 014705.
26 No assignment of the CuTPP $1s^C$ core level spectra is reported in ref. 25.
27 A. D. Adler, F. R. Longo, F. Kampas and J. J. Kim, *J. Inorg. Nucl. Chem.*, 1970, **32**, 2443.
28 A constant and fixed excitation energy (the Al Kα source – 1486.6 eV) has been used to record XPS spectra. The analyser work function has been then calibrated just once at the beginning of the experiment by employing an Au(111) single crystal.
29 The fitting of the CuTPP and CuTPP(F) $1s^C$ core levels implied the use of a series of constraints dictated by the chemical structure of the molecules. More specifically, the fitting has been performed by considering the number of different C atoms in the molecules, the FWHM of the four components to fit the feature A has been kept constant, while their areas were chosen according to the number of C atoms they represent. Furthermore, the relative energy differences between the four components to each other (*i.e.* C^{β}, C^{m}, C^{α}, and C^{25}) were selected and kept fixed, in agreement with the H_2TPP and H_2TPP(F) $1s^C$ core level fitting reported in ref. 14*a* and *b*.
30 A. D. Becke, *Phys. Rev. A: At., Mol., Opt. Phys.*, 1988, **38**, 3098; J. P. Perdew, *Phys. Rev. B: Condens. Matter Mater. Phys.*, 1986, **33**, 8822.
31 G. L. Miessler, P. J. Fischer and D. A. Tarr, *Inorg. Chem.*, Pearson, New York, 5th edn, 2013, p. 137.
32 J. C. Slater, *Quantum Theory of Molecules and Solids. The Self-Consistent-Field of Molecules and Solids*, McGraw-Hill, New York, 1974, vol. 4.
33 E. van Lenthe, E. J. Baerends and J. G. Snijders, *J. Chem. Phys.*, 1993, **99**, 4597; E. van Lenthe, E. J. Baerends and J. G. Snijders, *J. Chem. Phys.*, 1994, **101**, 9783; E. van Lenthe, A. W. Ehlers and E. J. Baerends, *J. Chem. Phys.*, 1999, **110**, 8943.
34 E. van Lenthe and E. J. Baerends, *J. Comput. Chem.*, 2003, **24**, 1142.
35 R. van Leeuwen and E. J. Baerends, *Phys. Rev. A: At., Mol., Opt. Phys.*, 1994, **49**, 2421.
36 M. Stener, G. Fronzoni and M. de Simone, *Chem. Phys. Lett.*, 2003, **373**, 115; M. Casarin, P. Finetti, A. Vittadini, F. Wang and T. Ziegler, *J. Phys. Chem. A*, 2007, **111**, 5270.
37 T. Ziegler and A. Rauk, *Theor. Chim. Acta*, 1977, **46**, 1.
38 R. Hoffmann, *Solids and Surfaces: A Chemist's View of Bonding in Extended Structures*, VCH, New York, 1988.
39 R. S. Mulliken, *J. Chem. Phys.*, 1955, **23**, 1833.
40 G. P. Moss, *Pure Appl. Chem.*, 1987, **59**, 779.
41 The optimized Cu–N bond lengths in CuTPP, CuTPP(F) and CuPc (2.019, 2.020, and 1.978 Å, respectively) agree quite well with available experimental data for CuTPP (2.000 Å)[42] and CuPc (1.946 Å).[43] CuPc optimized Cartesian coordinates are reported in Table S3 of the ESI†.
42 W. R. Scheidt, in *The Porphyrins III, Physical Chemistry, Part A*, ed. D. Dolphin, Academic Press, Inc., New York, 1978.
43 J. Ren, S. Meng, Y.-L. Wang, X.-C. Ma, Q.-K. Xue and E. Kaxiras, *J. Chem. Phys.*, 2011, **134**, 194706.
44 M. Rancan, J. Tessarolo, M. Casarin, P. L. Zanonato, S. Quici and L. Armelao, *Inorg. Chem.*, 2014, **53**, 7276.
45 Both in CuTPP and CuPc[14*d*] the Nalewajski–Mrozek[46] Cu–N bond multiplicity index amounts to 0.35. Moreover, Cu and N Hirshfeld[47] gross atomic charges have the same values in CuTPP and CuPc[14*d*] (Cu: 0.42; N: −0.15).
46 R. F. Nalewajski and J. Mrozek, *Int. J. Quantum Chem.*, 1994, **51**, 187; R. F. Nalewajski, J. Mrozek, S. J. Formosinho and A. J. C. Varandas, *Int. J. Quantum Chem.*, 1994, **52**, 1153; R. F. Nalewajski and J. Mrozek, *Int. J. Quantum Chem.*, 1996, **57**, 377; R. F. Nalewajski, J. Mrozek and G. Mazur, *Can. J. Chem.*, 1996, **74**, 1121; R. F. Nalewajski, J. Mrozek and A. Michalak, *Int. J. Quantum Chem.*, 1997, **61**, 589; R. F. Nalewajski, J. Mrozek and A. Michalak, *Pol. J. Chem.*, 1998, **72**, 1779.
47 F. L. Hirshfeld, *Theor. Chim. Acta*, 1977, **44**, 129.
48 The three occupied π fragment MOs (FMOs) of an isolated Py moiety ($^{Py}\pi_1$, $^{Py}\pi_2$ and $^{Py}\pi_3$) transform as the b_2 ($^{Py}\pi_1$), b_2 ($^{Py}\pi_2$) and a_2 ($^{Py}\pi_3$) irreducible representations of the C_{2v} symmetry point group. Besides the nodal plane corresponding to the Py molecular plane, both $^{Py}\pi_2$ and $^{Py}\pi_3$ are characterized by a further nodal plane perpendicular (⊥) to the molecule and passing either between C atoms in α and β positions with respect to N ($^{Py}\pi_2$) or through the N atom ($^{Py}\pi_3$). In the D_{4h} CuTPP and CuTPP(F) molecules, $^{Py}\pi_1$, $^{Py}\pi_2$ and $^{Py}\pi_3$ generate four linear combinations; those associated with $^{Py}\pi_2$ ($^{Py}\pi_3$) transform as $e_g + a_{2u} + b_{2u}$ ($e_g + a_{1u} + b_{1u}$). The three occupied π FMOs of a Ph fragment ($^{Ph}\pi_1$, $^{Ph}\pi_2$ and $^{Ph}\pi_3$) transform as the a_{2u} ($^{Ph}\pi_1$) and e_{1g} ($^{Ph}\pi_2$, $^{Ph}\pi_3$) irreducible representations of the D_{6h} symmetry point group. Besides the nodal plane corresponding to the Ph molecular plane, both $^{Ph}\pi_2$ and $^{Ph}\pi_3$ are characterized by a further ⊥ nodal plane passing either between C^{29} and C^{37} atoms (see Fig. 1, $^{Ph}\pi_2$) or corresponding to the PMC plane ($^{Ph}\pi_3$). In D_{4h} CuTPP and CuTPP(F) molecules, $^{Ph}\pi_1$, $^{Ph}\pi_2$ and $^{Ph}\pi_3$ generate four linear combinations; those associated with $^{Ph}\pi_2$ ($^{Ph}\pi_3$) transform as $a_{2g} + b_{1g} + e_u$ ($e_g + a_{1u} + b_{2u}$).
49 3D contour plots of N^{Py} based Pc^{2-} and TPP^{2-} σ ($17a_{1g}$, $28e_u$ and $15b_{1g}$ FMOs in Pc^{2-}; $21a_{1g}$, $29e_u$ and $11b_{1g}$ FMOs in TPP^{2-}) and π ($3b_{2u}$, $5e_g$ and $4a_{2u}$ FMOs in Pc^{2-}; the $3b_{2u}$, $11e_g$ and $10a_{2u}$ FMOs in TPP^{2-}) pairs are displayed in Fig. S1 of the ESI.† Displayed isosurfaces correspond to ± 0.02 $e^{1/2}$ $Å^{-3/2}$ values.

50 The $2a_{1u}$ MO corresponds, both in the TPP^{2-}/Pc^{2-} fragments and in the CuTPP/CuPc complexes, to a π orbital highly localized on the PMC (see Fig. S2 of the ESI†) and characterized by four nodal planes[51] passing through N^{py} (σ_v) and X^m (σ_d), X = C in TPP^{2-}/CuTPP and X = N in Pc^{2-}/CuPc. Such an orbital is directly related to the H_2Pc $4a_u$ HOMO[14d] and to the H_2TPP $10a_u$ second HOMO;[14a,52] moreover, it corresponds to the CuPc HOMO.[14d]

51 B. E. Douglas and C. A. Hollingsworth, *Symmetry in Bonding and Spectra*, Academic Press, New York, 1985.

52 The H_2Pc $4a_u$ and H_2TPP $10a_u$ MOs are quasi degenerate and their eigenvalues lie at −5.07 and −5.08 eV, respectively. Similar considerations hold for the $2a_{1u}$ FMO in Pc^{2-} and TPP^{2-}, which lie at 0.97 and 1.17 eV, respectively. The $2a_{1u}$ MO in CuPc and CuTPP lies at −5.01 and −4.98 eV, respectively.

53 D. E. Ellis and Z. Berkovitch-Yellin, *J. Chem. Phys.*, 1981, **74**, 2427.

54 GS energy eigenvalues of the $12b_{1g}$, $12a_{2u}$ and $2a_{1u}$ ↑ MOs are 4.65, 4.85 and 4.98 eV, respectively.

55 J. Berkowitz, *J. Chem. Phys.*, 1979, **70**, 2819.

56 D_{2h} H_2TPP and $H_2TPP(F)$ topmost lying occupied MOs are $13b_{1u}/10a_u$ and $22b_{1u}/19a_u$, respectively.[14b] D_{2h} b_{1u} and a_u irreducible representations correlate with the D_{4h} a_{2u} and a_{1u} ones, respectively.[51]

57 The energy shifts between the spectra herein reported (lower panel of Fig. 6) and those of ref. 14*a* and *b* are a consequence of the different work functions (taken into account to evaluate corresponding ionization energies – IEs) associated with different films. The energy shift of 0.7 eV between the red and black curves displayed in the lower panel of the Fig. 6 has been ascribed in ref. 14*b* to "the presence of dipoles at the $H_2TPP(F)/SiO_2$ interface". Similarly, the ΔIE of 1.4 eV between the CuTPP and CuTPP(F) HOMOs (Fig. 6 upper panel) has to be attributed to the different chemical nature of the two Cu(II) complexes. As such, if we would consider that the calculated HOMO IEs are 6.58 and 7.53 eV for CuTPP and CuTPP(F), respectively, it would sound reasonable to predict a ∼0.4 eV shift due to the presence of dipoles at the CuTPP(F)/Au(111) interface.

58 W. C. Trogler, D. E. Ellis and J. Berkowitz, *J. Am. Chem. Soc.*, 1979, **101**, 5896.

59 The GS energy eigenvalue of the fourth $^{Py}\pi_3$-based $8b_{1u}$ MO is −7.66 eV.

60 The actual energy position of $^{Ph}\pi$ MOs in $H_2TPP(F)$ is determined by two opposite effects: (i) the electron withdrawing properties of fluorine and (ii) the extensive mixing between fluorine decorated ^{Ph}C ($^{Ph}C(F)$) and F π orbitals. With specific reference to the latter effect, bonding and antibonding combinations, both of them completely occupied, are generated; the former are mainly localized on the F atoms while the latter are strongly concentrated on $^{Ph}C(F)$.[14b]

61 Despite the fact that the comparison of H_2Pc and CuPc $1s^C$ core level spectra (see Fig. 9 of ref. 14*d*) clearly testifies that both relative intensities and relative binding energies are very similar (a consequence of the great likeness of H_2Pc and CuPc carbon chemical structures), a tiny blue-shift of ∼0.1 eV characterizes every CuPc feature of the $1s^C$ core level spectrum.

62 M. Chen, X. Feng, L. Zhang, H. Ju, Q. Xu, J. Zhu, J. M. Gottfried, K. Ibrahim, H. Qian and J. Wang, *J. Phys. Chem. C*, 2010, **114**, 9908.

63 Due to the close similarity between CuTPP/CuTPP(F) and $H_2TPP/H_2TPP(F)$ $1s^C$ peak lineshapes, the fitting components of the former spectra have been labelled according to the final assignment of the latter ones.

64 J. C. Goll, K. T. Moore, A. Ghosh and M. J. Therien, *J. Am. Chem. Soc.*, 1996, **118**, 8344.

65 Analogous to the previously published results pertaining to H_2TPP,[14a] $H_2TPP(F)$,[14b] H_2Pc[14d] and CuPc,[14d] the LB94 functional provides absolute IEs of the $1s^C$- and $1s^N$-based MOs ∼5 eV higher than experimental values.

66 The CuTPP $1s^N$ BE (398.6 eV) agrees with literature values (398.2,[19] 398.3,[22] 398.8[25] and 398.9[18] eV); moreover, it coincides with the value reported by Scudiero *et al.*[21]

67 Upon switching from H_2Pc to CuPc the blue- and red-shifts undergone by >N and >NH $1s^N$ BEs are quite similar and they amount to 0.8 and 1.0 eV,[14d] respectively.

68 It can be useful to anticipate that the systematic red-shift revealed for the $1s^C$ BEs upon $H_2TPP/H_2TPP(F)$ → CuTPP/CuTPP(F) switching involves the $1s^F$ BEs too.

69 The absolute agreement between theory and experiment reported by Diller *et al.*[25] is certainly better than ours. Besides the different theoretical approach they adopted to evaluate $1s^N$ BEs ("ionization energies were obtained by subtracting the calculated total energies of the core hole state from that of the ground state"),[25] it has to be remarked that their XPS data pertaining to H_2TPP and CuTPP have been collected for films grown on the same conductive substrate. The main difference between their ΔSCF approximation and the approach herein adopted concerns the CuTPP $1s^N$ BE: 402.9[25] *vs.* 403.9 eV.

70 Experimental (theoretical) $1s^N$ ΔBE between CuTPP(F) and CuTPP is 0.6 (1.3) eV. Experimental (theoretical) $1s^N$ ΔBEs between $H_2TPP(F)$ and H_2TPP are 0.8 (1.3) eV for >N and 0.8 (1.2) eV for >NH (see Tables 1 and 2).

71 The CuTPP and CuTPP(F) $2p^{Cu}$ core level spectra displayed in Fig. 10 are affected by a high experimental data scattering and a bad signal-to-noise ratio as a consequence of the small amount of Cu atoms in the analysed molecules. Searching for the best fit (*i.e.* looking for the minimum χ square values) of peaks B″ and B′ is rather speculative and applying minimum χ square values for such highly scattered data would simply be a matter of taste. On this basis, we preferred to keep constant the intensity ratio between the different components related to $2p_{1/2}$ and $2p_{3/2}$ (for main components and satellite regions) in agreement with the theoretical expectations. This means that the A′/B′ and A″/B″ ratios have been kept constant according to the theoretical $2p_{1/2}/2p_{3/2}$ emission.

72 L. Wang, S. Chen, D. Qi, X. Gao and A. T. S. Wee, *Surf. Sci.*, 2007, **601**, 4212.

PCCP

PAPER

View Article Online
View Journal | View Issue

Cite this: *Phys. Chem. Chem. Phys.*, 2016, **18**, 24890

Electronic structure of CuTPP and CuTPP(F) complexes: a combined experimental and theoretical study II†

Giulia Mangione,[a] Mauro Sambi,[a] Silvia Carlotto,[a] Andrea Vittadini,[b] Giovanni Ligorio,[c] Melanie Timpel,[cd] Luca Pasquali,[efg] Angelo Giglia,[fh] Marco Vittorio Nardi[cd] and Maurizio Casarin*[ab]

Received 7th June 2016,
Accepted 29th June 2016

DOI: 10.1039/c6cp03956a

www.rsc.org/pccp

The unoccupied electronic structure of thick films of tetraphenylporphyrin and tetrakis(pentafluorophenyl)-porphyrin Cu(II) complexes (hereafter, CuTPP and CuTPP(F)) deposited on Au(111) has been studied by combining the outcomes of near-edge X-ray absorption fine structure (NEXAFS) spectroscopy with those of spin-unrestricted time-dependent density functional (TD-DFT) calculations carried out either within the scalar relativistic zeroth order regular approximation (ZORA) framework (C, N and F K-edges) or by using the Tamm–Dancoff approximation coupled to ZORA and including spin–orbit effects (Cu $L_{2,3}$-edges). Similarly to the modelling of NEXAFS outcomes pertaining to other Cu(II) complexes, the agreement between theory and experiment is more than satisfactory, thus confirming the open-shell TD-DFT to be a useful tool to look into NEXAFS results pertinent to Cu(II) compounds. The combined effect of metalation and phenyl (Ph) fluorine decoration is found to favour an extensive mixing between $^{Ph}\sigma^*$ and pristine porphyrin macrocyle (pmc) $^{pmc}\pi^*$ virtual levels. The lowest lying excitation in the C and N K-edge spectra of both CuTPP and CuTPP(F) is associated with a ligand-to-metal-charge-transfer transition, unambiguously revealed in the ^{CuTPP}N K-edge spectral pattern. Moreover, the comparison with literature data pertaining to the modelling of the $^{Cu(II)}L_{2,3}$ features in the phthalocyanine–Cu(II) (CuPc) complex provided further insights into how metal-to-ligand-charge-transfer transitions associated with excitations from $2p^{Cu(II)}$ AOs to low-lying, ligand-based π^* MOs may contribute to the Cu(II) $L_{2,3}$-edge intensity and thus weaken its believed relationship with the Cu(II)–ligand symmetry-restricted covalency. Despite the coordinative pocket of CuTPP/CuTPP(F) mirroring CuPc, the ligand-field strength exerted by the phthalocyanine ligand on the Cu(II) centre is experimentally found and theoretically confirmed to be slightly stronger than that experienced by Cu in CuTPP and CuTPP(F). On the whole, the obtained results complement those published in the near past by the same group on the occupied and empty states of the H_2TPP and H_2TPP(F) free ligands as well as on the occupied states of both CuTPP and CuTPP(F), thus providing the final piece to get a thorough description of electronic perturbations associated with the metalation and the Ph halogen decoration of H_2TPP.

1. Introduction

π-Conjugated organic molecules are well-known semiconducting materials, extensively used for thin film electronic and optoelectronic devices by exploiting their p-type carrier transport. Among them, porphyrins and their derivatives have been the subject of several investigations devoted to the study of their electronic and optical properties, which can be additionally tuned and enhanced through molecular engineering.[1–4] In fact, their pliable aromatic structure makes this class of molecules attractive for use in electronics,[5]

[a] *Dipartimento di Scienze Chimiche, Università degli Studi di Padova, via F. Marzolo 1, 35131 Padova, Italy. E-mail: maurizio.casarin@unipd.it*
[b] *Istituto di Chimica della Materia Condensata e di Tecnologie per l'Energia – ICMATE, via F. Marzolo 1, 35131 Padova, Italy*
[c] *Institute for Physics, Supramolecular Systems Division "SMS" Humboldt Universität zu Berlin, Brook-Taylor-Straße 6, 12489 Berlin, Germany*
[d] *Istituto dei Materiali per l'Elettronica ed il Magnetismo, IMEM-CNR, Sezione di Trento, via alla Cascata 56/C, Povo, 38100 Trento, Italy*
[e] *Dipartimento di Ingegneria "E. Ferrari", Università degli Studi di Modena e Reggio Emilia, via Vignolese 905, 41125 Modena, Italy*
[f] *Istituto Officina dei Materiali, IOM-CNR, Area Science Park, SS. 14 Km 163.5, 34149 Basovizza, Trieste, Italy*
[g] *Department of Physics, University of Johannesburg, PO Box 524, Auckland Park 2006, South Africa*
[h] *Istituto di Struttura della Materia, ISM-CNR, Area Science Park, SS. 14 Km 163.5, 34149 Basovizza, Trieste, Italy*

† Electronic supplementary information (ESI) available: Energy-ordered linear combinations of heavy atom 1s AOs; Γ_{XS} representation products corresponding to electric dipole allowed transitions in D_{4h} symmetry; excitation energies and oscillator strengths *f* of the C and N (C, N and F) 1s excitation spectra of CuTPP (CuTPP(F)) from spin-unrestricted SR-ZORA TD-DFT calculations; and a 3D plot of the $25e_g$ MO. See DOI: 10.1039/c6cp03956a

solar cells,[6] biomedicine,[7] and sensing,[8] thus actually pushing towards the realization of a promising new generation of solid state devices. A great deal of theoretical and experimental studies have been so far performed on free base porphyrins[9–13] as well as on molecules characterized by the presence of a metal centre,[14–18] also in the case of the *in vacuo* synthesis of metal-porphyrins with the generation of exotic complexes useful for applications in electronics and optoelectronics.[19,20] Moreover, the modification of the electronic transport properties from p- to n-type through the substitution of hydrogen-terminated species with halogen species such as fluorine[11b,c,18c] is an intriguing opportunity, impelling research activity towards the synthesis of organic systems showing both electron acceptor and donor characteristics and smoothening the path for the creation of a p–n junction fully based on organic materials. In this regard, it is noteworthy that modified π-conjugated molecules, such as porphyrins,[21–27] phthalocyanines and pentacenes,[28] have been studied for application in a new class of dye-sensitized photovoltaic cells,[29] sensing devices with improved sensitivity and selectivity,[30,31] and high efficiency photosensitizers to be used in photodynamic therapy.[32,33] Overall, it is thus evident that a comprehension, as intimate as possible, of perturbations induced in the electronic structure of free base porphyrins by metalation and halogen decoration is mandatory and, to this end, the results of an experimental and theoretical study devoted to the investigation of the unoccupied electronic structure of thick films of tetraphenylporphyrin and tetrakis(pentafluorophenyl)porphyrin–Cu(II) complexes (hereafter, CuTPP and CuTPP(F), respectively) are presented and discussed herein. By the way, this study complements the experimental and theoretical outcomes recently published by some of us about the occupied electronic structure ($1s^{C/N/F}$ and $2p^{Cu}$ core levels and valence band states) of CuTPP and CuTPP(F) thin layers.[18c]

Molecular thick films of title molecules grown on Au(111) have been probed by using near-edge X-ray absorption fine structure (NEXAFS)[34,35] spectroscopy to elucidate the nature, the localization and the relative energy positions of their low lying unoccupied molecular orbitals (MOs). In fact, the sensitivity of K- and L-edge spectra[36] to both the electronic structure and the local surroundings of the absorbing species makes NEXAFS spectroscopy solidly accepted as a site-sensitive probe of empty states. Moreover, agreeing with a well-established procedure,[11,18c,37] NEXAFS spectra collected from deposits of randomly oriented and weakly interacting molecules at the C, N, and F K-edges as well as at the Cu $L_{2,3}$-edges[36] have been rationalized by referring to the results of time dependent density functional (TD-DFT) calculations carried out on isolated molecules and by adopting the Amsterdam Density Functional (ADF) suite of programs (version 2014.01).[38]

2. Experimental and computational details

Experimental details

A thorough description of CuTPP(F) synthesis has been reported elsewhere.[18c] CuTPP and CuTPP(F) thick films have been grown onto an Au(111) single crystal surface, previously cleaned by repeated Ar^+ ion sputtering and annealing cycles (up to 550 °C). The absence of surface contamination (C, N, F, O, Cu) has been checked by means of X-ray photoelectron spectroscopy (XPS). CuTPP (purchased from Sigma-Aldrich) and CuTPP(F) (synthesized and purified in our laboratory)[18c] have been deposited in the preparation chamber (during evaporation, pressure $< 5 \times 10^{-8}$ mbar) *via* sublimation from a resistively heated pinhole source onto the Au(111) single crystal surface. The molecular layer mass-thickness has been monitored by a quartz crystal microbalance. The evaporation rate of both CuTPP and CuTPP(F) was approximately 0.1 Å s^{-1} (bulk density assumed to be 1.6 g cm^{-3}). The final thickness of both molecular films on Au(111) has been estimated to be ~50 nm; *i.e.*, thick enough to exclude any contribution from the Au substrate in the photoelectron spectra, contemporarily avoiding charging effects in the films. After the film deposition, the samples have been transferred into the analysis chamber for NEXAFS analyses. NEXAFS spectra have been recorded at the BEAR end station of the ELETTRA synchrotron facility in Trieste (Italy).[39] The spectra have been collected in total electron yield (TEY) mode (*i.e.*, drain current mode) at the C, N, and F K-edges as well as at the Cu $L_{2,3}$-edges,[36] and normalized to the incident photon flux and to the clean substrate signal. Spectral energies have been calibrated by referring to the $4f_{7/2}$ Au core level, which has been obtained from an Au(100) sputtered sample. The synchrotron beam was elliptically polarized with the dominating components lying in the horizontal (H) plane, and the corresponding ellipticity, defined as $\varepsilon = \left|\overrightarrow{E_V}\right|^2 \Big/ \left|\overrightarrow{E_H}\right|^2$, equal to 0.1 (V/H stands for the vertical/horizontal plane and ε = 1(0) for circularly (linearly) polarized light). Throughout the measurements, the incident angle of light with respect to the sample surface plane has been kept fixed at 54.7°. To correctly process the acquired data, each absorption spectrum has been first normalized to the drain current, which has been measured on an optical element (refocusing mirror) placed along the beam-line, and then normalized to the absorption spectrum attained under the same experimental conditions and energy range, on an Au(100) sputtered sample. The energy scale of each single spectrum has been re-calibrated taking into account the energy fluctuations of characteristic absorption features measured on the refocusing mirror.

Computational details

Multilayers of CuTPP and CuTPP(F) molecules randomly oriented and weakly interacting have been modelled by adopting the single molecule approach.[11,18c,37] Numerical experiments, carried out by using the ADF code,[38] have been run by assuming an idealized D_{4h} symmetry with phenyl groups perpendicular to the pristine porphyrin macrocycle (pmc) and by employing the structural parameters optimized in ref. 18c.[40] NEXAFS spectra at the C, N, and F K-edges in terms of their oscillator strength (f) distributions have been simulated by running spin-unrestricted scalar relativistic (SR) zeroth-order regular approximation (ZORA) TD-DFT calculations[41] suitably tailored to treat core electron excitations.[42] All-electron quadruple-ζ plus four polarization function (QZ4P) basis sets have been adopted for all the atoms.[43]

Moreover, QZ4P ZORA basis sets of symmetry-related atoms involved in the excitation processes have been extended with two further shells of diffuse functions by following the even tempered criterion. In fact, it is well known[41d,42] that this kind of function is needed to properly describe transitions toward high energy virtual orbitals and Rydberg states. The adiabatic local density approximation[44] has been employed to approximate the exchange correlation (XC) kernel, while the LB94 functional[45] has been used to approximate the XC potential in the self-consistent field calculations. Scaled ZORA orbital energies[46] instead of the ZORA orbital energies in the TD-DFT equations have been employed to improve deep core excitation energies (EEs). As far as the modelling of NEXAFS spectra at the Cu $L_{2,3}$-edges is concerned, TD-DFT ZORA calculations including spin–orbit (SO) effects, within the Tamm–Dancoff approximation (TDA),[47] have been run by adopting a QZ4P ZORA basis set for all the atoms.[43] Although the energy difference between the Cu $2p_{3/2}$ and $2p_{1/2}$ spinors should be large enough (*ca.* 20 eV) to avoid any coupling with each other in transitions starting from them,[18a,b,37] the whole Cu $2p_{3/2}/2p_{1/2}$ set was considered as the initial state.

Before moving to the next section, a few words about the evaluation of CuTPP/CuTPP(F) EEs are needed. Wang and Ziegler[48] have shown that spin-unrestricted TD-DFT calculations are able to provide a quite accurate estimate of EEs even in the case of open shell molecules.[49] CuTPP and CuTPP(F) ground states (GSs) are both characterized by the presence of a single hole in a Cu 3d-based orbital (the $x^2 - y^2$ one in the adopted framework), thus resulting in a doublet state. Core electron excitations imply either transition to this singly occupied MO (SOMO)[50] or transitions to completely unoccupied MOs. In the former case, both GS and excited states correspond to doublet states, if spin contamination is neglected, while two doublet states and one quartet state may be generated in the latter. Doublet → quartet excitations, implying spin–flip or double excitation processes, will be ignored herein and, similarly to our study on the occupied and unoccupied electronic structures of the phthalocyanine–Cu(II) complex (hereafter, CuPc),[37] C, N and F K-edge NEXAFS spectra will be assigned by limiting our attention to doublet → doublet excitations.

To favour the understanding of theoretical outcomes, title molecule eigenvalues have been graphically represented as density of states (DOS) by applying a 0.25 eV Lorentzian broadening factor. These plots, based on the Mulliken's prescription for partitioning the overlap density,[51] allow an easy inspection of the atomic composition of MOs over a broad range of energies. Partial density of states (PDOS) is:

$$\mathrm{PDOS}^{\nu}_{n\ell}(\varepsilon) = \sum_{p} \frac{\gamma}{\pi} \frac{f^{\nu}_{n\ell,p}}{\left(\varepsilon - \varepsilon_p\right)^2 + \gamma^2} \qquad (1)$$

while

$$\mathrm{DOS}(\varepsilon) = \sum_{\nu,n,\ell} \mathrm{PDOS}^{\nu}_{n\ell}(\varepsilon) = \sum_{p} \frac{\gamma}{\pi} \frac{g_p}{\left(\varepsilon - \varepsilon_p\right)^2 + \gamma^2} \qquad (2)$$

where γ is the Lorentzian broadening factor and $f^{\nu}_{n\ell,p}$ is the Mulliken's population contribution from atom ν, state $(n\ell)$ to the pth MO of energy ε_p and degeneracy g_p. We are perfectly aware that the Mulliken's prescription for partitioning the overlap density, even though uniquely defined, is rather arbitrary; nevertheless, it yields at least a qualitative idea of the electron localization. Finally, 3D contour plots have been obtained to get information about the localization and the bonding/antibonding character of selected MOs.

3. Results and discussion

Porphyrins are heterocyclic organic molecules constituted by four pyrrole subunits bonded through four methine bridges ($C^5/C^{10}/C^{15}/C^{20}$, collectively tagged as C^m in Fig. 1, where the recommended IUPAC numbering system has been adopted)[52] at their carbon atoms in the α-positions.

Despite the symmetry of CuTPP and CuTPP(F) complexes (D_{4h}) being higher than that of the H_2TPP and H_2TPP(F) free ligands (D_{2h}), many corresponding sets of atoms in metalated and pristine molecules may still be recognized: besides the central Cu(II) ion, (i) four equivalent pyrrolic nitrogen atoms ($N^{21}/N^{22}/N^{23}/N^{24}$), (ii) two different sets of carbon atoms occupying the so-called α ($C^1/C^4/C^6/C^9/C^{11}/C^{14}/C^{16}/C^{19}$) and β ($C^2/C^3/C^7/C^8/C^{12}/C^{13}/C^{17}/C^{18}$) positions with respect to N and collectively tagged as C^{Py}; (iii) the already mentioned C^m carbon atoms; and (iv) twenty-four Ph carbon atoms (C^{Ph}). Moreover, CuTPP(F) includes twenty fluorine atoms bonded to as many C^{Ph}.

It is well known that the ligand (L) donor atom K-edge NEXAFS spectra of transition metal (M) complexes with partly filled *n*d atomic orbitals (AOs) are usually characterized by quite intense pre-edge features[53] generated by the electric dipole allowed 1s → *m*p transitions whose intensity quantifies the amount of the L donor atom *m*p character in the unoccupied valence MOs. NEXAFS spectroscopy at the K-edge of L donor atoms thus provides a direct probe of the M–L symmetry restricted covalency.[54–56] This may be eventually complemented with the M $L_{2,3}$-edge NEXAFS outcomes associated with the electric dipole allowed 2p → *n*d transitions, which provide further information about the M *n*d participation in the unoccupied orbitals in

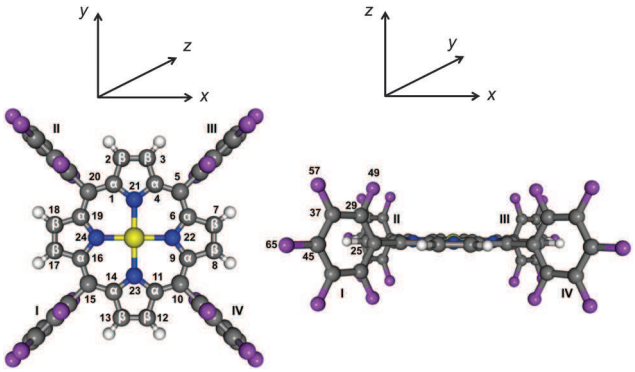

Fig. 1 Schematic plot of top and side views of CuTPP and CuTPP(F). The atom numbering corresponds to the one recommended by the IUPAC[52] and adopted by Nardi *et al.* in ref. 11, 18c and 37. In the selected framework, the pmc is coincident with the σ_h plane. Yellow and purple spheres correspond to Cu and H/F atoms in CuTPP and CuTPP(F), respectively.

the ligand-field manifold.[58] Despite $^{M}L_{2,3}$-edge XAS spectra of M complexes containing a huge amount of chemical information, one has to be well aware that a stiff theoretical analysis is needed to extract it. In fact, besides ligand-field and M–L covalency effects, the SO coupling between the possibly many final-state multiplets has to be considered.[59–62] As such, Cu(II) complexes correspond to the simplest possible case because, in a simplified one-electron picture, electric dipole allowed $2p^{Cu(II)} \rightarrow 3d^{Cu(II)}$ transitions generate a $2p^5 3d^{10}$ configuration, which has only two term symbols, and the corresponding spectral splitting is dominated by the 2p SO coupling contribution and the overall energetics and intensities are strongly influenced by ligand-field and covalency, respectively.[62d] In more detail, the intensity of the $2p^{Cu(II)} \rightarrow 3d^{Cu(II)}$ peak provides an estimate of the $3d^{Cu(II)}$ AO participation (the higher the intensity, the lower the L contribution and, accordingly, the M–L covalent character) to the single Cu(II)-based unoccupied spin orbital.[50,58] Even more specifically, taking the square planar $[CuCl_4]^{2-}$ molecular ion as a reference, Solomon and co-workers[58,63] proposed the use of the normalized intensities and relative positions of the Cu(II) $L_{2,3}$ features in different Cu(II) complexes as a gauge of the degree of Cu(II)–L covalency and of the ligand-field strength, respectively.[64]

Now, besides the general interest in as detailed a description as possible of the Cu–N interaction in title molecules,[18c] a further aim of the present contribution is to look for eventual differences distinguishing the Cu–N bonding in CuTPP/CuTPP(F) and CuPc, all of them sharing the same coordinative pocket.[65] To this end CuTPP/CuTPP(F) NEXAFS spectra at the $^{C/N/F}$K-edges and at the $^{Cu}L_{2,3}$-edges and their TD-DFT simulations in terms of *f* distributions will be exploited. Nevertheless, before tackling the assignment of CuTPP/CuTPP(F) NEXAFS spectra, a series of preliminary considerations about (i) the symmetry properties of linear combinations of $1s^{C/N/F}$ AOs (possible initial spin orbitals – isos – of K-edge NEXAFS transitions), (ii) the nature, the localization and the relative positions of CuTPP/CuTPP(F) unoccupied frontier[68] orbitals (possible final spin orbitals – fsos – in X-ray absorption processes), and (iii) the selection rules governing CuTPP/CuTPP(F) NEXAFS transitions, may be useful to easily follow the forthcoming discussion.

Among CuTPP and CuTPP(F) heavy atoms (C, N, F and Cu), the pmc ones lie in the σ_h plane, while C^{Ph} and F species may be either parallel ($\parallel$) or perpendicular ($\perp$) to σ_h. According to that, C^{25}, C^{45}, F^{65} and symmetry related atoms (see Fig. 1) are collectively tagged $C^{Ph}_{\parallel}$ and $F_{\parallel}$, while C^{29}, C^{37}, F^{49}, F^{57} and symmetry related atoms are labelled $C^{Ph}_{\perp}$ and $F_{\perp}$. Linear combinations of C, N and F 1s AOs span the following irreducible representations (IRs) of the D_{4h} symmetry point group:[69,70] $a_{1g} + b_{1g} + e_u$ (N); $a_{1g} + b_{2g} + e_u$ (C^m, $C^{Ph}_{\parallel}$, $F_{\parallel}$); $a_{1g} + a_{2g} + b_{1g} + b_{2g} + 2e_u$ (C^{Py}); $a_{1g} + b_{2g} + e_g + a_{2u} + b_{1u} + e_u$ ($C^{Ph}_{\perp}$ and $F_{\perp}$). As far as CuTPP and CuTPP(F) unoccupied spin orbitals are concerned, valuable information about them may be gained by looking at the C, N, F and Cu PDOSs of title molecules displayed in Fig. 2 where the lowest lying peaks associated with the empty levels are alphabetically labelled.

Similarly to the H_2TPP and H_2TPP(F) free ligands,[11a–c] the L peak in Fig. 2 is generated by 2p AOs of pmc atoms, while major contributions to the higher lying features M and N come from

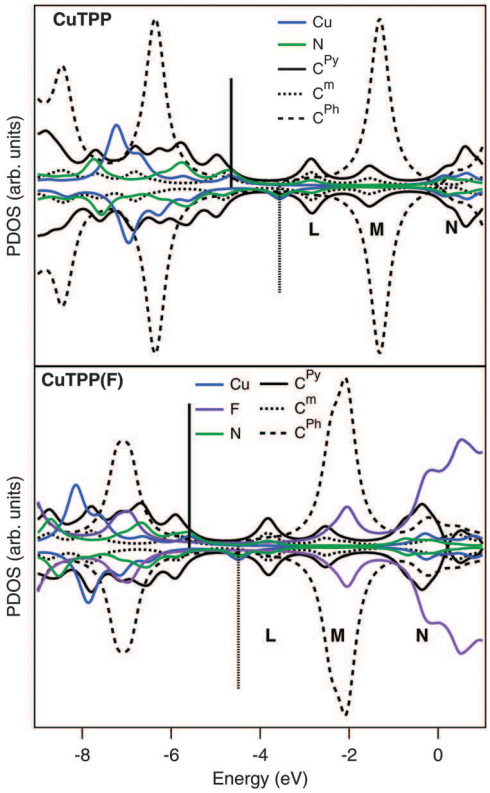

Fig. 2 CuTPP and CuTPP(F) PDOSs. Vertical bars represent the highest occupied MO (HOMO, full line)[50] and the lowest unoccupied MO (LUMO, dotted line) energies. Positive (negative) values refer to the spin ↓ (↑) PDOS.

C^{Ph} (CuTPP) and C^{Ph}/F (CuTPP(F)) 2p AOs (M) and H 1s AOs (N). More specifically, only the pmc based $\pi_\perp$* $13e_g$ ($22e_g$) MO (see Fig. 3) contribute to L in CuTPP (CuTPP(F)),[71–73] while at least nine (thirteen) MOs participate in the generation of M in CuTPP (CuTPP(F)).[74] Furthermore, among the MOs generating M, only one $\pi_\perp$* orbital, the $9b_{1u}$ and the $16b_{1u}$ MO in CuTPP in CuTPP(F), respectively, is present (see Fig. 3).

The square planar arrangement of the Cu(II) ion in both CuTPP and CuTPP(F) lifts the five-fold degeneracy of the Cu 3d AOs to generate four low-lying, completely occupied, MOs of symmetry a_{1g}, b_{2g}, and e_g as well as the b_{1g} SOMO. The Cu–N

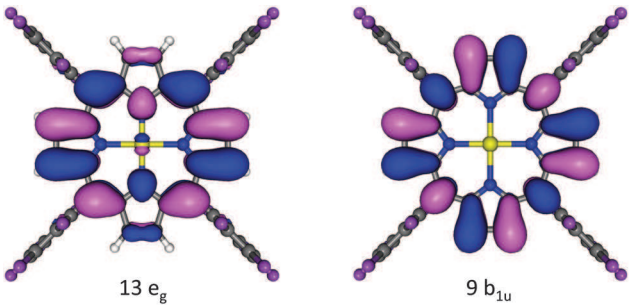

Fig. 3 (left) 3D plots of one partner of the CuTPP pmc based $\pi_\perp$* $13e_g$ (↑) MO; (right) 3D plots of the CuTPP pmc based $\pi_\perp$* $9b_{1u}$ (↑) MO. Displayed isosurfaces correspond to ± 0.02 $e^{1/2}$ Å$^{-3/2}$ values. The corresponding MOs in CuTPP(F) ($22e_g$ and $16b_{1u}$) are indistinguishable from those depicted herein.

interactions involving the Cu 3d-based a_{1g} (z^2), b_{1g} ($x^2 - y^2$), and b_{2g} (xy) AOs have a σ character, while those implying the e_g (xz, yz) AOs are of π nature. Besides the σ character and a high localization on the Cu(II) central ion, a Cu–N antibonding nature may also be foreseen for the b_{1g} SOMO.[37,49,50] According to that, CuTPP and CuTPP(F) GSs will transform into the b_{1g} IR, and the allowed electric dipole transitions will then imply[70]

$$\Gamma_{GS} \otimes \Gamma_{\mu} \otimes \Gamma_{XS} \supset a_{1g} \quad (3)$$

where Γ_{GS}, Γ_{μ} and Γ_{XS} correspond to the IRs of the GS (b_{1g}), the dipole moment operator (a_{2u} + e_u) and the electronic excited states ($\Gamma_{iso} \otimes b_{1g} \otimes \Gamma_{fso}$), respectively. Eqn (3) may then evolve to

$$b_{1g} \otimes a_{2u} \otimes \Gamma_{iso} \otimes b_{1g} \otimes \Gamma_{fso} = a_{2u} \otimes \Gamma_{iso} \otimes \Gamma_{fso} \supset a_{1g} \quad (4a)$$

$$b_{1g} \otimes e_u \otimes \Gamma_{iso} \otimes b_{1g} \otimes \Gamma_{fso} = e_u \otimes \Gamma_{iso} \otimes \Gamma_{fso} \supset a_{1g} \quad (4b)$$

thus pointing out that, within the approximation, which reduces the complete one-electron excited configuration space (1h–1p space) to the subspace where only the core electrons are excited, the allowed electric dipole transitions imply

$$\Gamma_{iso} \otimes \Gamma_{fso} = a_{2u} \quad (5a)$$

$$\Gamma_{iso} \otimes \Gamma_{fso} = e_u \quad (5b)$$

It has been already stressed that, besides the Cu(II) based b_{1g} SOMO,[50] low-lying π* MOs include the pmc-based $\pi_{\perp}$* e_g and b_{1u} orbitals[71,74] as well as the linear combinations of the Ph-based e_{2u} $\pi_{\parallel}$* levels, transforming into a_{2g}, b_{1g}, e_g, a_{1u}, b_{2u}, and e_u IRs in D_{4h}.[74] The site-sensitive nature of NEXAFS spectroscopy combined with eqn (5) and the results reported in Table S1 of the ESI,† allows us to foresee transitions, which should have significant f values (see Tables S2a and b of the ESI†), as well as their symmetry.[75]

Similarly to the H_2TPP and $H_2TPP(F)$ free ligands,[11c] CuTPP and CuTPP(F) C-based 1s → π* excitations may be split into two sets, the former including transitions of a_{2u} symmetry (hereafter, $\Pi_{\perp}$), the latter including e_u transitions (hereafter, $\Pi_{\parallel}$). $\Pi_{\perp}$ can be further split into two subsets, the former including transitions from C^{pmc} 1s-based isos (see Table S1, ESI;† hereafter, $^{pmc}\Pi_{\perp}$), the latter encompassing transitions from C^{Ph} 1s-based isos (hereafter, $^{Ph}\Pi_{\perp}$). Incidentally, $^{pmc}\Pi_{\perp}$ transitions are completely localized on the pmc and have been used in ref. 11c as an internal gauge of the fluorination effects on the H_2TPP electronic structure upon the H_2TPP → $H_2TPP(F)$ switching. The forthcoming assignment of the CuTPP and CuTPP(F) C, N and F K-edge spectral features will then be pursued by adopting the following strategy: starting from data pertinent to the free ligands and looking, with the help of spin-unrestricted SR-ZORA TD-DFT outcomes, at the eventual differences associated with the metalation and the concomitant increase in symmetry.

C K-edge spectra

The extended C K-edge NEXAFS spectra of CuTPP and CuTPP(F) are displayed in Fig. 4,[76] while their fitted [i] regions are reported in Fig. 5 (EE positions of fitting components are reported in Table 1).

Likewise H_2TPP[11c] and *trans*-$H_2TPP(NH_2)_2$,[78] the CuTPP EE region up to 290 eV is characterized by the presence of four main features (labelled with capital bold letters both in Fig. 4 and 5), which cover an energy range of ∼5 eV (see the fitted spectrum in the left upper panel of Fig. 5 and data reported in Table 1) and needed at least nine components to be properly fitted.

Moreover, perturbations upon fluorination in the CuTPP/CuTPP(F) pair appear quite similar to those revealed for the $H_2TPP/H_2TPP(F)$ one (see Fig. 5, where the C K-edge NEXAFS spectra of H_2TPP and $H_2TPP(F)$ are also included for comparison):[11c] an impressive intensity decrease (increase) of the B (C) feature, accompanied by a moderate shift toward higher EEs of the D peak and a substantial unresponsiveness of the lowest lying band A. Despite these similarities, the H_2TPP/CuTPP and $H_2TPP(F)$/CuTPP(F) spectral details are quite different. In particular, upon H_2TPP metalation: (i) no shoulder seems to be present any more on the lower EE side of the band A; (ii) band B is

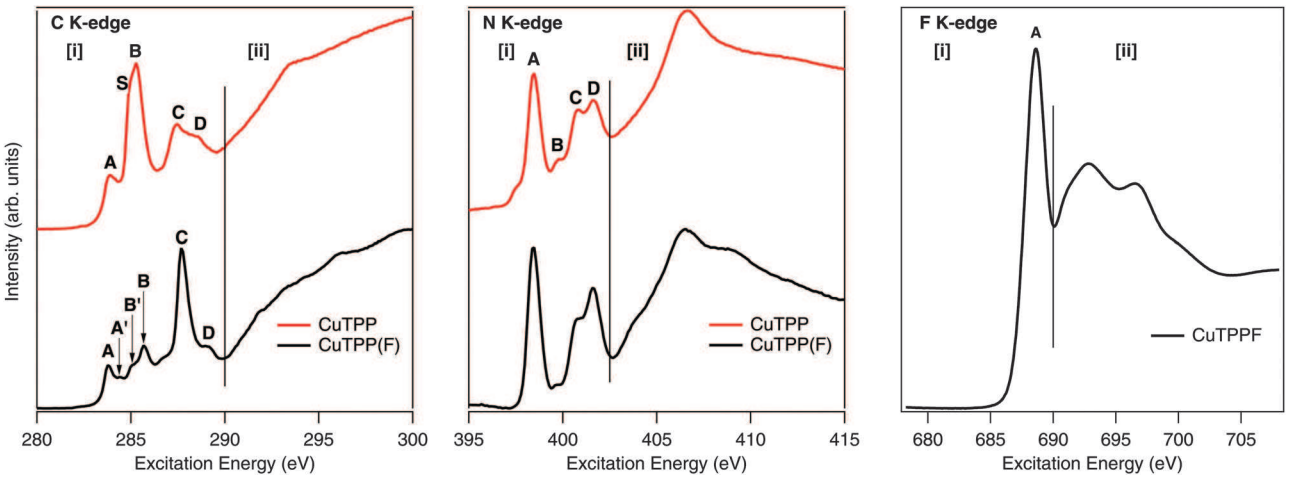

Fig. 4 Extended NEXAFS spectra of thick films of CuTPP (red line) and CuTPP(F) (black line) deposited on Au(111). Vertical lines at 290 eV (left), 402 eV (middle) and 691 eV (right) separate [i] and [ii] regions.[76]

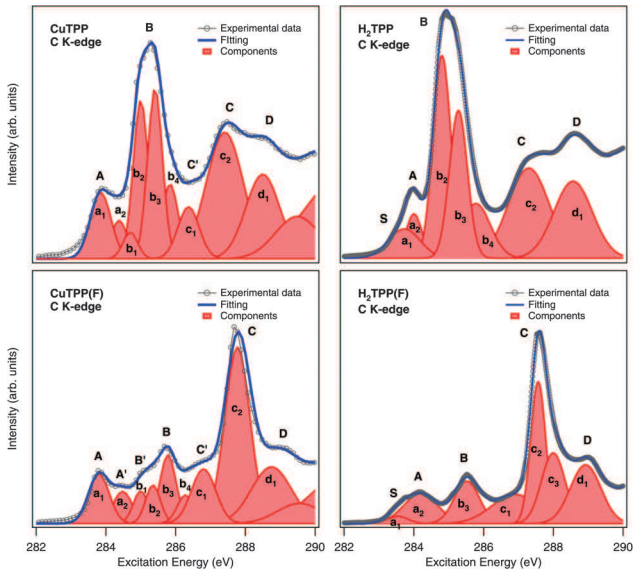

Fig. 5 Fitted [i] region of the C K-edge NEXAFS spectra of CuTPP (left upper panel) and CuTPP(F) (left lower panel). The fitted [i] region of the C K-edge NEXAFS spectra of H_2TPP (right upper panel)[11c] and $H_2TPP(F)$ (right lower panel)[11c] is also displayed for comparison. H_2TPP and $H_2TPP(F)$ fitting components have been labelled differently from ref. 11*a* and *c* to favour the comparison with CuTPP and CuTPP(F).

Table 1 Excitation energy position (eV) of C K-edge transitions (components a–d) for the fit of CuTPP and CuTPP(F) thick film spectra reported in Fig. 5. ΔEE between similar features for CuTPP and CuTPP(F) are also reported. Values pertaining to the free ligands are also reported in parentheses

	CuTPP (H_2TPP)	ΔEE	CuTPP(F) ($H_2TPP(F)$)	ΔEE
a_1	283.88 (283.72)	—	283.77 (283.53)	—
a_2	284.38 (284.00)	0.50 (0.28)	284.48 (284.19)	0.71 (0.66)
b_1	284.68	0.83	284.98	1.21
b_2	284.98 (284.81)	1.10 (1.09)	285.38	1.61
b_3	285.38 (285.28)	1.50 (1.56)	285.77 (285.53)	2.00 (2.00)
b_4	285.88 (285.78)	2.00 (2.06)	286.27	2.50
c_1	286.38	2.50	286.77 (286.90)	3.00 (3.37)
c_2	287.38 (287.30)	3.50 (3.58)	287.77 (287.57)	4.00 (4.04)
c_3			(288.00)	(4.47)
d_1	288.48 (288.57)	4.60 (4.85)	288.77 (288.93)	5.00 (5.40)

still asymmetric, but the highest intensity component lies at higher, rather than lower, EEs; and (iii) the poorly resolved feature D appears definitely less intense than C. Moving to $H_2TPP(F)$/CuTPP(F) differences: (i) again, no shoulder seems to be present on the lower EE side of A; (ii) two tiny features, labelled A′ and B′ in the left lower panel of Fig. 5, are well evident on the higher EE side of A and on the lower EE side of B; and (iii) the shoulder on the lower EE side of C (S) is much more evident in CuTPP(F) than in $H_2TPP(F)$.

In ref. 18*c* all the carbon species contributing to the CuTPP and CuTPP(F) $1s^C$ spectra have been identified. More specifically, the combined use of XPS and spin-unrestricted SR-ZORA DFT calculations allowed us to state the relative energy order of each single component associated with the emission from C^{pmc} and C^{Ph} 1s-based MOs (see Fig. 7 of ref. 18*c*). Moreover, similarly to H_2TPP and $H_2TPP(F)$,[11a,b] it has been revealed that the Ph ring fluorination is accompanied by a significant blue-shift of the C^{Ph} 1s core levels, while the C^{pmc} chemical species show less relevant differences upon CuTPP → CuTPP(F) switching. A preliminary, tentative assignment of the C K-edge spectra of CuTPP and CuTPP(F) may be then endeavoured by assuming that $^{pmc}\Pi_\perp$ transitions should have, like the free ligands, similar EEs in CuTPP and CuTPP(F), while the $\Pi_\parallel$ and, to a minor extent, the $^{Ph}\Pi_\perp$ ones should be blue shifted upon Ph fluorination. Accordingly, major contributions to the lowest lying NEXAFS spectral features of CuTPP and CuTPP(F) (the band A in CuTPP; the band envelope A + A′ in CuTPP(F)) should come from excitations (see Tables S1 and S2 of the ESI†) associated with $^{pmc}\Pi_\perp$ transitions and implying the excitation from the e_u linear combinations of C^m-/C^{Py}-based 1s AOs to the CuTPP (CuTPP(F)) $13e_g$ ($22e_g$) $^{pmc}\pi_\perp^*$ LUMO.[71–73] As such, it can be useful to remind that the S + A features of the H_2TPP and $H_2TPP(F)$ NEXAFS spectra (see the right panels of Fig. 5 and the EEs of the a_1 and a_2 components in Table 1) have been assigned to the seven lowest lying excitations, all of them corresponding to $\Pi_\perp$ transitions. Relative intensity variations of bands B and C when moving from CuTPP to CuTPP(F) (see the left panels of Fig. 5) ultimately state that major contributions to the intensity of the CuTPP band B and of the CuTPP(F) band C come from $\Pi_\parallel$ and $^{Ph}\Pi_\perp$.

Now, before tackling the detailed assignment of the CuTPP and CuTPP(F) C K-edge NEXAFS spectra, two further things deserve to be underlined: (i) the number of $1s^C$-based possible isos is rather large (twice the number of molecular skeleton C atoms,[44] see Fig. 1 and Table S1 of the ESI†) and (ii) the energy range covered by the linear combinations of the $1s^C$-based possible isos is narrower in CuTPP (1.0 eV) than in H_2TPP (1.6 eV), while it is very similar in CuTPP(F) and $H_2TPP(F)$ (3.5 and 3.6 eV, respectively). The highest lying NEXAFS features of the CuTPP(F) EE region [i] might then include contributions not only from 1s → π* but also from 1s → σ* excitations, the former (latter) having the $1s^C$-based linear combinations characterized by the highest (lowest) binding energies as isos.

EEs and *f* values pertaining to the CuTPP and CuTPP(F) $1s^C$ excitation spectra as obtained from spin-unrestricted SR-ZORA TD-DFT[41] calculations are reported in Tables S3 and S4 of the ESI,† respectively, while the corresponding f^C distributions in the EE range 280–291 eV are displayed in Fig. 6. The comparison between the CuTPP/CuTPP(F) NEXAFS patterns reported in Fig. 5 and the corresponding f^C distributions displayed in Fig. 6 confirms the well-known EE underestimation (~2 eV).[80] Moreover, even though the CuTPP/CuTPP(F) C PDOSs reported in Fig. 2 are certainly useful to foresee major contributions to the C K-edge NEXAFS features, spin-unrestricted SR-ZORA TD-DFT results are essential to look into their details.

With reference to data reported in Table S3 of the ESI,† and to the curves displayed in the left upper panel of Fig. 6, in agreement with our symmetry- and GS-based predictions, all but one of the C K-edge lower lying excitations hidden under the band A have to be assigned to $1s^C \rightarrow \pi_\perp^*$ transitions of a_{2u} symmetry; the exception is the $10e_u \rightarrow 12b_{1g}$ lowest-lying transition having a $C^{Py(\beta)}$ 1s → σ* character, an e_u symmetry and a

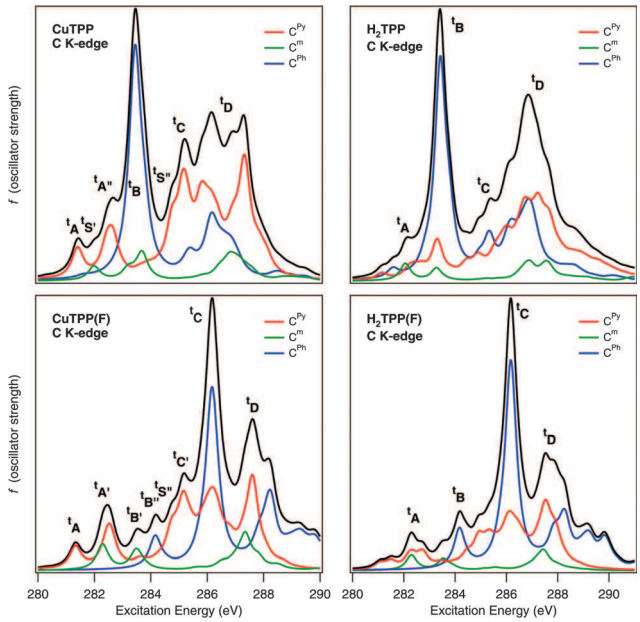

Fig. 6 Spin-unrestricted SR-ZORA TD-DFT $1s^C$ excitation spectra of CuTPP (left upper panel) and CuTPP(F) (left lower panel). Contributions from different isols[79] are also displayed. Convoluted profiles have been obtained by using a Lorentzian broadening of 0.25 eV. SR-ZORA TD-DFT $1s^C$ excitation spectra of H_2TPP (right upper panel)[11c] and H_2TPP(F) (right lower panel)[11c] are also displayed for comparison. SR-ZORA ionization limits may be deduced from the right panels of Fig. 7 of ref. 18c.

low f^C value (1.07×10^{-3}). In passing, the very weak $10e_u \rightarrow 12b_{1g}$ transition should lie on the lower EE side of the CuTPP A peak, ~1.1 eV apart the a_1 component, which includes, together with a_2 and b_1,[81] the five lowest lying a_{2u} transitions,[73] all of them $^{pmc}\Pi_\perp$. Similarly to the H_2TPP C K-edge spectrum, among the lowest lying transitions, two of them have the $9b_{1u}$ MO (the second lowest lying pmc-based $\pi_\perp$* orbital, see Fig. 3) as fso;[71–73] nevertheless, both transitions have a $^{pmc}\Pi_\perp$ nature (see in Table S3 of the ESI,† the isols[79] associated with the 5th and 6th excitations). Moreover, no $^{Ph}\Pi_\perp$ transition with $f^C \geq 10 \times 10^{-3}$ contributes to band A. On the whole, the assignment proposed herein for the CuTPP A feature agrees with the one suggested by Reid *et al.*,[82a] even though it is much more detailed than reported.

Consistent with the preliminary qualitative analysis of the CuTPP C K-edge spectral pattern, theoretical results state that major contributions to the intense spectral feature B are limited to $^{Ph}\Pi_\parallel$ e_u transitions (no $^{Ph}\Pi_\perp$ transition with $f^C \geq 10 \times 10^{-3}$ contributes to B), all of them characterized by quite large f^C values and whose fsos are all hidden under the peak M of the CuTPP PDOS (see Fig. 2).[74] Spin-unrestricted SR-ZORA TD-DFT outcomes prompt us to assign the components b_2 (b_4) of B to the excitation associated with $^{Ph}\Pi_\parallel$ transitions from $9e_u + 9a_{1g} + 6b_{2g}$ ($6e_u + 6a_{1g} + 3b_{2g}$) linear combinations of C^{45}-based (C^{25}-based) 1s AOs to the to $^2e_{2u}$-like $\pi_\parallel$* MOs,[74] while b_3 is associated with $^{Ph}\Pi_\parallel$ transitions from the b_{1u}/a_{2u} linear combinations of C^{29}-/C^{37}-based 1s AOs to the $^1e_{2u}$-like $\pi_\parallel$* 14 e_g MO (see Tables S1 and S3 of the ESI†).[74]

Despite the already mentioned EE underestimation, it is noteworthy that the ΔEE between the CuTPP b_4 and a_1 components (2.00 eV, see Table 1), very similar to the ΔEE between the same H_2TPP components (2.06 eV, see Table 1), is numerically reproduced by the ΔEE between ^{t}B and ^{t}A (2.04 eV). The results considered so far agree rather well with conclusions reported by Diller *et al.*[82b] about the close similarity between main transitions and fsos in H_2TPP and CuTPP; nevertheless, it has to be mentioned that spin-unrestricted SR-ZORA TD-DFT outcomes clearly indicate significant differences between them when isols[79] are considered (compare the left and right upper panels of Fig. 6).

Midway between bands B and C, an unresolved feature (labelled S in Fig. 5) at 286.4 eV is quite well evident in the CuTPP C K-edge NEXAFS spectrum. Spin-unrestricted SR-ZORA TD-DFT results (see Table S3 of the ESI†) prompt us to ascribe it to the $^{pmc}\Pi_\perp$ single excitation event $11e_u \rightarrow 15e_g$ (see in Fig. 6 the evident shoulder ^{t}S″ on the lower EE side of ^{t}C) at 284.75 eV. Parenthetically, the ΔEE between the CuTPP S and B spectral features (1.20 eV) is satisfactorily reproduced by theoretical calculations (1.32 eV).

Despite the application of a quite severe filtering to the excitation selection (only those with $f^C \geq 10 \times 10^{-3}$ have been included in Table S3 of the ESI†), a very large number of excitations contribute to bands C and D. Any attempt at providing them a detailed assignment would simply be a matter of taste. Nevertheless, even in such a disarming scenario, theoretical outcomes may be fruitfully exploited. Spin-unrestricted SR-ZORA TD-DFT results point out that: (i) all but one excitation significantly contributing to bands C and D have an a_{2u} symmetry (only the 22nd excitation included in Table S3 of the ESI† has an e_u symmetry); (ii) only one $^{Ph}\Pi_\perp$ transition (the 18th) contributes to the band envelope C + D; (iii) among excitations significantly contributing to bands C and D, only two of them (the 17th and the 22nd) have a 1s → σ* nature (both the 17th and the 22nd excitations have as isos linear combinations of C^{Ph}-based 1s AOs, see Table S3 of the ESI†); and (iv) main contributions to bands C and D come from C^{Py}-based isos, while the C^{Ph}-/C^m-based ones contribute to a minor extent (compare the left and the right upper panels of Fig. 6). On the whole, the above-mentioned similarity of main transitions and fsos in H_2TPP and CuTPP seems to be limited to the lower lying bands A and B because isos, fsos and the nature of excitations associated with the higher lying bands C and D are quite different in H_2TPP and CuTPP. As such, it has to be noted that neither Reid *et al.*[82a] nor Diller *et al.*[82b] provided any detailed assignment of the EE region covered by bands C and D in their contributions.

The marked differences characterizing the C K-edge NEXAFS spectra when moving from CuTPP to CuTPP(F) (compare the left upper and lower panels of Fig. 5) have been already stressed and, at a glance, they seem to be quite well reproduced by the spin-unrestricted SR-ZORA TD-DFT $^{CuTPP}f^C$ and $^{CuTPP(F)}f^C$ distributions (look at the left upper and lower panels of Fig. 6). Moreover, the comparison of data reported in Tables S3 and S4 of the ESI† indicates that $^{pmc}\Pi_\perp$ transitions can be straightforwardly identified. Interestingly, the lowest-lying $13e_u \rightarrow 15b_{1g}$ transition has the same EE of the CuTPP $10e_u \rightarrow 12b_{1g}$ one (280.26 *vs.* 280.28 eV, see Tables S3 and S4 of the ESI†),

the same $C^{Py(\beta)}$ 1s → σ* character, the same e_u symmetry and a very low f^C value (1.05×10^{-3}). Similar considerations hold for the a_{2u} transition no. 2, 3 and 4 whose isos and fsos are the same in CuTPP(F) and CuTPP and also their EEs are very similar, thus confirming what has been called by some of us in ref. 11*c* the electronic inertness of pristine pmc based $1s^C \rightarrow \pi_\perp^*$ transitions when comparing H_2TPP and H_2TPP(F) C K-edge NEXAFS spectra.

The cleaning up of the CuTPP(F) band envelope A + B from most of the $\Pi_\parallel$ contributions (no $^{Ph}\Pi_\perp$ transition contributes in CuTPP to the band envelope A + B) leaves a highly structured spectral pattern including several features (A + A′ + B′ + B in the left lower panel of Fig. 5). Spin-unrestricted SR-ZORA TD-DFT results allow us to assign with confidence the feature A to the lowest lying transition with an *f* value $\geq 10^{-3}$; *i.e.*, the $C^{Py(\beta)}$-based $14e_u \rightarrow 22e_g$ excitation. The poorly resolved band A′ and the lower EE side of the shoulder B′ (component b_1) are overall associated with the C^m-based $12e_u \rightarrow 22e_g$ and the $C^{Py(\alpha)}$-based $11e_u \rightarrow 22e_g$ excitations (see Table S4 of the ESI†), while the higher EE side of B′ (component b_2) and band B are ascribed as a whole to the closely spaced $C^{Py(\beta)}$- and C^m-based excitation no. 5–7. Interestingly, the analysis of corresponding fsols[79] reveals a quite extensive participation of Ph e_{2u}-based $\pi_\parallel^*$ orbitals limited, however, to the $^1e_{2u}$-based $6b_{2u}$ and $23e_g$ MOs.[74] As such, the Ph e_{2u}-based $\pi_\parallel^*$ orbitals opt-out both in the CuTPP and H_2TPP(F)[11c] $^{pmc}\Pi_\perp$ transitions clearly showing that not only the Ph fluorine decoration but also the H_2TPP(F) metalation favours this mixing. In addition to this, the involvement limited to the Ph $^1e_{2u}$-based $\pi_\parallel^*$ orbitals can be straightforwardly worked out by referring to eqn (5a) and to Table S1 of the ESI.† The Ph $^1e_{2u}$-based ($^2e_{2u}$-based) $\pi_\parallel^*$ orbitals transform into $a_{1u} + b_{2u} + e_g$ ($a_{2g} + b_{1g} + e_u$) IRs in both Cu(II) complexes; eqn (5a) is then fulfilled iff $\Gamma_{iso} = a_{2g}$, b_{1g} and e_u (a_{1u}, b_{2u} and e_g). The CuTPP/CuTPP(F) C^{pmc} 1s-based linear combinations are reported in Table S1 of the ESI,† and it is well evident that $^{pmc}\Pi_\perp$ transitions may have isos of symmetry a_{2g}, b_{1g} and e_u. The same thing does not hold when the Ph-based $^2e_{2u}$ $\pi_\parallel^*$ orbitals are considered; more specifically, no CuTPP/CuTPP(F) C^{pmc} 1s-based linear combination transforms into a_{1u}, b_{2u} or e_g.

As far as the b_4 component is concerned (see the left lower panel of Fig. 5), we propose to associate it with an e_u excitation having as isos all the linear combination of the C^{25}-based 1s AOs ($10a_{1g}$, $7b_{2g}$ and $9e_u$) and as fsos all the $^2e_{2u}$-like $\pi_\parallel^*$ MOs (excitation no. 8 in Table S4 of the ESI†).[74] Before going on, it deserves to be underlined that the CuTPP(F) ($EE_{b_4} - EE_{b_3}$) = 0.5 eV; *i.e.*, very close to the ΔEE between the 7th and the 8th excitations (0.65 eV). A further point has to be noticed. Linear combinations of C^{25} 1s-based AOs transform in CuTPP (CuTPP(F)) into $6a_{1g} + 3b_{2g} + 6e_u$ ($10a_{1g} + 7b_{2g} + 9e_u$) (see Table S1 of the ESI†). The estimate of the CuTPP ($6a_{1g} + 3b_{2g} + 6e_u$) → $\pi_\parallel^*$ ($^2e_{2u}$) EE is 283.77 eV (see Table S3 of the ESI†), while the CuTPP(F) ($10a_{1g} + 7b_{2g} + 9e_u$) → $\pi_\parallel^*$ ($^2e_{2u}$) EE is 284.16 eV (see Table S4 of the ESI†) with a theoretical ΔEE ∼ 0.4 eV. This value perfectly matches the ($^{CuTPP(F)}EE_{b_4} - {}^{CuTPP}EE_{b_4}$) = 0.4 eV (see Table 1). Moreover, the C^{25} strong involvement in the lowest lying $\Pi_\parallel$ transition is not particularly surprising because C^{25} atoms correspond to the only C^{Ph} species not decorated by fluorine. Trusting spin-unrestricted SR-ZORA TD-DFT results, besides the 8th excitation, the quasi degenerate $C^{Py(\beta)}$-based a_{2u} transitions (the 9th and 10th excitations having EEs = 284.72 and 284.76 eV, respectively; see Table S4 of the ESI†) should also contribute to the wide and unresolved feature S (component c_1). Remarkably, both the $24e_g$ and the $17b_{1u}$ virtual levels (fsos of the quasi degenerate $C^{Py(\beta)}$-based a_{2u} (transition no. 9 and 10) have a C^{Ph} σ* and C^{pmc} $\pi_\perp^*$ character. As already mentioned, a lot of closely spaced excitations contribute to the intense component c_2 and the wide and poorly resolved feature D of the CuTPP(F) C K-edge NEXAFS spectrum. Analogous to the CuTPP C K-edge NEXAFS spectrum, any detailed assignment of the EE region covered by bands C and D would be debatable. Nevertheless, according to our qualitative predictions, it is of some relevance to point out that $\Pi_\parallel$ transitions are hidden under c_2 (excitation no. 15 and 17) while, similarly to the free ligands, the $^{Ph}\Pi_\perp$ set does not contribute with any transition having $f \geq 10 \times 10^{-3}$ in the energy range we considered (280–290 eV).[83] Even though a significant contribution of excitations having a 1s → σ* nature to the intensity of bands C and D upon Ph fluorine decoration was not unexpected,[11c] it deserves to be underlined that several CuTPP(F) fsos have a C^{Ph} σ* and C^{pmc} $\pi_\perp^*$ character (see Table S4 and Fig. S1 of the ESI†). The absence of such evidence in H_2TPP(F) prompts us to ascribe it to a combined effect of the Ph fluorination and the increased symmetry associated with the ligand metalation.

N K-edge spectra

The extended N K-edge NEXAFS spectra of CuTPP and CuTPP(F) are displayed in Fig. 4,[76] while their fitted [i] regions are reported in Fig. 7 (EE positions of fitting components are reported in Table 2). At first glance, the CuTPP spectrum looks like those reported in the literature;[82] nevertheless, a detailed check reveals

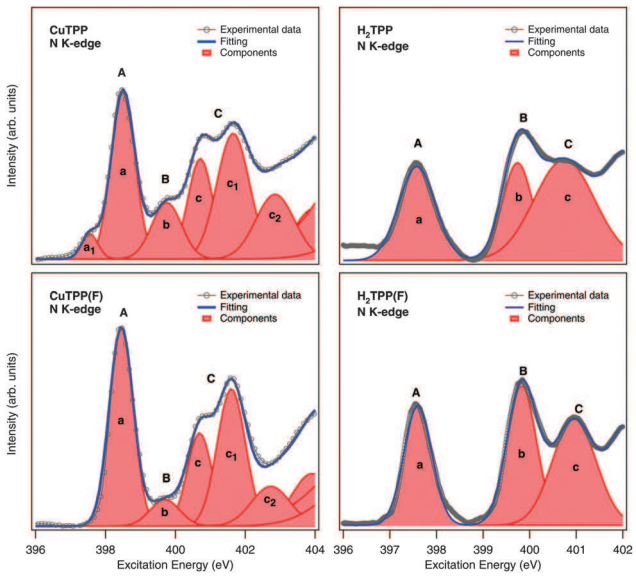

Fig. 7 Fitted [i] region of the N K-edge NEXAFS spectra of CuTPP (left upper panel) and CuTPP(F) (left lower panel). The fitted [i] region of the N K-edge NEXAFS spectra of H_2TPP (right upper panel)[11c] and H_2TPP(F) (right lower panel)[11c] is also displayed for comparison.

Table 2 Excitation energy position (eV) of N K-edge transitions (components a–c) for the fit of CuTPP and CuTPP(F) thick film spectra displayed in Fig. 7. ΔEE between similar features for CuTPP and CuTPP(F) are also reported. Values pertaining to the free ligands are also reported in parentheses

	CuTPP (H_2TPP)	ΔEE	CuTPP(F) (H_2TPP(F))	ΔEE
a_1	397.53			
a	398.53 (397.57)	1.00	398.47 (397.60)	
b	399.73 (399.74)	2.20 (2.17)	399.67 (399.83)	1.20 (2.23)
c	400.73 (400.75)	3.20 (3.18)	400.67 (400.96)	2.20 (3.36)
c_1	401.64	4.11	401.58	3.11
c_2	402.84	5.31	402.72	4.25

a series of quite relevant differences between data reported herein and those published by Reid *et al.*[82a] and Diller *et al.*[82b] Among them, the most evident concerns the presence on the lower and higher EE sides of the intense band A (see the left upper panel of Fig. 7) of two unresolved and rather weak features corresponding to the components a_1 and b at 397.57 and 399.77 eV, respectively (see Table 2). As such, the lowest lying spectral feature of the CuTPP N K-edge NEXAFS spectrum reported by Reid *et al.* (peak A in Fig. 7 of ref. 82*a*) is only asymmetric, being characterized by a barely visible shoulder on its lower EE side.

At variance with that, no shoulder seems to be present on the lower EE side of the lowest lying spectral feature of the N K-edge NEXAFS spectrum recorded by Diller *et al.* for the self-metalated H_2TPP on Cu(111) (see Fig. 6 and Table IV of ref. 82*b*). As far as the component b is concerned, this is not revealed in the extended N K-edge NEXAFS spectra reported by Reid *et al.*[82a] and Diller *et al.*[82b] Finally, the relative intensity of components c and c_1 in the left upper panel of Fig. 7 is opposite to the one reported by Diller *et al.*[82b] Before going on, it is mandatory to emphasize that great attention has been paid to reveal the possible radiation damage of the organic film during beam exposure. To this end, the $1s^C$ core level line-shape has been checked as a function of the photon dose and, under the adopted working conditions, no damage has ever been observed.

Regardless of differences from literature data,[82] the presence of just one type of N atom both in CuTPP and CuTPP(F) (which reduces the number of possible isos), the harsh symmetry constraints and the consequent inherent simplicity of the N K-edge spectra make the assignment of the lower lying spectral features straightforward. In this regard, it can be useful to remind that linear combinations of $1s^N$ AOs span the $a_{1g} + b_{1g} + e_u$ IRs of the D_{4h} symmetry point group (see Table S1 of the ESI†), while the N $\pi_\perp$* based MOs transform as $e_g + a_{2u} + b_{2u}$.[71] Low-lying excitations can then be associated with only the predictably weak $e_u\ 1s^N(e_u) \rightarrow \sigma^*(b_{1g})$ transition, as well as the $a_{2u}\ 1s^N(e_u) \rightarrow \pi_\perp^*(e_g)$ ones.[71] EEs and *f* values for CuTPP and CuTPP(F) $1s^N$ excitation spectra as obtained from spin-unrestricted SR-ZORA TD-DFT calculations are reported in Tables S5 and S6 of the ESI,† respectively, while corresponding f^N distributions in the EE range 393–399 eV are displayed in Fig. 8 where a_{2u} and e_u contributions are also included.

The comparison between NEXAFS patterns reported in Fig. 7 and the CuTPP/CuTPP(F) f^N distributions displayed in Fig. 8

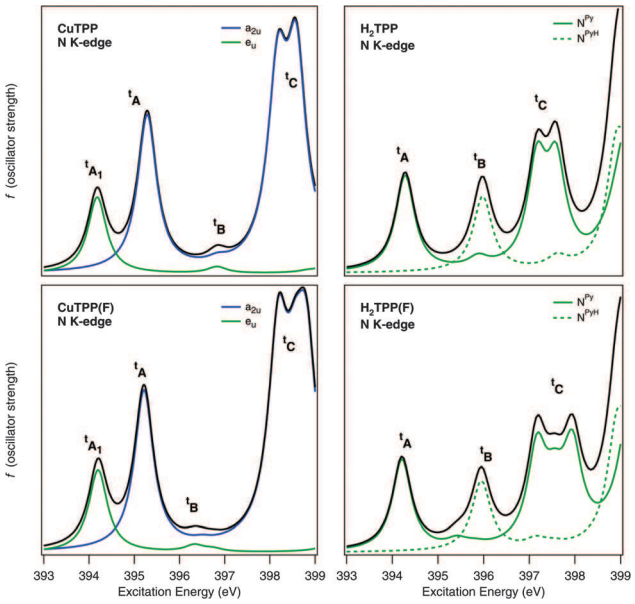

Fig. 8 Spin-unrestricted SR-ZORA TD-DFT $1s^N$ excitation spectra of CuTPP (left upper panel) and CuTPP(F) (left lower panel). Contributions from a_{2u} and e_u symmetries are also displayed. Convoluted profiles have been obtained by using a Lorentzian broadening of 0.25 eV. SR-ZORA TD-DFT $1s^N$ excitation spectra of H_2TPP (right upper panel)[11c] and H_2TPP(F) (right lower panel)[11c] are also displayed for comparison. SR-ZORA ionization limits may be deduced from the right panels of Fig. 8 of ref. 18*c*.

confirms the well-known EE underestimation (~3 eV).[80] Moreover, according to our qualitative predictions, the lowest lying component a_1 of the CuTPP N K-edge NEXAFS spectrum has to be associated with the $e_u\ 1s^N(2e_u) \rightarrow \sigma^*(12b_{1g})$ transition, while the intense feature A (component a, see the left upper panel of Fig. 7) is generated by the $a_{2u}\ 1s^N(2e_u) \rightarrow \pi_\perp^*(13e_g)$ one. Besides the remarkable experimental revealing of the L → M charge transfer (LMCT) transition and the very good agreement between experiment ($EE_a - EE_{a_1}$ = 1.0 eV, see Table 1) and theory ($EE_a - EE_{a_1}$ = 1.11 eV, see Table S5 of the ESI†), the comparison with theoretical data pertaining to CuPc[37] is particularly interesting. As a matter of fact, the lowest lying transitions of CuTPP and CuPc share the same nature (LMCT), have the same symmetry (e_u), are characterized by very close EEs (394.18 *vs.* 394.55 eV) and also the corresponding *f* values (9.0×10^{-3} *vs.* 10.1×10^{-3}) are very similar.[37] Moreover, it is noteworthy that the participation of the Cu $3d_{x^2-y^2}$ AO in the CuTPP $12b_{1g}$ LUMO (53%) and in the CuPc $16b_{1g}$ LUMO (52%) is substantially the same. On the whole, results so far considered ultimately confirm the close similarity of the Cu–L interaction in CuTPP and CuPc[37,18c] and then the relevant role played by the ionic contribution in the Cu–TPP bonding.

Similarly to the simulation of the H_2TPP N K-edge spectral features,[18c] the CuTPP EE region extending beyond the acomponent and including the poorly resolved band B and the double bumped band C is only semi-qualitatively reproduced by the CuTPP f^N distribution reported in Fig. 8. In fact, even though the experimental ($EE_b - EE_a$ = 1.29 eV) is quite satisfactorily reproduced by ($EE_{tA} - EE_{tB}$ = 1.54 eV), spin-unrestricted

SR-ZORA TD-DFT calculations definitely overestimate the ΔEE between components c and a, 2.29 *vs.* 2.94 eV.[84] Nevertheless, in agreement with the assignment of Reid *et al.*,[82a] components c and c_1 are both generated by excitations of a_{2u} symmetry (see Table S5 of the ESI†); the former associated with the $1b_{1g} \rightarrow 5b_{2u}$ transition and the latter to the $2e_u \rightarrow 15e_g$ one. It can also be useful to mention that the fsos of both transitions correspond to ${}^{pmc}\pi_\perp{}^*$ orbitals and the corresponding ΔEE (0.41 eV) very poorly reproduces the $(EE_{c_1} - EE_c)$ value (0.91 eV).

CuTPP and CuTPP(F) spectral patterns are quite similar and main differences are confined to the lower intensity of the weak band B and the disappearance of the a_1 feature, certainly hidden under the symmetric band A. As far as the latter evidence is concerned, this is not particularly surprising. As a matter of fact, theoretical outcomes pertinent to the CuTPP/CuTPP(F) (see Tables S3 and S4 of the ESI†) and H_2TPP/H_2TPP(F) C K-edges[18c] as well as to the H_2TPP/H_2TPP(F) N K-edge[18c] clearly indicate a tiny red-shift of EEs associated with transitions whose fsos correspond to the lowest lying ${}^{pmc}\pi_\perp{}^*$ orbitals. Now, the tiny blue-shift of the e_u $1s^N(5e_u) \rightarrow \sigma^*(15b_{1g})$ LMCT transition combined with the red-shift of the a_{2u} $1s^N(5e_u) \rightarrow \pi_\perp{}^*(22e_g)$ one has the effect of determining the a_1 fading in the CuTPP(F) N K-edge spectrum. Band A of the CuTPP(F) N K-edge spectrum is then assigned to the LMCT and $1s^N(5e_u) \rightarrow \pi_\perp{}^*(22e_g)$ transitions.

Differently from CuTPP,[84] no excitations with $f \geq 10^{-3}$ is revealed in the EE range between ${}^tA$ and ${}^tC$; moreover, as far as the double-bumped band C is concerned, it has to be pointed out that, similarly to CuTPP, both bumps have to be associated with a_{2u} excitations; nevertheless, the one lying at higher EE implies a transition from the $5e_u$ $1s^N$-based iso to the $25e_g$ fso, which, as already pointed out, contemporarily accounts for a σ* and ${}^{pmc}\pi_\perp{}^*$ character (see Table S6 and Fig. S1 of the ESI†).

F K-edge spectra

The [i] region of the F K-edge NEXAFS spectrum consists of a single intense band centred at 688.51 eV (see Fig. 4 and 9). Likewise H_2TPP(F),[11c] the experimental information is certainly poor; nevertheless, similarly to the modelling of the H_2TPP(F) F K-edge spectrum, the combined use of symmetry, orbitals and spectra appears to be the only option to get some information from experimental evidence.

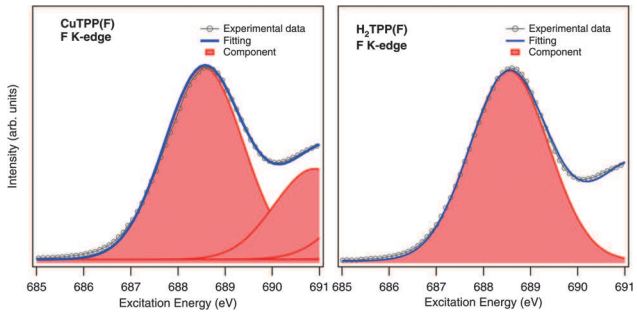

Fig. 9 Fitted [i] region of the F K-edge NEXAFS spectrum of CuTPP(F) (left panel). The fitted [i] region of the F K-edge NEXAFS spectrum of H_2TPP(F) (right panel)[11c] is also displayed for comparison.

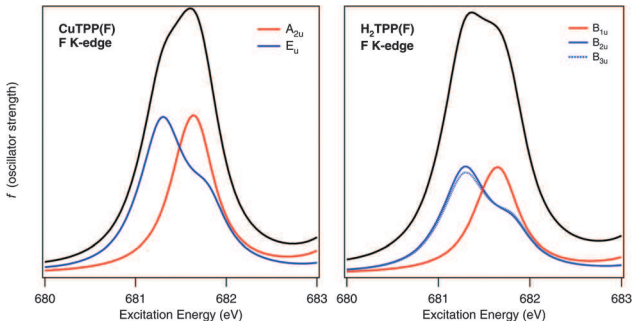

Fig. 10 Spin-unrestricted SR-ZORA TD-DFT $1s^F$ excitation spectrum of CuTPP(F) (left panel). Contributions from a_{2u} and e_u symmetries are also displayed. Convoluted profiles have been obtained by using a Lorentzian broadening of 0.25 eV. The SR-ZORA TD-DFT $1s^F$ excitation spectrum of H_2TPP(F) (right panel)[11c] is also displayed for comparison. SR-ZORA ionization limits may be deduced from the right panel of the Fig. 9 of ref. 18*c*.

$F_\parallel$-based ($F_\perp$-) linear combinations of 1s AOs transform into the $a_{1g} + b_{2g} + e_u$ ($a_{1g} + b_{2g} + e_g + a_{2u} + b_{1u} + e_u$) IRs of the D_{4h} symmetry point group (see Table S1 of the ESI†). Although the number of $1s^F$-based isos is quite large (40), they are quite closely spaced and the energy range they cover is rather narrow (see Fig. 9 of ref. 18*c*). EEs and *f* values associated with the $1s^F$ excitation spectrum as obtained from spin-unrestricted SR-ZORA TD-DFT calculations are reported in Table S7 of the ESI,† while the corresponding f^F distribution in the EE range 680–683 eV is displayed in Fig. 10 with contributions of different symmetries rather than of different imols.[79]

The agreement between experiment and theory is satisfactory (absolute EEs are underestimated by ~7 eV);[11c] moreover, data included in Table S7 of the ESI,† perfectly agree with theoretical outcomes pertaining to H_2TPP(F).[11c] In more detail, EEs of the five excitations reported in Table S7 of the ESI,† numerically match those of the eight excitations reported in Table 7 of the ESI† of ref. 11*c* (the $e_u - b_{2u} + b_{3u}$ in H_2TPP(F) – excitations associated with $1s^F \rightarrow {}^{Ph}\pi_\parallel{}^*$ transitions only involve $\pi_\parallel{}^*$–${}^1e_{2u}$ Ph-based orbitals and the two $a_{2u} - b_{1u}$ in H_2TPP(F) – excitations are associated to $1s^F \rightarrow \sigma^*$ transitions). This last evidence is perfectly in tune with the reversed linear dichroism in F K-edge NEXAFS data reported by de Oteyza *et al.* for fluorinated planar aromatic molecules, which emphasize "the significant overlap in energy of π* and σ* orbitals throughout the F K-edge spectrum".[85]

Cu $L_{2,3}$-edge spectra

In the near past, some of us have successfully modelled the $L_{2,3}$ spectra of a series of Cu(II) complexes: $[CuCl_4]^{2-}$,[18a] CuPc,[18a] the oxidized blue copper site in plastocyanin[18a] and Cu(acac)$_2$.[86,18b] As such, SO-ZORA TD-DFT-TDA[18] results revealed that, in addition to $2p_{3/2} \rightarrow 3d$ transitions, metal-to-ligand charge-transfer (MLCT) transitions involving low-lying ligand-based π* MOs may contribute to the L_3 intensity thus weakening its believed relationship with the M–L covalency. At the same time, theoretical results confirmed the legitimacy of using the Cu(II) L_3-edge position to get information about the ligand-field strength exerted on the Cu(II) centre.[18] The comparison of literature data pertaining to the

modelling of the CuPc L_3-edge NEXAFS spectrum[18] with those reported herein for CuTPP and CuTPP(F) complexes offers the following intriguing opportunities: (i) to further test the applicability of the SO-ZORA TD-DFT-TDA method to look into the $L_{2,3}$ spectral features of Cu(II) complexes; (ii) to get information about the ligand-field strength and the symmetry-restricted covalency in Cu(II) complexes sharing the same coordinative pocket; and (iii) to verify the sensitivity of the adopted theoretical approach.

$L_{2,3}$-edge NEFAXS spectra of CuTPP and CuTPP(F) recorded in the EE region 927–960 eV are superimposed in Fig. 11 with the CuPc $L_{2,3}$-edge NEFAXS spectrum, while CuTPP, CuTPP(F) and CuPc experimental (Exp) and theoretical (Theo) $L_{2,3}$ EEs are collected in Table 3. Moreover, the simulated L_3 $^{CuTPP}f$ and $^{CuTPP(F)}f$ distributions in the EE range 922–933 eV are reported in Fig. 12 together with the ^{CuPc}f one.

The comparison of experimental and theoretical L_3 values[87] confirms the well-known EE underestimation (~6 eV, see Table 3), which is ultimately due to XC potential deficiencies;[37,42] nonetheless, SO-ZORA TD-DFT-TDA calculations successfully reproduce both the coincident EE of the CuTPP and CuTPP(F) $^{Cu(II)}L_3$-edge and the little shift toward a higher EE of the CuPc $^{Cu(II)}L_3$-edge, indicative of a CuPc ligand-field strength slightly stronger than the CuTPP/CuTPP(F) one.[64]

Even though NEXAFS absolute intensities of CuTPP/CuTPP(F) and CuPc in Fig. 11 cannot be directly compared because of the different thicknesses of CuTPP/CuTPP(F) (50 nm) and CuPc (25 nm) films, f values associated with transitions generating $^{CuTPP}L_3$, $^{CuTPP(F)}L_3$ and $^{CuPc}L_3$ (see Fig. 12) are consistent with a very similar Cu–N symmetry-restricted covalency in the three complexes, thus further supporting the conclusions reported in ref. 18*c*. Similarly to the SO-ZORA TD-DFT-TDA $2p^{Cu}$ excitation spectra of CuPc (see Fig. 12) and $Cu(acac)_2$ (see the lower panel of Fig. 3 in ref. 18*b*), both $^{CuTPP}L_3$ and $^{CuTPP(F)}L_3$ are characterized by the presence of an evident shoulder on their lower EE side.

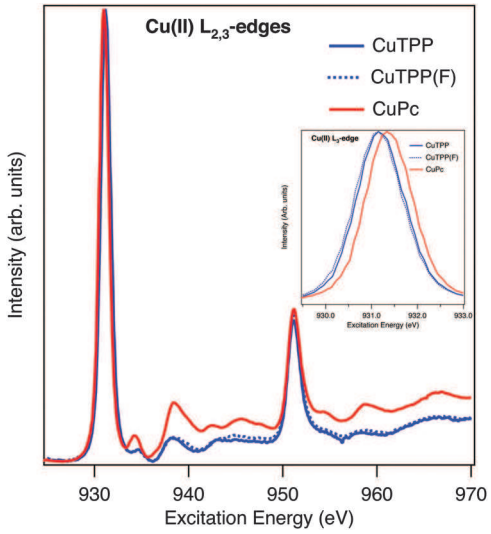

Fig. 11 Cu $L_{2,3}$-edge spectra of thick films of CuTPP (solid blue line) and CuTPP(F) (dotted blue line) deposited on Au(111). The Cu 2p excitation spectra of CuPc[18a,b] (red line) have also been included for comparison. The 929.5–933 eV EE range is displayed in the inset.

Table 3 Experimental and theoretical EEs (eV) for the $2p^{Cu}$ $L_{2,3}$ core excitation spectra of CuTPP, CuTPP(F) and CuPc

	CuTPP	CuTPP(F)[87]	CuPc[18]
$^{Exp}L_3$	931.2	931.2	931.4
$^{Exp}L_2$	951.2	951.2	951.4
$^{Theo}L_3$	925.35	925.30	925.75
$^{Theo}L_2$	945.64	—	946.00

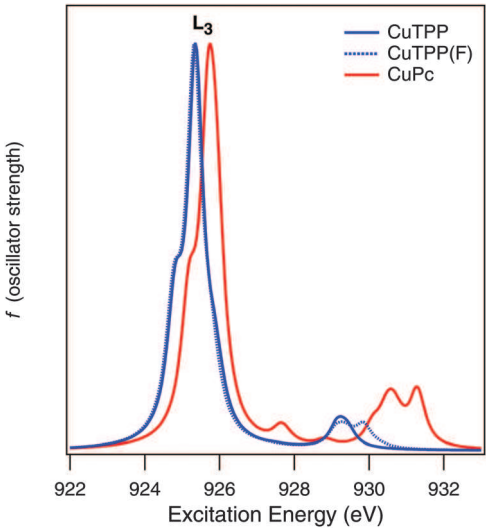

Fig. 12 SO-ZORA TD-DFT-TDA $2p^{Cu}$ excitation spectra of CuTPP (blue solid line) and CuTPP(F) (blue dotted line). The convoluted profiles were obtained with a Lorentzian broadening of 0.25 eV. The SO-ZORA TD-DFT-TDA $2p^{Cu}$ excitation spectra of CuPc[18a,b] (red solid line) have been also included for comparison.

Before going on, it has to be remarked that this shoulder is not revealed in the present measurements and this is likely due to the overall shortening of the lifetimes of the excited states in the condensed phase.[18c] The resulting broadening of the spectral lines is well beyond the experimental resolution, which is estimated to be *ca.* 0.5 eV in the present case.

Compositions, f values and EEs of transitions associated with $^{CuTPP}L_3$ and $^{CuTPP(F)}L_3$ are reported in Table 4, where the corresponding CuPc values are also included for comparison.[88] The inspection of data reported in Table 4 reveals that CuTPP and CuTPP(F) outcomes are, apparently, very similar to the CuPc ones.[18a,b] In detail, $^{CuTPP}L_3$ and $^{CuTPP(F)}L_3$ features are both generated by three excitations (hereafter, L_3^1, L_3^2 and L_3^3) whose energy spread is ~1 eV in CuTPP and CuTPP(F) (0.72 eV in CuPc); one transition contributes to L_3^1, while three of them are involved both in L_3^2 and L_3^3. Moreover, if we consider that the CuTPP (CuTPP(F)) $350a_{1/2}$ ($510a_{1/2}$) lowest unoccupied spinor is reminiscent of the SR $12b_{1g}$ ($15b_{1g}$) CuTPP (CuTPP(F)) LUMO and that the CuTPP (CuTPP(F)) $351a_{1/2}$–$354a_{1/2}$ ($511a_{1/2}$–$514a_{1/2}$) spinors are strongly related to the $13e_g$ ($22e_g$) MO (see Fig. 3), corresponding to the lowest lying $^{pmc}\pi_\perp^*$ (feature L in Fig. 2), all transitions reported in Table 4 have the same nature in CuTPP, CuTPP(F) and CuPc. Nevertheless, data reported in Table 4 clearly state that contributions provided to L_3^2 by MLCT

Table 4 SO-ZORA TD-DFT-TDA compositions, $f \times 10^3$ (in parentheses) and EE values (eV, in parentheses) of the transitions that generate L_3^n excitations in CuTPP and CuTPP(F). Data pertaining to CuPc are also included for comparison[a,b,c,d,e,f,g]

	CuTPP	CuTPP(F)	CuPc
L_3^1	$9a_{1/2} \rightarrow 350a_{1/2}^{(100)}$ (9.66, 924.81)	$9a_{1/2} \rightarrow 510a_{1/2}^{(100)}$ (9.66, 924.77)	$9a_{1/2} \rightarrow 294a_{1/2}^{(99)}$ (9.44, 925.18)
L_3^2	$7a_{1/2} \rightarrow 350a_{1/2}^{(90)}$ (30.7, 925.36) $9a_{1/2} \rightarrow 351a_{1/2}^{(1)}$ $10a_{1/2} \rightarrow 354a_{1/2}^{(1)}$	$7a_{1/2} \rightarrow 510a_{1/2}^{(97)}$ (30.3, 925.32) $9a_{1/2} \rightarrow 511a_{1/2}^{(2)}$ $10a_{1/2} \rightarrow 514a_{1/2}^{(1)}$	$7a_{1/2} \rightarrow 294a_{1/2}^{(79)}$ (21.6, 925.69) $9a_{1/2} \rightarrow 295a_{1/2}^{(13)}$ $10a_{1/2} \rightarrow 298a_{1/2}^{(8)}$
L_3^3	$10a_{1/2} \rightarrow 354a_{1/2}^{(72)}$ (2.59, 925.86) $9a_{1/2} \rightarrow 351a_{1/2}^{(26)}$ $7a_{1/2} \rightarrow 350a_{1/2}^{(2)}$	$10a_{1/2} \rightarrow 514a_{1/2}^{(69)}$ (3.00, 925.75) $9a_{1/2} \rightarrow 511a_{1/2}^{(28)}$ $7a_{1/2} \rightarrow 510a_{1/2}^{(3)}$	$10a_{1/2} \rightarrow 298a_{1/2}^{(46)}$ (12.1, 925.90) $9a_{1/2} \rightarrow 295a_{1/2}^{(33)}$ $7a_{1/2} \rightarrow 294a_{1/2}^{(20)}$

[a] Contributions to iso → fso of less than 1% are not reported. [b] ($f \times 10^3$) values of less than 5 are not reported. [c] Values pertaining to CuPc are from ref. 18*b*. [d] The Cu $2p_{3/2}$-based levels are CuTPP: $7a_{1/2}$–$10a_{1/2}$ at 934.18, 934.10, 933.99, and 933.98 eV; CuTPP(F): $7a_{1/2}$–$10a_{1/2}$ at 935.35, 935.27, 935.15, and 935.14 eV; CuPc: $7a_{1/2}$–$10a_{1/2}$ at 934.84, 934.76, 934.65, and 934.65 eV. [e] The parenthood of the Cu $2p_{3/2}$-based levels with SR ZORA Cu 2p-based MOs is CuTPP: $7a_{1/2} \rightarrow 1e_u^{(100)}$, $8a_{1/2} \rightarrow 1e_u^{(100)}$, $9a_{1/2} \rightarrow 1a_{2u}^{(67)} + 1e_u^{(33)}$, $10a_{1/2} \rightarrow 1a_{2u}^{(67)} + 1e_u^{(33)}$; CuTPP(F): $7a_{1/2} \rightarrow 1e_u^{(100)}$, $8a_{1/2} \rightarrow 1e_u^{(100)}$, $9a_{1/2} \rightarrow 1a_{2u}^{(67)} + 1e_u^{(33)}$, $10a_{1/2} \rightarrow 1a_{2u}^{(67)} + 1e_u^{(33)}$; CuPc: $7a_{1/2} \rightarrow 1e_u^{(100)}$, $8a_{1/2} \rightarrow 1e_u^{(100)}$, $9a_{1/2} \rightarrow 1a_{2u}^{(67)} + 1e_u^{(33)}$, $10a_{1/2} \rightarrow 1a_{2u}^{(67)} + 1e_u^{(33)}$. [f] The lowest unoccupied spinors of CuTPP, CuTPP(F) and CuPc are the $350a_{1/2}$, $510a_{1/2}$ and $294a_{1/2}$ ones, respectively. [g] The parenthood of the lowest unoccupied spinors of CuTPP, CuTPP(F) and CuPc with SR ZORA SOMOs is CuTPP: $350a_{1/2} \rightarrow 12b_{1g}^{(100)}$; CuTPP(F): $510a_{1/2} \rightarrow 15b_{1g}^{(100)}$; CuPc: $294a_{1/2} \rightarrow 16b_{1g}^{(100)}$.

transitions are definitely smaller in CuTPP and CuTPP(F) than in CuPc and the same thing holds when the CuTPP and CuTPP(F) L_3^3 *f* values are compared with the CuPc *f* one. The very good agreement between the CuTPP $\Delta EE_{L_3^3-L_3^1}$ (1.05 eV, see Table 4) and the experimental/theoretical ΔEE_{a-a_1} (1.0/1.11 eV, see Table 2 and Table S5 of the ESI†) in the CuTPP NEXAFS N K-edge spectrum is certainly noteworthy; nevertheless, even more important is the evidence that, despite the close similarity between TPP^{2-} and Pc^{2-} (the same donor atom, the same coordinative pocket, and quite similar electronic structures),[18c] the L_3 fine structure of their Cu(II) complexes is rather different.

$L_{2,3}$-edge spectra of CuTPP and CuTPP(F) are both characterized by the presence of a faint experimental feature at ~3.5 eV from L_3. A thorough inspection of the whole $^{CuTPP}f$ and $^{CuTPP(F)}f$ distributions revealed the presence of a series of very weak excitations between 929.0–929.6 eV and 929.0–930.0 eV in CuTPP and CuTPP(F), respectively. Those with largest *f* values (0.90×10^{-3} at 929.43 in CuTPP and 1.49×10^{-3} at 929.85 eV in CuTPP(F)) are associated with transitions from Cu $2p_{3/2}$ spinors to fso with tiny contributions from Cu s virtual AOs. No $^{CuTPP}L_3$ excitation is computed beyond 929.79 eV while $^{CuTPP(F)}L_3$ excitations beyond 930 eV are all characterized by very low *f* values.[87]

Even though it is well known[62g] that main deviations between experiment and theory concern the L_2 region, the SO-ZORA TD-DFT-TDA $^{CuTPP}L_2$–$^{CuTPP}L_3$ ΔEE (20.29 eV, see Table 3) satisfactorily reproduces the experimental value (20.0 eV, see Table 3).[87] Any further consideration about the L_2 feature is herein avoided as this EE region is not unambiguously determined by experiment.[62g]

4. Conclusions

Empty states of two π-conjugated molecules, the Cu(II) complexes of tetraphenylporphyrin and tetrakis(pentafluorophenyl)porphyrin, have been thoroughly investigated through the use of the synchrotron radiation light. According to a well-established procedure, experimental evidence collected from thick films of both molecules has been discussed and compared with the outcomes of numerical experiments carried out for isolated species in the framework of TD-DFT. Besides the often noticeable agreement between experiment and theory, the combined use of NEXAFS data recorded at the C, N and F K-edges as well as at the Cu $L_{2,3}$-edges provided new insights into the CuTPP and CuTPP(F) empty states and the Cu–L bonding scheme. Several contributions have been published in the past on these issues; however, we do believe that the present investigation, combined with the experimental and theoretical data reported in ref. 18*c*, represents a significant advance because, for the first time, all the relevant electronic shells (from the core levels of C, N, F and Cu to the occupied and unoccupied molecular orbitals) are consistently investigated with unprecedented detail. With specific reference to the outcomes reported herein, it has been ultimately settled that MLCT transitions may contribute to the higher EE side of the Cu L_3-edge in Cu(II) complexes characterized by the presence of low-lying, ligand-based π* MOs; nevertheless, the occurrence of these orbitals is a necessary but not sufficient condition. Overall, the SO-ZORA TD-DFT-TDA method is confirmed as a valuable and highly sensitive tool to look into the $L_{2,3}$ spectral features of Cu(II) complexes. As such, the M–L bonding in CuTPP, CuTPP(F) and CuPc is found to be very similar to the ionic contribution playing a leading role. Moreover, the ligand-field strength exerted by the phthalocyanine ligand on the Cu(II) centre is experimentally found and theoretically confirmed to be slightly stronger than that experienced by Cu(II) in CuTPP and CuTPP(F).

Acknowledgements

Prof. Luciano Pandolfo is acknowledged for the synthesis of CuTPP(F). Dr Bice Leone is kindly acknowledged for the helpful discussion. Dr Melanie Timpel gratefully acknowledges the support of a Feodor-Lynen-Fellowship of Alexander v. Humboldt Foundation, Bonn (Germany). Italian Ministry of University and Research (PRIN-2010BNZ3F2, project DESCARTES), University of

Padova (CPDA134272/13, project S_3MArTA), and Computational Chemistry Community (C_3P) of the University of Padova are kindly acknowledged.

References

1 *The Porphyrin Handbook*, ed. K. M. Kadish, K. M. Smith and R. Guillard, Academic Press, New York, 2000.
2 D. Dini and M. Hanack, *J. Porphyrins Phthalocyanines*, 2004, **8**, 915.
3 C. Di Natale, D. Monti and R. Paolesse, *Mater. Today*, 2010, **13**, 37.
4 J. M. Gottfried, *Surf. Sci. Rep.*, 2015, **70**, 259.
5 A. Tsuda and A. Osuka, *Science*, 2001, **293**, 79.
6 M. Planells, A. Forneli, E. Martínez-Ferrero, A. Sánchez-Díaz, M. A. Sarmentero, P. Ballester, E. Palomares and B. C. O'Regan, *Appl. Phys. Lett.*, 2008, **92**, 153506.
7 A. P. Castano, P. Mroz and M. R. Hamblin, *Nat. Rev. Cancer*, 2006, **6**, 535.
8 N. A. Rakow and K. S. Suslick, *Nature*, 2000, **406**, 710.
9 Y. Niwa, H. Kobayashi and T. J. Tsuchiya, *Chem. Phys.*, 1974, **60**, 799.
10 L. Scudiero, D. E. Barlow, U. Mazur and K. W. Hipps, *J. Am. Chem. Soc.*, 2001, **123**, 4073.
11 (*a*) M. Nardi, R. Verucchi, C. Corradi, M. Pola, M. Casarin, A. Vittadini and S. Iannotta, *Phys. Chem. Chem. Phys.*, 2010, **12**, 871; (*b*) M. Nardi, R. Verucchi, L. Aversa, M. Casarin, A. Vittadini, N. Mahne, A. Giglia, S. Nannarone and S. Iannotta, *New J. Chem.*, 2013, **37**, 1036; (*c*) M. V. Nardi, R. Verucchi, L. Pasquali, A. Giglia, G. Fronzoni, M. Sambi, G. Mangione and M. Casarin, *Phys. Chem. Chem. Phys.*, 2015, **17**, 2001.
12 E. J. Baerends, G. Ricciardi, A. Rosa and S. J. A. van Gisbergen, *Coord. Chem. Rev.*, 2002, **230**, 5.
13 N. V. Ivashin, O. P. Parkhots and S. Larsson, *J. Appl. Spectrosc.*, 2002, **69**, 659.
14 J. C. Goll, K. T. Moore, A. Ghosh and M. J. Therien, *J. Am. Chem. Soc.*, 1996, **118**, 8344.
15 M. P. de Jong, R. Friedlein, S. L. Sorensen, G. Öhrwall, W. Osikowicz, C. Tengsted, S. K. M. Jönsson, M. Fahlman and W. R. Salaneck, *Phys. Rev. B: Condens. Matter Mater. Phys.*, 2005, **72**, 035448.
16 G. Polzonetti, V. Carravetta, G. Iucci, A. Ferri, G. Paolucci, A. Goldoni, P. Parent, C. Laffon and M. V. Russo, *Chem. Phys.*, 2004, **296**, 87.
17 T. E. Shubina, H. Marbach, K. Flechtner, A. Kretschmann, N. Jux, F. Buchner, H.-P. Steinrück, T. Clark and J. M. Gottfried, *J. Am. Chem. Soc.*, 2007, **129**, 9476.
18 (*a*) G. Mangione, M. Sambi, M. V. Nardi and M. Casarin, *Phys. Chem. Chem. Phys.*, 2014, **16**, 19852; (*b*) G. Mangione, L. Pandolfo, M. Sambi, G. Ligorio, M. V. Nardi, A. Cossaro, L. Floreano and M. Casarin, *Eur. J. Inorg. Chem.*, 2015, 2707; (*c*) G. Mangione, S. Carlotto, M. Sambi, G. Ligorio, M. Timpel, A. Vittadini, M. V. Nardi and M. Casarin, *Phys. Chem. Chem. Phys.*, DOI: 10.1039/C6CP01423B.
19 F. Buchner, K. Flechtner, Y. Bai, E. Zilner, I. Kellner, H.-P. Steinrück, H. Marbach and J. M. Gottfried, *J. Phys. Chem. C*, 2008, **112**, 15458.
20 M. Nardi, R. Verucchi, R. Tubino and S. Iannotta, *Phys. Rev. B: Condens. Matter Mater. Phys.*, 2009, **79**, 125404.
21 J. J. A. van Kampen, T. M. Luider, P. J. A. Ruttink and P. C. Burgers, *J. Mass Spectrom.*, 2009, **44**, 1556.
22 X.-F. Ren, A.-M. Ren, J.-K. Feng and X. Zhou, *Org. Electron.*, 2010, **11**, 979.
23 K. M. Barkigia, P. Battioni, V. Riou, D. Mansuyb and J. Fajer, *Chem. Commun.*, 2002, 956.
24 G. L. Perlovich, O. A. Golubchikov and M. E. Klueval, *J. Porphyrins Phthalocyanines*, 2010, **4**, 699.
25 R. Pizzoferrato, R. Francini, S. Pietrantoni, R. Paolesse, F. Mandoj, A. Monguzzi and F. Meinardi, *J. Phys. Chem. A*, 2010, **114**, 4163.
26 M. Asghari-Khiavi and F. Safinejad, *J. Mol. Model.*, 2010, **16**, 499.
27 H. He, Y. Zhong, L. Si and A. Sykes, *Inorg. Chim. Acta*, 2011, **378**, 30.
28 S. Duhm, S. Hosoumi, I. Salzmann, A. Gerlach, M. Oehzelt, B. Wedl, T.-L. Lee, F. Schreiber, N. Koch, N. Ueno and S. Kera, *Phys. Rev. B: Condens. Matter Mater. Phys.*, 2010, **81**, 045418.
29 D. Wróbel, A. Siejak and P. Siejak, *Sol. Energy Mater. Sol. Cells*, 2010, **94**, 492.
30 X. Ma, J. Sun, M. Wang, M. Hub, G. Li, H. Chena and J. Huanga, *Sens. Actuators, B*, 2006, **114**, 1035.
31 R. D. Yang, J. Park, C. N. Colesniuc, I. K. Schuller, J. E. Royer, W. C. Trogler and A. C. Kummel, *J. Chem. Phys.*, 2009, **130**, 164703.
32 S. K. Pandey, A. L. Gryshuk, A. Graham, K. Ohkubo, S. Fukuzumi, M. P. Dobhal, G. Zheng, Z. Ou, R. Zhan and K. M. Kadish, *Tetrahedron*, 2003, **59**, 10059.
33 A. Serra, M. Pineiro, C. I. Santos, A. M. d'A. Rocha Gonsalves, M. Abrantes, M. Laranjo and M. F. Botelho, *Photochem. Photobiol.*, 2010, **86**, 206.
34 A. Bianconi, *X-ray Absorption: Principles, Applications, Techniques of EXAFS, SEXAFS and XANES*, John Wiley & Sons, New York, 1988, pp. 573–662.
35 J. Stöhr, *NEXAFS Spectroscopy*, Springer, Berlin, 1992.
36 The absorption edges are labelled in the order of increasing energy, K, L_1, L_2, L_3, M_1,..., corresponding to the excitation of an electron from the 1s ($S_{1/2}$), 2s ($S_{1/2}$), 2p ($P_{1/2}$), 2p ($P_{3/2}$), 3s ($S_{1/2}$),... orbitals (states), respectively.
37 M. V. Nardi, F. Detto, L. Aversa, R. Verucchi, G. Salviati, S. Iannotta and M. Casarin, *Phys. Chem. Chem. Phys.*, 2013, **15**, 12864.
38 (*a*) G. te Velde, F. M. Bickelhaupt, E. J. Baerends, C. Fonseca Guerra, S. J. A. van Gisbergen, J. G. Snijders and T. Ziegler, *J. Comput. Chem.*, 2001, **22**, 931; (*b*) C. Fonseca Guerra, J. G. Snijders, G. te Velde and E. J. Baerends, *Theor. Chem. Acc.*, 1998, **99**, 391; (*c*) ADF2014, SCM, Theoretical Chemistry, Vrije Universiteit, Amsterdam, The Netherlands, http://www.scm.com.
39 (*a*) S. Nannarone, F. Borgatti, A. DeLuisa, B. P. Doyle, G. C. Gazzadi, A. Giglia, P. Finetti, N. Mahne, L. Pasquali,

M. Pedio, G. Selvaggi, G. Naletto, M. G. Pelizzo and G. Tondello, *AIP Conf. Proc.*, 2004, **705**, 450; (*b*) L. Pasquali, A. DeLuisa and S. Nannarone, *AIP Conf. Proc.*, 2004, **705**, 1142.

40 Optimized coordinates of CuTPP and CuTPP(F) are reported as ESI† in ref. 18*c*.

41 (*a*) E. Van Lenthe, E. J. Baerends and J. G. Snijders, *J. Chem. Phys.*, 1993, **99**, 4597; (*b*) E. Van Lenthe, E. J. Baerends and J. G. Snijders, *J. Chem. Phys.*, 1994, **101**, 9783; (*c*) E. Van Lenthe, A. W. Ehlers, E. J. Baerends and J. G. Snijders, *J. Chem. Phys.*, 1999, **110**, 8543; (*d*) F. Wang, T. Ziegler, E. van Lenthe, S. van Gisbergen and E. J. Baerends, *J. Chem. Phys.*, 2005, **122**, 204103.

42 (*a*) G. Fronzoni, M. Stener, P. Decleva, F. Wang, T. Ziegler, E. van Lenthe and E. J. Baerends, *Chem. Phys. Lett.*, 2005, **416**, 56; (*b*) G. Fronzoni, M. Stener, P. Decleva, M. De Simone, M. Coreno, P. Franceschi, C. Furlani and K. C. Prince, *J. Phys. Chem. A*, 2009, **113**, 2914; (*c*) M. Casarin, P. Finetti, A. Vittadini, F. Wang and T. Ziegler, *J. Phys. Chem. A*, 2007, **111**, 5270.

43 E. van Lenthe and E. J. Baerends, *J. Comput. Chem.*, 2003, **24**, 1142.

44 E. K. U. Gross and W. Kohn, *Adv. Quantum Chem.*, 1990, **21**, 255.

45 R. van Leeuwen and E. J. Baerends, *Phys. Rev. A: At., Mol., Opt. Phys.*, 1994, **49**, 2421.

46 J. H. van Lenthe, S. Faas and J. G. Snijders, *Chem. Phys. Lett.*, 2000, **328**, 107.

47 S. Hirata and M. Head-Gordon, *Chem. Phys. Lett.*, 1999, **314**, 291.

48 F. Wang and T. Ziegler, *Mol. Phys.*, 2004, **102**, 2585.

49 M. Rancan, J. Tessarolo, M. Casarin, P. L. Zanonato, S. Quici and L. Armelao, *Inorg. Chem.*, 2014, **53**, 7276.

50 Both in CuTPP and CuTPP(F) the Cu(II) 3d-based SOMO corresponds to the highest occupied MO (HOMO).

51 R. S. Mulliken, *J. Chem. Phys.*, 1955, **23**, 1833.

52 G. P. Moss, *Pure Appl. Chem.*, 1987, **59**, 779.

53 (*a*) B. Hedman, K. O. Hodgson and E. I. Solomon, *J. Am. Chem. Soc.*, 1990, **112**, 1643; (*b*) S. E. Shadle, B. Hedman, K. O. Hodgson and E. I. Solomon, *Inorg. Chem.*, 1994, **33**, 4235; (*c*) S. E. Shadle, B. Hedman, K. O. Hodgson and E. I. Solomon, *J. Am. Chem. Soc.*, 1995, **117**, 7; (*d*) F. Neese, B. Hedman, K. O. Hodgson and E. I. Solomon, *Inorg. Chem.*, 1999, **38**, 4854.

54 According to C. K. Jørgensen,[57] the symmetry restricted covalency is the effect associated with the dilution, ruled by the complex symmetry, of d orbitals to make them become linear combinations of atomic orbitals (LCAO-MOs).

55 T. Glaser, B. Hedman, K. O. Hodgson and E. I. Solomon, *Acc. Chem. Res.*, 2000, **33**, 859.

56 E. I. Solomon, B. Hedman, K. O. Hodgson, A. Deya and R. K. Szilagyic, *Coord. Chem. Rev.*, 2005, **249**, 97.

57 C. K. Jørgensen, *Absorption Spectra and Chemical Bonding in Complexes*, Pergamon Press, Oxford, UK, 1962, p. 77.

58 R. K. Hocking and E. I. Solomon, *Struct. Bonding*, 2012, **142**, 155.

59 (*a*) F. de Groot, *Coord. Chem. Rev.*, 2005, **249**, 31; (*b*) F. de Groot and A. Kotani, *Core Level Spectroscopy of Solids*, CRC Press, Boca Raton, 2008.

60 D. Maganas, M. Roemelt, M. Hävecker, A. Trunschke, A. Knop-Gericke, R. Schlögl and F. Neese, *Phys. Chem. Chem. Phys.*, 2013, **15**, 7260.

61 M. Roemelt and F. Neese, *J. Phys. Chem. A*, 2013, **117**, 3069.

62 (*a*) P. S. Bagus, H. Freund, H. Kuhlenbeck and E. S. Ilton, *Chem. Phys. Lett.*, 2008, **455**, 331; (*b*) H. Ikeno, T. Mizoguchi and I. Tanaka, *Phys. Rev. B: Condens. Matter Mater. Phys.*, 2011, **83**, 155107; (*c*) I. Josefsson, K. Kunnus, S. Schreck, A. Föhlisch, F. de Groot, P. Wernet and M. Odelius, *J. Phys. Chem. Lett.*, 2012, **3**, 3565; (*d*) M. Roemelt, D. Maganas, S. DeBeer and F. Neese, *J. Chem. Phys.*, 2013, **138**, 204101; (*e*) D. Maganas, S. DeBeer and F. Neese, *Inorg. Chem.*, 2014, **53**, 6374; (*f*) D. Maganas, M. Roemelt, M. Hävecker, A. Trunschke, A. Knop-Gericke, R. Schlögl and F. Neese, *Phys. Chem. Chem. Phys.*, 2013, **15**, 7260; (*g*) D. Maganas, M. Roemelt, T. Weyhermüller, R. Blume, M. Hävecker, A. Knop-Gericke, S. DeBeer, R. Schlögl and F. Neese, *Phys. Chem. Chem. Phys.*, 2014, **16**, 264.

63 (*a*) S. J. George, M. D. Lowery, E. I. Solomon and S. P. Cramer, *J. Am. Chem. Soc.*, 1993, **115**, 2968; (*b*) S. DeBeer George, M. Metz, R. K. Szilagyi, H. Wang, S. P. Cramer, Y. Lu, W. B. Tolman, B. Hedman, K. O. Hodgson and E. I. Solomon, *J. Am. Chem. Soc.*, 2001, **123**, 5757; (*c*) R. Sarangi, N. Aboelella, K. Fujisawa, W. B. Tolman, B. Hedman, K. O. Hodgson and E. I. Solomon, *J. Am. Chem. Soc.*, 2006, **128**, 8286.

64 In Cu(II) complexes, the larger is the $L_{2,3}$ normalized intensity, the lower will be the M–L symmetry-restricted covalency; the higher is the L_3 EE, the stronger will be the ligand-field exerted on the Cu(II) centre.

65 The optimized Cu–N bond lengths in CuTPP, CuTPP(F) and CuPc (2.019, 2.020, and 1.978 Å, respectively)[18*c*] agree quite well with the available experimental data for CuTPP (2.000 Å)[66] and CuPc (1.946 Å).[67].

66 W. R. Scheidt, in *The Porphyrins III, Physical Chemistry, Part A*, ed. D. Dolphin, Academic Press, Inc., New York, 1978.

67 J. Ren, S. Meng, Y.-L. Wang, X.-C. Ma, Q.-K. Xue and E. Kaxiras, *J. Chem. Phys.*, 2011, **134**, 194706.

68 G. L. Miessler, P. J. Fischer and D. A. Tarr, *Inorganic Chemistry*, Pearson, New York, 5th edn, 2013, p. 137.

69 The energy-ordered linear combinations of C, N and F 1s AOs are collected in Table S1 of the ESI†.

70 B. E. Douglas and C. A. Hollingsworth, *Symmetry in Bonding and Spectra*, Academic Press, New York, 1985.

71 Linear combinations of pmc unoccupied $\pi_\perp$* frontier orbitals[68] transform into the $e_g + a_{1u} + a_{2u} + b_{1u} + b_{2u}$ IRs; C^{Py} p_z AOs contribute to all of them, while N (C^m) p_z AOs limit their participation to the $e_g + a_{2u} + b_{2u}$ ($e_g + a_{2u} + b_{1u}$) ones. The lowest lying pmc $\pi_\perp$* MOs are the CuTPP (CuTPP(F)) $13e_g$ and $9b_{1u}$ ($22e_g$ and $16b_{1u}$) MOs,[72] all of them characterized by a quite homogeneous localization on pmc atoms (see Fig. 3). Besides the σ_h nodal plane, common to all of them, each e_g partner is also anti-symmetric with respect to one of the two σ_v symmetry planes (either σ_{xz} or σ_{yz} in the selected framework), while b_{1u} MOs are anti-symmetric with respect to both σ_{xz} and σ_{yz} planes.[70]

Nodal properties of π* frontier orbitals have been emphasized here because they can be helpfully exploited to qualitatively foresee the localization of 1s → π* electric dipole allowed transitions.

72 Throughout the paper, the MO numbering is the one corresponding to the all-electron calculations independently of the adoption of the frozen core approximation.

73 The $D_{2h} \rightarrow D_{4h}$ symmetry increase implies the following correlations: $b_{1u} \rightarrow a_{2u}$; $a_u \rightarrow b_{1u}$; $(b_{2u} + b_{3u}) \rightarrow e_u$ and $(b_{2g} + b_{3g}) \rightarrow e_g$.[70] The $13e_g$ (in CuTPP) and $22e_g$ (in CuTPP(F)) MOs are strongly reminiscent of the quasi degenerate $12b_{2g}/12b_{3g}$ and $21b_{2g}/21b_{3g}$ MOs in H_2TPP and H_2TPP(F), respectively (see Fig. 4 of ref. 11*c*).

74 The nine (thirteen) MOs hidden under M in the PDOS of CuTPP (CuTPP(F)) are the following: $9b_{1u}$, $13b_{1g}$, $32e_u$, $4b_{2u}$, $9a_{2g}$, $3a_{1u}$, $14e_g$ ($16b_{1u}$, $16b_{1g}$, $43e_u$, $12a_{2g}$, $6b_{2u}$, $5a_{1u}$, $23e_g$, $34a_{1g}$, $44e_u$, $28b_{2g}$) MOs. With the exclusion of the CuTPP $\pi_\perp$* $9b_{1u}$ MO, the remaining eight orbitals correspond to the linear combinations of the Ph-based e_{2u} $\pi_\parallel$* levels. Among them, the $4b_{2u}$, $3a_{1u}$ and $14e_g$ orbitals are the e_{2u}-like $\pi_\parallel$* partners with a node on the C^{25} and C^{45} atoms (hereafter, $^1e_{2u}$), while the $13b_{1g}$, $32e_u$ and $9a_{2g}$ orbitals are hereafter labelled as $^2e_{2u}$. Similarly to CuTPP, the only CuTPP(F) pmc-based π* orbital is the $16b_{1u}$ one; the following eight MOs correspond to the linear combinations of the Ph-based e_{2u} $\pi_\parallel$* levels, antibonding in nature with respect to the C–F $\pi_\parallel$ interaction. Moreover, the $6b_{2u} + 5a_{1u} + 23e_g$ orbitals are the $^1e_{2u}$-like $\pi_\parallel$* partners with a node on the C^{25}, C^{45} and F^{65} atoms ($^2e_{2u}$-like $\pi_\parallel$* MOs correspond to $16b_{1g} + 43e_u + 12a_{2g}$ orbitals). As far as the $34a_{1g} + 44e_u + 28b_{2g}$ MOs are concerned, they have a C–F σ* character. Both in CuTPP and CuTPP(F), a huge number of closely spaced π* and σ* MOs is present beyond M. Their detailed list is useless and is not reported herein due to space reasons.

75 As a consequence of the very low number of Cu(II)-based $2p \rightarrow 3d$ transitions,[18*a*,*b*] no preliminary consideration about the CuTPP and CuTPP(F) Cu(II) $L_{2,3}$-edge spectra is reported herein.

76 The EE ranges considered in Fig. 4 have been split into two regions ([i] and [ii]). According to the literature,[11*c*,37,77] the former is usually associated with $1s^{C/N/F} \rightarrow \pi^*$ excitations, whereas the latter accounts for $1s^{C/N/F} \rightarrow \sigma^*$ valence transitions.

77 (*a*) R. De Francesco, M. Stener and G. Fronzoni, *J. Phys. Chem. A*, 2012, **116**, 2885; (*b*) M. Linares, S. Stafstrom and P. Norman, *J. Chem. Phys.*, 2009, **130**, 104305; (*c*) V. Yu. Aristov, O. V. Molodtsova, V. Maslyuk, D. V. Vyalikh, V. M. Zhilin, Yu. A. Ossipyan, T. Bredowe, I. Mertig and M. Knupfer, *Appl. Surf. Sci.*, 2007, **254**, 20.

78 A. Basagni, L. Colazzo, F. Sedona, M. Di Marino, T. Carofiglio, E. Lubian, D. Forrer, A. Vittadini, M. Casarin, A. Verdini, A. Cossaro, L. Floreano and M. Sambi, *Chem. – Eur. J.*, 2014, **20**, 14296.

79 The acronyms isol and fsol stand for iso- and fso-localizations, respectively.

80 The theoretical EE underestimation is ultimately due to the XC potential deficiencies.[11*c*,42].

81 The component a_2 of the CuTPP C K-edge NEXAFS actually pinpoints the onset of B.

82 (*a*) I. Reid, Y. Zhang, A. Demasi, A. Blueser, L. Piper, J. E. Downes, A. Matsuura, G. Hughes and K. E. Smith, *Appl. Surf. Sci.*, 2009, **256**, 720; (*b*) K. Diller, F. Klappenberger, M. Marschall, K. Hermann, A. Nefedov, C. Wöll and J. V. Barth, *J. Chem. Phys.*, 2012, **136**, 014705.

83 $^{Ph}\Pi_\perp$ transitions (a_{2u} transitions from C^{Ph} 1s-based isos) contribute to the C K-edge NEXAFS spectra of both H_2TPP[11*c*] and CuTPP (see Table S3, ESI†); no $^{Ph}\Pi_\perp$ transition has $f \geq 10 \times 10^{-3}$ neither in H_2TPP(F)[11*c*] nor in CuTPP(F).

84 The very weak ^{t}B feature is generated by a_{2u} and e_u excitations whose *f* values range between 2.5×10^{-3} and 1.8×10^{-3}, and for this reason not included in Table S5 of the ESI.† All of them have the same iso (the $2e_u$ orbital), while the fsos are either the ($\pi_\perp$*–$^1e_{2u}$)-based $14e_g$ orbital (a_{2u}) or the ($\pi_\perp$*–$^2e_{2u}$)-based $9a_{2g}$ (e_u).

85 D. G. de Oteyza, A. Sakko, A. El-Sayed, E. Goiri, L. Floreano, A. Cossaro, J. M. Garcia-Lastra, A. Rubio and J. E. Ortega, *Phys. Rev. B: Condens. Matter Mater. Phys.*, 2012, **86**, 075469.

86 $Cu(acac)_2$ stands for bis(acetylacetonato)copper.

87 The theoretical simulation of the CuTPP(F) L_2-edge *f* distribution by considering the whole Cu $2p_{3/2}/2p_{1/2}$ set as the initial state was out of our computational resources.

88 The EE calculations were performed with no symmetry. The spinor labelling is the one reported in: P. W. M. Jacobs, *Group Theory With Applications In Chemical Physics*, Cambridge University Press, Cambridge, 2005, p. 450.

